Magnetic Phase Transitions and Magnetic Structures in Mn-based Compounds

Kiecana, A.

DOI
10.4233/uuid:7851d718-d584-45ff-bc68-ab77188e286e

Publication date
2023

Document Version
Final published version

Citation (APA)
Kiecana, A. (2023). *Magnetic Phase Transitions and Magnetic Structures in Mn-based Compounds*. [Dissertation (TU Delft), Delft University of Technology]. https://doi.org/10.4233/uuid:7851d718-d584-45ff-bc68-ab77188e286e

Magnetic phase transitions and magnetic structures in Mn-based compounds

Anika Kiecana

MAGNETIC PHASE TRANSITIONS AND MAGNETIC STRUCTURES IN MN-BASED COMPOUNDS

MAGNETIC PHASE TRANSITIONS AND MAGNETIC STRUCTURES IN MN-BASED COMPOUNDS

Proefschrift

ter verkrijging van de graad van doctor
aan de Technische Universiteit Delft,
op gezag van de Rector Magnificus, Prof. dr. ir. T.H.J.J. van der Hagen,
voorzitter van het College voor Promoties,
in het openbaar te verdedigen op maandag 25 september 2023 om 15:00 uur

door

Anika KIECANA

Master of Science in Chemistry
Maria Curie-Skłodowska University, Lublin, Poland
geboren te Tomaszów Lubelski, Poland

Dit proefschrift is goedgekeurd door de promotoren.

Samenstelling promotiecommissie bestaat uit:

Rector Magnificus	voorzitter
Prof. dr. E. H. Brück	Technische Universiteit Delft, promotor
Dr. ir. N.H. van Dijk	Technische Universiteit Delft, promotor

Onafhankelijke leden:

Prof. dr. C. Pappas	Technische Universiteit Delft
Prof. dr. L. Caron	Bielefeld University, Germany
Prof. dr. P. Svedlindh	Uppsala University, Sweden
Dr. N. Dempsey	Institut Néel, France
Prof. dr. L.D.A. Siebbeles	Technische Universiteit Delft, reservelid

The work presented in this PhD thesis was carried out in the section of Fundamental Aspects of Materials and Energy (FAME) at the Faculty of Applied Sciences, Delft University of Technology. The project received financial support from NWO, Swiss Blue Energy and RSP Technology in the framework of Industrial Partnership Programmes IPP 680-91-013.

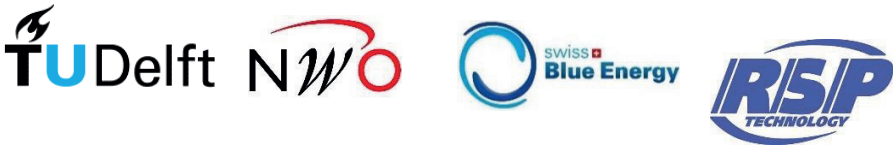

Keywords: Magnetocaloric effect, magnetic materials, phase transition, magnetic cooling, magnetic structures, $(Mn,Fe)_2(P,Si)$, antiperovskite carbides, half-Heusler alloys.

Printed by: ProefschriftMaken

Cover design: Paweł Kiecana

ISBN 978-94-6384-471-0

An electronic version of this dissertation is available at
https://repository.tudelft.nl/

Dedicated to my family

Contents

1

INTRODUCTION

The energy demand for space cooling, air conditioners (AC) and electrical fans is one of the most critical energy issues, the neglect of which will lead to a three-fold increase in energy demand by 2050 [1]. The demand for energy is determined by various aspects, including climate, societal, economic and technological developments [2]. Developing more efficient and accessible cooling technologies can suppress this trend in spite of the expected growth in cooling demand. It is anticipated that using more energy-efficient cooling technologies will reduce the energy consumption for space cooling in 2050 by 45% [1], [3]. Furthermore, using common refrigerants gives rise to deep concerns and leads to the search for more environmentally-friendly cooling systems. Among the various novel cooling technologies, magnetic cooling using the magnetocaloric effect (MCE) is a promising solution. Magnetic refrigerators can reach 60% of the Carnot efficiency, whereas, with conventional compressor-based technology, it is possible to achieve 40% [4]. Besides, compared with the vapour-compression refrigeration system, magnetic cooling is an environmentally-friendly technology as it enables the elimination of hazardous, toxic, corrosive, ozone-depleting and greenhouse substances, such as ammonia, chlorofluorocarbons, hydrochlorofluorocarbons and 1,1,1,2-tetrafluoroethane.

Industries are estimated to expel up to 60% of energy as waste heat. While the high-grade (> 922 K) and medium-grade heat ($505 - 922$ K) can be employed to produce mechanical/electrical work or can be utilized for heating purposes, the low-grade waste heat (< 505 K) is rejected due to the poor performance of energy harvesters in this temperature regime. According to recent studies, low-grade waste heat constitutes approximately 60% of the total waste heat, which also explains the importance of research on technologies enabling waste heat recovery in this temperature range. A recovery of low-grade waste heat is possible

using magnetocaloric materials (MCMs). Upon cyclic heating and cooling of MCMs, a time-varying magnetization is induced, which can be employed to produce electricity using motors, oscillators and generators [5], [6].

1.1. Magnetocaloric effect and magnetic refrigeration

The magnetocaloric effect (MCE) can be described as a heating or cooling of a magnetic material in an increasing or decreasing applied magnetic field, respectively. Although the existence of the magnetocaloric effect was first predicted using thermodynamic considerations by W. Thomson in 1860 [7], [8], the experimental discovery was made in 1917 by Weiss and Piccard, who observed a reversible temperature change of 0.7 K in nickel under the application and removal of a magnetic field of 1.5 T [9]. They distinguished the observed temperature change from the hysteresis heat and provided a thermodynamic explanation of their discovery. The first use of the MCE to reach temperatures below 1 K can be attributed to Giauque and MacDougall (1933). They experimentally achieved the temperature of 0.25 K by employing adiabatic demagnetization of a paramagnetic salt $Gd_2(SO_4)_3 \cdot 8\ H_2O$ with a magnetic field change of 0.8 T [10]. However, it took until 1976 before the first proof-of-concept magnetic refrigerator using pure Gd as a magnetocaloric material was built by Brown, reaching a temperature span of 47 K [11]. Despite the promising achievement of Brown, the magnetocaloric effect did not attract much attention until the discovery of the giant magnetocaloric effect (GMCE) in $Gd_5Si_2Ge_2$ by Pecharsky and Gschneidner (1997) [12]. The magnetocaloric effect is of particular interest to many researchers and new magnetocaloric materials (MCMs) are currently intensively explored. An overview of the main research groups focussing on the MCE is shown in Figure 1.1.

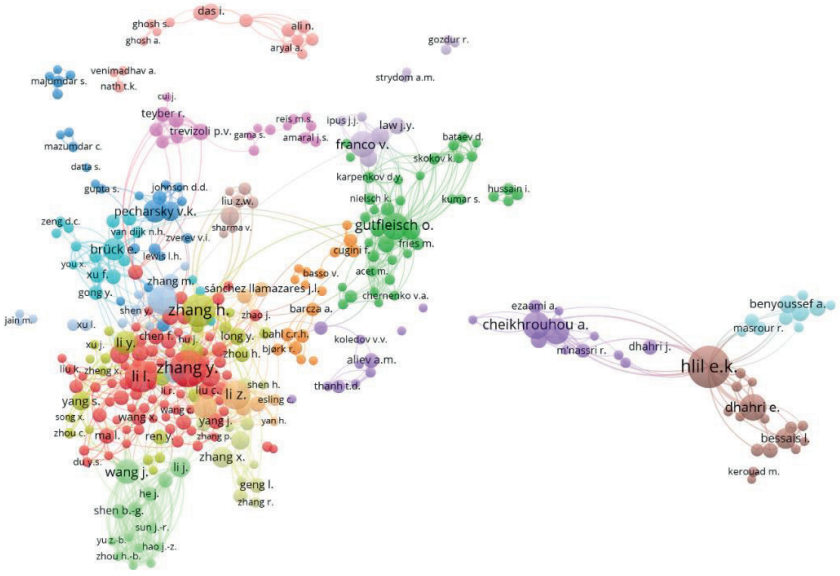

Figure 1.1: *Visualization of research groups studying the MCE (2022). A total number of 4408 researchers was found based on the Scopus database. In the presented overview, researchers with the highest number of publications in the field of MCE are presented. Lines indicate connections between various research groups.*

The magnetocaloric effect provides the foundation for magnetic refrigeration, in which a temperature change is observed upon exposing the magnetic material to a change in the externally applied magnetic field. Prototypes of magnetic refrigerators have recently been launched by Haier, BASF, Astronautics Corporation (USA), Cooltech and Magnotherm [13], [14], [64]. Although ferromagnetic materials are the most suitable for applications, it should be emphasized that the magnetocaloric effect is intrinsic to all magnetic materials. A schematic representation of the magnetic refrigeration cycle consisting of four characteristic steps is shown in Figure 1.2. In the initial step (1), the magnetic field is not applied ($\mu_0 H = 0$), and magnetic moments are randomized, which results in a large magnetic entropy Sm. In the second step (2), the magnetic field is applied to a material under adiabatic conditions, causing an alignment of the magnetic moments. The total entropy (S) includes the magnetic (Sm), lattice (Sl) and electronic (Se) contributions. Adiabatic conditions imply no change in the total entropy during the magnetization process ($\Delta S = 0$). When the magnetic entropy is reduced in the applied magnetic field, the magnetic entropy change is negative ($\Delta S_m < 0$). This leads to an increase in the lattice and electronic entropy, which consequently is observed as a rise in the temperature of the material. Next, the heat is transferred to the surrounding by a heat-transfer medium (3). Finally, the magnetic field is removed under adiabatic conditions, which causes an increase in S_m and a cooling of the magnetic material below ambient temperature (4) [15].

The temperature difference observed during the adiabatic demagnetization process is called adiabatic temperature change (ΔT_{ad}), which reveals by how many degrees the magnetic material can be cooled. When the magnetic field is applied isothermally, the MCE can be quantified using the isothermal magnetic entropy change ΔS_m, which corresponds to the amount of heat transported at a given temperature. Both these parameters are essential to evaluate the magnetocaloric effect in magnetic materials.

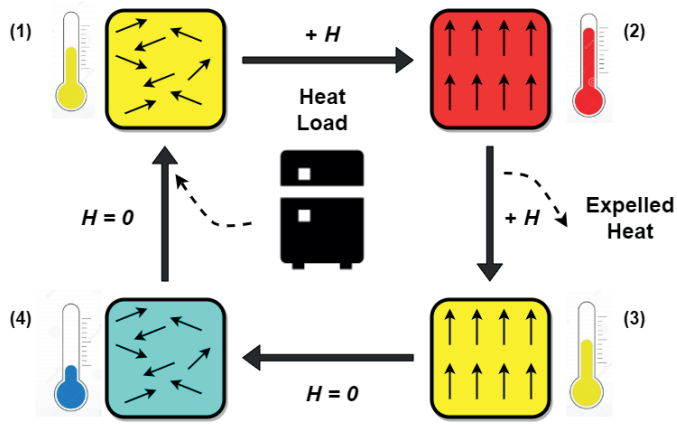

Figure 1.2: *Schematic visualization of a magnetic cooling cycle.*

1.2. Magnetocaloric materials

Magnetocaloric materials (MCMs) with the potential for practical use in commercial magnetic refrigerators should comply with several requirements. Promising magnetocaloric materials should consist of non-toxic, environmentally friendly and non-critical elements. The price, availability and accessibility are other significant factors that strongly narrow down the search of MCMs for commercial applications. Mn-based magnetocaloric materials can become a good alternative to expensive and not readily available materials due to a low cost and their high abundance. Additionally, a suitable MCM should possess a high mechanical and chemical stability and a good thermal conductivity. Given the fact that magnetocaloric materials for the purpose of magnetic cooling should be characterized by a large magnetic entropy change, ideally no thermal hysteresis (ΔT_{hys}) and a Curie temperature (T_C) close to room temperature, it becomes challenging to find suitable materials that satisfy all the aforementioned conditions.

Magnetocaloric materials can display either a first-order magnetic transition (FOMT) or a second-order magnetic transition (SOMT). Albeit materials exhibiting a FOMT show a significant magnetic entropy change (ΔS_m), which reflects a large magnetocaloric effect, a concomitant hysteresis hurdles the reversibility of the magnetization process and often contributes to a weakening of mechanical properties. On the other hand, the magnetic transition of materials showing a SOMT is non-hysteretic and the associated ΔS_m is generally lower. Hence, the materials at the border of a FOMT and a SOMT are of great interest for

practical application as they show a minimal hysteresis, while a significant magnetocaloric effect is maintained.

Thus far, various magnetic materials have been studied in terms of their magnetocaloric effect. Following the discovery of a giant magnetocaloric effect in $Gd_5Ge_2Si_2$ by Pecharsky and Gschneidner [12], materials showing a FOMT have been intensively studied, e.g.: Dy_5Si_3Ge [16], $(Mn,Fe)_2(P,X)$ compounds with X = As, Ge and Si [17]–[22], $RECo_2$ and $REAl_2$ (RE: rear earth metal) [23], $MnAs_{1-x}Sb_x$ [24], [25], $La(Fe_xSi_{1-x})_{13}$ compounds and their hydrides [26]–[28]. Despite a strong focus on the FOMT, extensive studies have also been dedicated to materials exhibiting a SOMT, e.g.: Gd [29], $AlFe_2B_2$ [30], $Gd_5Si_{4-x}Ge_x$ [31], RE_6Co_2Ga (RE = Ho, Dy, Gd) [23], $(Gd_{1-x}RE_x)_5Si_4$ (RE = Dy, Ho) [32], Mn_5PB_2 [33] and MnCoGe [34]. Gd is commonly used as a benchmark magnetocaloric material in magnetic refrigerator prototypes. Despite a large magnetic moment, a reversible SOMT and a T_C near room temperature (T_C = 294 K) [29], the practical use of Gd for commercially available magnetic coolers is limited due to the high cost and limited availability of this element. Therefore, in this dissertation we present research on the potential of Mn-based MCMs: $(Mn,Fe)_2(P,Si)$, Mn_3AC (A: Sn, Zn, Fe) and $(MnNiSi)_{1-x}(CrCoGe)_x$ alloys.

1.2.1. $(Mn,Fe)_2(P,Si)$ family of compounds

Fe_2P-based alloys attract much attention due to their interesting magnetic properties originating from the presence of two magnetic sites. The substitution of more than 10 at.% Si for P will induce a transformation from the hexagonal structure into the body-centred orthorhombic structure [35], [36]. It should be noted that the low T_C ($\approx$ 217 K) of the parent compound is an obstacle for its application in magnetic refrigerators. In order to avoid the change in the crystal structure, Fe atoms can be partially substituted by Mn. These modifications lead to the formation of interesting compounds of a generic formula $(Mn,Fe)_2(P,Si)$. With a tuneable T_C, a large $|\Delta S_m|$ and an adjustable thermal hysteresis (ΔT_{hys}), the $(Mn,Fe)_2(P,Si)$ family of compounds shows great potential for magnetic cooling and magnetic heat recovery purposes.

The $(Mn,Fe)_2(P,Si)$ alloys crystallize in the same hexagonal structure (space group: *P-62m*), as the parent compound (Fe_2P). The hexagonal unit cell of the $(Mn,Fe)_2(P,Si)$ compound is presented in Figure 1.3. Mn atoms preferentially occupy the pyramidal *3g* site and Fe has a preference for the tetrahedral *3f* site. The *3g* site is associated with a larger magnetic moment compared to the *3f* site. According to DFT calculations and neutron powder diffraction studies, Si preferentially occupies the *2c* site and P preferentially occupies the *1b* site [37], [38]. In a broad compositional range of $(Mn,Fe)_2(P,Si)$, the ferromagnetic (FM) to paramagnetic (PM) transition is accompanied by abrupt changes in the *a* and *c* lattice parameters, while the hexagonal crystal structure is preserved and the volume is hardly changed at the transition, indicating the magnetoelastic character of the transition. It has been proposed that a large MCE and the magnetoelastic nature of the transition originates from *"mixed magnetism"* – a coexistence of a weak magnetism of the Fe atoms in the presence of

a strong magnetism of the Mn atoms [39]. The Mn-rich region of this family of compounds has been studied in detail due to the possibility to obtain a giant magnetocaloric effect (GMCE) at ambient temperature accompanied by a small thermal hysteresis. The Fe-rich region of the $(Mn,Fe)_2(P,Si)$ system is less studied. However, these compounds are less expensive and can show a higher magnetic moment compared to Mn-rich alloys [21], [40].

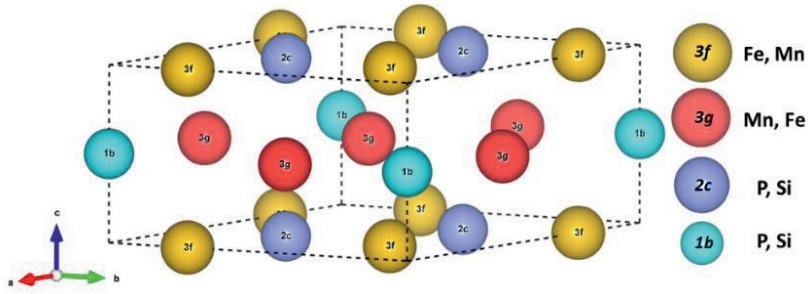

Figure 1.3: *Unit cell of the hexagonal $(Mn,Fe)_2(P,Si)$ structure with specified crystallographic sites.*

1.2.2. Mn-based antiperovskite carbides

Antiperovskite carbides Mn_3AC (where *A*: metal or semiconductor) possess a perovskite-type structure, but the positions of anions and cations are reversed. This also explains the other name of this class of compounds: "*inverse perovskites*". The cubic antiperovskite structure with general formula Mn_3AC is presented in Figure 1.4. While the Mn cations reside on the face-centred *3c* site, the *A* atoms occupy the *1a* corner site and the C atoms occupy a body-centred *1b* site. Antiperovskite carbides appear attractive due to their versatile functionalities and intriguing underlying magnetism. A wide variety of various physical phenomena such as superconductivity [41], the magnetovolume effect (MVE) [42], [43], the piezomagnetic effect [44], [45] and giant magnetoresistance (GMR) [46], [47] have been studied in these compounds. A strong coupling of the lattice, spin and electron carriers makes antiperovskites highly sensitive to subtle changes in the stoichiometry, applied magnetic field, temperature and pressure. In contrast to their perovskite analogues, antiperovskites show metallic behaviour, good thermal conductivity and enhanced mechanical stability. The compositions involve non-toxic and inexpensive elements, which is in favour of commercial applications.

Mn_3SnC crystallizes in the cubic structure (space group: *Pm-3m*), but despite its simple structure, the Mn atoms show two different magnetic moments. Two Mn atoms in the square configuration (*a-b* plane) carry a large AFM moment ($\mu_1 = 2.3\ \mu_B$/Mn) and one Mn atom has a smaller FM component ($\mu_2 = 0.7\ \mu_B$/Mn) along the *c*-axis [48], [49]. The stability of the cubic structure is determined by the ionic radii (*r*) implemented in the Goldschmidt tolerance factor τ:

$$\tau = \frac{r_A + r_{Mn}}{\sqrt{2}(r_C + r_{Mn})} \tag{1.1}$$

From Figure 1.4, presenting the unit cell of the antiperovskite compound, it can be seen that contact between the Mn, C and A ions occurs when:

$$d_{A-Mn} = r_A + r_{Mn} \tag{1.2}$$

$$d_{C-Mn} = r_C + r_{Mn} \tag{1.3}$$

Consequently, for the cubic structure the following relation is satisfied:

$$r_A + r_{Mn} = \sqrt{2}\,(r_C + r_{Mn}) \tag{1.4}$$

The presented relations explain the origin of the Goldschmidt tolerance factor (τ). It becomes apparent that the structure is cubic when the *A*-Mn and C-Mn bonds match, which results in τ = 1.0. A decrease in τ is ascribed to formation of lower symmetry structures as the stability of the structure is mainly ascribed to the electrostatic energy due to the arrangement of *A* ions in the Mn_3A cage around C atom. The value of τ is directly related to the packing fraction of ions in the unit cell. When *A* ions are too small, the Mn_6C octahedra tilt in order to reduce the amount of free space in the Mn sub-lattice. The symmetry of many perovskite-type compounds vary with the temperature. The low temperature structure is often of a lower symmetry (*hettotype*) and the high-temperature structure is usually cubic (*aristotype*) [50].

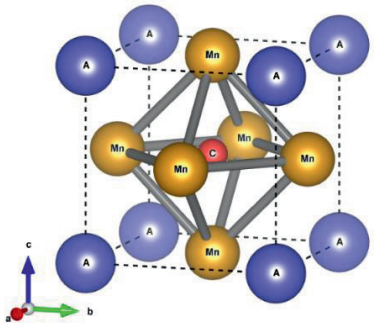

Figure 1.4: *Unit cell of the Mn_3AC antiperovskite carbide, where A is a metal or semiconductor.*

The study of the magnetocaloric effect in antiperovskite carbides is relatively new, and its emergence can be attributed to the discovery of a large MCE in Mn_3GaC [51] and Mn_3SnC [52]. In this work, special attention is laid on Mn_3SnC, exhibiting a non-hysteretic ferrimagnetic (FiM) to paramagnetic (PM) transition of first-order, which results in a large

MCE. Additionally, the magnetic transition occurs close to room temperature ($T_C \approx 273$ K), which makes this compound an ideal parent compound for the search of efficient and environmentally-friendly MCMs for cooling applications.

1.2.3. MnNiSi half-Heusler alloys

Mn*AX* compounds (*A*: Ni, Co; *X*: Si, Ge) have received considerable attention for their large magnetic entropy change (ΔS_m) associated with the potential magnetostructural transition (MST) near room temperature. An easily attained coupling between the magnetic ($T_C \approx$ 345-355 K) and structural ($T_{STR} \approx 650$ K) transitions in MnCoGe, makes these alloys intensively explored [34], [53], [54]. The MnNiSi-based half-Heusler alloys are less studied since the high T_C (≈ 622 K) of the parent compound followed by the first-order structural transition ($T_{STR} \approx 1210$ K) impedes the realisation of the magnetostructural coupling at room temperature [55]–[57]. On the other hand, MnNiSi-based alloys consist of abundant and inexpensive elements, which is advantageous for commercial use in magnetic refrigerators.

A martensitic transition occurs from the high-temperature hexagonal austenite phase (space group: $P6_3/mmc$) to the low-temperature orthorhombic phase (space group: *Pnma*). This structural transition is followed by a second-order PM-FM transition upon cooling. The hexagonal and orthorhombic unit cells of the MnNiSi are presented in Figure 1.5. To achieve a first-order magnetostructural transition (FOMST) in the vicinity of room temperature, various approaches have been used including off-stoichiometry [58], heat treatment [59], applied pressure [60], [61], element substitution and isostructural alloying [55], [56], [61]–[63]. It has been reported that using a single element doping is not sufficient to lower T_C and T_{STR} to room temperature. Therefore, most doping approaches focus on the substitution of two or three elements in order to sufficiently reduce the magnetic and structural transitions and achieve magnetostructural coupling at room temperature.

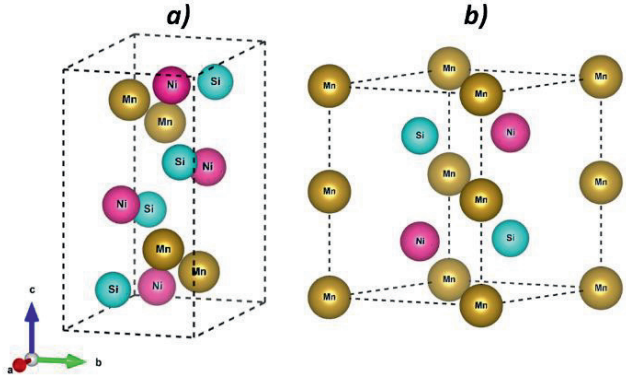

Figure 1.5: *Schematic visualization of a) the orthorhombic (Pnma) and b) the hexagonal ($P6_3/mmc$) structures of MnNiSi.*

1.3. Thesis outline

Among various magnetocaloric materials, Mn-based compounds appear especially promising. Mn is an abundant, innocuous and inexpensive element. Besides, a broad variety of alloys containing Mn possess a significant magnetic moment density. Therefore, the presented work focuses on magnetic, magnetocaloric, structural and microstructural properties of various Mn-based magnetocaloric materials: $(Mn,Fe)_2(P,Si)$, Mn_3AC (A: Sn, Zn, Fe), $(MnNiSi)_{1-x}(CrCoGe)_x$.

Chapter 2 provides the theoretical background of selected aspects. The derivation of magnetic entropy change with the use of thermodynamic relations is shown. Additionally, different types of exchange interactions and types of magnetic order are briefly described.

Chapter 3 presents a short overview of the experimental methods. In this chapter, sample preparation techniques, experimental methods and DFT calculations are introduced.

In **Chapter 4** the effect of Co and Ni substitution for Mn in Fe-rich $(Mn,Fe)_2(P,Si)$ compounds is discussed. In this work, we aimed to reduce T_C and thermal hysteresis (ΔT_{hys}) to obtain promising magnetic materials showing the magnetic transition near ambient temperature. The influence of Co and Ni on the formation and composition of the impurity phase and its impact on magnetic properties were studied. Mössbauer spectroscopy and DFT calculations were used to elucidate site substitution by dopant atoms and to explain changes in local magnetic moments.

Chapter 5 describes the effect of the heat treatment in various metal/non-metal ratios of Fe-rich $(Mn,Fe)_2(P,Si)$ melt-spun ribbons. SEM and EDS measurements were used to study the evolution of the microstructure and impurity phases as a function of composition and annealing temperature. The formation of a new impurity phase was observed in the metal-rich region. A correlation between lattice parameters and magnetic moments is discussed with respect to compositional changes upon heat treatment.

The influence of Zn substitution for Sn in $Mn_3Sn_{1-x}Zn_xC$ antiperovskite carbides is systematically studied in **Chapter 6**. The influence of doping on magnetic and magnetocaloric effect is discussed with reference to the literature. Neutron powder diffraction (NPD) was employed to study the evolution of the magnetic moment and magnetic structure upon increasing Zn doping and with temperature. A competition between the antiferromagnetic (AFM) and ferromagnetic (FM) interactions in the $Mn_3Sn_{1-x}Zn_xC$ system was revealed.

Chapter 7 discusses the impact of Fe substitution for Sn in $Mn_3Sn_{1-x}Fe_xC$ antiperovskite carbides. The evolution of the microstructure upon Fe doping was studied using SEM/EDS and the magnetic entropy change was measured for the most promising compounds. The effect of Fe doping on the magnetic structure was revealed using neutron powder diffraction. DFT calculations were utilized to elucidate the influence of Fe doping on magnetic properties in $Mn_3Sn_{1-x}Fe_xC$ alloys.

The effect of isostructural alloying of MnNiSi with CrCoGe is presented in **Chapter 8**. The changes in T_C and the structural transition (T_{STR}) were studied using SQUID and high-temperature DSC measurements. The impact of CrCoGe alloying on the character of the structural transition and magnetic properties was shown. DFT calculations revealed the site occupancy by Cr, Co and Ge.

References

[1] "The Future of Cooling" OECD, 2018, doi: 10.1787/9789264301993-en.

[2] A. Deroubaix, I. Labuhn, M. Camredon, B. Gaubert, P.-A. Monerie, M. Popp, J. Ramarohetra, Y. Ruprich-Robert, L. G. Silvers, G. Siour, "Large uncertainties in trends of energy demand for heating and cooling under climate change", *Nat. Commun.*, *12*(1), pp. 6–13, 2021, doi: 10.1038/s41467-021-25504-8.

[3] E. Brück, "Developments in magnetocaloric refrigeration", *J. Phys. D. Appl. Phys.*, *38*(23), 2005, doi: 10.1088/0022-3727/38/23/R01.

[4] C. Zimm, A. Jastrab, A. Sternberg, V. Pecharsky, K. Gschneidner, M. Osborne, and I. Anderson, "Description and Performance of a Near-Room Temperature Magnetic Refrigerator", *Adv. Cryog. Eng.*, pp. 1759–1766, 1998, doi: https://doi.org/10.1007/978-1-4757-9047-4_222.

[5] R. A. Kishore and S. Priya, "Low-grade waste heat recovery using the reverse magnetocaloric effect", *Sustain. Energy Fuels*, *1*(9), pp. 1899–1908, 2017, doi: 10.1039/c7se00182g.

[6] D. Dzekan, A. Waske, K. Nielsch, and S. Fähler, "Efficient and affordable thermomagnetic materials for harvesting low grade waste heat", *APL Mater.*, *9*(1), 2021, doi: 10.1063/5.0033970.

[7] W. Thomson, *Cyclopedia of the Physical Sciences*. Richard Green and Company, p. 838, 1860.

[8] W. Thomson, "On the thermoelastic, thermomagnetic, and pyroelectric properties of matter", *Phil. Mag.*, *5*(28), pp. 4–27, 1878, doi: 10.1080/14786447808639378.

[9] P. Weiss and A. Piccard, "Le phénomène magnétocalorique", *J. Phys. Theor. Appl.*, *7*(1), pp. 103–109, 1917.

[10] W. F. Giauque and D. P. MacDougall, "Attainment of temperatures below 1° absolute by demagnetization of $Gd_2(SO_4)_{38}H_2O$", *Phys. Rev.*, *43*(9), p. 768, 1933, doi: 10.1103/PhysRev.43.768.

[11] G. V. Brown, "Magnetic heat pumping near room temperature", *J. Appl. Phys.*, *47*(8), pp. 3673–3680, 1976, doi: 10.1063/1.323176.

[12] V. K. Pecharsky and K. A. Gschneidner, "Giant magnetocaloric effect in $Gd_5(Si_2Ge_2)$", *Phys. Rev. Lett.*, *78*(23), pp. 4494–4497, 1997, doi: 10.1103/PhysRevLett.78.4494.

[13] Sustainable brands, (6 January 2015). *BASF, Haier, Astronautics Corp Unveil Next-Gen Refrigeration Technology at CES 2015.* Retrieved from: https://sustainablebrands.com/read/chemistry-materials-packaging/basf-haier-astronautics-corp-unveil-next-gen-refrigeration-technology-at-ces-2015.

[14] Businesswire (15 June 2016), *Cooltech Applications Launches the First Magnetic Cooling System for Commercial Refrigeration.* Retrieved from: https://www.businesswire.com/news/home/20160615005178/en/Cooltech-Applications-Launches-the-First-Magnetic-Cooling-System-for-Commercial-Refrigeration#:~:text=Release Summary-,Cooltech Applications launches the first magnetic cooling system for commercial.

[15] O. Tegus, E. Brück, K. H. J. Buschow, and F. R. De Boer, "Transition-metal-based magnetic refrigerants for room-temperature applications", *Nature*, *415*(6868), pp. 150–152, 2002, doi: 10.1038/415150a.

[16] K. A. Gschneidner Jr., V. K. Pecharsky, A. O. Pecharsky, V. V Ivtchenko, and E. M. Levin, "The nonpareil R $_5$(Si_xGe_{1-x})$_4$", *J. Alloys Compd.*, *303-304*(1-2), pp. 214–222, 2000, doi: https://doi.org/10.1016/S0925-8388(00)00747-7.

[17] A. Yan, K. H. Müller, L. Schultz, and O. Gutfleisch, "Magnetic entropy change in melt-spun MnFePGe (invited)", *J. Appl. Phys.*, *99*(8), 2006, doi: 10.1063/1.2162807.

[18] J. L. Wang, S. J. Campbell, O. Tegus, E. Brück, and S. X. Dou, "Magnetic phase transition in $MnFeP_{0.5}As_{0.4}Si_{0.1}$", *J. Phys. Conf. Ser.*, *217*(1), 2010, doi: 10.1088/1742-6596/217/1/012132.

[19] O. Tegus, G. X. Lin, W. Dagula, B. Fuquan, L. Zhang, E. Brück, F. R. de Boer, and K. H. J. Buschow, "A model description of the first-order phase transition in $MnFeP_{1-x}As_x$", *J. Magn. Magn. Mater.*, *290-291* PA, pp. 658–660, 2005, doi: 10.1016/j.jmmm.2004.11.325.

[20] N. H. Dung, L. Zhang, Z. Q. Ou, and E. Brück, "Magnetoelastic coupling and magnetocaloric effect in hexagonal Mn-Fe-P-Si compounds", *Scr. Mater.*, *67*(12), pp. 975–978, 2012, doi: 10.1016/j.scriptamat.2012.08.036.

[21] Z. Q. Ou, L. Zhang, N. H. Dung, L. Caron, and E. Brück, "Structure, magnetism and magnetocalorics of Fe-rich $(Mn,Fe)_{1.95}P_{1-x}Si_x$ melt-spun ribbons", *J. Alloys Compd.*, *710*, pp. 446–451, 2017, doi: 10.1016/j.jallcom.2017.03.266.

[22] J. Lai, B. Huang, X. Miao, N. van Thang, X. You, M. Maschek, L. van Eijck, D. Zeng, N. van Dijk, and E. Brück, "Combined effect of annealing temperature and vanadium substitution for mangetocaloric $Mn_{1.2-x}V_xFe_{0.75}P_{0.5}Si_{0.5}$ alloys", *J. Alloys Compd.*, *803*, pp. 671–677, 2019, doi: 10.1016/j.jallcom.2019.06.239.

[23] D. Guo, L.M. Moreno-Ramírez, C. Romero-Muñiz, Y. Zhang, Y. Zhang, J.-Y. Law, V. Franco, J. Wang, and Z. Ren., "First- and second-order phase transitions in RE_6Co_2Ga (RE = Ho, Dy or Gd) cryogenic magnetocaloric materials", *Sci. China Mater.*, *64*(11), pp. 2846–2857, 2021, doi: 10.1007/s40843-021-1711-5.

[24] L. Tocado, E. Palacios, and R. Burriel, "Adiabatic measurement of the giant magnetocaloric effect in MnAs", *J. Therm. Anal. Calorim.*, *84*(1), pp. 213–217, 2006, doi: 10.1007/s10973-005-7180-z.

[25] H. Wada, T. Morikawa, K. Taniguchi, T. Shibata, Y. Yamada, and Y. Akishige, "Giant magnetocaloric effect of $MnAs_{1-x}Sb_x$ in the vicinity of first-order magnetic transition", *Phys. B Condens. Matter*, *328*(1-2), pp. 114–116, 2003, doi: 10.1016/S0921-4526(02)01822-7.

[26] V. Paul-Boncour and L. Bessais, "Tuning the magnetocaloric properties of the $La(Fe,Si)_{13}$ compounds by chemical substitution and light element insertion", *Magnetochemistry*, *7*(1), pp. 1–18, 2021, doi: 10.3390/magnetochemistry7010013.

[27] A. Boutahar, M. Phejar, V. P. Boncour, L. Bessais, and H. Lassri, "Theoretical work in magnetocaloric effect of $LaFe_{13-x}Si_x$ compounds", *J. Supercond. Nov. Magn.*, *27*(8), pp. 1795–1800, 2014, doi: 10.1007/s10948-014-2542-z.

[28] A. Fujita, S. Fujieda, Y. Hasegawa, and K. Fukamichi, "Itinerant-electron metamagnetic transition and large magnetocaloric effects in (formula presented) compounds and their hydrides", *Phys. Rev. B - Condens. Matter Mater. Phys.*, *67*(10), p. 12, 2003, doi: 10.1103/PhysRevB.67.104416.

[29] S. Yu Dankov, A. M. Tishin, V. K. Pecharsky, and K. A. Gschneidner, "Magetic phase transitions and the magnetothermal properties of gadolinium", *Phys. Rev. B*, *57*(6), pp. 3478–3490, 1998.

[30] X. Tan, P. Chai, C. M. Thompson, and M. Shatruk, "Magnetocaloric effect in $AlFe_2B_2$: Toward magnetic refrigerants from earth-abundant elements", *J. Am. Chem. Soc.*, *135*(25), pp. 9553–9557, 2013, doi: 10.1021/ja404107p.

[31] V. K. Pecharsky and K. A. Gschneidner Jr., "Tunable magnetic regenerator alloys with a giant magnetocaloric effect for magnetic refrigeration from ∼20 to ∼290 K", *Appl. Phys. Lett.*, *70*(24), pp. 3299–3301, 1997, doi: 10.1063/1.119206.

[32] W. Wu, Z. Feng, and L. Guo, "Estimation on magnetic refrigeration material $(Gd_{1-x}RE_x)_5Si_4$ (RE = Dy, Ho)", *J. Mater. Sci. Technol.*, *22*(6), pp. 839–842, 2006.

[33] Z. G. Xie, D. Y. Geng, and Z. D. Zhang, "Reversible room-temperature magnetocaloric effect in Mn_5PB_2", *Appl. Phys. Lett.*, *97*(20), pp. 2–5, 2010, doi: 10.1063/1.3518064.

[34] N. T. Trung, V. Biharie, L. Zhang, L. Caron, K. H. J. Buschow, and E. Brück, "From single- to double-first-order magnetic phase transition in magnetocaloric $Mn_{1-x}Cr_xCoGe$ compounds", *Appl. Phys. Lett.*, *96*(16), pp. 2010–2012, 2010, doi: 10.1063/1.3399774.

[35] L. Severin, L. Haggstrom, L. Nordstrom, Y. Andersson, and B. Johansson, "Magnetism and crystal structure in orthorhombic Fe_2P: A theoretical and experimental study", *J. Phys. Condens. Matter*, *7*(1), pp. 185–198, 1995, doi: 10.1088/0953-8984/7/1/016.

[36] L. Haggstrom, L. Severin, and A. Yvonne, "Experimental and theoretical studies of Si/P substituted orthorombic Fe_2P", *Hyperfine Interact.*, *95*, pp. 2075–2079, 1994, doi: 10.1021/jp9531974.

[37] F. Guillou, G. Porcari, H. Yibole, N. Van Dijk, and E. Brück, "Taming the first-order transition in giant magnetocaloric materials", *Adv. Mater.*, *26*(17), pp. 2671–2675, 2014, doi: 10.1002/adma.201304788.

[38] N. H. Dung, Z. Q. Ou, L. Caron, L. Zhan, D. T. C. Thanh, G. A. de Wijs, R. A. de Groot, K. H. J. Buschow, and E. Brück, "Mixed magnetism for refrigeration and energy conversion", *Adv. Energy Mater.*, *1*(6), pp. 1215–1219, 2011, doi: 10.1002/aenm.201100252.

[39] M. F. J. Boeije, M. Maschek, X. F. Miao, N. V. Thang, N. H. Van Dijk, and E. Brück, "Mixed magnetism in magnetocaloric materials with first-order and second-order magnetoelastic transitions", *J. Phys. D. Appl. Phys.*, *50*(17), 2017, doi: 10.1088/1361-6463/aa5db9.

[40] X. F. Miao, Y. Mitsui, A. I. Dugulan, L. Caron, N. V. Thang, P. Manuel, K. Koyama, K. Takahashi, N. H. van Dijk, and E. Brück, "Kinetic-arrest-induced phase coexistence and metastability in $(Mn,Fe)_2(P,Si)$", *Phys. Rev. B*, *94*(9), 2016, doi: 10.1103/PhysRevB.94.094426.

[41] N. Hoffmann, T. F. T. Cerqueira, J. Schmidt, and M. A. L. Marques, "Superconductivity in antiperovskites", *npj Comput. Mater.*, *8*(1), p. 150, 2022, doi: 10.1038/s41524-022-00817-4.

[42] K. Takenaka and H. Takagi, "Giant Negative Thermal Expansion in Ge-Doped Anti-Perovskite Manganese Nitrides", *Appl. Phys. Lett.*, *87*, p. 261902, 2005, doi: 10.1063/1.2147726.

[43] T. Hamada and K. Takenaka, "Giant negative thermal expansion in antiperovskite manganese nitrides", *J. Appl. Phys.*, *109*, 2011, doi: 10.1063/1.3540604.10.1063/1.3540604.

[44] J. Zemen, Z. Gercsi, and K. Sandeman, "Piezomagnetism as a counterpart of the magnetovolume effect in magnetically frustrated Mn-based antiperovskite nitrides", *Phys. Rev. B*, *96*, 2017, doi: 10.1103/PhysRevB.96.024451.

[45] P. Lukashev, R. F. Sabirianov, and K. Belashchenko, "Theory of the piezomagnetic effect in Mn-based antiperovskites", *Phys. Rev. B - Condens. Matter Mater. Phys.*, *78*(18), 2008, doi: 10.1103/PhysRevB.78.184414.

[46] Y. B. Li, W. F. Li, W. J. Feng, Y. Q. Zhang, and Z. D. Zhang, "Magnetic, transport and magnetotransport properties of $Mn_{3+x}Sn_{1-x}C$ and $Mn_3Zn_ySn_{1-y}C$ compounds", *Phys. Rev. B - Condens. Matter Mater. Phys.*, *72*(2), pp. 1–8, 2005, doi: 10.1103/PhysRevB.72.024411.

[47] B. S. Wang, W. J. Lu, S. Lin, J. C. Lin, P. Tong, B. C. Zhao, W. H. Song, and Y. P. Sun, "Magnetic / structural diagram , chemical composition-dependent magnetocaloric effect in self-doped antipervoskite compounds $Sn_{1-x}CMn_{3+x}$ ($0 \leq x \leq 0.40$)", *J. Magn. Magn. Mater.*, *324*, pp. 773–781, 2012, doi: 10.1016/j.jmmm.2011.09.014.

[48] E. T. Dias, K. R. Priolkar, A. Das, G. Aquilanti, Ö. Çakir, M. Acet, and A. K. Nigam, "Effect of local structural distortions on magnetostructural transformation in Mn_3SnC", *J. Phys. D. Appl. Phys.*, *48*(29), 2015, doi: 10.1088/0022-3727/48/29/295001.

[49] J. Yan, Y. Sun, Y. Wen, L. Chu, M. Wu, Q. Huang, C. Wang, J. W. Lynn, and Y. Chen, "Relationship between spin ordering, entropy, and anomalous lattice

variation in $Mn_3Sn_{1-e}Si_{\varepsilon}C_{1-\delta}$ compounds", *Inorg. Chem.*, *53*(4), pp. 2317–2324, 2014, doi: 10.1021/ic403063t.

[50] M. T. Sebastian, Dielectric materials for wireless communication, *ABO_3 type perovskites*, pp. 161 – 203, 2008, doi:10.1016/B978-0-08-045330-9.00006-6.

[51] T. Tohei, H. Wada, and T. Kanomata, "Negative magnetocaloric effect at the antiferromagnetic to ferromagnetic transition of Mn_3GaC", *J. Appl. Phys.*, *94*(3), 1800–1802, 2003, doi: 10.1063/1.1587265.

[52] B. S. Wang, P. Tong, Y. P. Sun, X. Luo, X. B. Zhu, G. Li, X. D. Zhu, S. B. Zhang, Z. R. Yang, W. H. Song, and J. M. Dai, "Large magnetic entropy change near room temperature in antiperovskite $SnCMn_3$", *Epl*, *85*(4), 2009, doi: 10.1209/0295-5075/85/47004.

[53] P. E. Markin, N. V. Mushnikov, E. G. Gerasimov, A. V. Proshkin, and A. S. Volegov, "Magnetic and magnetocaloric properties of $(MnCo)_{1-x}Ge$ compounds", *Phys. Met. Metallogr.*, *114*(11), 893–903, 2013, doi: 10.1134/S0031918X13110082.

[54] X. Si, Y. Liu, Y. Shen, W. Yu, X. Ma, Z. Zhang, Y. Xu, and T. Gao, "Critical behavior and magnetocaloric effect near room temperature in $MnCo_{1-x}Ti_xGe$ alloys", *Intermetallics*, *93*, pp. 30–39, 2018, doi: 10.1016/j.intermet.2017.11.001.

[55] L. M. Moreno-Ramírez, Díaz-García, J. Y. Law, A. K. Giri, and V. Franco, "Hysteresis, latent heat and cycling effects on the magnetocaloric response of $(NiMnSi)_{0.66}(Fe_2Ge)_{0.34}$ alloy", *Intermetallics*, *131*, p. 107083, 2021, doi: 10.1016/j.intermet.2020.107083.

[56] J. Chen, H. G. Zhang, E. K. Liu, M. Yue, Q. M. Lu, W. H. Wang, G. H. Wu, and J. X. Zhang, "Wide temperature window of magnetostructural transition achieved in $Mn_{0.4}Fe_{0.6}NiSi_{1-x}Ga_x$ by a two-step isostructural alloying process", *AIP Adv.*, *6*(5), pp. 0–6, 2016, doi: 10.1063/1.4944704.

[57] P. Dutta, S. Pramanick, S. Chattopadhyay, D. Das, and S. Chatterjee, "Observation of colossal magnetocaloric effect and its dependence on applied hydrostatic pressure in thermally cycled $Mn0.53Fe_{0.47}NiSi_{0.53}Ge_{0.47}$ alloy", *J. Alloys Compd.*, *735*, pp. 2087–2091, 2018, doi: 10.1016/j.jallcom.2017.11.379.

[58] A. Ghosh, P. Sen, and K. Mandal, "Measurement protocol dependent magnetocaloric properties in a Si-doped Mn-rich Mn-Ni-Sn-Si off-stoichiometric Heusler alloy", *J. Appl. Phys.*, *119*, 2016, doi: 10.1063/1.4948962.

[59] J. H. Chen, T. Poudel Chhetri, A. Us Saleheen, D. P. Young, I. Dubenko, N. Ali, and S. Stadler, "Effects of heat treatments on magneto-structural phase transitions in MnNiSi-FeCoGe alloys", *Intermetallics*, *112*, 2019, doi: 10.1016/j.intermet.2019.106547.

[60] T. Samanta, D. L. Lepkowski, A. U. Saleheen, A. Shankar, J. Prestigiacomo, I. Dubenko, A. Quetz, I. W. H. Oswald, G. T. McCandless, J. Y. Chan, P. W. Adams, D. P. Young, N. Ali, and S. Stadler, "Effects of hydrostatic pressure on magnetostructural transitions and magnetocaloric properties in $(MnNiSi)_{1-x}(FeCoGe)_x$", *J. Appl. Phys.*, *117*(12), 2015, doi: 10.1063/1.4916339.

[61] P. Lloveras, T. Samanta, M. Barrio, I. Dubenko, N. Ali, J.-L. Tamarit, and S. Stadler, "Giant reversible barocaloric response of $(MnNiSi)_{1-x}(FeCoGe)_x$ (x = 0.39, 0.40, 0.41)", *APL Mater.*, *7*(6), pp. 0–9, 2019, doi: 10.1063/1.5097959.

[62] S. Ghosh, P. Sen, and K. Mandal, "Magnetostructural transition and large magnetocaloric effect in $(Mn_{0.6}Fe_{0.4})NiSi_{1-x}Al_x$ (x = 0.06–0.08) alloys," *J. Magn. Magn. Mater.*, *500*, pp. 0–21, 2020, doi: 10.1016/j.jmmm.2019.166345.

[63] C. L. Zhang, Y. G. Nie, H. F. Shi, E. J. Ye, J. Q. Zhao, Z. D. Han, H. C. Xuan, and D. H. Wang, "Tunable magnetostructural coupling and large magnetocaloric effect in $Mn_{1-x}Ni_{1-x}Fe_{2x}Si_{1-x}Ga_x$," *J. Magn. Magn. Mater.*, *432*, pp. 527–531, 2017, doi: 10.1016/j.jmmm.2017.02.046.

[64] Next generation cooling. Retrieved from: https://www.magnotherm.com/.

2

THEORETICAL ASPECTS

The magnetic entropy change (ΔS_m) and adiabatic temperature change (ΔT_{ad}) are used to quantify the magnetocaloric effect (MCE). In the present work, the magnetic entropy change was derived from the temperature-dependent magnetization (*M-T*) curves measured at varying magnetic fields using the Maxwell equation. The Maxwell equation and its derivation is hereby presented by means of thermodynamic relations. This part is followed by a short overview of exchange interactions and the main types of magnetic order discussed in this work.

2.1. Derivation of the isothermal entropy change

From the first law of thermodynamics, the differential change in the internal energy of the system (dU) can be defined as:

$$dU = dQ + dW \tag{2.1}$$

where dQ is the differential change of heat and dW is the differential element of work done on the system. A differential change of heat can be expressed in terms of entropy (S) as:

$$dQ = TdS \tag{2.2}$$

In the equilibrium state, a differential element of work done on the system can be written as:

$$dW = \sum_i J_i dX_i \tag{2.3}$$

where J_i represents forces acting on the system and X_i is a state variable, which describes the response of the system to the force J_i. Consequently, the volume change dV due to the pressure (P) will lead to $dW = -PdV$, and the work done on the system with the magnetization change dM in the magnetic field $\mu_0 H$ can be written as: $dW = \mu_0 H dM$.

Considering the above relations, the differential of the internal energy U can be written as:

$$dU = TdS - PdV + \mu_0 H dM \tag{2.4}$$

The thermodynamic potentials – Helmholtz free energy (F) and Gibbs free energy (G) can be defined as:

$$F(X,T) = U - TS \tag{2.5}$$

$$G(J,T) = F - J_i X_i \tag{2.6}$$

The thermodynamic properties of a magnetic system can be described by the Gibbs free energy G, which depends on the magnetic field $\mu_0 H$, temperature T and pressure P. The differential Gibbs free energy $G(T, P, \mu_0 H)$ can be derived using a Legendre transformation:

$$G = U - TS + PV - \mu_0 HM \tag{2.7}$$

By the incorporation of equation 2.4 in 2.7, the differential Gibbs free energy is obtained:

$$dG = -SdT + VdP - Md\mu_0 H \tag{2.8}$$

At constant pressure, the total differential of G can be defined as:

$$dG(T, \mu_0 H) = \left(\frac{\partial G}{\partial T}\right)_{\mu_0 H} dT + \left(\frac{\partial G}{\partial \mu_0 H}\right)_T d\mu_0 H \tag{2.9}$$

According to Clairaut's (Schwarz's) theorem, the symmetry of the second derivatives will hold at a point if the second partial derivatives are continuous. As a consequence, the second derivatives are equal, and the relations between corresponding derivatives are presented as:

$$\left(\frac{\partial}{\partial \mu_0 H}\left(\frac{\partial G}{\partial T}\right)_{\mu_0 H}\right)_T = \left(\frac{\partial}{\partial T}\left(\frac{\partial G}{\partial \mu_0 H}\right)_T\right)_{\mu_0 H} \tag{2.10}$$

The internal parameters of the system such as: entropy (S), volume (V) and magnetization (M) can be obtained from the Gibbs free energy:

$$S(T, \mu_0 H, P) = -\left(\frac{\partial G}{\partial T}\right)_{\mu_0 H, P} \tag{2.11}$$

$$V(T, \mu_0 H, P) = \left(\frac{\partial G}{\partial P}\right)_{T, \mu_0 H} \tag{2.12}$$

$$M\,(T,\mu_0 H,P) = -\left(\frac{\partial G}{\partial \mu_0 H}\right)_{T,P} \tag{2.13}$$

Implementing the equations 2.11 – 2.13 into 2.10 leads to the following Maxwell relation:

$$\left(\frac{\partial S}{\partial \mu_0 H}\right)_T = \left(\frac{\partial M}{\partial T}\right)_{\mu_0 H} \tag{2.14}$$

Consequently, from the integration of equation 2.14, the isothermal entropy change upon varying the magnetic field from $\mu_0 H_0$ to $\mu_0 H_1$ is obtained:

$$\Delta S(T,\Delta\mu_0 H) = \int_{\mu_0 H_0}^{\mu_0 H_1} \left(\frac{\partial M(T)}{\partial T}\right)_{\mu_0 H} d(\mu_0 H) \tag{2.15}$$

2.2. Exchange interactions

In the following sub-section, different types of exchange interactions in insulators and metals are briefly discussed.

2.2.1. Exchange interactions in insulators

The *superexchange interaction* describes the interaction between cations (M) bridged by an intermediate non-magnetic anion (e.g. oxygen ion). A schematic illustration of the three main types of superexchange interactions is presented in Figure **2.1.** The superexchange involves both direct exchange and electron transfer. The exchange can be either ferromagnetic (FM) or antiferromagnetic (AFM) depending on the angle between M-O-M bonds and orbitals occupation. When the electron transfer occurs between half-filled orbitals, the interactions are antiferromagnetic and ferromagnetic interactions occur for an electron transfer between half-filled and empty orbitals [1]–[3]. The magnetic properties caused by superexchange interactions are explained in terms of the Goodenough-Kanamori rules [4], [5].

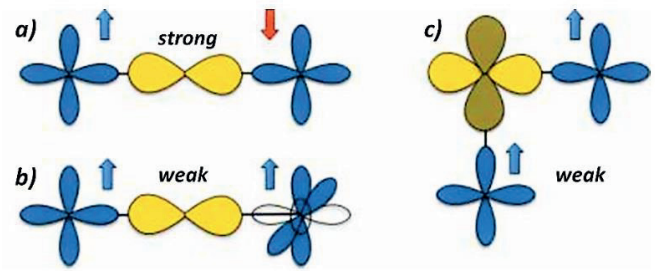

Figure 2.1: *Three main types of superexchange interactions: a) AFM interactions occurring between half-filled d-orbitals through the same p-orbital, b) FM interactions between half-filled and empty d-orbitals mediated by the same p-orbital, c) FM interactions between two half-filled d-orbitals through different p-orbitals [6].*

The *Dzyaloshinskii-Moriya interaction* is also called an antisymmetric exchange, as it occurs in materials with spins canting away from their antiferromagnetic axis. This type of interaction occurs in materials already exhibiting superexchange interactions between coupled ions and is observed as weak intrinsic ferromagnetism in antiferromagnets, with magnetic moments perpendicular to the AFM sublattice, as schematically presented in Figure 2.2 [2], [7], [8].

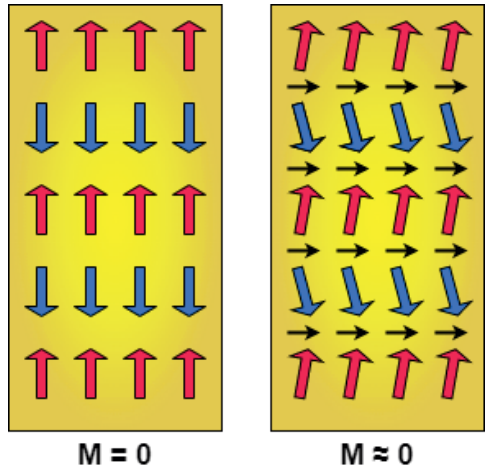

Figure 2.2: *Schematic visualization of Dzyaloshinskii-Moriya interactions. The red and blue arrows indicate opposite spin directions and the black arrows indicate the emergence of weak ferromagnetism in the presence of antiferromagnetism.*

2.2.2. Exchange interactions in metals

The exchange interaction arising from the overlap of magnetic orbitals of two adjacent ions is called a *direct exchange* and is particularly pronounced in *3d* metals due to their large electron cloud. The exchange energy of a system is explained as a difference in the energy between parallel and antiparallel configurations in a two-spin system. According to Pauli's principle, two fermions cannot occupy the same quantum state, i.e. have all quantum numbers with the same value. In a lattice, the many-electron system with atomic spins $\boldsymbol{S}_i$ and $\boldsymbol{S}_j$ can be simplified to:

$$H = -2\sum_{i>j} J_{ij}\boldsymbol{S_i} \bullet \boldsymbol{S_j} \tag{2.16}$$

where J is the exchange constant, indicating the character of magnetic interactions. The positive value of J ($J > 0$) indicates the presence of ferromagnetic interactions, whereas a negative value of J ($J < 0$) implies antiferromagnetic interactions between two spins. The exchange interaction in half-filled bands is antiferromagnetic (Mn, Cr) and partially occupied

bands promote ferromagnetic interactions (Fe, Co, Ni). The correlation between the character of exchange interactions and the interatomic ratio was first studied in 1930 by Slater [9]. A large distance between magnetic atoms gives rise to $J > 0$ and ferromagnetic interactions, while a low distance results in antiferromagnetic interactions and $J < 0$. When the overlap of the wave function is too small due to an interatomic distance that is too large, the direct exchange coupling is too weak to overcome thermal excitations, which gives rise to paramagnetism [2], [3], [8], [10].

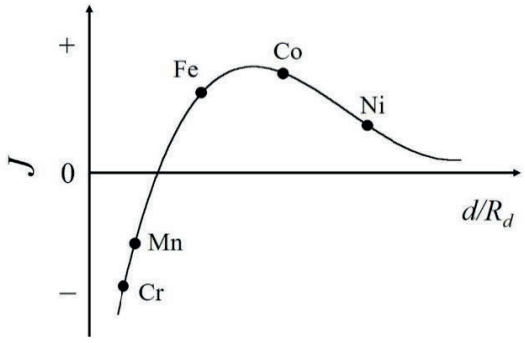

Figure 2.3: *Beth-Slater curve for the magnetic exchange interaction as a function of interatomic spacing, where d indicates the atomic distance and Rd is the radius of the 3d orbital. The positive value of the exchange energy results in the parallel alignment of spins and FM coupling. The negative value of J implies an antiparallel alignment of spins and AFM coupling [11].*

The *Rudermann-Kittel-Kasuya-Yosida* (*RKKY*) *interaction* occurs due to the coupling between the localized magnetic moments in the *d* and *f*-shell electrons by conduction electrons. It is a type of indirect exchange that couples magnetic moments over large distances. A localized magnetic moment leads to a polarization of the conduction electrons and a coupling between the core spins at large distances, which falls off with r^{-3}. The distance between localized magnetic moments determines the character of magnetic interactions (ferromagnetic or antiferromagnetic) [2], [7], [10], [12]. The effective coupling between the localized spins (J_{eff}) is given as:

$$J_{eff} \approx \frac{9\pi J_{sf}^2 v^2 F(\xi)}{64\varepsilon_F} \tag{2.17}$$

where: J_{sf} is the exchange between localized and conduction electrons, v is the number of conduction electrons per atom, ε_F is the Fermi energy and $F(\xi)$ is the RKKY function [2].

The polarization for conduction electrons is proportional to the RKKY function $F(\xi)$, presented in Figure 2.4.

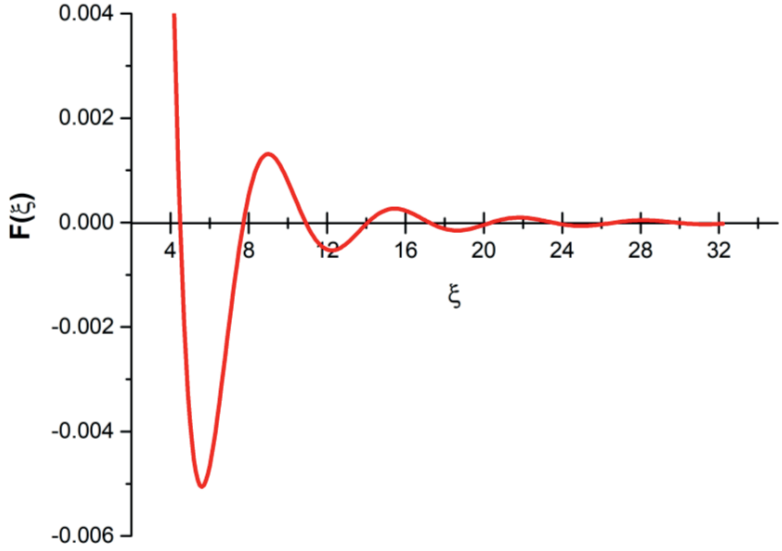

Figure 2.4: *RKKY function F(ξ).*

Double exchange originates from Coulomb and kinetic-exchange interactions between *3d* ions, having localized and delocalized electrons. To enable the electron transfer, two valence configurations are required, as in $LaMnO_3$ (Mn^{3+}, Mn^{4+}) or Fe_3O_4 (Fe^{2+}, Fe^{3+}). If the alignment of the spins is parallel, the electron transfer is possible, but for the antiparallel alignment the charge transfer is prevented by a large energy barrier associated with Hund's rule. The mechanism of double exchange is schematically presented in Figure 2.5.

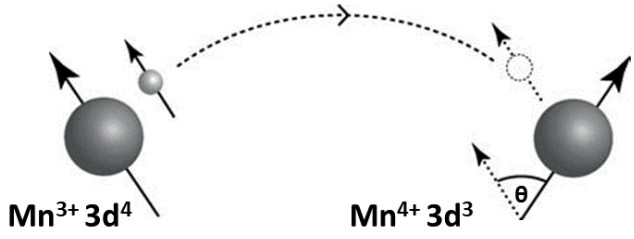

Figure 2.5: *Double exchange between Mn^{3+} and Mn^{4+} [2].*

The *s-d* model describes the interaction between delocalized electrons in a metal and an isolated magnetic ion. Regardless of the sign of the coupling constant J_{sd}, this interaction can lead to a long-range FM coupling between isolated magnetic ions [2]. The energy of *d*-levels and *s*-conduction states overlaps, leading to a virtual bound state in which the *3d* moments are modified by the *s-d* interaction. Before tunneling into the delocalized state, the itinerant *s*-electron experiences a coupling of its spin to other electrons in a temporarily bound atomic-like state. At the same time, an isolated magnetic ion comprises *d*-electrons and surrounding itinerant *s*-electrons participating in *s-d* interactions. The host conduction band is uniformly spin-polarized in the opposite direction to the localized ion, which is an effect of Kondo binding. Below the Kondo temperature (T_K), the antiparallel electron cloud quenches the magnetic moment of the ion to zero in the theoretical limit [12]–[14].

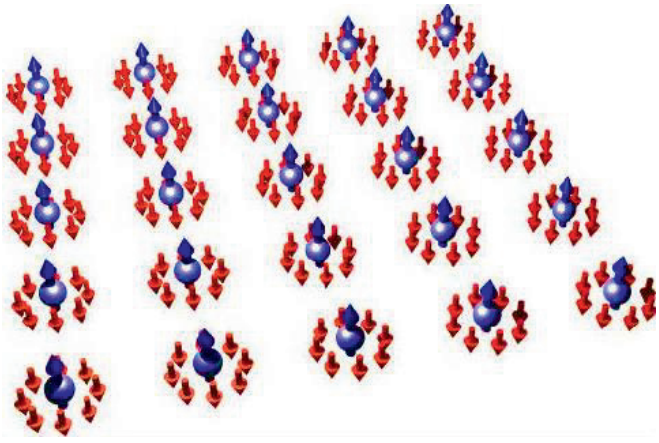

Figure 2.6: *Schematic visualization of the s-d model. The conduction electrons (red arrows) surround the localized electrons (blue arrows) in the lattice.*

2.3. Types of magnetic order

2.3.1. Ferromagnetism

Ferromagnets are characterized by spontaneous magnetization (M) in the ordered state, which occurs due to a long-range alignment of the magnetic moments. Since the spins align in the same direction, the exchange parameter takes a positive value at each point ($J > 0$). In order to minimize the magnetostatic energy, the crystalline compound is divided into domains, which are spontaneously magnetized along the easy magnetization direction. Due to the varying orientation of the magnetic moments between different domains, the net magnetization is zero. When a magnetic field is applied to a material, it causes domain walls to move and leads to the growth of domains that are aligned with the magnetic field. Since magnetic moments are already aligned within a magnetic domain, the saturation magnetization can be achieved at low magnetic fields, and a slight increase in magnetization at higher fields can be ascribed to a further alignment of magnetic moments in magnetic domains. The spontaneous magnetization decreases with increasing temperature and

disappears at the Curie Temperature (T_C) when thermal energy exceed the exchange energies resulting from neighbouring spins [2], [3], [14].

In the Weiss theory, the molecular field will act to align neighbouring magnetic moments due to the dominant positive exchange interactions. The molecular field describes the effect of the ordering of a system and is responsible for the presence of spontaneous magnetization in each domain. Since the molecular field varies with magnetization M, the internal field H_m can be assumed as:

$$H_m = n_W M \tag{2.18}$$

where n_W is a temperature-independent molecular field constant (Weiss constant), which characterizes the strength of a molecular field. In ferromagnets the value of n_W is positive. In the external magnetic field H, the internal magnetic field experienced by magnetic moments (H^i) can be shown as follows:

$$H^i = H + H_m = H + n_W M \tag{2.19}$$

The values of molecular fields are often found to be extremely large due to considerable Coulomb energies involved in the exchange interactions [2], [3], [8].

2.3.2. Curie-Weiss Law

The susceptibility (χ) is a quantity which enables the study of magnetic identity of the material in an applied magnetic field using the following relation:

$$\chi = \frac{M}{H} \tag{2.20}$$

The susceptibility can be derived from magnetization measurements (M) in a given applied magnetic field (H) as a function of measured temperature (T) and is defined with respect to the intrinsic magnetic field accounting for the demagnetizing field. The response of the material in the non-magnetic state to an applied magnetic field can arise from the paramagnetic or diamagnetic contribution. Among diamagnetic contributions, orbital (core) diamagnetism occurs in all materials. The occurrence of diamagnetism is often explained by Lenz's law: if the magnetic flux is changed by the externally applied magnetic field, the induced current generates a magnetic field opposing the applied magnetic field. Therefore, the value of the diamagnetic susceptibility is negative ($\chi < 0$), whereas for paramagnetic materials the susceptibility takes positive values ($\chi > 0$). The weak diamagnetic contribution is temperature-independent, which allows for data corrections, but due to its very low magnitude, a diamagnetic contribution is often neglected. Thus, the term *diamagnet* is used for materials with exclusively the diamagnetic contribution to the susceptibility.

In contrast to the diamagnetic contribution, the paramagnetic response occurs only in magnetic materials. In the non-magnetic state ($T > T_C$), thermal fluctuations are stronger than magnetic interactions between atoms and the material is in the disordered (paramagnetic) state. At temperatures exceeding T_C, the susceptibility often follows the

Curie-Weiss law, which is derived from Curie's law ($\chi = C/T$) upon the incorporation of the molecular field by Weiss:

$$\chi = \frac{C}{T - \theta_{CW}} \tag{2.21}$$

In equation 2.21, C is the Curie constant and θ_{CW} is the Curie-Weiss temperature. The Curie constant C is related to the number of unpaired electrons and can be described as:

$$C = \frac{\mu_0 n {g_j}^2 \mu_B^2 J(J+1)}{3k_B} \tag{2.22}$$

where μ_0 is the permeability of free space, μ_B – Bohr magneton, k_B – Boltzmann constant, n – number of magnetic ions per unit volume, J – total angular momentum and g_j – its g-tensor.

The Curie constant is often written in terms of the calculated effective moment (μ_{eff}) for the magnetic ion:

$$\mu_{eff} = g_J \sqrt{J(J+1)} \mu_B \tag{2.23}$$

$$C = \frac{\mu_0 n \mu_{eff}^2}{3k_B} \tag{2.24}$$

The calculated value of the effective moment per magnetic ion can be compared with the value derived using the Curie constant (C) from the molar susceptibility (m^3/mol) in the paramagnetic regime:

$$\mu_{eff} = \sqrt{8C}\, \mu_B \tag{2.25}$$

Both the Curie constant (C) and the Curie-Weiss temperature (θ_{CW}) can be derived from the inverse susceptibility measured as a function of temperature. While the slope of the curve has the value $1/C$, the y-intercept corresponds to $-\theta_{CW}/C$, and the x-intercept indicates the value of θ_{CW}.

The value of the Curie-Weiss temperature (θ_{CW}) reflects the molecular field's strength, which enables the study of magnetic correlations between atoms. When the molecular field aligns with the externally applied magnetic field, the value of θ_{CW} is positive, indicating positive (ferromagnetic) interactions between ions and the negative value of θ_{CW} indicates the presence of antiferromagnetic interactions. If the plot of the inverse susceptibility as a function of temperature shows a curvature rather than a linear trend, additional temperature-independent contributions to the susceptibility are expected (χ_0), e.g., core diamagnetism, Pauli or van Vleck paramagnetism. In the case of a non-linear behavior, a modified form of the Curie-Weiss law can be presented as:

$$\chi = \frac{C}{T - \theta_{CW}} + \chi_0 \tag{2.26}$$

A schematic graph presenting the shape of the Curie-Weiss fit depending on the presence of additional contributions is shown in Figure 2.7. It can be seen that the Curie-Weiss fit obeys the linear trend in an ideal case. The presence of even a minor positive or negative contribution results in a deviation from the linear trend [2], [15].

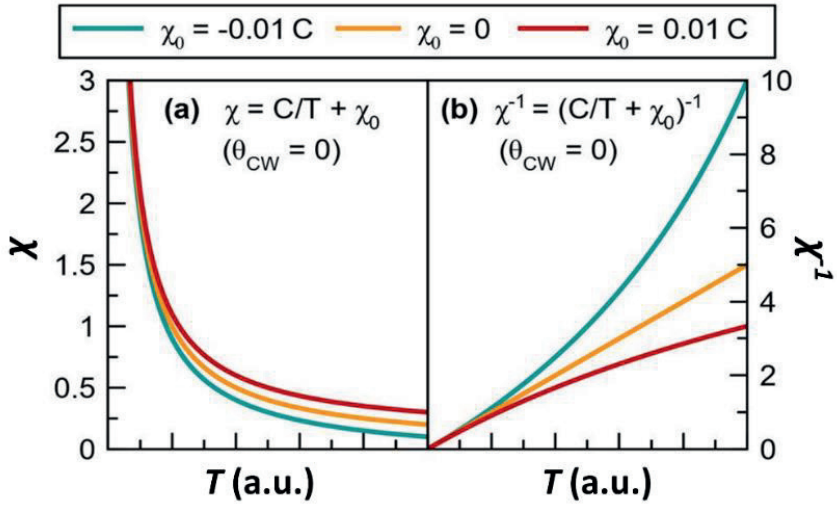

Figure 2.7: *Effect of the temperature-independent contribution (χ_0) on the Curie-Weiss behavior [15].*

2.3.3. Antiferromagnetism

The idea of two sublattices with equal magnetic moments, but pointing in opposite directions, was first discussed in 1936 by Louis Néel. The nearest magnetic moments align antiparallel to each other, which results in negative exchange interactions ($J < 0$). Consequently, the net magnetization is zero. The antiferromagnetic (AFM) transition is marked by a peak in the magnetic susceptibility, called the Néel temperature (T_N). In contrast to ferromagnetic interactions, antiferromagnetic interactions are not easily satisfied. The inability of the system to reach a single ground state often leads to frustration, which mainly entails lattices with an odd number of magnetic moments (e.g. triangular or Kagomé lattices). Elements such as Cr, Mn and many of their alloys (Fe_3Mn, MnSe, CrPt), transition-metal fluorides, sulphides and oxides are often antiferromagnetic [2], [3], [14]. Antiferromagnets possess a magnetic structure at the atomic level, but do not generate stray fields due to absence of a spontaneous magnetization. Therefore, the antiferromagnetic materials appear especially promising for data storage, e.g. antiferromagnetic magnetoresistive random access memory (AF-MRAM) and antiferromagnetic magnetoelectric random access memory (AF-MERAM) [16].

2.3.4. Ferrimagnetism

Ferrimagnetism (FiM) is another type of magnetic order with antiparallel magnetic sublattices, but unlike antiferromagnetism, the magnetic moments found on sublattices *A* and *B* are of a different magnitude. A different number of *A* and *B*-type atoms per unit cell and their non-identical magnetic moments lead to a spontaneous magnetization at low temperatures. As in the case of antiferromagnetism, the exchange interactions between the adjacent spins are negative ($J < 0$). The molecular field of each sublattice is different, which results in a different temperature dependence. The transition from the ordered magnetic state to a paramagnetic state occurs at the critical temperature, known as the ferrimagnetic Néel temperature (T_C). If one sublattice dominates at low temperatures and another one at higher temperatures, the net magnetization can be reduced to zero at the compensation temperature (T_{COMP}), followed by a sign change at higher temperatures, as schematically presented in Figure 2.8 [2], [14].

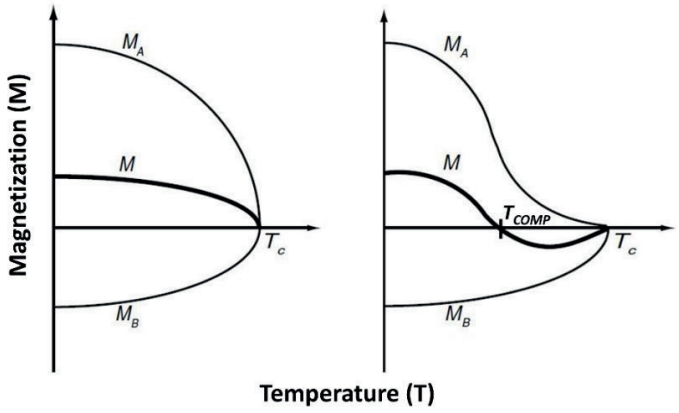

Figure 2.8: *Schematic view of the magnetization for sublattices A and B in a ferrimagnet [2].*

The most explored classes of ferrimagnets are ferrites, which crystallize in the spinel type of structure ($MO \bullet Fe_2O_3$ with M: Zn^{2+}, Co^{2+}, Fe^{2+}, Ni^{2+}, Cu^{2+}, Mn^{2+}) and garnets ($R_3Fe_5O_{12}$ with R: rare earth atom). Most ferrimagnets are insulators, implying that the material can be used in high frequency applications. Ferrite cores are used in inductors, chokes and transformers for switched-mode power supplies (SMPS). Unlike ferromagnets, an oscillating magnetic field does not induce a voltage leading to eddy currents and heating of the material [17].

References

[1] S. Trotzky, P. Cheiner, S. Folling, M. Feld, U. Schnorrberger, A. M. Rey, A. Polkovnikov, E. A. Demler, M. D. Lukin, and I. Bloch, "Time-Resolved Observation and Control of Superexchange Interactions with Ultracold Atoms in Optical Lattices", *J. Sci*, *319*(5861), pp. 295-299, 2008, https://doi.org/10.1126/science.115084.

[2] J. M. D. Coey, *Magnetism and Magnetic Materials*. Cambridge: Cambridge University Press, 2010.

[3] K. H. J. Buschow and F. R. de Boer, *Physics of Magnetism and Magnetic Materials*, 2003.

[4] J. B. Goodenough, "Theory of the role of covalence in the perovskite-type manganites [La,M(II)]MnO_3", *Phys. Rev.*, *100*(2), pp. 564–573, 1955, doi: 10.1103/PhysRev.100.564.

[5] J. Kanamori, "Superexchange interaction and symmetry properties of electron orbitals", *J. Phys. Chem. Solids*, *10*(2-3), pp. 87–98, 1959, doi: 10.1016/0022-3697(59)90061-7.

[6] S. V Streltsov and D. I. Khomskii, "Orbital physics in transition metal compounds: new trends," *Physics-Uspekhi*, *60*(11), pp. 1121–1146, 2017, doi: 10.3367/ufne.2017.08.038196.

[7] E. R. Blessman, "Magnetic couplings", *Mach. Des.*, *61*(3), 1989, pp. 105–108, 1989.

[8] S. Blundell, *Magnetism in Condensed Matter*. OXFORD Univ. Press, 2001, doi: 10.1017/CBO9781107415324.004.

[9] J. C. Slater, "Atomic Shielding Constants", *Phys. Rev.*, *36*(1), pp. 57–64, 1930, doi: 10.1103/PhysRev.36.57.

[10] W. Nolting and A. Ramakanth, *Quantum theory of magnetism*. Springer Berlin Heidelberg, 2009: doi:10.1007/978-3-540-85416-6.

[11] J. Kitagawa, K. Sakaguchi, T. Hara, F. Hirano, N. Shirakawa, and M. Tsubota, "Interstitial atom engineering in magnetic materials", *Metals (Basel).*, *10*(12), pp. 1–24, 2020, doi: 10.3390/met10121644.

[12] A. E. Bell and A. D. Caplin, "Dilute transition metal alloys and the kondo problem", *Contemp. Phys.*, *16*(4), pp. 375–394, 1975, doi: 10.1080/00107517508210819.

[13] A. Okiji, "Bound State due to the s-d Exchange Interaction", *Prog. Theor. Phys.*, *36*(4), pp. 712–725, 1966.

[14] C. M. Hurd, "Varieties of magnetic order in solids", *Contemp. Phys.*, *23*(5), pp. 469–493, 1982, doi: 10.1080/00107518208237096.

[15] S. Mugiraneza and A. M. Hallas, "Tutorial: a beginner's guide to interpreting magnetic susceptibility data with the Curie-Weiss law", *Commun. Phys.*, *5*(1), 2022, doi: 10.1038/s42005-022-00853-y.

[16] T. Kosub, M. Kopte, R. Huhne, P. Appel, B. Shields, P. Maletinsky, R. Hubner, M.O. Liedke, J. Fassbender, O.G. Schmidt, and D. Makarov, "Purely antiferromagnetic magnetoelectric random access memory", *Nat. Commun.*, *8*(1), pp. 1–7, 2017, doi: 10.1038/ncomms13985.

[17] Y. Zhang, X. Feng, Z. Zheng, Z. Zhang, K. Lin, X. Sun, G. Wang, J. Wang, J. Wei, P. Vallobra, Y. He, Z. Wang, L. Chen, K. Zhang, Y. Xu, and W. Zhao, "Ferrimagnets for spintronic devices: From materials to applications", *Appl. Phys. Rev.*, *10*, p. 11301, 2023, doi: 10.1063/5.0104618.

3

EXPERIMENTAL METHODS

The materials discussed in this thesis were prepared in the group of Fundamental Aspects of Materials and Energy (FAME) at the Faculty of Applied Sciences, Delft University of Technology (TU Delft). X-Ray diffraction (XRD), magnetization (SQUID, VSM), differential scanning calorimetry (DSC), high-temperature DSC and Mössbauer spectroscopy measurements were performed in the Department of Radiation, Science and Technology (RST). The neutron powder diffraction (NPD) measurements were performed in the Reactor Institute Delft (RID). Scanning electron microscopy (SEM) coupled with energy-disperse X-ray spectroscopy (EDS) and Electron Probe Microanalysis (EPMA) were performed in the Department of Materials Science and Engineering, at the 3mE Faculty. In this section, the methods of sample preparation and sample characterization are shortly described.

3.1. Sample preparation

3.1.1. High energy ball milling

Ball-milling is used for grinding and fabrication of alloys from powders. In **Chapter 4**, the $(Mn,Fe)_2(P,Si)$ compounds were prepared using a planetary ball-mill, employing a Fritsch Pulverisette 5 with four tungsten-carbide cylindrical vessels [1]. The calculated amounts of starting materials (powders) were placed together with seven tungsten-carbide balls in the grinding pot. An inert atmosphere was provided by sealing jars under an Ar atmosphere in order to avoid oxidation of starting materials during the milling process. In the next step, the grinding jars were placed on a rotating disc, moving in the opposite direction to the rotating vessels. During the double rotation, powders become trapped between the

surfaces of colliding walls of the jar and balls. Thus, a mechanical force is applied to materials, which results in their deformation. Mechanical deformation can be seen as a modification of the coordination shells of atoms, which leads to structural excitations. These excitations cause an enhancement in the chemical reactivity due to receded thermodynamic equilibrium [2]. The ball milling time of 10 h at a constant speed of 350 rpm was adopted, in which a sequence of 15 min of milling followed by a 10 min break was applied. With the use of the ball-milling technique, approximately 10 g of the final material can be obtained from one grinding bowl. A schematic illustration of the ball-milling process and the planetary ball-mill Pulverisette 5 are presented in Figure **3.1**.

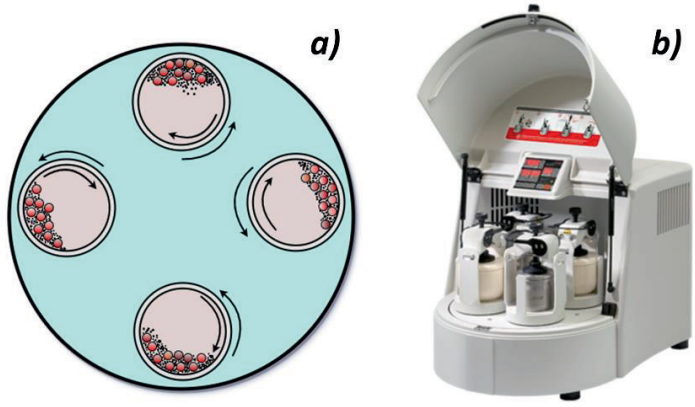

Figure 3.1: *a) Schematic drawing of the ball-milling and b) picture of the planetary ball mill Pulverisette 5 [1].*

3.1.2. Melt-spinning

Melt-spinning is a rapid solidification technique used to produce alloys in the form of strips (ribbons). In the melt-spinning process, a molten alloy is subjected to a rapid cooling reaching 10^6 K/s, which ensures the formation of nanocrystalline or metallic glassy materials. The $(Mn,Fe)_2(P,Si)$ materials described in **Chapter 5** were prepared using this technique, employing the melt-spinner produced by Edmund Bühler GmbH [3]. First, the Mn, Fe, Fe_2P and Si powders were ball-milled for 2 h at a constant speed of 350 rpm. As obtained powders were pressed into pellets of a diameter of 10 mm and inserted in the quartz tube with a nozzle on the bottom. The samples were melted in an Ar atmosphere (800 mbar) upon applying radio frequency RF current in a water cooled induction coil, which led to a rise in the temperature and melting of a material placed in the quartz tube. Following the completion of melting, the liquid alloy was ejected through a nozzle by Ar overpressure onto a fast-rotating Cu wheel (about 45 m/s). With a single melt-spinning run, about 5 g of sample can be obtained. As obtained ribbons were subsequently collected, sealed in quartz tubes under Ar atmosphere

(200 mbar) and annealed for 2 h at 1313, 1373 or 1433 K before being quenched to room temperature. The major advantage of this method is a higher purity of obtained ingots. Oxide impurities are rejected during the melt-spinning process, resulting in improved magnetic properties of the materials obtained [4]. A schematic drawing of the melt-spinning process and a picture of the melt-spinner are shown in Figure 3.2.

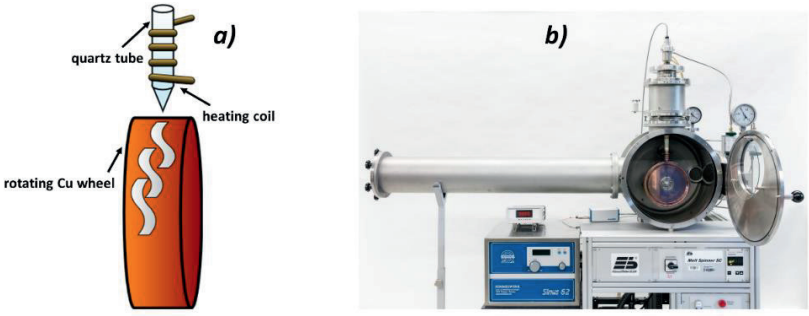

Figure 3.2: *a) Schematic drawing of the melt spinning, b) melt spinner (Edmund Bühler GmbH) [3].*

3.1.3. Liquid phase sintering

The liquid phase sintering process entails a coexistence of solid and liquid phase/s for a certain period of time. In the process of liquid-phase sintering, the mass transfer and diffusion of elements in a liquid phase is faster than in a solid state. In **Chapter 6** and **Chapter 7**, the Mn-based antiperovskite carbides $Mn_3Sn_{1-x}Zn_xC$ and $Mn_3Sn_{1-x}Fe_xC$ were prepared using this technique. During sintering, a solid fraction (Mn, C, Fe) coexists with a liquid phase (Sn, Zn). The stoichiometric proportions of starting materials were thoroughly mixed, pressed into pellets, sealed in quartz tubes in Ar atmosphere and subjected to annealing at 1023 K for 120 h. The process of liquid phase sintering is schematically presented in Figure 3.3. and can be divided into the following stages:

(*solid state*): The powders of constituent elements are mixed together. Below the melting point of the liquid phase, the solid-state sintering occurs upon heating (a).

(*rearrangement*): The liquid phase wets the solid and fills the empty spaces between grains. The bonds of the sinter are dissolved, which induces grain fragmentation and rearrangement (b).

(*solution-precipitation*): Grain coarsening and densification due to improved transport rates in the liquid phase. The grain growth contributes to the removal of the residual porosity (c).

(*final densification*): Annihilation of pores and simultaneous coarsening and bonding, which increases the rigidity of an alloy (d) [5].

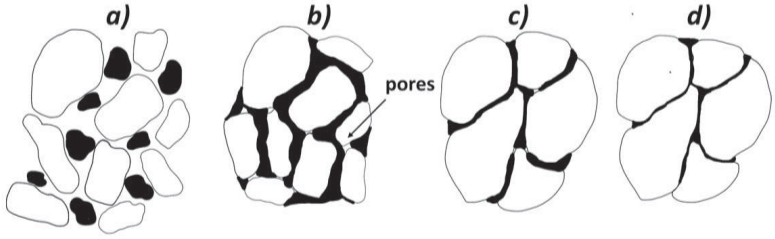

Figure 3.3: *Schematic illustration of the liquid-state sintering.*

3.1.4. Arc melting

Arc melting is used to produce high-purity ingots from chips and pieces of starting materials. In the present study, a home-built arc melter was used. A schematic drawing of the arc-melting and a picture of the used arc-melter are shown in Figure 3.4. A detailed description of the arc-melter is presented in the work of Boeije [6]. During the process of arc melting, constituent elements are melted in a protective Ar atmosphere on a water-cooled copper crucible, utilizing an electric discharge arc struck between a water-cooled tungsten electrode and the copper crucible. The chamber is evacuated and filled with high purity Ar to provide an inert atmosphere during melting. The arc plasma can reach temperatures in excess of 4000 K. The tungsten cathode withstands high temperatures due to water cooling and its high melting point (3695 K) compared to used manganese (1519 K), nickel (1728 K), silicon (1683 K), chromium (2180 K), cobalt (1768 K) and germanium (1211 K). The molten materials form a button floating on the water-cooled copper. To improve homogeneity of the final alloy, the sample was overturned and re-melted five times. By using this method, it is possible to obtain approximately 5 grams of the final material. The $(MnNiSi)_{1-x}(CrCoGe)_x$ half-Heusler alloys, described in **Chapter 8**, were prepared using this method. As-melted samples were sealed in quartz tubes in an Ar atmosphere and annealed for 120 h at 880 K.

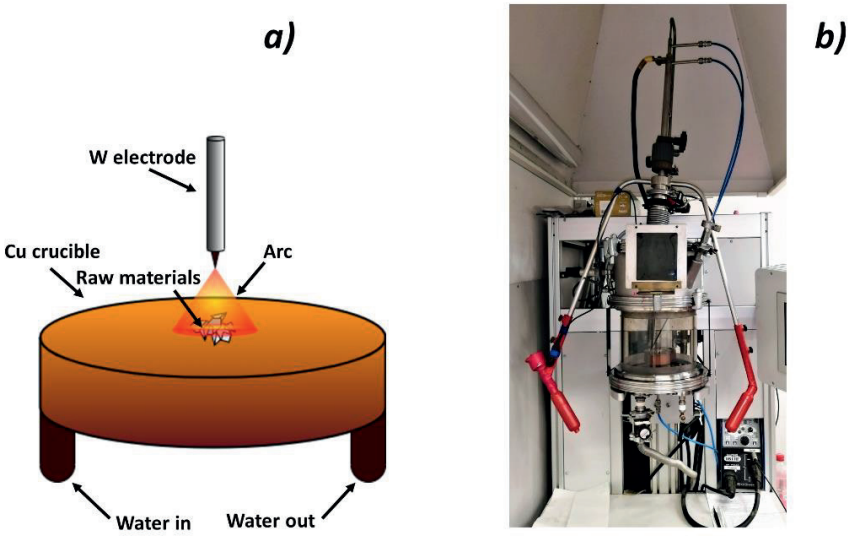

Figure 3.4: *a) Schematic illustration of arc melting, b) home-built arc melter.*

3.1.5. Heat treatment

The obtained samples often require an appropriate heat treatment in order to reduce the amount of impurity phases and improve the homogeneity of the final alloy. After the fabrication process, prepared samples were sealed in quartz tubes under 200 mbar Ar atmosphere to avoid oxidation during the annealing process. In the next step, quartz tubes containing pressed samples were inserted to a vertical oven, which allows fast quenching into water when the bottom window is opened and the holding wire is cut. The time and the temperature of the heat treatment were chosen independently for selected compounds. The details of the heat treatment procedure are given in later sections. **Chapter 5** focuses specifically on the effect of the heat treatment on magnetic, structural and microstructural properties of $(Mn,Fe)_y(P,Si)$ materials in various metal/non-metal (M/NM) ratios y. To reduce the formation of the $(Mn,Fe)_3Si$ impurity phase, the $(Mn,Fe)_y(P,Si)$ compounds were placed in a hot oven and rapidly cooled into water (**Chapter 4, Chapter 5**). The $(MnNiSi)_{1-x}(CrCoGe)_x$ alloys (**Chapter 8)** were treated likewise. On the other hand, the Mn-based antiperovskites $Mn_3Sn_{1-x}M_xC$ (M: Zn, Fe) were inserted into a cold oven, slowly heated to a target temperature and finally slowly oven-cooled (**Chapter 6, Chapter 7**).

3.2. Sample characterization

3.2.1. X-ray diffraction

The scattering of X-rays from the electron cloud of atoms gives a diffraction pattern, which delivers information about the crystal structure's periodicity. In the present research, X-ray diffraction (XRD) was used for the identification of phases and their fractions, indexing, the calculation of lattice constants and site occupancies. X-Ray diffraction patterns were measured using a PANalytical X-pert Pro diffractometer with Cu K_α radiation (λ = 1.5406 Å) in the 2θ range from 10 to 100° at a step of 0.08°. The temperature-dependent XRD measurements were performed using an Anton Paar TTK450 sample chamber. The measured patterns were refined using the Rietveld refinement implemented in the Fullprof software [7], [8].

3.2.2. Superconducting quantum interference device

A superconducting quantum interference device (SQUID) is a highly sensitive magnetometer, which can detect extremely low magnetic fields reaching 10^{-14} T employing two parallel Josephson junctions. A Josephson junction consists of two superconductors separated by a thin insulating layer, allowing for the passage of electrons. Upon constant bias current, the voltage oscillates with a phase change at the junctions, which depends on a magnetic flux change. The measured oscillations enable the evaluation of the flux change. A SQUID magnetometer is used to determine the magnetization of a given specimen as a function of temperature and magnetic field [9], [10]. The transition temperatures and the thermal hysteresis were derived from the measurements at 0.01 T. The magnetic entropy change (ΔS_m) was calculated using Maxwell relations from the measured *M-T* curves at various magnetic fields. In this study, magnetic measurements were performed in magnetic fields up to 5 T and in the temperature range of 5 – 370 K with a sweep rate of 2 K/min, using MPMS-XL and MPMS-5S magnetometers produced by Quantum Design. The reciprocating sample option mode (RSO) was used, which allows to average over a large number of movements in a short time frame. Before the measurement, a given specimen of a mass 1-3 mg was placed in a gelatine capsule, which was further embedded in a polypropylene (PP) straw.

3.2.3. Vibrating sample magnetometer

A vibrating sample magnetometer (VSM) implemented in Quantum Design VersaLab for the Physical Property Measurement System (PPMS) was used to measure the magnetic properties of compounds with transition temperatures exceeding the calibration range of the SQUID [11]. The use of the VSM allows us to measure magnetic properties for temperatures of 50 – 650 K and in magnetic fields of 0 – 3 T. During the VSM measurement, the studied specimen (5 – 15 mg) oscillates with a frequency of 40 Hz near a detection coil, which induces a voltage upon changing the magnetic flux. The VSM system is able to detect magnetic moment-changes larger than 10^{-9} Am^2.

3.2.4. Differential scanning calorimetry

Differential Scanning Calorimetry (DSC) measures a change in the heat flow between the studied material and a well-defined reference at the same temperature. From the temperature difference between the sample and the reference, a specific heat capacity can be derived. The measurements were conducted using the TA-Q2000 DSC instrument equipped with a liquid nitrogen system. From the position and shape of the DSC curve, the transition temperature, specific heat capacity, latent heat and homogeneity of the compound can be studied. The measurements were conducted in the temperature range of 100 – 573 K with a constant sweep rate of 10 K/min for a specimen of 20 – 40 mg.

High-temperature DSC measurements were conducted using a TGA-DSC module implemented in the Seteram 96 line calorimeter in the temperature range of 300 – 1300 K with a sweep rate of 10 K/min.

3.2.5. Electron microscopy

Scanning electron microscopy (SEM, JEOL JSM 6500 F, Japan) with coupled energy dispersive X-ray spectroscopy (EDS) measurements were carried out to study morphology and to verify the compositions of selected compounds. The measurements using the backscattered electron (BSE) detector were used to study the distribution of different phases. Both elastic and inelastic scattering is produced upon the interaction of accelerated electrons and a target sample. Atoms of a higher atomic number (Z) have a higher probability to produce elastic scattering due to their larger cross-section areas. Consequently, phases containing atoms of a higher Z number appear brighter than phases of a lower atomic number. The melt-spun ribbons were attached to the resin in the process of cold-mounting in order to avoid the damage introduced by high temperature and pressure. Samples obtained via ball-milling and arc-melting were prepared in the process of hot-mounting. As-prepared specimens were subjected to sanding and subsequently polished using 3 μm and 1 μm diamond paste. A varying voltage of 10 – 15 kV was used during the measurement. While the measurement using low voltage is more surface-sensitive, the use of a higher voltage provides more details about the layers beneath the surface at the cost of the ability to study surface morphology.

Electron Probe Micro Analysis (EPMA) measurements were performed utilising JEOL JXA 8900R microprobe with an electron beam energy of 10 keV and beam current of 200 nA. The compositions measured at selected points were determined using X-ray intensities of the elements present. The obtained intensities were further processed with matrix correction software (CITZAF). In comparison to EDS measurements, the EPMA technique provides very accurate information on the chemical compositions.

3.2.6. Neutron powder diffraction

Neutron Powder Diffraction (NPD) patterns were measured using the neutron powder diffractometer PEARL at the Reactor Institute Delft (the Netherlands) with a neutron wavelength of $\lambda = 1.67$ Å. The Rietveld refinement implemented in the Fullprof software was

used to refine nuclear and magnetic structures. While the X-rays are scattered by the electron cloud, neutrons are scattered by the nuclei of atoms (nuclear scattering) and the magnetic moments of the ions (magnetic scattering). Due to a difference in the scattering lengths of nuclei, the positions of atoms can be determined, including a differentiation between different isotopes of the same element. The magnetic moment of neutron interacts with magnetic moments of the studied compound. Consequently, the type of magnetic order and the size of the magnetic moments can be determined. In this thesis, unpolarised neutron diffraction was used to reveal the magnetic order and to study the thermal evolution of magnetic moments in antiperovskites $Mn_3Sn_{1-x}Zn_xC$ and $Mn_3Sn_{1-x}Fe_xC$. The samples with a mass of about 4 g were placed in a vanadium can and were measured at various temperatures in the range of 4 – 550 K.

3.2.7. Mössbauer spectroscopy

Mössbauer spectroscopy is a technique utilising the Mössbauer effect, which is the recoilless emission and subsequent absorption of γ photons by nuclei. The changes in energy levels associated with the emission/absorption of γ photons give information about the local environment of the probed atom. We can distinguish three main hyperfine interactions: isomer shift, quadrupole splitting and magnetic hyperfine splitting. The isomer shift occurs due to the interaction between protons of the nucleus and electrons. The study of the isomer shift provides information about the oxidation state, spin state, electronegativity and covalency. The interaction between the nuclear quadrupole moment and a non-uniform electric field in the nucleus is observed as the quadrupole splitting, from which site symmetry, oxidation and spin states can be derived. The interaction between the magnetic dipole moment and the nucleus' magnetic field results in magnetic splitting, from which magnetic properties can be studied. As a result, Mössbauer spectroscopy provides precise information about the chemical, magnetic and structural properties of studied compounds [12]–[14]. In the present study, Mössbauer spectroscopy was used to elucidate the impact of Co substitution in Fe-rich $(Mn,Fe)_2(P,Si)$ compounds. Transmission ^{57}Fe Mössbauer spectra were obtained at 130 and 350 K. A constant-acceleration spectrometer with a sinusoidal velocity spectrometer using a $^{57}Co(Rh)$ source was used. The obtained spectra were fitted using the Mosswinn 4.0 program.

3.2.8. DFT calculations

Density functional theory (DFT) is an approach to find solutions to the Schrödinger equation, which describes the quantum behaviour of electrons present in the system:

$$E\psi = \left[-\frac{\hbar^2}{2m} \sum_{i=1}^{N} \nabla_i^2 + \sum_{i=1}^{N} V(\mathbf{r_i}) + \sum_{i=1}^{N} \sum_{j<i} U(r_i, r_j) \right] \psi \tag{3.1}$$

Schrödinger's theory assumes that the wave function of the system contains all the information about the quantum system. In the presented Schrödinger equation, the terms in

brackets refer to the kinetic energy of an electron, the interaction energy between each electron and atomic nuclei and the interaction energy between electrons, respectively. The electronic wave function (ψ) refers to the spatial coordinates of each electron from the total N electrons in the system and E is the time independent ground state energy of electrons. In real systems, the number of electrons is significantly larger than the number of nuclei, which leads to multi-dimensional functions required for the wave function. In the presented form of the Schrödinger equation, the individual wave function of the electron cannot be found without considering wave functions related to interactions with all the other electrons in the system, which makes the Schrödinger equation a many-body problem [15].

Density-functional theory (DFT) is an atomistic method of simulation used to investigate the electronic structure of many-body systems. The fundamental mathematical theorems and derivations were described in the works of Walter Kohn, Pierre Hohenberg and Lu Jeu Sham [16], [17]. According to the first theorem, the total electronic energy is a functional of the charge density $n(r)$. The second theorem postulates that the electron density, which minimizes the energy of the functional, corresponds to the solution of the Schrödinger equation. As a result, the Schrödinger equation can be solved by finding the electron density in three dimensions.

In the present work, the Vienna ab-initio simulation software (VASP) was utilised to perform DFT calculations. The interactions between electrons and ions were described by the projector-augmented wave (PAW) method. The DFT calculations were used to describe magnetic and electronic properties. Details regarding DFT calculations are described in the following chapters.

References

[1] Planetary mill Pulversette 5/4, 2020. Retrieved from: https://www.fritsch-international.com/sample-preparation/milling/planetary-mills/details/product/pulverisette-54-classic-line/.

[2] F. K. Ukrakaev, “Mechanism and kinetics of mechanochemical processes”. *High-energy ball milling – mechanochemical processing of nanopowders*. Woodhead Publishing Limited, 2010.

[3] Melt spinning, 2022. Retrieved from: https://www.edmund-buehler.de/en/materials-science/melt-spinning.

[4] M. R. Pagnola, J. U. Vivero, and A. G. Marrugo, “Magnetic Materials by Melt Spinning Method, Structural Characterization, and Numerical Modeling”, *New Uses Micro Nanomater.*, 2018, doi: 10.5772/intechopen.77368.

[5] R. de Oro Calderon, C. Gierl-Mayer, and H. Danninger, "Fundamentals of Sintering: Liquid Phase Sintering", *Encycl. Mater. Met. Alloy.*, pp. 481–492, 2021, doi: 10.1016/B978-0-12-819726-4.00127-7.

[6] M. Boeije, *Electron density studies on magnetic systems, PhD Thesis*, 2017.

[7] H. M. Rietveld, "A profile refinement method for nuclear and magnetic structures", *J. Appl. Crystallogr.*, *2*(2), pp. 65–71, 1969, doi: 10.1107/s0021889869006558.

[8] J. Rodríguez-Carvajal, "Recent advances in magnetic structure determination by neutron powder diffraction", *Phys. B Phys. Condens. Matter*, *192*(1-2), 1993, doi: 10.1016/0921-4526(93)90108-I.

[9] M. Buchner, K. Höfler, B. Henne, V. Ney, and A. Ney, "Tutorial: Basic principles, limits of detection, and pitfalls of highly sensitive SQUID magnetometry for nanomagnetism and spintronics", *J. Appl. Phys.*, *124*(16), 2018, doi: 10.1063/1.5045299.

[10] H. Lueken, "Superconducting Quantum Interference Device Magnetometry", *Methods Phys. Chem.*, *1*(1), 2012, doi: 10.1002/9783527636839.ch25.

[11] "Vibrating Sample Magnetometer (VSM) Option User's Manual", *Quantum Des. Inc.*, Part Number 1096-100, B0, 2011.

[12] E. Kuzmann, Z. Homonnay, Z. Klencsar, and R. Szalay, "^{57}Fe Mössbauer Spectroscopy as a Tool for Study of Spin States and Magnetic Interactions in Inorganic Chemistry", Molecules, *26*(4), p. 1062, 2021, doi: https://doi.org/10.3390/molecules26041062.

[13] D. Fruchart, S. Haj-Khlifa, P. de Rango, M. Balli, R. Zach, W. Chajec, P. Fornal, J. Stanek, W. Kaprzyk and J. Tobola, "Structure and magnetic properties of bulk synthesized $Mn_{2-x}Fe_xP_{1-y}Si_y$ compounds from magnetization,^{57}Fe Mössbauer spectroscopy, and electronic structure calculations", *Crystals*, *9*(1), pp. 1–27, 2019, doi: 10.3390/cryst9010037.

[14] Y. Yoshida and G. Langouche, *Mössbauer Spectroscopy - tutorial book*. Springer US, 2019, doi: https://doi.org/10.1007/978-3-642-32220-4.

[15] D. S. Sholl and J. A. Steckel, *Density functional theory : a practical introduction.* John Wiley & Sons, 2009, doi: 10.1002/9780470447710 LK.

[16] W. Kohn and L. J. Sham, "Self-Consistent Equations Including Exchange and Correlation Effects", *Phys. Rev.*, *140*(4A), pp. 1133–1138,1965, doi: 10.1103/PhysRev.140.A1133.

[17] P. Hohenberg and W. Kohn, "Inhomogeneous Electron Gas", *Phys. Rev.*, *136*(3B), pp. 864–871, 1964, doi: 10.1103/PhysRev.136.B864.

4

Effect of Co and Ni doping on the structure, magnetic and magnetocaloric properties of Fe-rich $(Mn,Fe)_2(P,Si)$ compounds

Abstract

The effect of Co and Ni doping on the structure, magnetic and magnetocaloric properties of Fe-rich $(Mn,Fe)_2(P,Si)$ compounds was studied. With increasing Co and Ni content, both the Curie temperature (T_C) and the thermal hysteresis (ΔT_{hys}) decreased, whereas the hexagonal P-62m crystal structure was maintained. A pronounced reduction in hysteresis was observed upon Co doping, while a significant reduction in Curie temperature was found upon Ni doping. Mössbauer spectroscopy measurements and DFT calculations indicated the substitution of Fe at the 3f site for both Co and Ni doping. Rietveld refinement of the X-ray diffraction data showed that Co substitute atoms in the main phase and the impurity phase, while Ni exhibits an affinity to the main phase. Magnetization measurements on the Co doped samples revealed an increase in magnetization for 2 at.% of Co, followed by a decrease for higher concentrations. DFT calculations showed that the magnetic moment on the 3f site is enhanced by Co substitution, whereas an opposite trend was observed for Ni substitution.

4.1. Introduction

Magnetic refrigeration based on the magnetocaloric effect (MCE) has a high potential to become a sustainable alternative for traditional compressor-based refrigeration. Systems using magnetocaloric materials (MCM) offer many advantages when compared to well-established cooling technologies. The efficiency of the compressor-based refrigerators originally developed in the 19th century saturates around 40 % of Carnot efficiency. In contrast, with magnetic cooling, it is viable to reach 60 % of Carnot efficiency, leading to significantly reduced energy consumption. In addition to this, systems that use MCMs do not involve hazardous, ozone-depleting gases, and the noise is reduced due to the elimination of compressors [1]–[4]. These advantages and the need for exploring environmentally-friendly technologies make magnetic cooling a very promising replacement for conventional gaseous-refrigerant-based systems.

Promising and applicable magnetocaloric materials should comply with several requirements: they should exhibit a large MCE in the proper temperature range and in low magnetic fields, since the maximum required magnetic field is directly related to cost to generate the magnetic field by permanent magnets. MCMs should also consist of non-toxic, abundant, non-critical, and readily available elements. Additionally, promising materials should display mechanical and chemical stability, a large saturation magnetization (M_s), high thermal conductivity, low specific heat and a large temperature span [5]. A wide temperature span implies that T_C can be easily tailored in a broad temperature range utilizing various approaches, e.g., doping, heat treatment and a varying magnetic field. Among all known MCMs, the generic $(Mn,Fe)_2(P,Si)$ family that crystallizes in the hexagonal Fe_2P-type structure appears to be one of the most promising [6]. The Mn-rich compounds have been explored extensively since it was found that in this region it is feasible to obtain materials with a small hysteresis and yet exhibiting a giant magnetocaloric effect (GMCE) near room temperature [6–8]. However, as reported by Ou and co-workers [9], [10], the Fe-rich region of the $(Mn,Fe)_2(P,Si)$ system can potentially also be favorable since compounds with a higher Fe content can show an even larger magnetic moment compared to Mn-rich materials.

The $(Mn,Fe)_2(P,Si)$ family of compounds consists of neither toxic nor expensive elements. However, controlling the thermal hysteresis originating from the first-order magnetic transition (FOMT) is a prerequisite for practical applications. The character of the transition and the magnitude of hysteresis can be tuned by utilizing appropriate doping, e.g., V, B, C, N, and changes in the heat treatment [11]–[16]. Various studies show that Co doping of $(Mn,Fe)_2(P,Si)$ compounds can effectively reduce the thermal hysteresis and the transition temperature [5], [17], [18]. Nevertheless, due to the high criticality of Co, ethical issues, and a high price, it is essential to minimize the use of Co and look for possible replacements [19]. Recent research shows that Ni can be a good alternative for Co as it leads to similar tuning effects on ΔT_{hys} and T_C [17], [18], [20]. However, the substitution of Co and Ni for Mn in the Fe-rich $(Mn,Fe)_2(P,Si)$ alloys has not yet been studied. Therefore, in this work, we present experimental results on Co and Ni substitution for Mn focussing on the magnetic, magnetocaloric, and structural properties of Fe-rich $(Mn,Fe)_2(P,Si)$ compounds.

4.2. Experimental

4.2.1. Sample preparation

Polycrystalline $(Mn,Fe,Co)_{1.95}(P,Si)$ and $(Mn,Fe,Ni)_{1.95}(P,Si)$ compounds were prepared by high-energy ball-milling under Ar atmosphere and subsequent solid-state reactions. We prepared two series of samples: $Mn_{0.62-x}Fe_{1.33}Co_xP_{0.66}Si_{0.34}$ and $Mn_{0.62-x}Fe_{1.33}Ni_xP_{0.66}Si_{0.34}$ ($0 \leq x \leq 0.12$). Stoichiometric proportions of powders: Mn (99.7%), Fe (99.0%), Fe_2P (99.5%), Si (99.7%), Co (99.8%), Ni (99.9%), were weighed, mixed, and ball milled by a Fritsch Pulverisette planetary ball-mill for 10 h with a constant speed of 350 rpm. Approximately 2 g of ball-milled powder was pressed into pellets and subsequently sealed in quartz tubes in 200 mbar protective Ar atmosphere. As-prepared samples were annealed at 1373 K for 20 h and finally quenched into water. In order to eliminate the so-called "virgin effect" originating from the metastability of the quenched phase, all samples were pre-cooled in liquid nitrogen before being manually powdered [21].

4.2.2. Instrumental methods

Transmission ^{57}Fe Mössbauer spectra were collected at 350 and 130 K with a conventional constant-acceleration spectrometer with a sinusoidal velocity spectrometer, using a ^{57}Co(Rh) source. The Mössbauer spectra were fitted with a binomial distribution model as described earlier for $FeMnP_{1-x}As_x$ using the Mosswinn 4.0 program [22]. The analysis of Mössbauer data was done in collaboration.

The X-ray diffraction patterns were collected using a PANalytical X-pert Pro diffractometer with Cu-K_α radiation (1.54056 Å). Structural parameters were obtained by Rietveld refinement implemented in the Fullprof software [23].

Electron Probe Micro Analysis (EPMA) measurements were conducted with a JEOL JXA 8900R microprobe using an electron beam with energy of 10 keV and beam current of 200 nA employing Wavelength Dispersive Spectrometry (WDS). The obtained intensity ratios were processed with a matrix correction program CITZAF [24]. The EPMA measurements were conducted as part of a collaboration with the 3mE.

Magnetic measurements were conducted using superconducting quantum interference devices (SQUID) MPMS-XL and MPMS-5S magnetometers, in the temperature range of 5-370 K with a constant sweep rate of 2 K/min in applied magnetic fields up to 5 T.

The differential scanning calorimetry (DSC) measurements were carried out using a TA-Q2000 DSC with a constant sweep rate of 10 K/min.

4.2.3. Computational methods

In this work, the preferred site occupancy of the doping atoms and the change in the local magnetic moments has been computed for $Mn_{0.62-x}Fe_{1.33}Co_xP_{0.66}Si_{0.34}$ and $Mn_{0.62-x}Fe_{1.33}Ni_xP_{0.66}Si_{0.34}$, within the framework of density functional theory (DFT). The Vienna Ab Initio simulation package (VASP) [25], [26], in the projected augmented wave (PAW) method [27], [28], was employed to perform the DFT calculations using the

generalized gradient approximation of Perdew-Burke-Ernzerhof (PBE) for the exchange correlation functional [29]. The following orbitals were treated as valence electrons: *3p*, *3d* and *4s* for Mn; *3d* and *4s* for Fe, Ni and Co; *3s* and *3p* for P and Si.

The ***k***-space integrations were performed with the Methfessel-Paxton method [30] of second order with a smearing width of 0.05 eV. The lattice parameters and atomic positions were relaxed for a force convergence of 0.1 meV/Å, while the energies were converged to 1 μeV. The kinetic energy cut-off was set at 400 eV for all calculations. Calculations to determine the site preference for the Ni and Co atoms were performed using a 2×2×1 supercell. The structural degrees of freedom were fully relaxed on a gamma centred ***k***-grid of 5×5×11. For the undoped system, the obtained lattice parameters were $a = 6.12$ Å and $c = 3.26$ Å. To study the effect of the dopants on magnetic properties in this system, a 2×2×4 supercell was utilized with a 5×5×5 ***k***-grid. For the band structure and the density of state calculations (DOS) a smaller 2×1×1 supercell with the composition $Mn_{0.66}Fe_{1.25}P_{0.66}Si_{0.33}T_{0.08}$ (T = Ni, Co) and ***k***-grid of 5×7×11 was used. For the DOS calculations the ***k***-space integrations were performed with the tetrahedron method. The DFT calculations were done in collaboration.

4.3. Results and discussion

4.3.1. Hyperfine field interactions

In the $(Mn,Fe)_2(P,Si)$ family of compounds, Mn atoms show a preference to the pyramidal *3g* site, which is marked by a larger magnetic moment, whereas Fe atoms preferentially occupy *3f* sites, associated with a smaller magnetic moment [7], [31]. In the Fe-rich region, the *3f* site is fully occupied by Fe, and the *3g* site is partially occupied by Mn and partially by Fe [32]. A schematic representation of the crystal structure is shown in Figure **4.1.** As supported by density functional theory (DFT) calculations, the magnetic moment of Fe at the *3g* site is lower than for the preferential Mn atoms at the same site [32], [33].

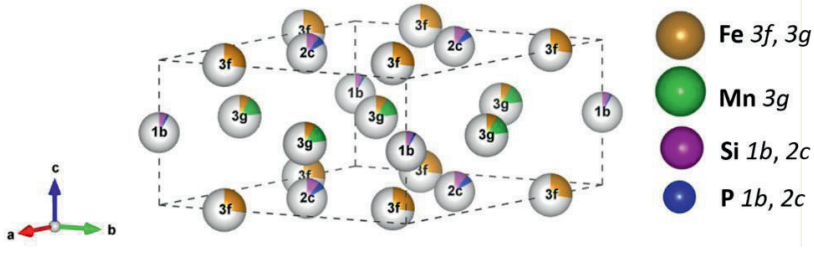

Figure 4.1: *Schematic representation of the crystal structure with the atom occupancy (from DFT) of the parent compound* $Mn_{0.62}Fe_{1.33}P_{0.66}Si_{0.34}$.

Mössbauer spectroscopy was carried out for a reference sample and three other samples containing Co (0, 4, 6, 12 at.%). The Mössbauer spectra recorded at 350 and 130 K

are shown in Figure 4.2. In the high-temperature paramagnetic (PM) phase, a single broad absorption line can be seen. In the low-temperature ferromagnetic (FM) phase, a more complex absorption profile is observed that includes six broad spectral lines, indicating a distribution in hyperfine field. Due to the fact that atoms of P and Si are randomly distributed over the *2c* and *1b* sites, slightly different sextets are observed in the FM state, reflecting the five inequivalent neighbours of the Fe atoms [22]. All fitted Mössbauer parameters, including the hyperfine fields and spectral contributions, are given in Table 4.1.

The aim of performed Mössbauer spectroscopy was to elucidate the influence of the Co substitution on the magnetic properties. In the Fe-rich region, the tetrahedral *3f* site is fully occupied by Fe atoms. The hyperfine field is found to decrease at this site, as indicated in Table 4.1. This indicates the substitution by Co, which has a significantly smaller magnetic moment at the *3f* site than the Fe atoms [33]. Alternatively, Fe might be substituted by Co at both sites, as it would lead to similar changes of the hyperfine field. However, this possibility is less likely to occur since the substitution of Fe by Co at the *3f* site was also supported by DFT calculations. The observed hyperfine field decrease at the pyramidal *3g* site originates from the diminishing amount of Mn in Co-doped samples and increasing amount of Fe at the *3g* Wyckoff position, which is associated with a significantly lower magnetic moment. Additionally, for the sample with the highest Co concentration (12 at.%), we observe the formation of an additional structure, most likely Fe-Co, which suggests that the limit for maximum Co substitution was reached.

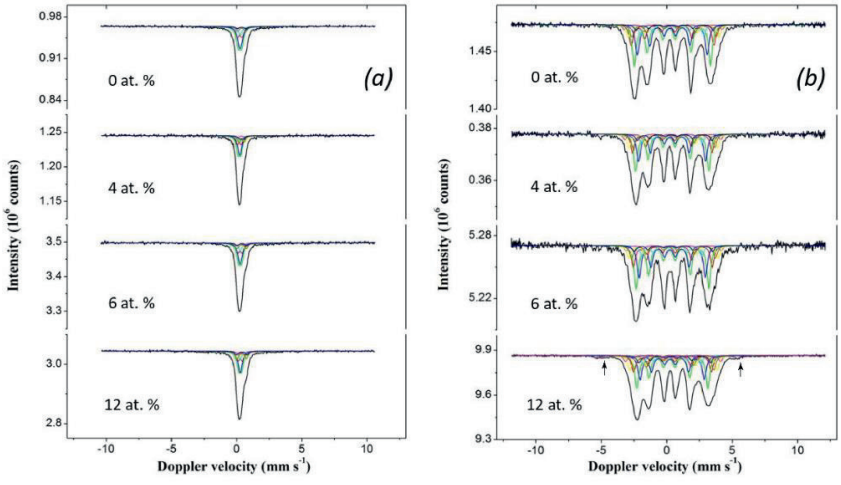

Figure 4.2: *Mössbauer spectra obtained for $Mn_{0.62-x}Fe_{1.33}Co_xP_{0.66}Si_{0.34}$ (x = 0, 4, 6, 12 at.%) measured at (a) 350 K and (b) 130 K.*

Table 4.1: *Mössbauer fitted parameters of $Mn_{0.62-x}Fe_{1.33}Co_xP_{0.66}Si_{0.34}$ in the PM (350 K) and the FM (130 K) state.*

Atomic percent of Co (%)	*T (K)*	*IS* (mm·s^{-1})*	*QS* (mm·s^{-1})*	*Hyperfine field* (T)*	*Γ (mm·s^{-1})*	*Phase*	*Spectral contribution (%)*
0	350	0.25	0.22	-	0.35	P1	77
		0.38	0.66	-	0.35	(*3f*)	
						P2	23
						(*3g*)	
	130	0.31	0.23	17.5	0.35	F1	74
		0.43	0.22	21.0	0.35	(*3f*)	
						F2	26
						(*3g*)	
4	350	0.24	0.19	-	0.29	P1	69
		0.36	0.50	-	0.29	(*3f*)	
						P2	31
						(*3g*)	
	130	0.30	0.21	16.8	0.34	F1	70
		0.40	0.24	20.5	0.34	(*3f*)	
						F2	30
						(*3g*)	
6	350	0.26	0.20	-	0.33	P1	68
		0.36	0.68	-	0.33	(*3f*)	
						P2	32
						(*3g*)	
	130	0.32	0.21	16.7	0.35	F1	63
		0.40	0.24	20.7	0.35	(*3f*)	
						F2	27
						(*3g*)	
12	350	0.27	0.19	-	0.36	P1	66
		0.38	0.66	-	0.36	(*3f*)	
						P2	34
						(*3g*)	
	130	0.31	0.20	16.3	0.35	F1	64
		0.42	0.23	20.0	0.35	(*3f*)	
		0.28	-0.51	33.3	0.35	F2	33
						(*3g*)	
						F3	3

Experimental uncertainties: Isomer shift: I.S. ± 0.01 mm s^{-1}; Quadrupole splitting: Q.S. ± 0.01 mm s^{-1}; Line width: Γ ± 0.01 mm s^{-1}; Hyperfine field: ± 0.1 T; Spectral contribution: ± 3%; F/P: ferromagnetic/paramagnetic phases.

4.3.2. Structural and microstructural characterisation

The X-Ray diffraction (XRD) patterns of Co and Ni-doped samples measured at 348 K clearly indicate that all samples crystallize in the hexagonal Fe_2P-type structure (space group

P-62m). A Rietveld refinement of the XRD data for the parent compound is shown in Figure 4.3. All samples were measured in the PM state, i.e., well above their transition temperature. Although the metal-deficiency stoichiometry was applied in order to prevent the formation of the cubic $(Mn,Fe)_3Si$ impurity phase (space group *Fm-3m*) [34], Rietveld refinement of the measured XRD patterns confirmed the presence of a small fraction (< 4 wt.%), of a metal-rich impurity phase in each sample, and a minor amount (~ 1 wt.%) of Fe-Co impurity phase in $Fe_{1.33}Mn_{0.50}Co_{0.12}P_{0.66}Si_{0.35}$, which is in agreement with Mössbauer results. The excessive amount of metal content was also confirmed by EPMA measurements performed for Co and Ni-doped samples (x = 0.06, 0.12). As presented in Table 4.2, a significantly higher metal to non-metal (M/NM) ratio is observed in the selected samples, which prompts the occurrence of the metal-rich $(Mn,Fe)_3Si$ impurity phase. The impurity phase is present in the form of micro-sized inclusions (**Fig. S1** in the Supplementary Material). It is widely acknowledged that the metal-rich impurity tends to accumulate at grain boundaries. However, in the examined sample, it was difficult to distinguish individual grains and their boundaries. The porosity of the sample was determined using ImageJ software and found to be 8.2%. The partial elimination of grain boundaries caused by porosity can enhance mechanical stability and reduce thermal hysteresis. The results obtained from XRD and EPMA measurements indicate that further optimization of $(Mn,Fe)_2(P,Si)$ is necessary to avoid the impurity phase.

Table 4.2: *Aimed and found compositions, and M/NM ratios of Co and Ni-doped samples.*

Sample		Aimed Composition	Found Composition	Ratio
Doping type	Content (x)	Main Phase	Main phase	M/NM
Co	0.06	$Fe_{1.33}Mn_{0.56}Co_{0.06}P_{0.66}Si_{0.34}$	$Fe_{1.37}Mn_{0.61}Co_{0.06}P_{0.64}Si_{0.31}$	2.04/0.95
	0.12	$Fe_{1.33}Mn_{0.50}Co_{0.12}P_{0.66}Si_{0.34}$	$Fe_{1.38}Mn_{0.55}Co_{0.12}P_{0.64}Si_{0.31}$	2.05/0.95
Ni	0.06	$Fe_{1.33}Mn_{0.56}Ni_{0.06}P_{0.66}Si_{0.34}$	$Fe_{1.38}Mn_{0.62}Ni_{0.06}P_{0.65}Si_{0.30}$	2.06/0.95
	0.12	$Fe_{1.33}Mn_{0.50}Ni_{0.12}P_{0.66}Si_{0.34}$	$Fe_{1.37}Mn_{0.54}Ni_{0.12}P_{0.65}Si_{0.33}$	2.03/0.98

The counting error: Fe and Mn - 0.15 wt. %; Si, P, Co, Ni - 0.05 wt. %.

The unit cell volume of the primary phase decreased gradually with increasing Co and Ni content since both of these elements have a smaller covalent radius than the substituted atoms: the covalent radii for Co and Ni are 1.26 and 1.24 Å, while they are significantly larger for Fe and Mn with values of 1.39 and 1.32 Å for Mn and Fe, respectively. The decrease in unit-cell volume upon doping confirms the substitutional effect of these elements. It is noticeable that with increasing Co content, the unit-cell volume of the $(Mn,Fe)_3Si$ impurity phase exhibits a similar trend as the main phase. On the contrary, the unit-cell volume of the impurity phase present in the $Mn_{0.62-x}Fe_{1.33}Ni_xP_{0.66}Si_{0.34}$ series does not significantly change, indicating that Ni exhibits a strong affinity to the main phase (Figure 4.4). The preference of Co to both – the main phase and the impurity phase might contribute to a slightly diminished effect on the decrease in T_C when compared to the Ni-doped samples.

As proposed by Dung and co-workers, the relation between the *c/a* ratio and T_C reflects changes in the atomic distances upon doping [35]. It can be seen in Figure 4.5a that the *c/a* ratio increases with Co content and is accompanied by the decrease in T_C, remaining almost constant beyond 8 at.% of doping. In contrast to the Co-doped samples, as depicted in Figure 4.5b. the Ni-doped samples show that T_C and *c/a* changes linearly in the opposite sense. From the XRD patterns it is found that in $Mn_{0.62-x}Fe_{1.33}Ni_xP_{0.66}Si_{0.34}$ series, with increasing Ni content, the (300) and (002) reflections shift towards each other, indicating that the lattice parameters *a* and *c* move in the opposite sense (Figure 4.6).

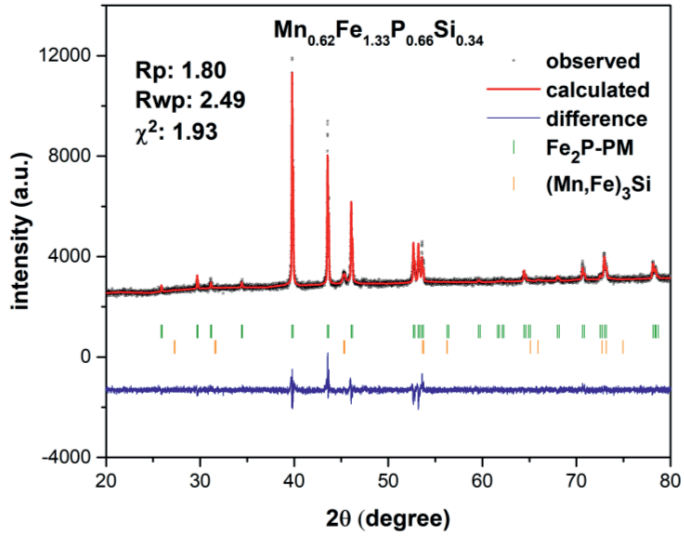

Figure 4.3: *Observed and calculated XRD patterns of $Mn_{0.62}Fe_{1.33}P_{0.66}Si_{0.34}$.*

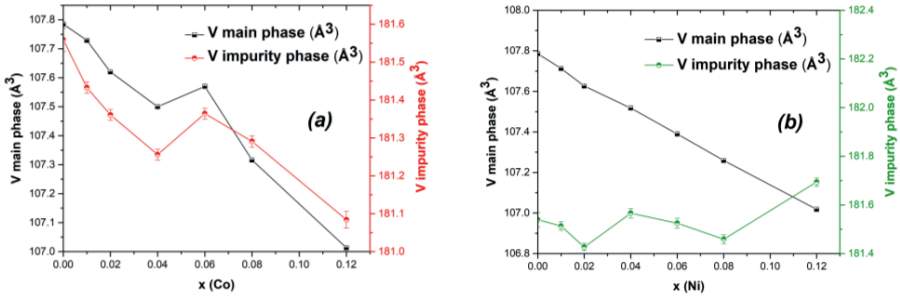

Figure 4.4: *Composition dependence of the volume (main phase and impurity phase) of the (a) $Mn_{0.62-x}Fe_{1.33}Co_xP_{0.66}Si_{0.34}$ and (b) $Mn_{0.62-x}Fe_{1.33}Ni_xP_{0.66}Si_{0.34}$ derived from X-ray diffraction patterns measured at 348 K (PM state).*

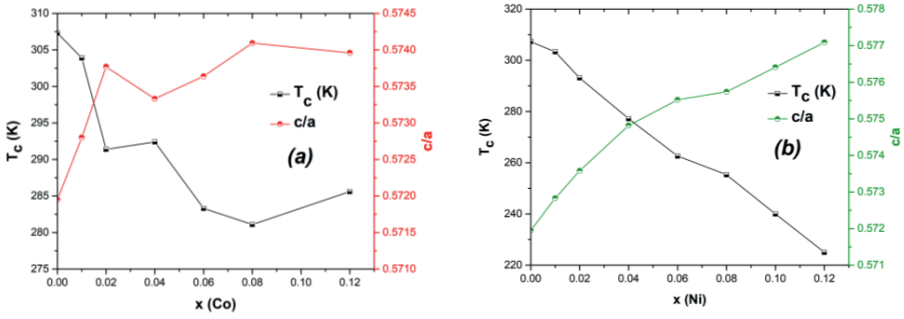

Figure 4.5: *Composition dependence of the T_c upon heating and c/a ratio derived from X-ray diffraction patterns measured at 348 K (PM state) of the (a) $Mn_{0.62-x}Fe_{1.33}Co_xP_{0.66}Si_{0.34}$ and (b) $Mn_{0.62-x}Fe_{1.33}Ni_xP_{0.66}Si_{0.34}$.*

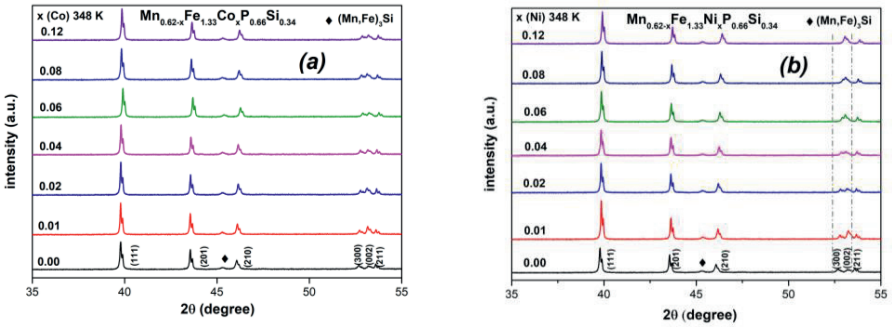

Figure 4.6: *X-ray diffraction patterns of (a) $Mn_{0.62-x}Fe_{1.33}Co_xP_{0.66}Si_{0.34}$ and (b) $Mn_{0.62-x}Fe_{1.33}Ni_xP_{0.66}Si_{0.34}$ recorded at 348 K (PM state). With increasing Ni content, the (300) and (002) reflections shift towards each other, indicating that the lattice parameters a and c move in opposite direction.*

4.3.3. Magnetic properties

The temperature-dependent magnetization for the $Mn_{0.62-x}Fe_{1.33}Co_xP_{0.66}Si_{0.34}$ and $Mn_{0.62-x}Fe_{1.33}Ni_xP_{0.66}Si_{0.34}$ compounds measured in 1 T is shown in Figure 4.7**.** It is found that T_C decreases with increasing Co and Ni content, which is in good agreement with results published by van Thang and co-workers [17] and Ou and co-workers [18]. In $Mn_{0.62-x}Fe_{1.33}Co_xP_{0.66}Si_{0.34}$, we observe that T_C and the thermal hysteresis decrease linearly up to 6 at.% Co doping and do not significantly change after exceeding the before-mentioned concentration. As obtained from the DSC measurements, upon 12 at.% of Co doping, T_C decreased from 308.4 to 283.3 K and the thermal hysteresis decreased from 11.0 to 3.9 K. In $Mn_{0.62-x}Fe_{1.33}Ni_xP_{0.66}Si_{0.34}$, the thermal hysteresis also reaches a constant value for approximately 6 at.% of Ni, however the change in T_C is not retained. In the Ni-doped samples T_C changed from 308.4 to 226.6 K for 12 at.% of doping, and the thermal hysteresis decreased from 11.0 to 4.9 K. These results are consistent with the observed behaviour for

the *c/a* ratio derived from XRD measurements. The effect of a reduced hysteresis was more pronounced in Co-doped samples, as depicted in Figure 4.8. The thermal hysteresis is controlled by the energy barrier for nucleation and thus, provides an important insight into the effect of doping on the character of the magnetic transition. The decrease in the hysteresis upon doping relates to the electronic configuration of Co and Ni, as both of these atoms have an incomplete *3d* orbital and a filled *4s* orbital (7 and 8 of *3d* electrons, for Co and Ni respectively), contributing to the weakening of the energy barrier for nucleation [5], [18]. As the energy barrier for nucleation is reduced, the FOMT weakens accordingly. In both series of samples, the changes in T_C and the thermal hysteresis are accompanied by the gradual decrease in the latent heat, from 6.2 kJ/kg to 0.9 kJ/kg and 0.7 kJ/kg for 12 at.% of Co and Ni doping, respectively. The changes in the latent heat and thermal hysteresis clearly indicate that dopant atoms weaken the strength of the first-order magnetic transition.

The insert of the Figure 4.7a presents the field dependence of the saturation magnetization (M_S) for the $Mn_{0.62-x}Fe_{1.33}Co_xP_{0.66}Si_{0.34}$ samples. It shows that M_S increases and reaches a maximum well above the reference value for 2 at.% Co, before the decrease. As shown in Figure 4.7b, for the $Mn_{0.62-x}Fe_{1.33}Ni_xP_{0.66}Si_{0.34}$ samples, the trend of increasing magnetization for a small doping is not observed. This behaviour suggests that Fe-rich $(Mn,Fe,Co)_{1.95}(P,Si)$ alloys might exhibit a similar magnetic behaviour as the Fe-Co alloys. Various studies show that the average magnetic moment of Fe-Co alloy reaches the highest value for a small Co content (20-25 at.%) before a decrease is observed [36]–[38]. The reason responsible for a rapid increase in M_S for a small Co doping is complex and is related to changes in the magnetic moment and electronic structure [39]. When a Co atom is respectively replacing an Fe atom with 8 e^- in the outermost shells, the structure gathers an additional *3d* e^-. The abrupt change in the saturation magnetization is explained by the increase in the mean magnetic moment caused by the enhancement of the magnetic moment of Fe, whereas the magnetic moment of Co remains almost unchanged [37], [38].

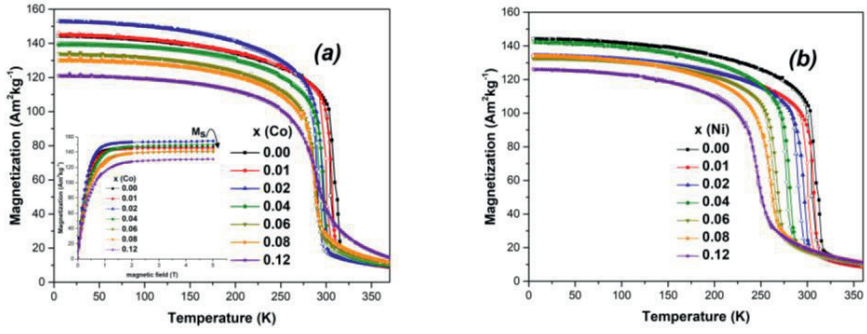

Figure 4.7: *Temperature dependence of the magnetization of (a) $Mn_{0.62-x}Fe_{1.33}Co_xP_{0.66}Si_{0.34}$ and (b) $Mn_{0.62-x}Fe_{1.33}Ni_xP_{0.66}Si_{0.34}$ compounds measured in a magnetic field of 1 T. The insert shows the field dependence of $Mn_{0.62-x}Fe_{1.33}Co_xP_{0.66}Si_{0.34}$ measured at 5 K.*

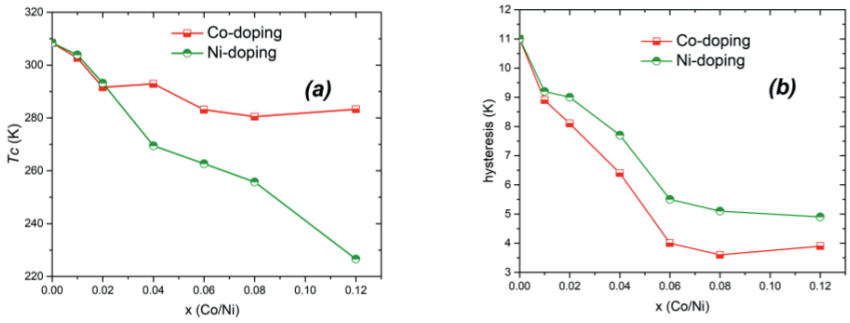

Figure 4.8: *(a) The composition dependence of the T_C for Co and Ni doped samples and (b) changes in the thermal hysteresis as the function of doping content obtained from DSC measurements.*

4.3.4. DFT calculations

DFT calculations were performed in order to investigate the preferential doping site and the change in the local magnetic moments in the Fe-rich $(Mn,Fe,Co)_{1.95}(P,Si)$ and $(Mn,Fe,Ni)_{1.95}(P,Si)$ compounds. To investigate the site preference, dopant atoms were placed on either *3g* or *3f* crystallographic sites. The energy cost of forming each structure (E_f) is calculated as the difference between energies of doped (E_d) and pure (E_p) compounds, including the chemical potential contribution of the dopant atom (μ_d) and substituted atom (μ_s), as indicated in Eq. (4.1). The chemical potentials are obtained by first optimizing the structure for each element and then taking the value of total energy per atom.

$$E_f = E_{doped} + \mu_s - (E_{pure} + \mu_d) \tag{4.1}$$

To investigate the favorable site for the doping atoms, one Fe atom from the *3f* site was substituted and subsequently, one Mn/Fe atom from the *3g* site by a dopant atom. From the DFT calculations, we see in Table 4.3 that for both – Co and Ni doping, the lowest formation energy is assigned to the *3f* site, indicating that Co and Ni substitute Fe at this site. These calculations support the findings of Mössbauer spectroscopy results discussed in section 4.3.1. Earlier studies have shown that correlation effects in the $(MnFe)_2(P,Si)$ family of compounds have no remarkable impact on the magnetic properties and electronic structure [40]. However, according to the previous DFT calculations [33], [41], the unusual magnetocaloric properties of the $(Mn,Fe)_2(P,Si)$ across the ferromagnetic transition arise from the "mixed magnetism", which indicates the presence of an electron instability of the *3f* moments in the presence of stable *3g* moments. The magnitude of the Co and Ni magnetic moment at the *3f* site is remarkably lower in comparison to that of the substituted Fe, mainly due to the fact that the dopant atoms have more *3d* valence electrons. DFT calculations revealed that the total magnetic moment decreases with increasing doping content. It has been

calculated that the total magnetic moment decreases from 4.26 μ_B/f.u. to 4.22 μ_B/f.u. upon 8 at.% Co doping. However, for 2 at.% Co, we observe a significant difference in the local magnetic moment of Fe, in comparison to the corresponding Ni-doped sample. As shown in Figure 4.9 upon 2 at.% Co doping we observe a local moment enhancement on the *3f* site, whereas for 2 at.% Ni doping Figure 4.10 indicates a strong weakening of the Fe magnetic moment on the *3f* site, which again is in good agreement with the magnetic measurements discussed in section 4.3.3.

The band structure of Co and Ni doped $(Mn,Fe)_2(P,Si)$ for both spin up and spin down channels reveals metallic nature (**Fig. S2** and **S3** in the Supplementary Material). The observed difference in magnetic behaviour upon Co and Ni doping in $(Mn,Fe)_2(P,Si)$ can be explained by the change in the density of states (DOS) at the Fermi level. The partial DOS for Co and Ni are presented in Figure 4.11, whereas the total DOS are shown in Figure 4.12. According to ab-initio calculations performed for the doped $(Mn,Fe)_2(P,Si)$ [33], in the Co-doped system, a sharp peak of DOS resides at the Fermi level. This implies that a minor change in the DOS at the Fermi level can result in pronounced changes in magnetic behaviour. The difference between Co and Ni doping is especially highlighted in Figure 4.12. Unlike for Co-doped $(Mn,Fe)_2(P,Si)$, the DFT calculations did not predict the presence of a sharp peak at the Fermi level for the Ni-doped system, which indicates that abrupt changes in the magnetic properties are in this case not expected.

Table 4.3: *Formation energy calculated per formula unit (eV/f.u.) for Co and Ni substitution.*

Site	*Formation energy (Co)*	*Formation energy (Ni)*
3g (Mn)	-4.085	-4.287
3g (Fe)	-4.236	-4.466
3f (Fe)	-4.387	-4.516

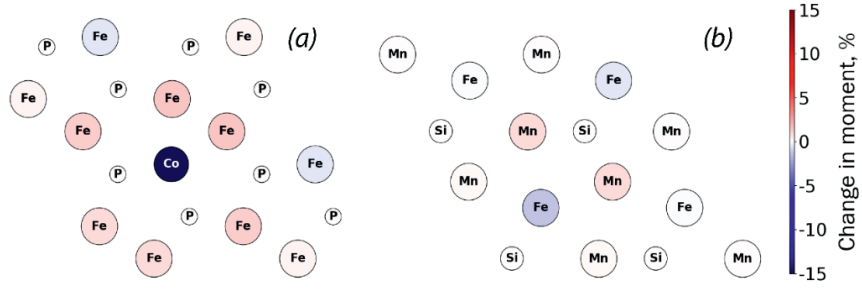

Figure 4.9: *Change of the local magnetic moment upon 2 at.% Co doping in the (a) 3f site and (b) 3g site. Note that Co prefers the 3f site.*

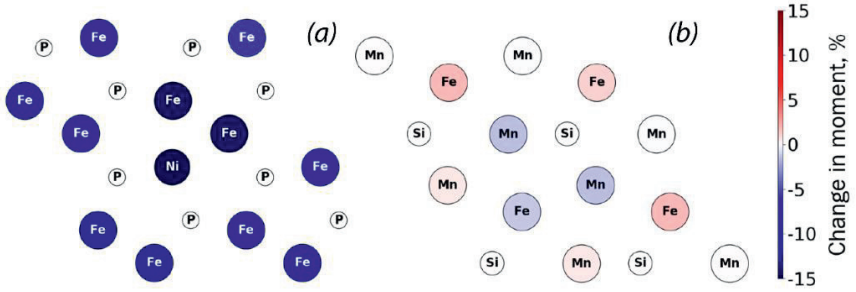

Figure 4.10: *Change of the local magnetic moment upon 2 at.% Ni doping in the (a) 3f site and (b) 3g site. Note that Ni prefers the 3f site.*

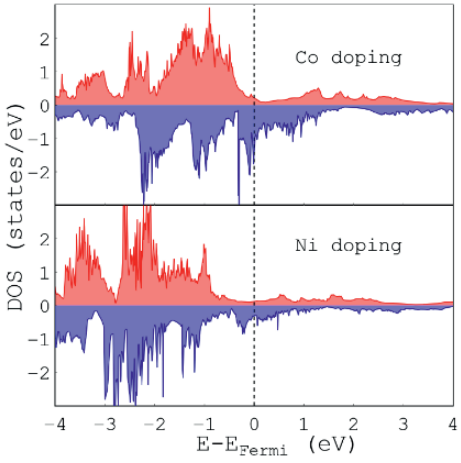

Figure 4.11: *Partial DOS of $Mn_{0.66}Fe_{1.25}T_{0.08}P_{0.66}Si_{0.33}$ (T = Co, Ni) compounds for Co and Ni in the vicinity of Fermi level. Spin up and spin down states are coloured with red and blue respectively. Zero represents the Fermi energy.*

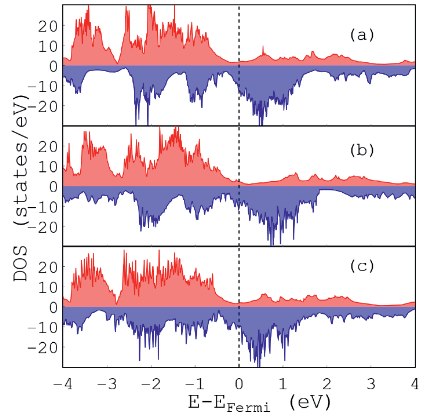

Figure 4.12: *Total DOS for (a) $Mn_{0.66}Fe_{1.33}P_{0.66}Si_{0.33}$, (b) $Mn_{0.66}Fe_{1.25}Co_{0.08}P_{0.66}Si_{0.33}$ and (c) $Mn_{0.66}Fe_{1.25}Ni_{0.08}P_{0.66}Si_{0.33}$ in the vicinity of Fermi level. Spin up and spin down states are coloured with red and blue respectively. Zero represents the Fermi energy.*

4.4. Conclusions

The $Mn_{0.62-x}Fe_{1.33}Co_xP_{0.66}Si_{0.34}$ and $Mn_{0.62-x}Fe_{1.33}Ni_xP_{0.66}Si_{0.34}$ alloys were prepared by ball-milling and a subsequent solid-state reaction. The effect of Co and Ni doping on the structure and magnetic properties has been systematically studied using Mössbauer spectroscopy, XRD, EPMA, DSC and magnetization measurements. The obtained results were compared with DFT calculations. All the compounds crystallize in the hexagonal Fe_2P structure with a small amount of the metal-rich $(Mn,Fe)_3Si$ impurity phase for all samples, indicating that further optimization of the $(Mn,Fe)_2(P,Si)$ composition might be important to further optimize the properties. Mössbauer spectroscopy and DFT calculations revealed that the doping atoms substitute Fe at the *3f* site. It is found, that Co and Ni doping both weaken the ferromagnetic ordering and the energy barrier for nucleation, resulting in a decrease in T_C and the thermal hysteresis. On account of the electronic structure of Ni and its preference to the main phase, the decrease in T_C is more pronounced in Ni-doped samples. Although DFT calculations predict a decrease of the total magnetic moment with increasing doping content, an increase in magnetization is observed well above the reference value for 2 at.% of Co. Besides, the DFT calculations show that Co doping, contrary to Ni, enhances the local magnetic moment of Fe atoms at the *3f* site.

References

[1] E. Brück, "Developments in magnetocaloric refrigeration", *J. Phys. D. Appl. Phys.*, *38*(23), 2005, doi: 10.1088/0022-3727/38/23/R01.

[2] E. Brück, O. Tegus, D. T. C. Thanh, and K. H. J. Buschow, "Magnetocaloric refrigeration near room temperature (invited)", *J. Magn. Magn. Mater.*, *310*(2), pp. 2793–2799, 2007, doi: https://doi.org/10.1016/j.jmmm.2006.10.1146.

[3] O. Gutfleisch, M. A. Willard, E. Brück, C. H. Chen, S. G. Sankar, and J. P. Liu, "Magnetic materials and devices for the 21st century: Stronger, lighter, and more energy efficient", *Adv. Mater.*, *23*(7), pp. 821–842, 2011, doi: 10.1002/adma.201002180.

[4] A. Gschneidner, V. K. Pecharsky, and A. O. Tsokol, "Recent developments in magnetocaloric materials", *Reports Prog. Phys.*, *68*(6), pp. 1479–1539, 2005, doi: 10.1088/0034-4885/68/6/R04.

[5] V. Chaudhary, X. Chen, and R. V. Ramanujan, "Iron and manganese based magnetocaloric materials for near room temperature thermal management", *Prog. Mater. Sci.*, *100*, pp. 64–98, 2019, doi: 10.1016/j.pmatsci.2018.09.005.

[6] F. Guillou, G. Porcari, H. Yibole, N. Van Dijk, and E. Brück, "Taming the first-order transition in giant magnetocaloric materials", *Adv. Mater.*, *26*(17), pp. 2671–2675, 2014, doi: 10.1002/adma.201304788.

[7] N. H. Dung, Z. Q. Ou, L. Caron, L. Zhang, D. T. C. Thanh, G. A. de Wijs, R. A. de Groot, K. H. J. Buschow, and E. Brück, "Mixed magnetism for refrigeration and energy conversion", *Adv. Energy Mater.*, *1*(6), pp. 1215–1219, 2011, doi: 10.1002/aenm.201100252.

[8] N. H. Dung, L. Zhang, Z. Q. Ou, L. Zhao, L. van Ejck, A. M. Mulders, M. Avdeev, E. Suard, N. H. van Dijk, and E. Brück, "High/low-moment phase transition in hexagonal Mn-Fe-P-Si compounds", *Phys. Rev. B - Condens. Matter Mater. Phys.*, *86*(4), 2012, doi: 10.1103/PhysRevB.86.045134.

[9] Z. Q. Ou, L. Zhang, N. H. Dung, L. Caron, and E. Brück, "Structure, magnetism and magnetocalorics of Fe-rich $(Mn,Fe)_{1.95}P_{1-x}Si_x$ melt-spun ribbons," *J. Alloys Compd.*, *710*, pp. 446–451, 2017, doi: 10.1016/j.jallcom.2017.03.266.

[10] X. F. Miao, Y. Mitsui, A. I. Dugulan, L. Caron, N. V. Thang, P. Manuel, K. Koyama, K. Takahashi, N. H. van Dijk, and Brück, "Kinetic-arrest-induced phase coexistence and metastability in $(Mn,Fe)_2(P,Si)$", *Phys. Rev. B*, *94*(9), 2016, doi: 10.1103/PhysRevB.94.094426.

[11] J. Lai, B. Huang, X. Miao, N. H. van Thang, X. You, M. Maschek, L. van Eijck, D. Zeng, N. H. van Dijk, and E. Brück, "Combined effect of annealing temperature and vanadium substitution for mangetocaloric $Mn_{1.2-x}V_xFe_{0.75}P_{0.5}Si_{0.5}$ alloys", *J. Alloys Compd.*, *803*, pp. 671–677, 2019, doi: 10.1016/j.jallcom.2019.06.239.

[12] J. Lai, X. You, A. I. Dugulan, B. Huang, J. Liu, M. Maschek, L. van Eijck, N. H. van Dijk, and E. Brück, "Tuning the magneto-elastic transition of $(Mn,Fe,V)_2(P,Si)$

alloys to low magnetic field applications", *J. Alloys Compd.*, *821* p. 153451, 2020, doi: 10.1016/j.jallcom.2019.153451.

[13] N. V. Thang, H. Yibole, N. H. van Dijk, and E. Brück, "Effect of heat treatment conditions on MnFe(P,Si,B) compounds for room-temperature magnetic refrigeration", *J. Alloys Compd.*, *699*, pp. 633–637, 2017, doi: 10.1016/j.jallcom.2016.12.402.

[14] X. F. Miao, N. V. Thang, L. Caron, H. Yibole, R. I. Smith, N. H. van Dijk, and E. Brück, "Tuning the magnetoelastic transition in $(Mn,Fe)_2(P,Si)$ by B, C, and N doping", *Scr. Mater.*, *124*, pp. 129–132, 2016, doi: 10.1016/j.scriptamat.2016.07.015.

[15] N. V. Thang, H. Yibole, X. F. Miao, K. Goubitz, L. van Eijck, N. H. van Dijk, and E. Brück, "Effect of Carbon Doping on the Structure and Magnetic Phase Transition in $(Mn,Fe)_2(P,Si)$", *Jom*, *69*(8), pp. 1432–1438, 2017, doi: 10.1007/s11837-017-2400-0.

[16] Q. Zhou, Z. G. Zheng, Z. G. Qiu, Y. Hong, Y. Mozharivskyj, and D. C. Zeng, "Effect of Carbon Doping on the Structure and Magnetocaloric Properties of $Mn_{1.15}Fe_{0.80}P_{0.50}Si_{0.50}$ Compounds", *J. Supercond. Nov. Magn.*, *32*(12), pp. 3987–3994, 2019, doi: 10.1007/s10948-019-05184-8.

[17] N. van Thang, N. H. van Dijk, and E. Brück, "Tuneable giant magnetocaloric effect in $(Mn,Fe)_2(P,Si)$ materials by Co-B and Ni-B co-doping", *Materials (Basel)*, *10*(1), 2017, doi: 10.3390/ma10010014.

[18] Z. Q. Ou, N. H. Dung, L. Zhang, L. Caron, E. Torun, N. H. van Dijk, O. Tegus, and E. Brück, "Transition metal substitution in Fe_2P-based $MnFe_{0.95}P_{0.50}Si_{0.50}$ magnetocaloric compounds", *J. Alloys Compd.*, *730*, pp. 392–398, 2018, doi: 10.1016/j.jallcom.2017.09.315.

[19] C. Banza Lubaba Nkulu, L. Caas, V. Haufroid, T. de Putter, N. D. Saenen, T. Kayembe-Kitenge, P. Musa Obadia, D. Kyanika Wa Mukoma, J.-M. Lunda Ilunga, T. S. Nawrot, O. Luboya Numbi, E. Smolders, and B. Nemery, "Sustainability of artisanal mining of cobalt in DR Congo", *Nat. Sustain.*, *1*(9), pp. 495-504, 2018, doi: 10.1038/s41893-018-0139-4.

[20] H. Wada, T. Takahara, K. Katagiri, T. Ohnishi, K. Soejima, and K. Yamashita, "Recent progress of magnetocaloric effect and magnetic refrigerant materials of Mn compounds (invited)", *J. Appl. Phys.*, 117(17), 2015, doi: 10.1063/1.4914120.

[21] M. Fries, L. Pfeuffer, E. Bruder, T. Gottschall, S. Ener, L. V. B. Diop, T. Gröb, K. P. Skokov, and O. Gutfleisch, "Microstructural and magnetic properties of Mn-Fe-P-Si (Fe_2P-type) magnetocaloric compounds", *Acta Mater.*, *132*, pp. 222–229, 2017, doi: 10.1016/j.actamat.2017.04.040.

[22] R. P. Hermann, O. Tegus, E. Brück, K. H. J. Buschow, F. R. de Boer, G. J. Long, and F. Grandjean, "Mössbauer spectral study of the magnetocaloric $FeMnP_{1-x}As_x$ compounds," *Phys. Rev. B - Condens. Matter Mater. Phys.*, *70*(21), pp. 1–9, 2004, doi: 10.1103/PhysRevB.70.214425.

[23] J. Rodríguez-Carvajal, "Recent advances in magnetic structure determination by neutron powder diffraction", *Phys. B Phys. Condens. Matter*, *192*(1-2), 1993, doi: 10.1016/0921-4526(93)90108-I.

[24] J. T. Armstrong, "Quantitative elemental analysis of individual microparticales with electron beam instruments", *Electron Probe Quantization*, pp. 261–285, 1991.

[25] G. Kresse and J. Hafner, "Ab Initio Molecular Dynamics for Liquid Metals", *Phys. Rev. B. Condens. Matter*, *47*, pp. 558–561, 1993, doi: 10.1103/PhysRevB.47.558.

[26] G. Kresse and J. Furthmüller, "Efficiency of ab-initio total energy calculations for metals and semiconductors using a plane-wave basis set", *Comput. Mater. Sci.*, *6*(1), pp. 15–50, 1996, doi: 10.1016/0927-0256(96)00008-0.

[27] P. E. Blöchl, "Projector augmented-wave method", *Phys. Rev. B*, *50*(24), pp. 17953–17979, 1994, doi: 10.1103/PhysRevB.50.17953.

[28] G. Kresse and D. Joubert, "From ultrasoft pseudopotentials to the projector augmented-wave method", *Phys. Rev. B*, *59*(3), pp. 1758–1775, 1999, doi: 10.1103/PhysRevB.59.1758.

[29] J. P. Perdew, K. Burke, and M. Ernzerhof, "Generalized Gradient Approximation Made Simple", *Phys. Rev. Lett.*, *77*(18), pp. 3865–3868, 1996, doi: 10.1103/PhysRevLett.77.3865.

[30] M. Methfessel and A. T. Paxton, "High-precision sampling for Brillouin-zone integration in metals", *Phys. Rev. B*, *40*(6), pp. 3616–3621, 1989, doi: 10.1103/PhysRevB.40.3616.

[31] M. F. J. Boeije P. Roy, F. Guillou, H. Yibole, X. F. Miao, L. Caron, D. Banerjee, N. H. van Dijk, R. A. de Groot, and and E. Brück, "Efficient Room-Temperature Cooling with Magnets", *Chem. Mater.*, *28*(14), pp. 4901–4905, 2016, doi: 10.1021/acs.chemmater.6b00518.

[32] D. Fruchart, S. Haj-Khlifa, P. de Rango, M. Balli, R. Zach, W. Chajec, P. Fornal, J. Stanek, S. Kasprzyk, and J. Tobola, "Structure and Magnetic Properties of Bulk Synthesized Mn_{2-x} $Fe_xP_{1-y}Si_y$ Compounds from Magnetization, ^{57}Fe Mössbauer Spectroscopy, and Electronic Structure Calculations", *Crystals*, *9*(1), p. 37, 2019, doi: 10.3390/cryst9010037.

[33] P. Roy, E. Torun, and R. A. De Groot, "Effect of doping and elastic properties in $(Mn, Fe)_2(Si, P)$", *Phys. Rev. B*, *93*(9), 2016, doi: 10.1103/PhysRevB.93.094110.

[34] N. H. Dung, L. Zhang, Z. Q. Ou, and E. Brück, "From first-order magneto-elastic to magneto-structural transition in $(Mn,Fe)_{1.95}P_{0.50}Si_{0.50}$ compounds", *Appl. Phys. Lett.*, *99*(9), pp. 0–6, 2011, doi: 10.1063/1.3634016.

[35] N. H. Dung, L. Zhang, Z. Q. Ou, and E. Brück, "Magnetoelastic coupling and magnetocaloric effect in hexagonal Mn-Fe-P-Si compounds", *Scr. Mater.*, *67*(12), pp. 975–978, 2012, doi: 10.1016/j.scriptamat.2012.08.036.

[36] C. Rizal, J. Kolthammer, R. K. Pokharel, and B. C. Choi, "Magnetic properties of nanostructured Fe-Co alloys", *J. Appl. Phys.*, *113*(11), 2013, doi: 10.1063/1.4795267.

[37] C. Paduani and J. C. Krause, "Electronic structure and magnetization of Fe-Co alloys and multilayers," *J. Appl. Phys.*, *86*(1), pp. 578–583, 1999, doi: 10.1063/1.370769.

[38] V.-T. Tran, C.-C. Fu, and K. Li, "Predicting magnetization of ferromagnetic binary Fe alloys from chemical short range order", *Comput. Mater. Sci.*, *172*, p. 109344, 2020, doi: https://doi.org/10.1016/j.commatsci.2019.109344.

[39] D. Kim, J. Kim, J. Lee, M. K. Kang, S. H. Park, J. Kim, Y.-H. Choa, and J.-H. Lim, "Enhanced Magnetic Properties of FeCo Alloys by Two-Step Electroless Plating", *J. Electrochem. Soc.*, *166*(4), pp. D131–D136, 2019, doi: 10.1149/2.1251902jes.

[40] E. K. Delczeg-Czirjak, M. Pereiro, L. Bergqvist, Y. O. Kvashnin, I. Di Marco, G. Li, L. Vitos, O. Eriksson, "Origin of the magnetostructural coupling in $FeMnP_{0.75}Si_{0.25}$", *Phys. Rev. B - Condens. Matter Mater. Phys.*, *90*(21), 2014, doi: 10.1103/PhysRevB.90.214436.

[41] H. Yamada and K. Terao, "First-order transition of Fe_2P and anti-metamagnetic transition", *Phase Transitions*, *75*(1-2), pp. 231–242, 2002, doi: 10.1080/01411590290023120.

Supplementary material for Chapter 4

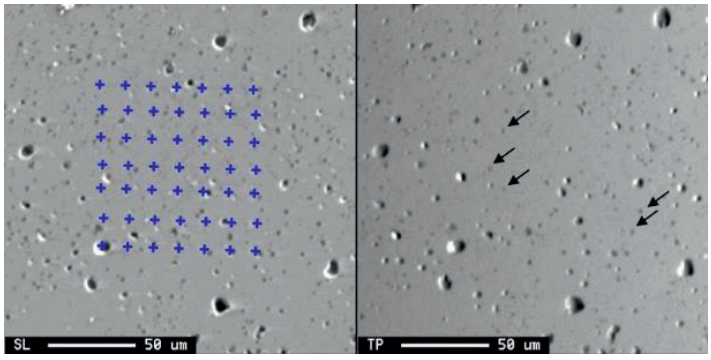

Fig. S1. *Secondary electron image (SL) and Topographical backscatter electron image (TP) for $Mn_{0.56}Fe_{1.33}Co_{0.06}P_{0.66}Si_{0.34}$. The crosses indicate measurement locations and arrows indicate impurities in the form of micro-sized inclusions. It can be seen that the grain boundaries cannot be clearly distinguished.*

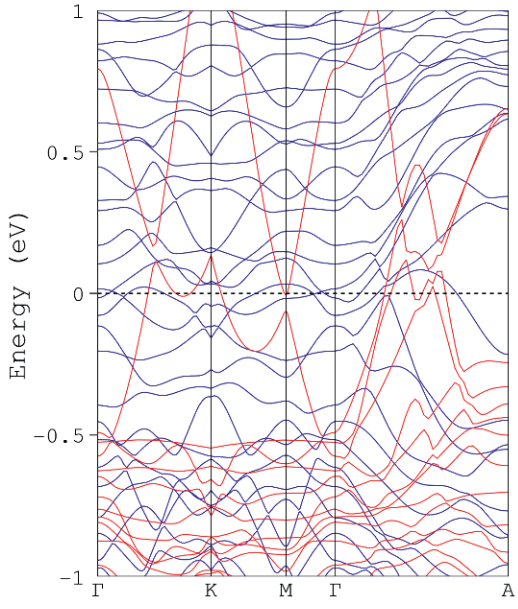

Fig. S2. *Band structure of $Mn_{0.66}Fe_{1.25}Co_{0.08}P_{0.66}Si_{0.33}$ along the high-symmetry directions. Red lines depict the spin up channel, while blue lines correspond to the spin down channel. Fermi level is marked by a dashed line.*

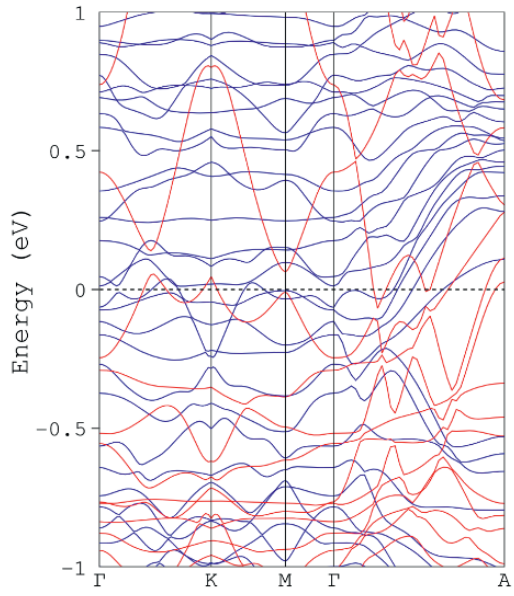

Fig. S3. *Band structure of* $Mn_{0.66}Fe_{1.25}Ni_{0.08}P_{0.66}Si_{0.33}$ *along the high-symmetry directions. Red lines depict the spin up channel, while blue lines correspond to the spin down channel. Fermi level is marked by a dashed line.*

5

Effect of the heat treatment on the microstructure, magnetism and magnetocaloric effect in Fe-rich $(Mn,Fe)_y(P,Si)$ melt-spun ribbons

Abstract

The effect of the heat treatment on the magnetism, magnetocaloric effect and microstructure formation has been systematically studied in Fe-rich $(Mn,Fe)_y(P,Si)$ melt-spun ribbons ($1.80 \leq y \leq 2.00$). XRD, SEM and EDS measurements demonstrate that a metal deficiency prompts the stable (Mn,Fe)Si phase, whereas in the metal-rich region the $(Mn,Fe)_3Si$ phase is formed. It is found that the annealing temperature influences the composition and lattice parameters of the $(Mn,Fe)_y(P,Si)$ alloys, which greatly affects the Curie temperature (T_C). For the optimal metal/non-metal ratio y the magnetic entropy change ($|\Delta S_m|$) is found to increase from 5.5 to 15.0 $Jkg^{-1}K^{-1}$ in a magnetic field change of 2 T by varying the annealing temperature from 1313 to 1433 K, indicating an enhancement of the first-order magnetic transition (FOMT). The presented results reveal that the secondary phase and magnetic properties in the $(Mn,Fe)_y(P,Si)$ system can be tuned by varying the annealing temperature and by adjusting the metal/non-metal ratio y.

5.1. Introduction

The magnetocaloric effect (MCE), discovered in 1917 by Weiss and Picard [1], is a phenomenon that corresponds to a change of temperature caused by the exposure of a material to an externally applied magnetic field. Although the giant magnetocaloric effect (GMCE) was first observed in Fe-Rh alloy by Annaorazov and co-workers [2], the interest in the application of magnetocaloric materials (MCM) in magnetic cooling started from the discovery of the GMCE in $Gd_5Ge_2Si_2$ by Pecharsky and Gschneidner [3]. This breakthrough research was followed by another milestone: the demonstration of near room-temperature magnetic-refrigeration prototype by Zimm and co-workers [4]. In comparison to traditional cooling technologies, magnetic cooling provides a significantly higher efficiency, and the environmental impact is reduced due to the elimination of hazardous, toxic and ozone-depleting refrigerants [5]. Materials exhibiting a first-order magnetic transition (FOMT) attract special attention due to the presence of a GMCE, usually associated with it [6]–[8]. Until now, many promising families of MCMs for the near-room temperature refrigeration have been studied intensively, e.g.: Fe-Rh [9]–[11], $Gd_5(Si,Ge)_4$ [3], [12], [13], $LaFe_{13-x}Si$ [14]–[16], $(Mn,Fe)_2(P,X)$, (X=As, Ge, Si) and its doped compounds [8], [17]–[20] and Heusler alloys [21], [22].

Among the mentioned magnetocaloric materials, the $(Mn,Fe)_2(P,Si)$ family of compounds that exhibit a large MCE in low magnetic fields near room temperature have drawn considerable attention. The Fe-rich region of the $(Mn,Fe)_2(P,Si)$ system is especially of interest due to its large magnetic moment and low costs of starting materials [20]. It has recently been reported that in this family of compounds, the metal/non-metal ratio (M/NM) has a significant impact on the final performance of the material [6], [23]. Additionally, the magnetocaloric response of the $(Mn,Fe)_2(P,Si)$ system appears to be highly sensitive to the synthesis route, particularly to the heat treatment conditions [24]–[26]. In order to reduce the annealing time and avoid oxides impurities, all samples in this study were prepared by melt spinning. Notwithstanding extensive studies on the impact of optimization and annealing, the effect of the heat treatment for different M/NM ratios on the final performance of the material and formation of impurity phases was not investigated yet. Therefore, the main objective of this work is to study the effect of the metal content and the heat treatment on the magnetic properties, microstructure and impurity phase formation in Fe-rich $(Mn,Fe)_y(P,Si)$ melt-spun ribbons.

5.2. Experimental methods

$Mn_{0.68}Fe_{y-0.68}P_{0.66}Si_{0.34}$ (y = 2.00, 1.95, 1.90, 1.85, 1.80) compounds were prepared by melt spinning and subsequent annealing. These compounds will for simplicity in the following be denoted as $(Mn,Fe)_y(P,Si)$, where y then also corresponds to the M/NM ratio in the $(Mn,Fe)_y(P,Si)$ system. Appropriate amounts of the starting materials (powders): Mn (99.9%; Alfa Aesar), Si (99.7%; American elements), MnP (99.8%; BASF), Fe_2P (99.9%; BASF), were weighed, mixed and ball milled together for 1 h at 350 rpm. The purity of starting materials was determined on a metals basis. Powders were pressed into pellets and

put into a quartz tube with a nozzle at the bottom. The as-spun ribbons were obtained by melting and ejection of the alloy through the nozzle on a rotating copper wheel. Prepared ribbons were placed in quartz tubes and sealed under 200 mbar Ar atmosphere before utilizing various heat treatments. All samples were annealed for 2 h at different temperatures. In order to minimize the formation of the metal-rich $(Mn,Fe)_3Si$ impurity phase, the oven was set to a target temperature before inserting the samples. In the first part of this study, we focussed on the optimization of the M/NM ratio. Therefore, the as-spun ribbons were annealed at 1373 K, which was found to be the optimal annealing temperature in an earlier report by Thang and co-workers [26]. In the second part of this study, we investigate the effect of the heat treatment by comparing samples from the first part of this study with melt-spun ribbons annealed at 1313 and 1433 K.

X-ray diffraction patterns were collected using a PANalytical X-pert Pro diffractometer with Cu-K_α radiation. Structural parameters and phase fractions were obtained by Rietveld refinement using the Fullprof program [27]. Magnetic measurements were conducted using superconducting quantum interference devices (SQUID) MPMS-XL and MPMS-5S magnetometers in the reciprocating sample option (RSO) mode, in the temperature range of 5-370 K with a constant sweep rate of 2 K/min. Differential scanning calorimetry (DSC) measurements were conducted using a TA-Q2000 DSC with a constant sweep rate of 10 K/min. Scanning electron microscopy (SEM, JEOL JSM 6500F, Japan) coupled with energy-disperse X-ray spectroscopy (EDS) was used to characterize the microstructure and the composition of the primary and secondary phases in selected melt-spun ribbons.

5.3. Results and discussion

5.3.1. Optimization of the metal content

XRD patterns for all samples were collected at 348 K to ensure that measured lattice parameters are derived for the same magnetic state. The refinements of the XRD data revealed that all compounds crystallize in the hexagonal Fe_2P-type structure (space group *P-62m*), as presented in Figure 5.1. Upon decreasing the M/NM ratio, the amount of metal-rich impurity $(Mn,Fe)_3Si$ (space group: *Fm-3m*) decreases. The lattice parameters derived in the PM state indicate the inflection point for the alloy $y = 1.90$, with a lattice parameter $a = 6.01636(4)$ Å, and $c = 3.44518(3)$ Å, as depicted in Figure 5.2**.** Further reduction of the metal content contributes to the occurrence of the non-metal rich impurity (Mn,Fe)Si (space group: $P2_13$). The phase fractions of the two impurity phases are presented in Figure 5.3, indicating a minimum total impurity content near $y = 1.90$. It should be noted that the minimum of two impurity phases can be found between 1.85 and 1.90. The refinements for the $y = 2.00$ and 1.80 samples are shown in Figure 5.4**.** It is worth recalling that in the non-metal rich region of the $(Mn,Fe)_y(P,Si)$ family of compounds, the hexagonal $(Mn,Fe)_5Si_3$ impurity phase (space group: $P6_3/mcm$) is expected [6]. The unexpected formation of the (Mn,Fe)Si phase is most likely related to an instability of the Fe-rich $(Mn,Fe)_5Si_3$ phase, which decomposes at temperatures below 800 °C [28], [29]. This behaviour also implies an Fe-rich and Si-rich composition of this impurity phase in the investigated region of the $(Mn,Fe)_y(P,Si)$ system.

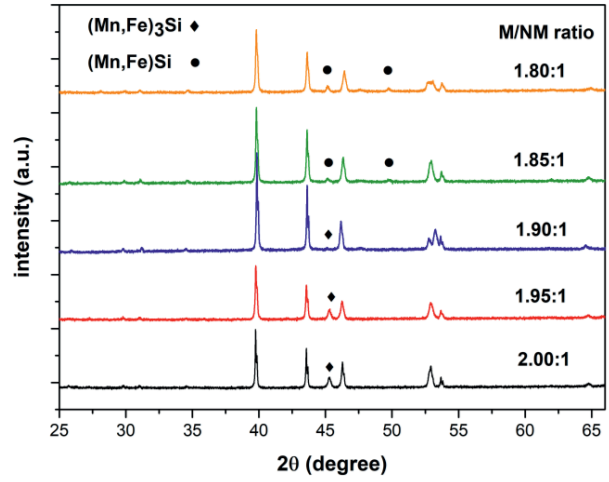

Figure 5.1: *XRD patterns measured for the $(Mn,Fe)_y(P,Si)$ alloys annealed at 1373 K (y = 1.80, 1.85, 1.90, 1.95, 2.00).*

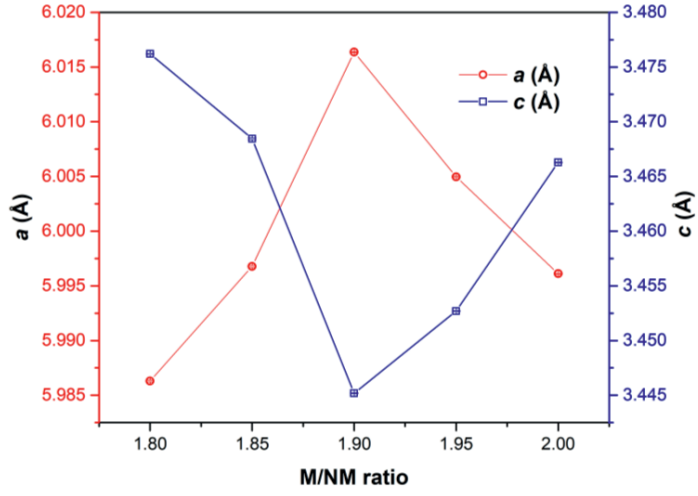

Figure 5.2: *Lattice parameters a and c of the $(Mn,Fe)_y(P,Si)$ compounds, derived from the XRD patterns measured at 348 K. Error bars are within the size of the markers.*

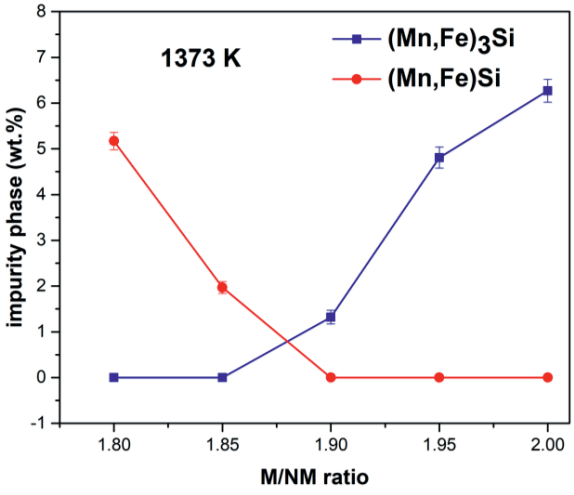

Figure 5.3: *Fraction of the secondary phase as a function of the M/NM ratio y.*

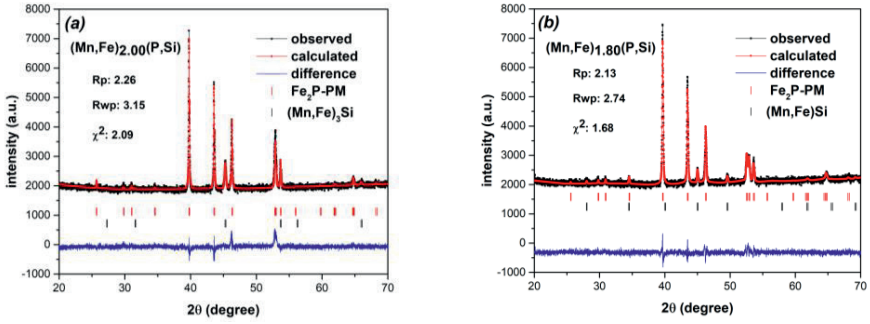

Figure 5.4: *Observed and calculated XRD patterns of a) $(Mn,Fe)_{2.00}(P,Si)$, b) $(Mn,Fe)_{1.80}(P,Si)$ in the paramagnetic state.*

In Figure **5.5** the temperature dependent magnetization (*M-T*) in an applied magnetic field of 1 T and the field dependent magnetization (*M-H*) at a temperature of 5 K are presented for the compounds annealed at 1373 K. The ferromagnetic transition temperature T_C was determined from the maximum in the temperature derivative of the magnetization $|dM/dT|$, as shown in Figure **5.6a.** The highest value of $|dM/dT|$ is observed for $y = 1.95$, suggesting the largest magnetic entropy change $|\Delta S_m|$. Decreasing y from 2.00 to 1.90 initially results in an increase in T_C from 251.3 to 310.1 K and a decrease in thermal hysteresis (ΔT_{hys}) from 33.3 to 8.3 K. A further decrease in the metal content y results in a decrease in T_C and a significant increase in hysteresis; by lowering y from 1.90 to 1.80 the value of T_C is reduced to 178.5 K and the thermal hysteresis is enhanced to 75.7 K. These pronounced changes in

T_C and ΔT_{hys} upon decreasing the metal content might be a consequence of a significant Si depletion caused by the occurrence of the non-metal rich (Mn,Fe)Si impurity phase. The values of $|\Delta S_m|$ were calculated from the *M-T* curves using the Maxwell equation:

$$\Delta S_m(T,H) = \int_{\mu_0 H_1}^{\mu_0 H_2} \left(\frac{\partial M(T)}{\partial T}\right)_H d(\mu_0 H) \tag{5.1}$$

The values of $|\Delta S_m|$ in a magnetic field change of 2 T are as follows: 0.8, 10.9, 13.2, 17.4, 9.9 $Jkg^{-1}K^{-1}$ for $y = 1.80$, 1.85, 1.90, 1.95, 2.00, respectively (see Fig. 6b). The highest T_C and the smallest thermal hysteresis ΔT_{hys} is observed for $y = 1.90$, which is also the composition that shows the lowest amount of impurity phases. However, the largest value of $|\Delta S_m|$ is observed for $y = 1.95$, which is due to a steeper transition and an almost equally large magnetization compared to $y = 1.90$. Similar observations were recently reported by Li and co-workers [6]. The shift of the optimal y towards a lower value ($y < 2.00$) can be due to possible losses of non-metals (P, Si) occurring during the sample preparation. Previous reports show a similar trend for compounds prepared using various methods [6], [23]. Therefore, we expect that the main reason responsible for a shift of the optimal M/NM ratio is ascribed to a prompt formation of the $(Mn,Fe)_3Si$ impurity phase, which forms when $y = 1.95$. By reducing secondary phases, the composition of the main phase is close to the nominal ratio.

The $(Mn,Fe)_2(P,Si)$ compounds are known to undergo a ferromagnetic-to-paramagnetic (FM-PM) transition upon heating. The *M-H* curve for $y = 1.80$ shows a broad magnetic hysteresis accompanied by a peculiar magnetic behaviour when the magnetic field is applied for the first time. It is noticeable that in low magnetic field (< 1 T), the *M-H* curve exhibits a typical FM-like behaviour and at higher magnetic fields, a metamagnetic transition occurs, which is incomplete even at 5 T. As seen in Figure **5.7**, this behaviour is not observed in decreasing field or in subsequent re-applied increasing magnetic field, which indicates that the initial (metastable) magnetic state is not restored. The metamagnetic transition originates from an incomplete first-order transition caused by kinetic arrest. A kinetic arrest has been reported in many materials, including the Fe_2P family of compounds [30]–[34]. The presented results show that the observed metamagnetic transition might occur as a result of the off-stoichiometry in $(Mn,Fe)_2(P,Si)$ compounds.

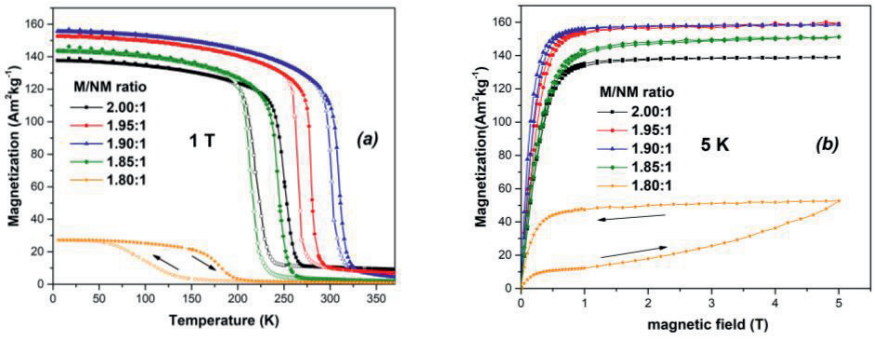

Figure 5.5: *a) Temperature dependent magnetization M-T measured in an applied field of $\mu_0 H$ = 1 T and b) field dependence of magnetization M-H at a temperature of T = 5 K for the $(Mn,Fe)_y(P,Si)$ alloys annealed at 1373 K.*

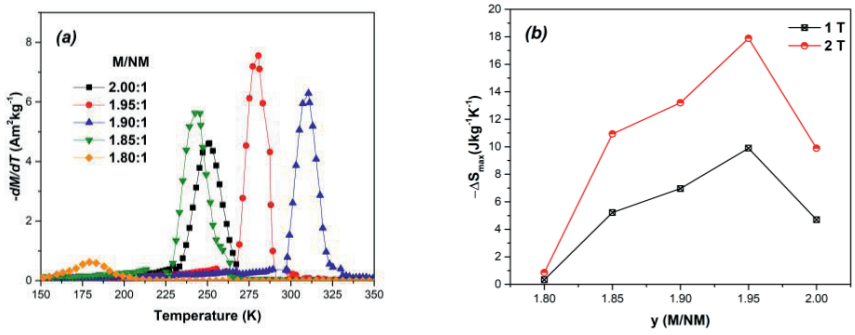

Figure 5.6: *a) Temperature derivative of the magnetization (-dM/dT) as a function of temperature measured in a field of 1 T, b) magnetic entropy change ($-\Delta S_m$) as a function of the metal/non-metal ratio for the $(Mn,Fe)_y(P,Si)$ alloys.*

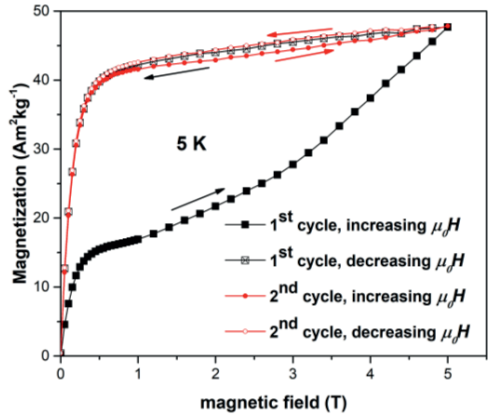

Figure 5.7: *Isothermal magnetization versus magnetic field (M-H) curves for y = 1.80 measured at 5 K.*

5.3.2. Influence of the annealing temperature

The amount of the $(Mn,Fe)_3Si$ impurity phase is slightly affected by the heat treatment conditions and shows a decreasing trend upon increasing annealing temperature, as shown in Figure **5.8**. As seen in the inset of Figure **5.8**, the diffraction peaks become sharper and narrower with increasing annealing temperature, which is attributed to enhanced homogeneity and a larger particle size. For $y = 2.00$ the amount of the $(Mn,Fe)_3Si$ impurity phase fraction reduces from 7.7 to 5.5 wt.% when the annealing temperature rises from 1313 to 1433 K. The observed decrease in the $(Mn,Fe)_3Si$ impurity phase shows a different trend than observed for the V-doped $(Mn,Fe)_2(P,Si)$ system, reported by Lai and co-workers [35]. For $y = 1.80$ the amount of the (Mn,Fe)Si impurity phase is hardly affected by the annealing temperature and corresponds to roughly 5 wt.%.

Figure **5.9a** shows that an increase in the annealing temperature from 1313 to 1373 K hardly affects the value of the *c/a* ratio. Consequently, the changes in T_C for samples annealed at 1313 and 1373 K should mainly originate from variations in the main phase composition caused by the presence of an impurity phase. The most pronounced difference appears for alloys $y = 1.90$, 1.95 and 2.00, annealed at 1433 K. As shown in Figure **5.9b**, the change in the *c/a* ratio is reflected by the opposite behaviour for T_C. The impact of a change in lattice parameter should be reflected most reliably by alloys containing the lowest amount of secondary phase. With increasing annealing temperature, the lattice parameter *a* increases by 0.08% and lattice parameter *c* decreases by 0.2% in the compound $y = 1.90$. An increase in the lattice parameter *a* leads to an increase in the distance between Fe and Si atoms in the *a-b* plane, which results in weakened chemical bonding. An opposite behaviour of the lattice parameter *c* causes a decrease in the distance between the interlayers of Mn and Fe atoms. These changes are expected to result in enhanced magnetic interactions [36], [37]. As a result, in Figure **5.10a** an increase in T_C and in saturation magnetization (M_s) is found upon an increasing annealing temperature. A sharper magnetic transition and an increase in M_s leads

to an increase in $|\Delta S_m|$, as depicted in Figure 5.10b. This highlights the positive impact of the highest annealing temperature but it should be noted that exceeding the temperature of 1433 K might result in melting of the alloy [7]. From Table 5.1 it can be observed that ΔT_{hys} and latent heat (L) increase simultaneously with annealing temperature in compounds containing a relatively low amount of secondary phases (y = 1.85-1.95), indicating an enhancement of the FOMT for these compounds. To determine the latent heat, we measured the total area under the peak curve of the phase transition using DSC. These changes are accompanied by an increase in M_s which is caused by improved homogeneity and changes in the interatomic distances, as previously discussed. As can be seen for $y = 1.90$ in Figure 5.10b, $|\Delta S_m|$ increases greatly from 5.5 to 15.5 $Jkg^{-1}K^{-1}$, whereas ΔT_{hys} increases from 1.9 to 9.9 K. The presence of a broad double peak in $|\Delta S_m|$ indicates that an annealing temperature of 1313 K is insufficient to provide homogeneity. In the $(Mn,Fe)_2(P,Si)$ alloys, the FOMT originates from an electronic redistribution around the *3f* site. Hence, the enhancement of the FOMT upon increasing annealing temperature can be linked to changes in the lattice parameters and an increased Fe occupation at the *3f* site [35], as indicated by XRD refinements. The refined occupancies of Fe are summarized in Table 5.2. An unexpected change in latent heat can be observed for $y = 2.00$; the highest value of the latent heat is observed for the alloy annealed at 1373 K. This result indicates the strongest FOMT at the annealing temperature of 1373 K, which is most probably related to changes in the composition of the main phase.

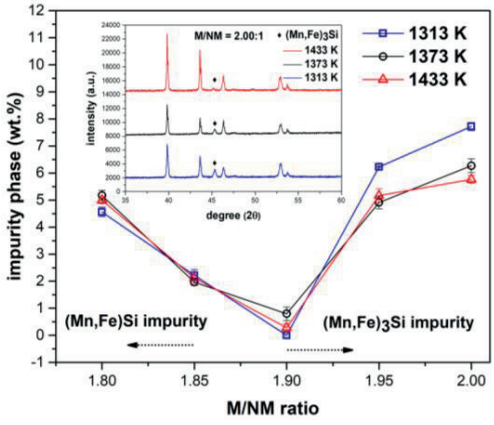

Figure 5.8: *Impurity phase fraction as a function of the metal/non-metal (M/NM) ratio y at different annealing temperatures. The inset shows the XRD patterns for y = 2.00 annealed at 1313, 1373 and 1433 K.*

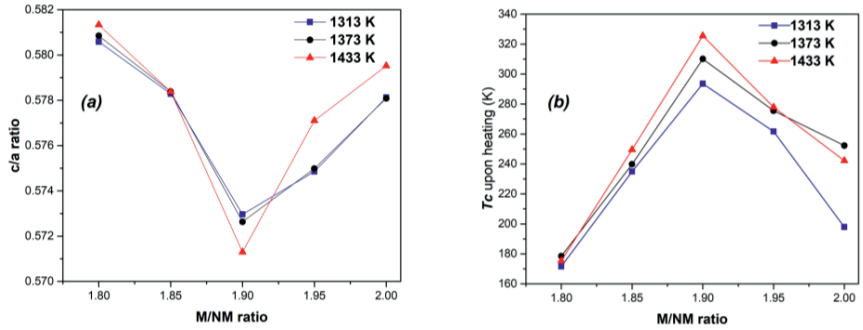

Figure 5.9: *Changes in a) c/a ratio and b) T_C as a function of the metal/non-metal (M/NM) ratio y for different annealing temperatures.*

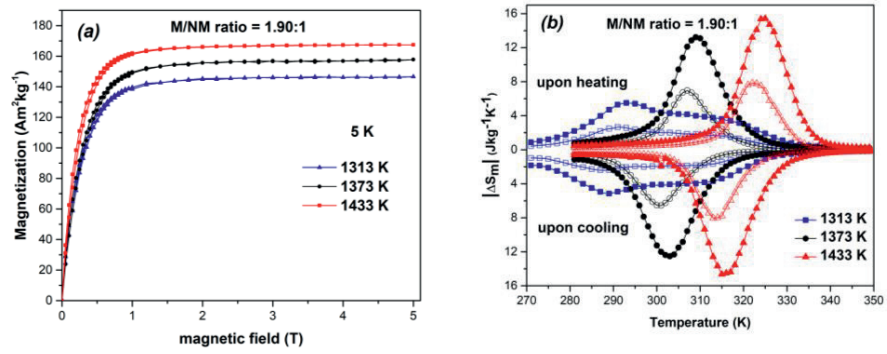

Figure 5.10: *Impact of the annealing temperature on a) the saturation magnetization (M_s), b) the magnetic entropy change $|\Delta S_m|$ in 1 T (open symbols) and 2 T (filled symbols) of the alloy y = 1.90.*

Table 5.1: *Collected data of T_C, ΔT_{hys}, L and M_s for $(Mn,Fe)_y(P,Si)$ annealed at 1313, 1373 and 1433 K. The latent heat L of the sample with y = 1.80 was not measured because the transition temperature occurs below the calibrated range of the DSC.*

	1313 K				1373 K				1433 K			
y	T_C (K)	ΔT_{hys} (K)	*L* (Jg^{-1})	M_s (Am^2kg^{-1})	T_C (K)	ΔT_{hys} (K)	*L* (Jg^{-1})	M_s (Am^2kg^{-1})	T_C (K)	ΔT_{hys} (K)	*L* (Jg^{-1})	M_s (Am^2kg^{-1})
1.80	171.6	71.8	-	36.1	178.5	75.7	-	52.6	175.4	79.2	-	61.3
1.85	235.0	19.0	1.9	148.4	239.8	22.1	4.8	151.2	249.6	31.6	5.3	156.8
1.90	293.6	1.9	1.1	146.6	310.1	8.3	6.5	157.8	325.6	9.9	7.4	167.5
1.95	261.7	5.8	2.9	154.8	275.5	12.1	5.7	156.7	277.9	18.3	6.6	158.7
2.00	197.9	22.1	0.4	133.7	251.3	33.3	5.1	138.8	242.2	39.9	3.8	152.8

Table 5.2: *Refined occupancies of Fe at the 3f and 3g site for $(Mn,Fe)_y(P,Si)$ annealed at 1313, 1373 and 1433 K. It is assumed that Mn exclusively occupies the 3g site [38].*

y	1313 K		1373 K		1433 K	
	3f (Fe)	*3g (Fe)*	*3f (Fe)*	*3g (Fe)*	*3f (Fe)*	*3g (Fe)*
1.80	0.216(1)	0.049(1)	0.221(2)	0.057(1)	0.222(1)	0.059(1)
1.85	0.182(2)	0.048(1)	0.191(3)	0.051(2)	0.193(1)	0.071(2)
1.90	0.222(1)	0.068(2)	0.236(1)	0.076(2)	0.246(2)	0.073(1)
1.95	0.180(1)	0.056(3)	0.197(1)	0.051(2)	0.268(1)	0.072(1)
2.00	0.208(2)	0.091(1)	0.256(1)	0.066(1)	0.264(1)	0.084(1)

5.3.3. Microstructure and impurity phase formation

To investigate the effect of the annealing temperature and metal content on the microstructure, the impurity phase formation and its influence on the magnetic properties, SEM/EDS analysis was performed for 6 samples: $y = 1.80$ and 2.00, annealed at 1313, 1373 and 1433 K.

In the $(Mn,Fe)_2(P,Si)$ system grain boundaries are preferred places for the formation of the $(Mn,Fe)_3Si$ impurity phase. Secondary phases tend to collect at grain boundaries, which lowers the interfacial energy between neighbouring crystallites [39], [40]. As shown in Figure **5.11a-c**, the (Mn,Fe)Si impurity phase segregates in the form of oval-shaped inclusions in the grain interior. An increase in the annealing temperature appears to weaken the mechanical properties as seen by an increase in the number of cracks. The effect of the annealing temperature on the formation of this impurity phase is found to be negligible. However, a reduction in the number of smaller inclusions (< 1 μm) is noticeable, most probably due to a coarsening into larger particles as the total amount of the impurity phase remained constant according to the XRD refinements. In addition to this, the composition of the (Mn,Fe)Si phase does not significantly change for increasing annealing temperatures. Therefore, the observed increase in the Fe content for the main phase might be ascribed to an enhanced homogeneity. The Si content shows the opposite trend, which in consequence, leads to minor changes in T_C. Alternatively, the rise in Fe content might indicate the presence of an amorphous Fe-rich impurity (not visible with XRD), which decreases with increasing annealing temperature. The compositions of the primary and impurity phases are collected in Table **5.3**. It can be noticed that the observed M/NM ratio of both the main and the impurity phase show some deviation from the expected composition. As the Mn/Fe ratio is in good agreement with the expected values, the obtained metal-rich compositions result from a deficiency of the non-metal that could possibly occur during sample preparation and/or as a result of the impurity phase formation. The Fe-rich and Si-rich composition of the impurity phase confirms that this phase is a product of Fe_5Si_3 degradation, as indicated in section 5.3.1. In the $(Mn,Fe)_2(P,Si)$ family of compounds T_C increases and the hysteresis decreases with increasing Fe and Si contents [20], [41]. Therefore, the occurrence of this impurity phase might contribute to a significant decrease in T_C and an increase in hysteresis, which is observed for $y = 1.85$ and 1.80.

Contrary to the non-metal-rich region, it appeared that the annealing temperature had a notable impact on the formation and the composition of the metal-rich $(Mn,Fe)_3Si$ impurity phase. Similar to the non-metallic sample, it has been observed that an increase in annealing temperature results in an increase in the number of cracks on the surface. This observation allows us to conclude that the mechanical properties of the sample undergo a decline. It can be seen in the inset of Figure **5.12a**, that after the annealing at 1313 K the compound is still inhomogeneous, as demonstrated by the presence of dendritic structures [24], which is in agreement with previously discussed magnetization results. As depicted in Figure **5.12a-c**, upon a further increase in the annealing temperature, grain growth can be observed, while the dendritic structures disappear. The grain size of the $y = 2.00$ sample

annealed at 1313 K does not exceed 5 µm and grain boundaries are pronounced, indicating an accumulation of the metal-rich impurity in this region. The increase in annealing temperature to 1373 K caused an enlargement of grains to about 30 µm. This grain growth is accompanied by a decrease in their number density, which also reduces the number of possible sites for the precipitation of the impurity phase. Hence, the reduction in grain-boundary density might contribute to a decreasing amount of the $(Mn,Fe)_3Si$ phase, as reported in section 5.3.2. After annealing at the highest temperature (1433 K), only fragmentary grain boundary precipitates are observed (indicated by arrows). Slight changes in composition of this impurity phase are observed, unlike the previously discussed (Mn,Fe)Si phase. It can be seen that with increasing annealing temperature, the amount of Fe in the impurity phase increases and the content of P decreases. Both the decrease in the amount of the secondary phase and the change in its composition directly impacts the composition of the main phase and thus, the magnetic properties. The highest T_C is observed for the alloy annealed at 1373 K, as an increase in Fe and Si content leads to a rise in T_C. Likewise, the lowest T_C is found for the alloy annealed at 1313 K as the Fe and Si content in this compound is the lowest. It is worth to recall that the difference in the *c/a* ratio for alloys annealed at 1313 and 1373 K is negligible. It is also worth emphasising that despite a linear decrease in the amount of the $(Mn,Fe)_3Si$ phase, this trend is not observed for T_C due to changes in the composition of the secondary phase. The presented results show that optimization of the heat treatment in the $(Mn,Fe)_y(P,Si)$ requires a careful consideration of the secondary phases and their transformation behaviour during the annealing process.

Table 5.3: *Compositions of the main and secondary phases in $(Mn,Fe)_{1.80}(P,Si)$ and $(Mn,Fe)_{2.00}(P,Si)$ alloys annealed at 1313, 1373 and 1433 K. Experimental uncertainties: Mn: ± 1.7 at.%, Fe: ± 1.2 at.%, P: 0.2 at.%, Si ± 0.2 at.%.*

Alloy	Main phase (*at.%*)	Secondary phase (*at.%*)	M/NM ratio	
			Main phase	Secondary phase
$y = 2.00$ – 1313 K	$Mn_{26.9}Fe_{47.0}P_{19.0}Si_{7.1}$	$Mn_{15.0}Fe_{61.9}P_{4.6}Si_{18.5}$	2.83	3.33
$y = 2.00$ – 1373 K	$Mn_{25.6}Fe_{48.7}P_{18.2}Si_{7.5}$	$Mn_{14.9}Fe_{63.5}P_{0.8}Si_{20.8}$	2.89	3.63
$y = 2.00$ – 1433 K	$Mn_{26.1}Fe_{47.9}P_{18.7}Si_{7.3}$	$Mn_{12.5}Fe_{66.8}P_{0.4}Si_{20.3}$	2.84	3.83
$y = 1.80$ – 1313 K	$Mn_{27.5}Fe_{46.5}P_{19.2}Si_{7.1}$	$Mn_{6.3}Fe_{51.3}P_{1.2}Si_{41.2}$	2.81	1.36
$y = 1.80$ – 1373 K	$Mn_{26.7}Fe_{47.4}P_{19.3}Si_{6.6}$	$Mn_{6.7}Fe_{50.3}P_{2.1}Si_{40.9}$	2.86	1.33
$y = 1.80$ – 1433 K	$Mn_{26.6}Fe_{48.3}P_{18.7}Si_{6.4}$	$Mn_{6.4}Fe_{51.3}P_{1.3}Si_{41.0}$	2.98	1.36

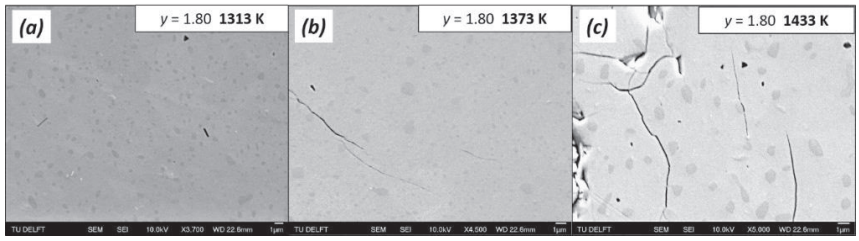

Figure 5.11: *SEM images of $(Mn,Fe)_{1.80}(P,Si)$ annealed at a) 1313 K, b) 1373 K, c) 1433 K.*

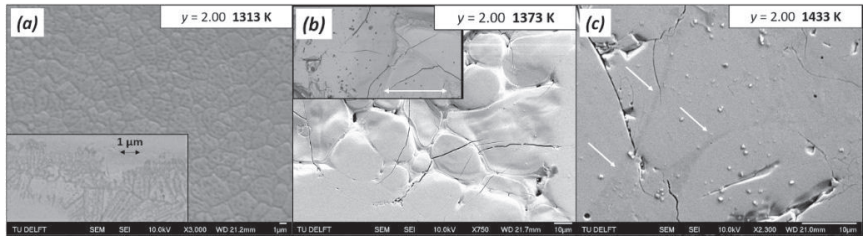

Figure 5.12: *SEM images of $(Mn,Fe)_{2.00}(P,Si)$ annealed at a) 1313 K, b) 1373 K, c) 1433 K. The insets show BSE images of a) dendritic-like structures, b) grain boundary region. Grain boundary precipitates are indicated by arrows.*

5.4. Conclusions

The effect of the annealing temperature and the optimization of the metal/non-metal ratio was investigated in Fe-rich $(Mn,Fe)_y(P,Si)$ melt-spun ribbons. While y decreases from 2.00 to 1.90, a reduction in the metal-rich impurity phase $(Mn,Fe)_3Si$, an increase in the Curie temperature (T_C) and a decrease in thermal hysteresis (ΔT_{hys}) is observed. A further decrease of metal content from 1.90 to 1.80 caused a decrease in T_C and a significant increase in ΔT_{hys}. Additionally, in the metal-deficient region of $(Mn,Fe)_y(P,Si)$, the formation of the (Mn,Fe)Si phase is observed, which is assigned to a degradation of the unstable and primary formed Fe_5Si_3 compound. With increasing annealing temperature, an increase in $|\Delta S_m|$, T_C and ΔT_{hys} is observed in the optimized compound (y =1.90), indicating an enhancement of the FOMT. It was found that the annealing temperature hardly influences the formation and the composition of the (Mn,Fe)Si impurity phase. On the other hand, the amount of the $(Mn,Fe)_3Si$ impurity phase slightly decreased with increasing annealing temperature, which might be assigned to grain growth and a reduced number of grain boundaries. A decrease in the $(Mn,Fe)_3Si$ impurity phase content was accompanied by changes in the main phase composition, which was directly reflected in the magnetic properties of the prepared compounds.

References

[1] P. Weiss and A. Piccard, "Le phénomène magnétocalorique", *J. Phys. Theor. Appl.*, *7*(1), pp. 103–109, 1917.

[2] M. P. Annaorazov, K. A. Asatryan, G. Myalikgulyev, S. A. Nikitin, A. M. Tishin, and A. L. Tyurin, "Alloys of the FeRh system as a new class of working material for magnetic refrigerators", *Cryogenics (Guildf).*, *32*(10), pp. 867–872, 1992, doi: 10.1016/0011-2275(92)90352-B.

[3] V. K. Pecharsky and K. A. Gschneidner, "Giant magnetocaloric effect in $Gd_5(Si_2Ge_2)$", *Phys. Rev. Lett.*, *78*(23), pp. 4494–4497, 1997, doi: 10.1103/PhysRevLett.78.4494.

[4] C. Zimm, A. Jastrab, A. Sternberg, V. Pecharsky, K. Gschneidner, M. Osborne, and I. Anderson, "Description and Performance of a Near-Room Temperature Magnetic Refrigerator", in *Advances in Cryogenic Engineering*, P. Kittel, Ed. Boston, MA: Springer US, pp. 1759–1766, 1998, doi: 10.1007/978-1-4757-9047-4_222.

[5] E. Brück, "Developments in magnetocaloric refrigeration", *J. Phys. D. Appl. Phys.*, *38*(23), 2005, doi: 10.1088/0022-3727/38/23/R01.

[6] C. F. Li, Z. G. Zheng, W. H. Wang, J. Y. Liu, L. Lei, and D. C Zeng, "Effect of M/NM ratios on structural and magnetic properties of $(Mn,Fe)_2(P,Si)$ compounds", *Phys. B Condens. Matter*, *594*, 2020, doi: 10.1016/j.physb.2020.412309.

[7] Z. G. Zheng, Z. R. Zhu, H. Y. Yu, D. C. Zeng, Y. H. Li, A. He, and Y. Mozharivskyj, "Large magnetic entropy change and magnetic phase transitions in rapidly quenched bulk Mn-Fe-P-Si alloys", *J. Alloys Compd.*, *725*, pp. 1069–1076, 2017, doi: 10.1016/j.jallcom.2017.07.243.

[8] Z. Q. Ou, N. H. Dung, L. Zhang, L. Caron, E. Torun, N. H. van Dijk, O. Tegus, and E. Brück, "Transition metal substitution in Fe_2P-based $MnFe_{0.95}P_{0.50}Si_{0.50}$ magnetocaloric compounds", *J. Alloys Compd.*, *730*, pp. 392–398, 2018, doi: 10.1016/j.jallcom.2017.09.315.

[9] R. R. Gimaev, A. A. Vaulin, A. F. Gubkin, and V. I. Zverev, "Peculiarities of Magnetic and Magnetocaloric Properties of Fe-Rh Alloys in the Range of Antiferromagnet–Ferromagnet Transition", *Phys. Met. Metallogr.*, *121*(9), pp. 823–850, 2020, doi: 10.1134/S0031918X20090045.

[10] Y. Cao, Y. Yuan, Y. Shang, V. I. Zverev, R. R. Gimaev, R. Barua, R. L. Hadimani, L. Mei, G. Guo, and H. Fu, "Phase transition and magnetocaloric effect in particulate Fe-Rh alloys", *J. Mater. Sci.*, *55*(27), pp. 13363–13371, 2020, doi: 10.1007/s10853-020-04921-y.

[11] A. Chirkova, K. P. Skokov, L. Schultz, N. V. Baranov, O. Gutfleisch, and T. G. Woodcock, "Giant adiabatic temperature change in FeRh alloys evidenced by direct measurements under cyclic conditions", *Acta Mater.*, *106*, pp. 15–21, 2016, doi: 10.1016/j.actamat.2015.11.054.

[12] A. M. G. Carvalho, C. S. Alves, A. de Campos, A. A. Coelho, S. Gama, F. C. G. Gandra, P. J. von Ranke,"The magnetic and magnetocaloric properties of $Gd_5Ge_2Si_2$ compound under hydrostatic pressure", *J. Appl. Phys.*, *97*(10), pp. 2003–2006, 2005, doi: 10.1063/1.1860932.

[13] C. S. Alves, S. Gama, A. Coelho, E. J. R. Plaza, A. M. G. Carvalho, L. P. Cardoso, and A. C. Persiano, "Giant magnetocaloric effect in $Gd_5(Si_2Ge_2)$ alloy with low purity Gd," *Mater. Res.*, *7*(4), pp. 535–538, 2004, doi: 10.1590/s1516-14392004000400005.

[14] J. Lyubina, R. Schäfer, N. Martin, L. Schultz, and O. Gutfleisch, "Novel Design of $La(Fe,Si)_{13}$ Alloys Towards High Magnetic Refrigeration Performance", *Adv. Mater.*, *22*(33), pp. 3735–3739, 2010, doi: 10.1002/adma.201000177.

[15] V. Paul-Boncour and L. Bessais, "Tuning the magnetocaloric properties of the $La(Fe,Si)_{13}$ compounds by chemical substitution and light element insertion", *Magnetochemistry*, *7*(1), pp. 1–18, 2021, doi: 10.3390/magnetochemistry7010013.

[16] A. Boutahar, M. Pejar, V. P. Boncour, L. Bessais, and H. Lassri, "Theoretical work in magnetocaloric effect of $LaFe_{13-x}Si_x$ compounds", *J. Supercond. Nov. Magn.*, *27*(8), pp. 1795–1800, 2014, doi: 10.1007/s10948-014-2542-z.

[17] A. Yan, K.-H. Müller, L. Schultz, and O. Gutfleisch, "Magnetic entropy change in melt-spun MnFePGe (invited)", *J. Appl. Phys.*, *99*(8), 2006, doi: 10.1063/1.2162807.

[18] Z. Q. Ou, L. Caron, N. H. Dung, L. Zhang, and E. Brück, "Interstitial boron in MnFe(P,As) giant-magnetocaloric alloy", *Results Phys.*, *2*, pp. 110–113, 2012, doi: 10.1016/j.rinp.2012.09.005.

[19] M. Yue, Z. Q. Li, X. L. Wang, D. M. Liu, J. X. Zhang, and X. B. Liu, "Crystal structure and magnetic transition of MnFePGe compound prepared by spark plasma sintering", *J. Appl. Phys.*, *105*(7), pp. 7–10, 2009, doi: 10.1063/1.3056157.

[20] Z. Q. Ou, L. Zhang, N. H. Dung, L. Caron, and E. Brück, "Structure, magnetism and magnetocalorics of Fe-rich $(Mn,Fe)_{1.95}P_{1-x}Si_x$ melt-spun ribbons", *J. Alloys Compd.*, *710*, pp. 446–451, 2017, doi: 10.1016/j.jallcom.2017.03.266.

[21] P. Devi, C. S. Mejia, M. G. Zavareh, K. K. Dubey, P. Kushwaha, Y. Skourski, C. Felser, M. Nicklas, and S. Singh, "Improved magnetostructural and magnetocaloric reversibility in magnetic Ni-Mn-In shape-memory Heusler alloy by optimizing the geometric compatibility condition", *Phys. Rev. Mater.*, *3*(6), pp. 1–6, 2019, doi: 10.1103/PhysRevMaterials.3.062401.

[22] A. M. Aliev, A. B. Batdalov, I. K. Kamilov, V. V. Koledov, V. G. Shavrov, V. D. Buchelnikov, J. Garcia, V. M. Prida, and B. Hernando, "Magnetocaloric effect in ribbon samples of Heusler alloys Ni-Mn-M (M = In,Sn)", *Appl. Phys. Lett.*, *97*(21), 2010, doi: 10.1063/1.3521261.

[23] M. Fries, L. Pfeuffer, E. Bruder, T. Gottschall, S. Ener, L. V. B. Diop, T. Gröb, K. P. Skokov, and O. Gutfleisch, "Microstructural and magnetic properties of Mn-Fe-P-Si (Fe_2P-type) magnetocaloric compounds", *Acta Mater.*, *132*, pp. 222–229, 2017, doi: 10.1016/j.actamat.2017.04.040.

[24] J. W. Lai, Z. G. Zheng, B.W. Huang, H. Y. Yu, Z. G. Qiu, Y. L. Mao, S. Zhang, F. M. Xiao, D. C. Zeng, K. Goubitz, and E. Brück, "Microstructure formation and magnetocaloric effect of the Fe_2P-type phase in $(Mn,Fe)_2(P, Si, B)$ alloys," *J. Alloys Compd.*, *735*, pp. 2567–2573, 2018, doi: 10.1016/j.jallcom.2017.11.287.

[25] J. Lai, X. You, A. I. Dugulan, B. Huang, J. Liu, M. Maschek, L. van Eijck, N. H. van Dijk, and E. Brück, "Tuning the magneto-elastic transition of $(Mn,Fe,V)_2(P,Si)$ alloys to low magnetic field applications", *J. Alloys Compd.*, *821* p. 153451, 2020, doi: 10.1016/j.jallcom.2019.153451.

[26] N. V. Thang, H. Yibole, N. H. van Dijk, and E. Brück, "Effect of heat treatment conditions on MnFe(P,Si,B) compounds for room-temperature magnetic refrigeration", *J. Alloys Compd.*, *699*, pp. 633–637, 2017, doi: 10.1016/j.jallcom.2016.12.402.

[27] H. M. Rietveld, "A profile refinement method for nuclear and magnetic structures", *J. Appl. Crystallogr.*, *2*(2), pp. 65–71, 1969, doi: 10.1107/s0021889869006558.

[28] D. B. Rogers, "Magnetic and Mössbauer Effect Studies of Mn_5Si_3: Fe_5Si_3 Solid Solutions", *323*, pp. 311–323, 1972.

[29] L. Pal, K. G. Suresh, and A. K. Nigam, "Effect of Mn substitution on the magnetic and magneto-transport properties of $Fe_{3-x}Mn_xSi$ ($0 \leq x \leq 1.25$) alloys", *J. Appl. Phys.*, vol. 113, no. 9, pp. 0–7, 2013, doi: 10.1063/1.4794126.

[30] X. F. Miao, Y. Mitsui, A. I. Dugulan, L. Caron, N. V. Thang, P. Manuel, K. Koyama, K. Takahashi, N. H. van Dijk, and E. Brück, "Kinetic-arrest-induced phase coexistence and metastability in $(Mn,Fe)_2(P,Si)$", *Phys. Rev. B*, *94*(9), 2016, doi: 10.1103/PhysRevB.94.094426.

[31] V. K. Sharma, M. K. Chattopadhyay, and S. B. Roy, "Kinetic arrest of the first order austenite to martensite phase transition in $Ni_{50}Mn_{34}In_{16}$: Dc magnetization studies", *Phys. Rev. B - Condens. Matter Mater. Phys.*, *76*(14), pp. 3–6, 2007, doi: 10.1103/PhysRevB.76.140401.

[32] A. Banerjee, K. Kumar, and P. Chaddah, "Conversion of a glassy antiferromagnetic-insulating phase to an equilibrium ferromagnetic-metallic phase by devitrification and recrystallization in Al substituted $Pr_{0.5}Ca_{0.5}MnO_3$", *J. Phys. Condens. Matter*, *21*(2), pp. 0–12, 2009, doi: 10.1088/0953-8984/21/2/026002.

[33] A. Banerjee, A. K. Pramanik, K. Kumar, and P. Chaddah, "Coexisting tunable fractions of glassy and equilibrium long-range-order phases in manganites", *J. Phys. Condens. Matter*, *18*(49), pp. 1–9, 2006, doi: 10.1088/0953-8984/18/49/L02.

[34] X. F. Miao, N. V. Thang, L. Caron, H. Yibole, R. I. Smith, N. H. van Dijk, and E. Brück, "Tuning the magnetoelastic transition in $(Mn,Fe)_2(P,Si)$ by B, C, and N doping", *Scr. Mater.*, *124*, pp. 129–132, 2016, doi: 10.1016/j.scriptamat.2016.07.015.

[35] J. Lai, B. Huang, X. Miao, N. van Thang, X. You, M. Maschek, L. van Eijck, D. Zeng, N. van Dijk, and E. Brück, "Combined effect of annealing temperature and vanadium substitution for mangetocaloric $Mn_{1.2-x}V_xFe_{0.75}P_{0.5}Si_{0.5}$ alloys", *J. Alloys Compd.*, *803*, pp. 671–677, 2019, doi: 10.1016/j.jallcom.2019.06.239.

[36] E. K. Delczeg-Czirjak, Z. Gercsi, L. Bergqvist, O. Eriksson, L. Szunyogh, P. Nordblad, B. Johansson, and L. Vitos, "Magnetic exchange interactions in B-, Si-, and As-doped Fe_2P from first-principles theory", *Phys. Rev. B - Condens. Matter Mater. Phys.*, *85*(22), pp. 1–7, 2012, doi: 10.1103/PhysRevB.85.224435.

[37] I. Batashev, G. A. de Wijs, N. H. van Dijk, and E. Brück, "Lithiation of the Fe_2P-based magnetocaloric materials: A first-principles study", *J. Magn. Magn. Mater.*, *537*, p. 168179, 2021, doi: 10.1016/j.jmmm.2021.168179.

[38] Z. Q. Ou, L. Zhang, N. H. Dung, L. van Eijck, A. M. Mulders, M. Avdeev, N. H. van Dijk, and E. Brück, "Neutron diffraction study on the magnetic structure of Fe_2P-based $Mn_{0.66}Fe_{1.29}P_{1-x}Si_x$ melt-spun ribbons", *J. Magn. Magn. Mater.*, vol. 340, pp. 80–85, 2013, doi: 10.1016/j.jmmm.2013.03.028.

[39] C. Vargel, "Intergranular corrosion", *Corros. Alum.*, pp. 185–197, 2020, doi: 10.1016/b978-0-08-099925-8.00015-6.

[40] G. Gottstein and L. S. Shvindlerman, *Grain boundary migration in metals: Thermodynamics, kinetics, application.* CRC Press, 1999.

[41] J. V. Leitão, M. van der Haar, A. Lefering, and E. Brück, "Magnetic and magnetocaloric exploration of Fe rich $(Mn,Fe)_2(P,Ge)$", *J. Magn. Magn. Mater.*, *344*, pp. 49–54, 2013, doi: 10.1016/j.jmmm.2013.05.032.

6

Competing magnetic interactions, structure and magnetocaloric effect in $Mn_3Sn_{1-x}Zn_xC$ antiperovskite carbides

Abstract

Structural, magnetic and magnetocaloric properties of $Mn_3Sn_{1-x}Zn_xC$ antiperovskite carbides have been studied. With increasing Zn content the first-order magnetic transition (FOMT) is weakened. The Curie temperature (T_C) reduces first from 273 to 197 K and when $x > 0.3$, T_C increases, reaching its maximum of 430 K for $x = 1.0$. An increase in T_C is accompanied by pronounced changes in magnetic behaviour and a significant rise in magnetization from 21.8 to 76.2 Am^2kg^{-1} for $x = 0.8$ in the maximum applied magnetic field of 5 T. Neutron powder diffraction (NPD) was employed to study the magnetic structure of $Mn_3Sn_{1-x}Zn_xC$ compounds. The refinement of the NPD data for $x = 0.3$ revealed a magnetic structure with propagation vector $\mathbf{k}$ = (½, ½, 0) with a decrease in the canted antiferromagnetic (AFM) moment, which results in a reduction of the negative volume change at the magnetic transition and a decrease in the magnetocaloric effect (MCE). For $x = 0.4$, the magnetic structure is described by a propagation vector $\mathbf{k}$ = (½, ½, ½) for the AFM moment which dominates at low temperature, with the presence of a minor ferromagnetic (FM) component with a $\mathbf{k}$ = (0, 0, 0) propagation vector, which confirms the presence of the ferrimagnetic (FiM) state. For a higher Zn content ($x = 0.6$), the magnetic moment originates mainly from the FM component found on three independent Mn positions and an additional AFM moment oriented in the a-b plane. The results presented confirm the presence of competing AFM-FM interactions in $Mn_3Sn_{1-x}Zn_xC$ antiperovskite carbides.

6.1. Introduction

The severe impact of traditional compressor-based cooling technologies has pointed the research interest towards seeking alternative cooling systems. Magnetic refrigeration, which utilizes the magnetocaloric effect (MCE), has attracted broad attention due to a number of advantages over traditional compressor-based technologies [1]–[6]. Magnetocaloric materials (MCM) exhibiting a first-order magnetic phase transition (FOMT) attract particular attention since they provide a large magnetic entropy change ($|\Delta S_m|$), which reflects their cooling capacity. On the other hand, the FOMT is usually associated with a large thermal hysteresis (ΔT_{hys}), which is an obstacle for the practical application of these compounds. Therefore, systems showing a reversible MCE and exhibiting a second-order magnetic transition (SOMT) appear interesting, though their $|\Delta S_m|$ is significantly lower compared to the FOMT compounds. Various materials exhibiting a SOMT have been studied in terms of their magnetocaloric effect, e.g.: RE_6Co_2Ga (RE = Ho, Dy, Gd) [7], $(Gd_{1-x}RE_x)_5Si_4$ (RE = Dy, Ho) [8], Mn_5PB_2 [9], $RECo_{12}B_6$ (RE = Ce, Pr, Nd) [10], $RENiGa_2$ [6], $RE_2Cr_2C_3$ (RE = Er, Ho, Dy) [11].

Mn-based antiperovskites Mn_3AX (A = metal or semiconductor; X = C, N) display a broad variety of interesting phenomena such as giant magnetoresistance (GMR) [12], [13], superconductivity [14], magnetovolume effect (MVE) [15], [16], piezomagnetic effect [17], [18], barocaloric effect [19] and magnetocaloric effect [20]–[22]. Unlike their perovskite analogues, antiperovskites show metallic behaviour, a good thermal conductivity and a high mechanical stability. In addition, Mn-based alloys consist of abundant, relatively innocuous and inexpensive elements, which enable their practical application in magnetic cooling systems. A particularly large MCE has been recently found in Mn_3SnC [22], [23] and Mn_3GaC [20], [24]. The Mn_3SnC compound shows a sharp and non-hysteretic FOMT transition from the low-temperature ferrimagnetic (FiM) ordered state consisting of antiferromagnetic (AFM) and ferromagnetic (FM) sublattices, to a high-temperature paramagnetic (PM) state, with $T_C \approx 278$ K [21], [22], [25]. In another antiperovskite compound – Mn_3ZnC, a transition from a non-collinear FiM state to a FM state ($T_N \approx 233$ K) is followed by a FM-PM transition ($T_C \approx 420$ K) [26], [27]. Recent studies deploying ab-initio methods and Monte Carlo (MC) simulations revealed a great potential of the $Mn_3(Sn,Zn)C$ system for the purposes of magnetic refrigeration [26]. Since the systematic investigation of MCE in the $Mn_3Sn_{1-x}Zn_xC$ system was thus far not reported, our main objective was a detailed study on the magnetism, structure and MCE in these compounds using experimental techniques and DFT calculations.

6.2. Experimental details

Polycrystalline $Mn_3Sn_{1-x}Zn_xC$ ($0.0 \le x \le 1.0$) compounds were prepared from Mn (99.7%), Sn (99.9%), Zn (99.9%) and C (99.9%) powders. Stoichiometric proportions of starting materials were thoroughly mixed, pressed into pellets and subsequently sealed in quartz tubes under 200 mbar Ar atmosphere. To compensate for C losses during the annealing process, 10 wt.% extra graphite was added. Since the boiling point of Zn is relatively low (1180 K),

significant Zn losses were observed in Zn-rich compounds. Therefore, extra Zn was added to compounds of $x \geq 0.4$ to compensate for metal losses. As-prepared samples were annealed at 1023 K for 120 h and subsequently oven-cooled.

The X-ray diffraction patterns were collected employing a PANalytical X-pert Pro diffractometer using Cu-K_α radiation ($\lambda = 1.54$ Å) equipped with an Anton Paar TTK450 low-temperature chamber. Rietveld refinement implemented in the Fullprof software was used for indexing and lattice constant calculations [28], [29]. Neutron powder diffraction (NPD) data were collected at various temperatures in the magnetic and PM state (4 to 475 K), using the neutron powder diffraction instrument PEARL ($\lambda = 1.67$ Å) at the Reactor Institute Delft, the Netherlands. The Rietveld refinement using Fullprof program has been used to elucidate the magnetic structure and magnetic moments. In the refinement, coherent neutron scattering lengths of -0.3730, 0.6225, 0.5680, 0.6646 ($\times 10^{-12}$ cm) were used for Mn, Sn, Zn, C, respectively. Superconducting quantum interference devices (SQUID) MPMS-XL and MPMS-5S magnetometers using the reciprocating sample option mode (RSO) were employed to collect the magnetization data, in the temperature range of 5 to 370 K with a constant sweep rate of 2 K/min and in applied magnetic fields up to 5 T. High-temperature magnetic measurements were performed utilizing a Vibrating Sample Magnetometer (VSM) implemented in the Quantum Design VersaLab.

Density of States (DOS) calculations were performed for $Mn_3Sn_{1-x}Zn_xC$ ($0 \leq x \leq 1.0$) in the framework of density functional theory utilizing the Vienna Ab Initio simulation package (VASP) [30], [31] in the projector augmented-wave (PAW) method [32], [33]. The generalized gradient approximation of Perdew–Burke–Ernzerhof (PBE) [34] was used for the exchange-correlation functional. The **k**-space integrations were performed with the Methfessel-Paxton method of second order [35] with a smearing width of 0.2 meV. Valence electron configurations considered in the calculations were: Mn 3*p*, 3*d* and 4*s*; Sn 4*d*, 5*s* and 5*p*; Zn 3*d*, 4*s* and C 2*p*. The relaxation was performed for a 2×2×2 supercell consisting of 24 atoms, by integration of the Brillouin zone on a gamma-centred **k**-grid with a 3×3×3 mesh for a force convergence of 0.1 meV/Å. To calculate DOS, the integration of the Brillouin zone was performed utilizing the tetrahedron method with Blöchl corrections with a 9×9×9 grid. The plane-wave cut-off energy for all calculations was set at 520 eV. The DFT calculations were done in collaboration.

6.3. Results and discussion

6.3.1. Structural properties

The X-Ray diffraction (XRD) patterns of the $Mn_3Sn_{1-x}Zn_xC$ compounds measured at 298 K are shown in Figure **6.1a**. The Rietveld refinement of the measured patterns revealed formation (> 90 wt.%) of the cubic antiperovskite type *Pm*-3*m* structure (space group 221) accompanied by minor impurity phases of C, MnO and $MnSn_2$. As presented in Figure **6.1b**, the lattice parameter a and the distance between the nearest Mn atoms ($d_{Mn-Mn} = \frac{\sqrt{2}}{2}a$) decrease linearly with increasing Zn content as the covalent radius of Zn (1.22 Å) is

significantly smaller in size compared to Sn (1.39 Å), which also confirms the substitutional effect of Zn-doping. As suggested by Guillaud [36], for various Mn-based compounds (e.g. MnBi, MnSb, MnAs), the lowest distance between nearest Mn atoms giving rise to positive (FM) exchange interactions was experimentally estimated to be about 2.81 Å. Therefore, a Mn-Mn distance below 2.81 Å should correspond to negative (AFM or FiM) interactions. In the studied system, positive interactions between Mn atoms at room temperature occur for $x \geq 0.5$, thus for a Mn-Mn distance of 2.79 to 2.77 Å. Despite the preserved cubic lattice structure, confirmed by XRD analysis, local distortions of the Mn_6C octahedra can lead to deviations in the Mn-Mn distance. To confirm the presence of local distortions further research is needed employing other instrumental techniques, e.g. EXAFS [23], [37]. Alternatively, the critical distance of 2.72 Å, empirically estimated for Mn_4N, can be more adequate for the $Mn_3Sn_{1-x}Zn_xC$ system, as also suggested by Li and co-workers [12]. The experimental value of the Mn-Mn distance is determined for alloys, in which magnetic order is considered in terms of direct exchange interactions. Previous studies suggested the presence of different mechanisms in antiperovskites, such as the Ruderman-Kittel-Kasuya-Yosida (RKKY) interactions [38], [39]. Unlike the previously mentioned Mn-based compounds, Mn_4N crystallizes in the antiperovskite type of structure and shows a ferrimagnetic behaviour, which can lead to a better match of the experimentally estimated critical distance between Mn atoms. The refinements of the XRD data collected at 298 K for $x = 0.0$ and $x = 1.0$ are shown in Figure **6.2a** and Figure **6.2b**.

The temperature dependence of the lattice parameter obtained for $Mn_3Sn_{1-x}Zn_xC$ in the temperature range 120 to 298 K is shown in Figure **6.3**. As observed for a Zn content in the range $0.0 \leq x \leq 0.3$, the magnetic transition is accompanied by a discontinuous jump in the lattice parameter without a change in crystal symmetry, which suggests that the FiM-PM transition is of first order. The values of $\Delta a/a$ at the transition are 0.09, 0.09, 0.08, 0.07 %, for $x = 0.0$, 0.1, 0.2, 0.3, respectively. In the vicinity of the magnetic transition, a coexistence of two phases with the same cubic symmetry, but with slightly different lattice parameters, can be seen. The temperature evolution of the (200) diffraction peak across the magnetic transition for $x = 0.1$ is depicted in **Fig. S1** in the Supplementary Material**.** This gradual decrease in $\Delta a/a$ suggests a suppression of the FOMT and a shift towards a SOMT. It can be noticed that for $x = 1.0$ measured at 120 K, a splitting in the lattice parameter can be seen, which reveals a distortion of the high-symmetry cubic phase towards the tetragonal *P4/mmm* structure (space group 123) with lattice parameters $a = b = 3.9191(3)$ Å and $c = 3.9149(4)$ Å. The low-temperature XRD pattern of Mn_3ZnC is shown in **Fig. S2** (Supplementary Material). The distortion towards the tetragonal structure occurring in Mn_3ZnC can theoretically be deduced using the Goldschmidt tolerance factor (τ), which describes the stability of the antiperovskite lattice structure based on the ionic radii of the atoms:

$$\tau = \frac{r_{Sn/Zn} + r_{Mn}}{\sqrt{2}(r_C + r_{Mn})} \tag{6.1}$$

The structure of the highest (cubic) symmetry is stable when the Mn-C and Zn/Sn-C bonds are well-matched, which results in one degree of freedom and $\tau = 1.00$. However, in

real systems, the cubic structure is adopted for compounds with τ = 0.91 to 1.00 and a decrease in the Goldschmidt tolerance factor results in the formation of lower symmetry structures [40]. Due to the presence of metallic and covalent bonds in antiperovskites, the tolerance factor rarely provides precise information. Nevertheless, it can be noted that in comparison to Mn_3SnC (τ = 1.03), the Goldschmidt tolerance factor for Mn_3ZnC is significantly lowered (τ = 0.97) towards the tetragonal structure (τ = 0.71 – 0.90), which also explains the distortion of the cubic structure.

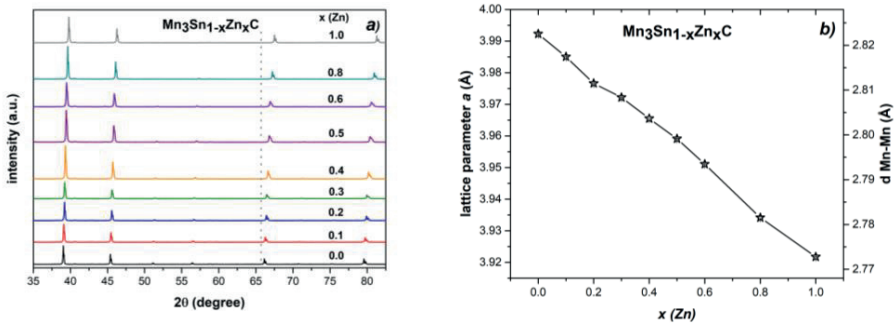

Figure 6.1: *a) Stacked XRD patterns measured at 298 K, b) composition dependence of the lattice parameter a and the nearest Mn-Mn distance in $Mn_3Sn_{1-x}Zn_xC$ compounds measured at 298 K. The error bars are smaller than the size of the marker.*

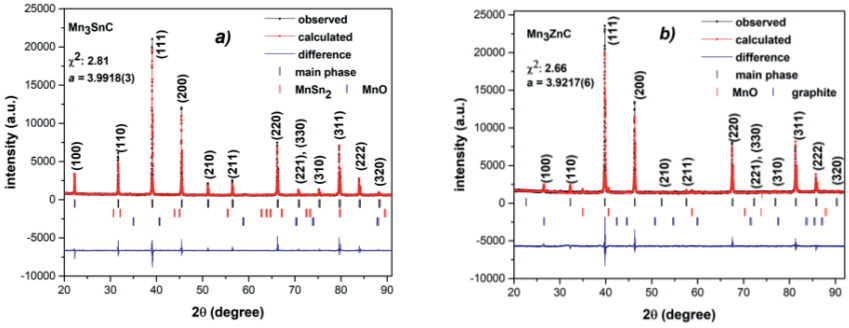

Figure 6.2: *Observed and calculated XRD patterns of a) Mn_3SnC and b) Mn_3ZnC at 298 K.*

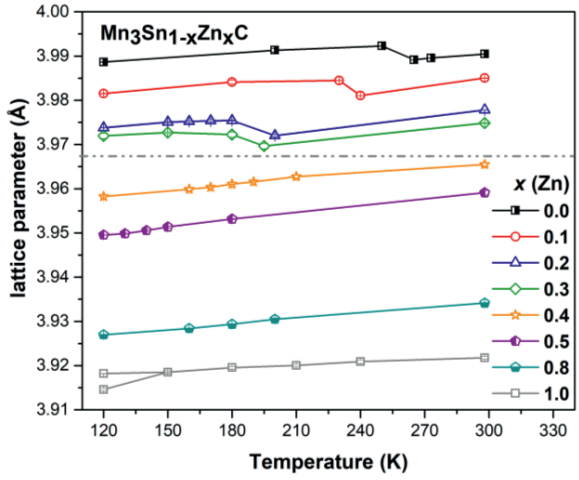

Figure 6.3: *Temperature dependence of lattice parameter a for $Mn_3Sn_{1-x}Zn_xC$ obtained from the XRD measurements. The error bars are smaller than the size of the marker.*

6.3.2. Magnetic and magnetocaloric properties

The temperature dependence of the magnetization measured at 0.01 and 1 T are shown in Figure **6.4a** and Figure **6.4b**, respectively. The parent compound – Mn_3SnC, exhibits a sharp FiM-PM transition with $T_C = 273$ K, which is in good agreement with previous reports [12], [21], [25], [41]–[43]. The characteristic *S*-shape of the Arrott plots in the vicinity of T_C (Figure **6.5a**) is indicative of the FOMT. It can be noticed that samples of x (Zn) < 0.4 all show similar magnetic behaviour. Namely, the FiM-PM transition is observed upon increasing temperature. As evidenced by the thermal hysteresis in the external magnetic field of 0.01 T, these compounds undergo a FOMT, which is also in agreement with a discontinuous change of the lattice parameter reported in section 6.3.1. The compound with $x = 0.4$ shows a significant change in magnetic behaviour. It can be seen that the magnetization gradually increases with increasing temperature, reaching its maximum at 170 K, which corresponds to the Néel temperature (T_N), defined by the maximum of magnetization derived from *M-T* curves at 0.01 T, as shown in Figure **6.4a**. The Curie temperature is determined by the maximum from the derivative of the temperature dependence of the magnetization ($|dM/dT|$) measured at 0.01 T. Since magnetization does not approach zero at low temperatures, T_N is most likely ascribed to a FiM-FM transition, followed by a FM-PM transition upon heating, with T_C at 217 K. The changes in T_C and T_N in the $Mn_3Sn_{1-x}Zn_xC$ system are presented in Figure **6.5b**. The magnetic behaviour of the $Mn_3Sn_{1-x}Zn_xC$ compounds with $x \geq 0.4$ resembles Mn_3ZnC, for which two subsequent transitions can be observed. Recent studies revealed the influence of the packing fraction on the local distortions of the Mn_6C octahedra, leading to long and short Mn-Mn distances, while the cubic structure remains unaltered [23], [44], [45]. With increasing Zn content, the packing

fraction decreases, which results in more space for the distortion of the Mn_6C octahedra. Consequently, pronounced changes in magnetic behaviour can be observed due to the variation in the long and short Mn-Mn distances, aiding FM and AFM interactions, respectively. Additionally, in alloys of a higher Zn content ($x > 0.3$), a characteristic broadening of the magnetization curve can be observed at low magnetic fields. This broadened transition smears out when higher magnetic fields ($\mu_0 H > 0.2$ T) are applied, as depicted in Figure 6.6 for $x = 0.8$. In these compounds, the span of the magnetic phases broadens significantly upon increasing Zn content, which suggests competing FM-AFM interactions, as previously observed in $Mn_{1-x}Fe_xSnC$ [46] and $Mn_3Ga_{1-x}Sn_xC$ [47].

The field dependence of the magnetization measured at 5 K and in magnetic fields up to 5 T revealed a significant increase in magnetization from 21.8 to 76.2 Am^2kg^{-1} for a change in Zn content from $x = 0.0$ to 0.8, as presented in Figure 6.7a. The magnetic isotherms measured at 5 K reveal the presence of magnetic hysteresis in the compounds with $x > 0.3$, which can be ascribed to the existence of the FiM ordering. The field-dependent magnetization for x (Zn) = 0.4 shows an initial rise, followed by a linear increase in magnetization for higher magnetic fields (Figure 6.7b). It is apparent that the magnetization does not saturate in the maximum applied magnetic field of 5 T, which in combination with accompanying magnetic hysteresis suggests the presence of a low-temperature FiM state.

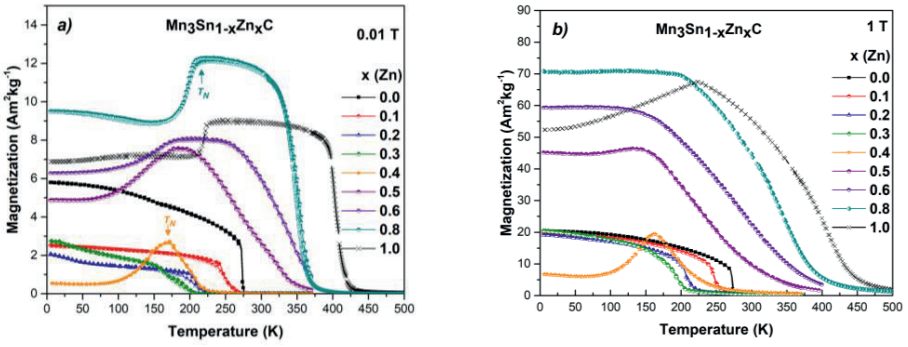

Figure 6.4: *Temperature dependence of the magnetization of $Mn_3Sn_{1-x}Zn_xC$ compounds measured in a magnetic field of a) 0.01 T, b) 1 T. The systematic error in magnetization δM is 0.5 % or less, the systematic error in the temperature $\delta T = 0.1 + 0.001T$ K or less [48].*

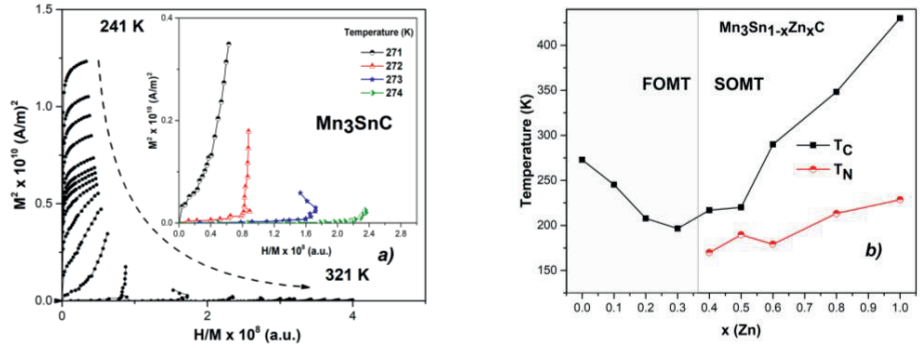

Figure 6.5: *a) Arrott plots derived for Mn_3SnC from isofield curves measured upon heating in the vicinity of T_C, b) changes in T_C and T_N as a function of Zn content in $Mn_3Sn_{1-x}Zn_xC$ compounds. The error bars for T_C and T_N are within the marker size (±1 K).*

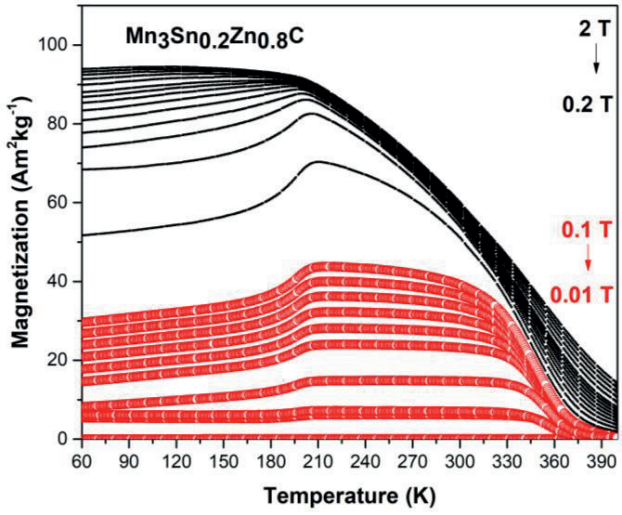

Figure 6.6: *Temperature dependence of the magnetization measured for x (Zn) = 0.8 in magnetic fields up to 2 T.*

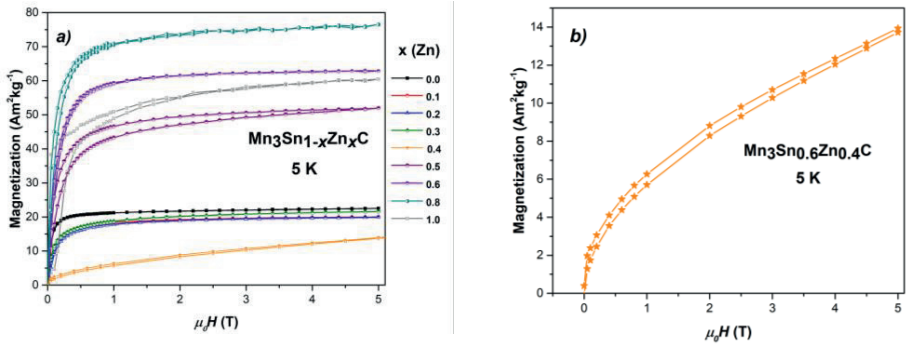

Figure 6.7: *a) Field dependence of magnetization for $Mn_3Sn_{1-x}Zn_xC$ compounds measured at 5 K, b) field dependence of the magnetisation for the compound with x (Zn) = 0.4 measured at 5 K. The systematic error in magnetization δM is < 0.5 %, the systematic error in the magnetic field δH is < 0.1 % [48].*

In Mn-based antiperovskites, the magnetic coupling through Mn-*X*-Mn channels competes with the direct interactions between Mn atoms [49], [50]. We argue that Zn doping initially suppresses the exchange interactions between Mn atoms due to enhanced C-*2p* Mn-*3d* hybridization, which subsequently results in a decrease in T_C, as observed for $x < 0.3$. The enhanced hybridization can be seen as the overlap of the energy range for C-*2p* and Mn-*3d* orbitals in the density of states (DOS) plots presented in Figure **6.8a-c**. However, when $x \geq 0.4$, then the direct exchange between Mn atoms is strongly enhanced, which leads to an abrupt increase in T_C. This phenomenon seems to be universal in many Mn-based antiperovskites since a similar initial decrease in T_C followed by an increase for a higher doping content was previously observed in structurally similar compounds: $Mn_{3+x}Sn_{1-x}C$ [12], [41], $Mn_3Ga_{1-x}Sn_xC$ [47], $Mn_3Sn_{1-x}In_xC$ [45], $Mn_3Sn_{1-x}Si_xC$ and $Mn_{3-x}Fe_xSnC$ [46].

According to our DFT calculations, Mn-*3d* electrons mainly contribute to the DOS at the Fermi level (E_F). As seen for the parent compound (Mn_3SnC) in Figure **6.8a**, a sharp peak of DOS is located at E_F, which implies a strong dependence of structural and magnetic properties upon altering the number of conduction electrons. As a result, changes in magnetic behaviour are expected upon doping, which agrees with magnetization results discussed earlier. Due to the enhanced hybridization between C-*2p* Mn-*3d* states, the width of the bands increases. Consequently, it can be seen in Figure **6.8b** that the population of the majority and the minority spins becomes equalized, which suppresses the spin polarization and results in a decrease in the magnetic moment, as experimentally observed for $x = 0.4$. In Figure **6.8c**, presenting $x = 1.0$, an opposite behaviour of the majority and minority spins is noticeable, which reflects enhanced magnetization, in agreement with our observations for $x > 0.4$. Therefore, the results from DFT calculations are consistent with the earlier discussed magnetic properties.

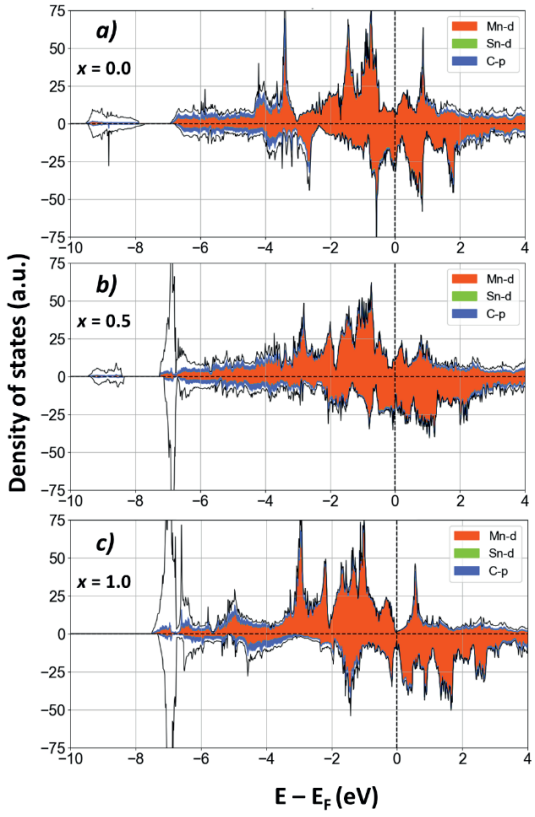

Figure 6.8: *DOS of $Mn_3Sn_{1-x}Zn_xC$ in the vicinity of Fermi level (E_F) for: a) x = 0.0, b) x = 0.5 and c) x = 1.0.*

The magnetic entropy change $|\Delta S_m|$ was calculated from the *M-T* curves in applied magnetic fields up to 2 T using one of the Maxwell relations:

$$\Delta S_m(T,H) = \int_{\mu_0 H_1}^{\mu_0 H_2} \left(\frac{\partial M(T)}{\partial T}\right)_H d(\mu_0 H) \tag{6.2}$$

As shown in Figure 6.9, the values of $|\Delta S_m|$ decrease rapidly upon doping, while the peaks broaden significantly. It is notable that the change in $|\Delta S_m|$ is related to the relative change in the lattice parameter $|\Delta a/a|$ at the magnetic transition, as observed for compounds of $x < 0.4$. As proposed by Gschneidner and co-workers [51], the larger the volume change at the transition, the larger the structural entropy change, and thus, the total entropy change. A correlated decrease in $|\Delta S_m|$ and $|\Delta a/a|$ upon increasing Zn doping indicates the magneto-elastic nature of the transition. However, it can be noticed that $|\Delta S_m|$ decreases rapidly for a low dopant content ($x = 0.1$), whereas the volume change at the transition is comparable to

the parent compound. As proposed for Mn_3SnC, a large MCE is associated with a reconstruction of the Fermi surface in the vicinity of the magnetic transition [22]. Therefore, it is suggested that doping suppresses the reconstruction of the electronic structure and leads to a decrease in MCE. The significance of the electronic entropy in antiperovskites and its correlation to the FOMT has been studied in detail [52]. The change in charge transfer upon Zn doping awaits detailed clarification using X-ray magnetic circular dichroism [53] or X-ray absorption near-edge structure measurements [45], [54]. Our results highlight a strong correlation between various degrees of freedom, which results in a strong sensitivity to minor changes in chemical composition. The values of $|\Delta S_m|$, T_C and total magnetic moment (per formula unit) derived from magnetization measurements are presented in Table **6.1**. The presence of the inverse MCE can be seen for higher Zn contents ($x \geq 0.4$). However, this effect remains significant only for $x = 0.4$, showing a value of -0.6 $Jkg^{-1}K^{-1}$. The value of $|\Delta S_m|$ obtained experimentally for Mn_3SnC is in good agreement with experimental results reported by Cakir and co-workers [21] and Monte Carlo simulations performed recently by Benhouria and co-workers [26]. Despite a good agreement for Mn_3SnC, an expected increase in $|\Delta S_m|$ upon increasing Zn content was not observed in our study.

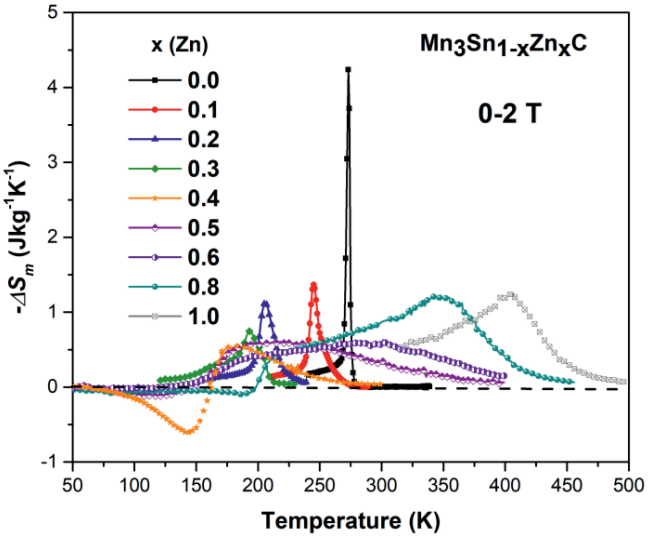

Figure 6.9: *Magnetic entropy change ($-\Delta S_m$) of $Mn_3Sn_{1-x}Zn_xC$, derived from M-T curves measured in a magnetic field change of 2 T.*

Table 6.1: *Collected values of the Curie temperature (T_C), the Néel temperature ($T_{N,}$), the magnetic entropy change ($-\Delta S_m$) and the magnetic moment per formula unit (μ) derived from the SQUID measurements at 5 K and in a maximum applied magnetic field of 5 T. The estimated error in T_C and T_N is ± 1 K. The SQUID measurement provides the accuracy of 1%.*

x (Zn)	T_C (K)	T_N (K)	$-\Delta S_m$ (Jkg^{-1}K^{-1})		μ (μ_B/f.u.)
			1 T	2 T	
0.0	273	-	2.1	4.3	1.2
0.1	245	-	0.6	1.4	1.0
0.2	208	-	0.5	1.1	1.0
0.3	197	-	0.3	0.8	1.1
0.4	217	170	0.3	0.6	0.7
0.5	220	190	0.3	0.6	2.5
0.6	290	179	0.3	0.6	3.0
0.8	348	213	0.6	1.2	3.5
1.0	430	229	0.7	1.3	2.6

6.3.3. Neutron diffraction results

In order to obtain a better understanding of the magnetic structure and the magnetic response of prepared compounds, three alloys with a different Zn content (x = 0.3, 0.4, 0.6) have been selected and measured using neutron powder diffraction (NPD). As reported in Section 6.3.2, the selected samples show a distinctly different magnetic behaviour, despite the relatively small variation in composition. Although the crystal structure of $Mn_3Sn_{1-x}Zn_xC$ remains cubic in the whole temperature range, the Mn moments in the magnetic unit cell, generated using the propagation vector **k** = (½, ½, 0), are of two different types. As reported for the parent compound, two Mn atoms in the square configuration (*a*-*b* plane) carry a large AFM moment (μ_1 = 2.3 μ_B/Mn) and one Mn atom has a smaller FM component (μ_2 = 0.7 μ_B/Mn) along the *c*-axis [37], [55]. The neutron diffraction patterns at 100 K with fits that only include the contribution of the nuclear structure are shown in Figure **6.10**. For clarity, the nuclear fit includes the main and secondary phases, but the peaks marked in the refinement refer only to the main phase. As a result, the position and intensity of magnetic peaks can be derived from the difference between the observed intensity and the nuclear fit (blue line). Although the nuclear structure is similar in each case, the magnetic structure of these three alloys is expected to be distinctly different, judging from the pronounced differences in magnetic contribution to the patterns. The fits of both the nuclear and magnetic contributions are shown in Figure **6.11a-c**. The magnetic peak present at 2θ = 18.9° in all patterns corresponds to the AFM magnetic phase of MnO (being magnetic below T_N = 117 K) and is therefore not included in the refinement.

The refinement of the neutron powder diffraction patterns in the PM state was used to elucidate site occupancies. The atoms of Sn/Zn, Mn and C were placed at the *1a* (0,0,0), *3c* (0,1/2,1/2) and *1b* (1/2,1/2,1/2) sites, respectively. The Rietveld refinement of the occupancies revealed a slight deficiency of corner sites that mainly pertains to Sn atoms. As a result, the refined compositions can be denoted as: $Mn_{3.05}Sn_{0.65}Zn_{0.30}C_{1.00}$, $Mn_{3.00}Sn_{0.55}Zn_{0.40}C_{1.05}$, $Mn_{3.10}Sn_{0.30}Zn_{0.55}C_{1.05}$, for the nominal Zn content x = 0.3, 0.4, 0.6, respectively. These Sn/Zn deficient and Mn-rich compositions might indicate partial occupancy of the *1a* site by Mn atoms, which can result in additional Mn-Mn interactions. Since a similar magnetic behaviour was observed in earlier studies [12], [45], [56], we claim that this minor occupancy of *1a* site by Mn is not responsible for the changes observed in the magnetic structure of the compounds studied here.

The magnetic structure of x = 0.3 is described with a propagation vector **k** = (½,½,0), which indicates that the magnetic unit cell becomes doubled in both the *a* and *b* directions. The magnetic spin alignment of the Mn moments, obtained from the neutron data collected at 100 K is presented in Figure **6.12a**. Similar to the parent compound, the magnetic moments of the two Mn atoms form a canted AFM square arrangement (μ_1), whereas one Mn moment shows FM order (μ_2) along the *c* axis and aligns in the *a*-*b* plane. The FM order is described by propagation vector **k** = (0,0,0). Although the magnetic structure is similar to Mn_3SnC, the magnitude of the μ_1 magnetic moment decreases to 1.6(2) μ_B/Mn and the μ_2 moment increases to 1.03(4) μ_B/Mn, at the lowest measured temperature of 4 K. The Curie-Weiss fit to the paramagnetic susceptibility yielded an effective moment of 4.2 μ_B/f.u, calculated as $\mu_{eff} = \sqrt{8C}\,\mu_B$ where C is the Curie constant derived from the inverse susceptibility χ^{-1} as a function of temperature. The positive value of the Curie-Weiss temperature (θ_{CW} = 115.3 K) confirms the presence of FM interactions in this compound. The plots of the inverse susceptibility as a function of the temperature can be found in the Supplementary Material (**Fig. S3**). The attained value of the effective moment is in agreement with the total magnetic moment of 4.2(3) μ_B/f.u obtained from neutron diffraction results at 4 K. In spite of the expected increase in $|\Delta S_m|$ due to a reduction of the AFM component [21], in our study we observe an opposite effect. According to previous studies on antiperovskites: $Mn_3Cu_{1-x}Ge_xN$ [57], [58], $Mn_3Sn_{1-x}Si_xC_y$ [56] and Mn_3NiN [59], the AFM spin arrangement obtained with a propagation vector **k** = (½,½,0) is responsible for the presence of the magneto-volume effect (MVE). In our study, this finding is supported by the alleviation of the AFM component upon doping, accompanied by a reduction of $\Delta a/a$, as shown in Section 3.1. As a result, a decrease in the AFM component contributes to a reduction of $|\Delta S_m|$ due to a weakening of the magnetoelastic nature of the transition. The correlation between the MVE and AFM spin arrangement relates to a geometrical corner-sharing-type frustration that occurs due to the octahedral arrangement of the Mn atoms. It is worth mentioning that a broader shape of magnetic peaks at low scattering angles might indicate the presence of an incommensurate magnetic structure, which would imply the existence of frustrated Mn_6C octahedra. The use of an incommensurate propagation vector **k** = (0.49,0.49,0.02) yielded a slight improvement to the fit. The AFM spin arrangement obtained using an incommensurate

propagation vector and the corresponding refinement of the NPD pattern measured at 100 K is shown in **Fig. S4** in the Supplementary Material**.**

The magnetic reflections of x = 0.4 are distinctly different compared to the previously presented x = 0.3, and can be fitted using the AFM propagation vector **k** = (½,½,½), which indicates that magnetic structure doubles in the *a*, *b* and *c* directions with respect to the nuclear unit cell. The observed change in magnetic structure agrees well with a notable change in magnetic properties discussed in section 6.3.2. As evidenced from the refinement of the neutron diffraction data at 4 K, two Mn atoms in the *a*-*b* plane possess a large AFM moment (μ_1) with a refined size of 1.57(4) μ_B/Mn. The use of an additional propagation vector **k** = (0,0,0) revealed the presence of a minor FM moment (μ_2) on the third Mn atom. The FM moment increases with temperature and reaches the maximum value of 0.5(1) μ_B/Mn at 130 K. Therefore, the total magnetic moment of 3.2(2) μ_B/f.u obtained from the NPD at 4 K is predominantly ascribed to the AFM component. While the calculated μ_{eff} = 4.8 μ_B/f.u. is in fair agreement with the total magnetic moment obtained from the refinement of the NPD data, the value of magnetic moment derived from magnetic measurements at 5 K is remarkably lower (0.7 μ_B/f.u) due to the evident lack of saturation in the maximum applied magnetic field of 5 T. The spin alignment at 100 K for x = 0.4 is presented in Figure **6.12b**. The presence of a FM moment is in good agreement with the field-dependent magnetization results measured at 5 K and a positive value of the Curie-Weiss temperature (θ_{CW} = 209.9 K) derived from the inverse susceptibility as a function of temperature.

The low-temperature neutron diffraction pattern of x = 0.6 was likewise fitted using two propagation vectors **k** = (½,½,0) and **k** = (0,0,0), which confirms that FiM ordering exists below T_N, as also inferred from the macroscopic magnetization measurements and discussed in Section 6.3.2. With a use of a propagation vector **k** = (0,0,0) it was found that all three Mn atoms carry a FM moment along the *b* axis. The contribution of the FM moment can clearly be seen here as an increase in the intensity of the existing nuclear peaks. The refined FM moments are of different size: two Mn atoms have a lower FM moment of 0.6(1) μ_B/Mn, and one Mn atom carries a large FM moment of 1.2(1) μ_B/Mn, as revealed from the refinement of the data collected at 100 K. Additionally, on two Mn atoms in the *a*-*b* plane a small AFM component of 0.41(4) μ_b/Mn has been found. The FM and AFM spin alignment of x = 0.6, obtained from the refinement of the NPD data collected at 100 K is presented in Figure **6.12c**. It can be noticed that the position of peaks refined using AFM propagation vector **k** = (½,½,½) is exactly the same as for x = 0.4, though their intensity is greatly reduced, indicating a weakening of the AFM contribution. The total magnetic moment of 3.2(2) μ_B/f.u. determined by neutron diffraction measured at 100 K originates mainly from the FM moments, thus this value is in good agreement with the size of the magnetic moment determined from the SQUID measurement (μ = 3.0 μ_B/f.u.), while from the Curie-Weiss fit, the calculated effective magnetic moment of μ_{eff} = 4.4 μ_B/f.u. was obtained. It can be noticed that the magnetic moment of studied compounds does not saturate in the maximal applied

magnetic fields of 5 T, which explains a higher value obtained from neutron diffraction compared to the SQUID measurements.

The temperature evolution of the magnetic moments for the x = 0.3, 0.4, 0.6 compounds is shown in Figure **6.13a-d**. As presented for x = 0.3 (Figure **6.13a**), the magnitude of the AFM moment μ_1 decreases rapidly above 130 K, whereas the magnitude of the FM moment μ_2 remains almost invariant in the magnetic state. It can be seen that both moments coexist to the transition temperature and disappear in the PM state. The temperature evolution of x = 0.4 is presented in Figure **6.13b**. The AFM moment dominates at 4 K but reduces drastically upon increasing temperature. Above T_N the AFM moment vanishes entirely and only a weak FM moment exists, which also disappears above T_C. The evolution of the magnetic moment for x = 0.6 is depicted in Figure **6.13c**. It can be seen that the Mn FM moments μ_2 and μ_3 decrease steadily with increasing temperature. The decrease in the weak AFM moment is more pronounced, and above T_N only the FM moments exist. The competition between the AFM and FM components occurs from the point when the first-order magnetic transition is altered towards the second-order and can be seen as the growth of the FM moment at the expense of the AFM sub-lattice.

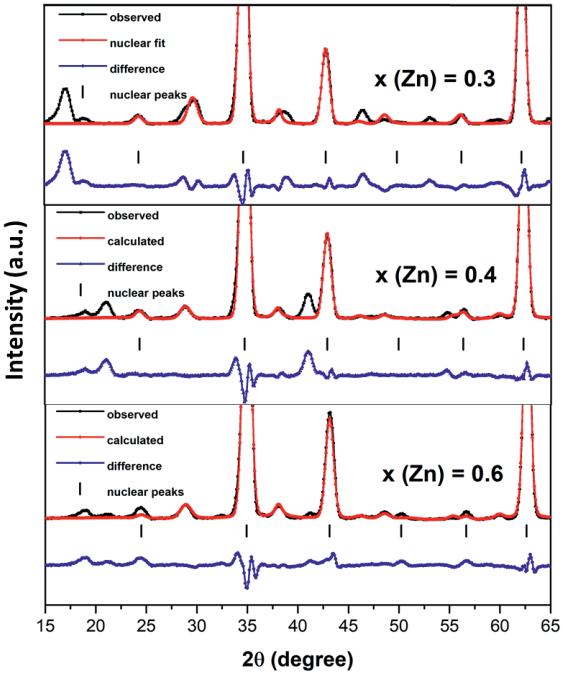

Figure 6.10: *Neutron diffraction patterns at 100 K with a fit of only the nuclear contribution.*

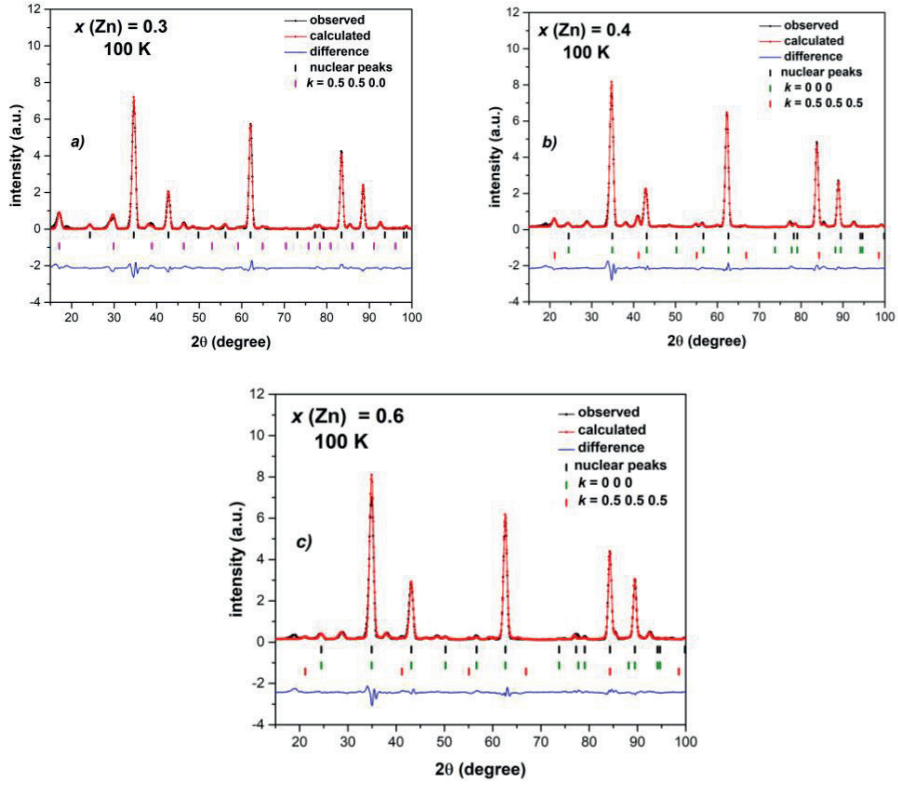

Figure 6.11: *Neutron diffraction patterns at 100 K with a fit of both the nuclear and magnetic contributions.*

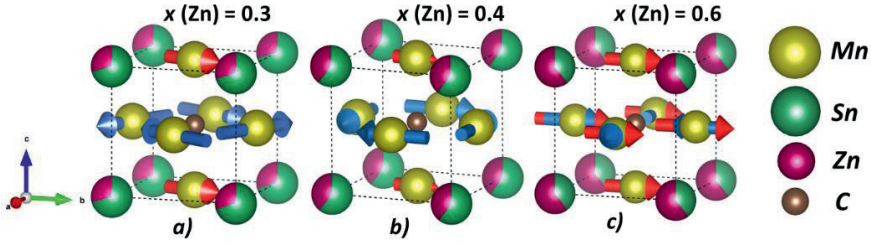

Figure 6.12: *Magnetic spin alignment of the Mn moments in a nuclear unit cell structure obtained from NPD at 100 K for a) x (Zn) = 0.3, b) x (Zn) = 0.4, c) x (Zn) = 0.6. The partial occupancies represent the aimed compositions. The blue and red vectors indicate the AFM and FM moments, respectively.*

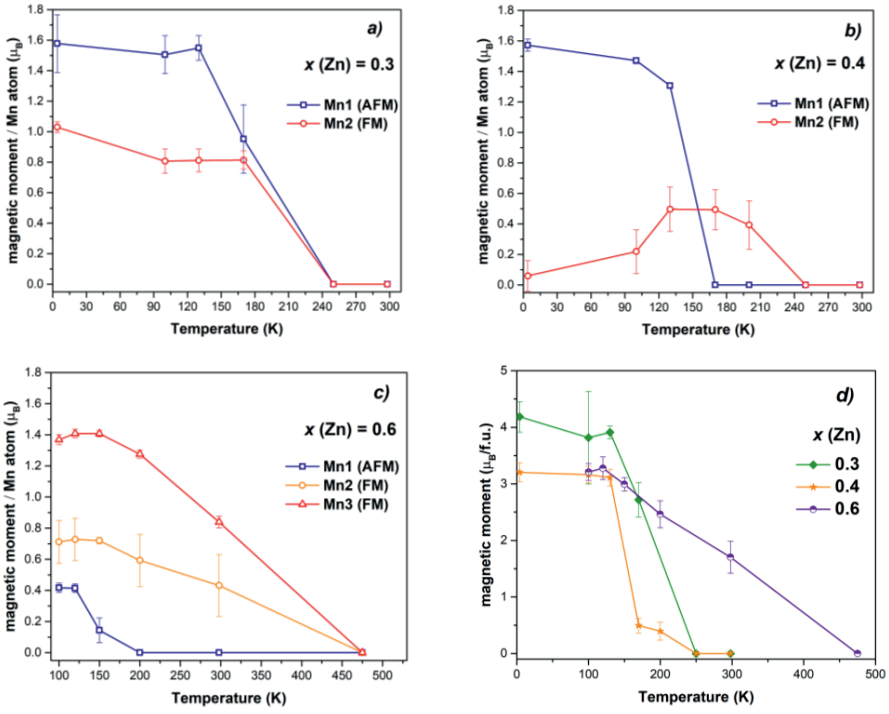

Figure 6.13: *Temperature evolution of magnetic moments in $Mn_3Sn_{1-x}Zn_xC$ for a) x = 0.3, b) x = 0.4, c) x = 0.6 obtained from NPD. d) Temperature evolution of the total magnetic moment for x = 0.3, 0.4, 0.6.*

6.4. Conclusions

The present study reveals the impact of Zn substitution in $Mn_3Sn_{1-x}Zn_xC$ antiperovskite carbides on the structural, magnetic and magnetocaloric properties. The substitution of Zn for Sn destabilizes the cubic structure, which results in the formation of a low-temperature tetragonal structure for x = 1.0. An initial decrease in T_C is accompanied by suppression of the first-order magnetic transition (FOMT) and an alleviation of the magneto-volume effect (MVE) effect, which contributes to a reduction of the magnetic entropy change ($|\Delta S_m|$). An increase in T_C for higher Zn doping ($x > 0.3$) occurs along with pronounced changes in magnetic behaviour. Namely, the FiM-PM transition transforms into a FiM-FM-PM transition. Neutron powder diffraction reveals the presence of complex magnetic structures in $Mn_3Sn_{1-x}Zn_xC$ and a competition between AFM and FM interactions. The magnetic structure of x (Zn) = 0.3 is similar to the parent compound and can be described using the propagation vector **k** = (½,½,0). However, a decrease in the AFM component and an increase in the FM moment can be seen. The magnetic structure of compounds with higher Zn doping can be described using two propagation vectors **k** = (0,0,0) and **k** = (½,½,½). It was found that in the x = 0.4 and 0.6 compounds the AFM moment decreases and the FM moment increases upon increasing Zn doping.

References

[1] E. Brück, "Developments in magnetocaloric refrigeration", *J. Phys. D. Appl. Phys.*, *38*(23) 2005, doi: 10.1088/0022-3727/38/23/R01.

[2] A. Smith, C. R. H. Bahl, R. Bjork, K. Engelbrecht, K. K. Nielsen, and N. Pryds, "Materials challenges for high performance magnetocaloric refrigeration devices", *Adv. Energy Mater.*, *2*(11), pp. 1288–1318, 2012, doi: 10.1002/aenm.201200167.

[3] V. Chaudhary, X. Chen, and R. V. Ramanujan, "Iron and manganese based magnetocaloric materials for near room temperature thermal management", *Prog. Mater. Sci.*, *100*, pp. 64–98, 2019, doi: 10.1016/j.pmatsci.2018.09.005.

[4] P. Xu, L. Hu, Z. Zhang, H. Wang, and L. Li, "Electronic structure, magnetic properties and magnetocaloric performance in rare earths (RE) based RE_2BaZnO_5 (RE = Gd, Dy, Ho, and Er) compounds", *Acta Mater.*, *236*, p. 118114, 2022, doi: 10.1016/j.actamat.2022.118114.

[5] Y. Zhang, J. Zhu, S. Li, Z. Zhang, J. Wang, and Z. Ren, "Magnetic properties and promising magnetocaloric performances in the antiferromagnetic $GdFe_2Si_2$ compound", *Sci. China Mater.*, *65*(5), pp. 1345–1352, 2022, doi: 10.1007/s40843-021-1967-5.

[6] D. Guo, L. M. Moreno-Ramírez, J. Law, Y. Zhang, and V. Franco, "Excellent cryogenic magnetocaloric properties in heavy rare-earth based $HRENiGa_2$ (HRE = Dy , Ho , or Er) compounds", *66*(1), pp. 249–256, 2023.

[7] D. Guo, L.M. Moreno-Ramírez, C. Romero-Muñiz, Y. Zhang, Y. Zhang, J.-Y. Law, V. Franco, J. Wang, and Z. Ren., "First- and second-order phase transitions in RE_6Co_2Ga (RE = Ho, Dy or Gd) cryogenic magnetocaloric materials", *Sci. China Mater.*, *64*(11), pp. 2846–2857, 2021, doi: 10.1007/s40843-021-1711-5.

[8] W. Wu, Z. Feng, and L. Guo, "Estimation on magnetic refrigeration material $(Gd_{1-x}RE_x)_5Si_4$ (RE = Dy, Ho)", *J. Mater. Sci. Technol.*, *22*(6), pp. 839–842, 2006.

[9] Z. G. Xie, D. Y. Geng, and Z. D. Zhang, "Reversible room-temperature magnetocaloric effect in Mn_5PB_2", *Appl. Phys. Lett.*, *97*(20), pp. 2–5, 2010, doi: 10.1063/1.3518064.

[10] Z. Ma, P. Xu, J. Ying, Y. Zhang, and L. Li, "Insight into the structural and magnetic properties of $RECo_{12}B_6$ (RE = Ce , Pr , Nd) compounds : A combined experimental and theoretical investigation", *Acta Mater.*, *247*, p. 118757, 2023, doi: 10.1016/j.actamat.2023.118757.

[11] Y. Zhang, S. Li, L. Hu, X. Wang, L. Li, and M. Yan, "Excellent magnetocaloric performance in the carbide compounds RE2Cr2C3 (RE = Er, Ho, and Dy) and their composites", *Mater. Today Phys.*, *27*, p. 100786, 2022, doi: 10.1016/j.mtphys.2022.100786.

[12] Y. B. Li, W. F. Li, W. J. Feng, Y. Q. Zhang, and Z. D. Zhang, "Magnetic, transport and magnetotransport properties of $Mn_{3+x}Sn_{1-x}C$ and $Mn_3Zn_ySn_{1-y}C$ compounds", *Phys. Rev. B - Condens. Matter Mater. Phys.*, *72*(2), pp. 1–8, 2005, doi: 10.1103/PhysRevB.72.024411.

[13] X. H. Zhang, Y. Yin, Q. Yuan, J. C. Han, Z. H. Zhang, J. K. Jian, J. G. Zhao, and B. Song, "Magnetoresistance reversal in antiperovskite compound $Mn_3Cu_{0.5}Zn_{0.5}N$", *J. Appl. Phys.*, *115*, p. 123905, 2014, doi: 10.1063/1.4869797.

[14] N. Hoffmann, T. F. T. Cerqueira, J. Schmidt, and M. A. L. Marques, "Superconductivity in antiperovskites", *npj Comput. Mater.*, *8*(1), p. 150, 2022, doi: 10.1038/s41524-022-00817-4.

[15] K. Takenaka and H. Takagi, "Giant Negative Thermal Expansion in Ge-Doped Anti-Perovskite Manganese Nitrides", *Appl. Phys. Lett.*, *87*, p. 261902, 2005, doi: 10.1063/1.2147726.

[16] T. Hamada and K. Takenaka, "Giant negative thermal expansion in antiperovskite manganese nitrides", *J. Appl. Phys.*, *109*, 2011, doi: 10.1063/1.3540604.

[17] J. Zemen, Z. Gercsi, and K. Sandeman, "Piezomagnetism as a counterpart of the magnetovolume effect in magnetically frustrated Mn-based antiperovskite nitrides", *Phys. Rev. B*, *96*, 2017, doi: 10.1103/PhysRevB.96.024451.

[18] P. Lukashev, R. F. Sabirianov, and K. Belashchenko, "Theory of the piezomagnetic effect in Mn-based antiperovskites", *Phys. Rev. B Condens. Matter Mater. Phys.*, *78*(18), 2008, doi: 10.1103/PhysRevB.78.184414.

[19] D. Boldrin, E. Mendive-Tapia, J. Zemen, J. B. Staunton, T. Hansen, A. Aznar, J.-L. Tamarit, M. Barrio, P. Lloveras, J. Kim, X. Moya, and L. F. Cohen, "Multisite Exchange-Enhanced Barocaloric Response in Mn_3NiN", *Phys. Rev. X*, *8*(4), pp. 1–9, 2018, doi: 10.1103/PhysRevX.8.041035.

[20] T. Tohei, H. Wada, and T. Kanomata, "Negative magnetocaloric effect at the antiferromagnetic to ferromagnetic transition of Mn_3GaC", *J. Appl. Phys.*, *94*(3), pp. 1800–1802, 2003, doi: 10.1063/1.1587265.

[21] Çaklr, F. Cugini, M. Solzi, K. Priolkar, M. Acet, and M. Farle, "Dynamics of nonergodic ferromagnetic/antiferromagnetic ordering and magnetocalorics in antiperovskite Mn_3SnC", *Phys. Rev. B*, *96*(1), pp. 1–6, 2017, doi: 10.1103/PhysRevB.96.014436.

[22] B. S. Wang, P. Tong, Y. P. Sun, X. Luo, X. B. Zhu, G. Li, X. D. Zhu, S. B. Zhang, Z. R. Yang, W. H. Song, and J. M. Dai, "Large magnetic entropy change near room temperature in antiperovskite $SnCMn_3$", *Europhys. Lett.*, *85*, 2009, doi: 10.1209/0295-5075/85/47004.

[23] V. N. Gaonkar, E. T. Dias, A. Das, A. K. Nigam, and K. R. Priolkar, "Modulations in magnetostructural coupling in C and Sn deficient Mn_3SnC", *J. Magn. Magn. Mater.*, *488*, 2019, doi: 10.1016/j.jmmm.2019.165357.

[24] N. Ennassiri, N. Tahiri, O. El Bounagui, H. Ez-Zahraouy, and A. Benyoussef, "Structural, electronic, magnetic, and magnetocaloric properties in metallic antiperovskite compound Mn_3GaC", *Mater. Res. Bull.*, *98*, 2017, pp. 335–339, 2018, doi: 10.1016/j.materresbull.2017.10.029.

[25] V. N. Gaonkar, E. T. Dias, A. B. Dey, R. P. Giri, A. K. Nigam, and K. R. Priolkar, "Role of Tin and Carbon in the magnetic interactions in Mn_3SnC", *J. Magn. Magn. Mater.*, *471*, 2019, pp. 215–219, 2019, doi: 10.1016/j.jmmm.2018.09.070.

[26] Y. Benhouria, M. Kibbou, N. Khossossi, J. Foshi, I. Essaoudi, A. Oubelkacem, A. Ainane, and R. Ahuja, "Carbides-anti-perovskites Mn_3(Sn, Zn)C: Potential candidates for an application in magnetic refrigeration", *Phys. E Low-Dimensional Syst. Nanostructures*, *124*, p. 114317, 2020, doi: 10.1016/j.physe.2020.114317.

[27] S. M. L. Teicher, I. K. Svenningsson, L. M. Schoop, and R. Seshadri, "Weyl nodes and magnetostructural instability in antiperovskite Mn_3ZnC", *APL Mater.*, *7*(12), 2019, doi: 10.1063/1.5129689.

[28] J. Rodríguez-Carvajal, "Recent advances in magnetic structure determination by neutron powder diffraction", *Phys. B Phys. Condens. Matter*, *192*(1-2), 1993, doi: 10.1016/0921-4526(93)90108-I.

[29] H. M. Rietveld, "A profile refinement method for nuclear and magnetic structures", *J. Appl. Crystallogr.*, *2*(2), pp. 65–71, 1969, doi: 10.1107/s0021889869006558.

[30] G. Kresse and J. Furthmüller, "Efficiency of ab-initio total energy calculations for metals and semiconductors using a plane-wave basis set", *Comput.Mater. Sci.*, *6*(1), pp. 15–50, 1996, doi: 10.1016/0927-0256(96)00008-0.

[31] G. Kresse and J. Hafner, "Ab initio molecular dynamics for liquid metals", *Phys. Rev. B*, *47*(1), pp. 558–561, 1993, doi: 10.1103/PhysRevB.47.558.

[32] P. E. Blöchl, "Projector augmented-wave method", *Phys. Rev. B*, *50*(24), pp. 17953–17979, 1994, doi: 10.1103/PhysRevB.50.17953.

[33] G. Kresse and D. Joubert, "From ultrasoft pseudopotentials to the projector augmented-wave method", *Phys. Rev. B*, *59*(3), pp. 1758–1775, 1999, doi: 10.1103/PhysRevB.59.1758.

[34] J. P. Perdew, K. Burke, and M. Ernzerhof, "Generalized Gradient Approximation Made Simple", *Phys. Rev. Lett.*, *77*(18), pp. 3865–3868, 1996, doi: 10.1103/PhysRevLett.77.3865.

[35] M. Methfessel and A. T. Paxton, "High-precision sampling for Brillouin-zone integration in metals", *Phys. Rev. B*, *40*(6), pp. 3616–3621, 1989, doi: 10.1103/PhysRevB.40.3616.

[36] C. P. Guillaud, "Discussion", *Rev. Mod. Phys.*, *25*(1), pp. 119–121, 1953, doi: 10.1103/RevModPhys.25.119.

[37] E. T. Dias, K. R. Priolkar, A. Das, G. Aquilanti, Ö. Çakir, M. Acet, and A. K. Nigam, "Effect of local structural distortions on magnetostructural transformation in Mn_3SnC", *J. Phys. D. Appl. Phys.*, *48*(29), 2015, doi: 10.1088/0022-3727/48/29/295001.

[38] B. S. Wang, P. Tong, Y. P. Sun, X. Luo, X. B. Zhu, G. Li, X. D. Zhu, S. B. Zhang, Z. R. Yang, W. H. Song "Large magnetic entropy change near room temperature in antiperovskite $SnCMn_3$," *Epl*, *85*(4), 2009, doi: 10.1209/0295-5075/85/47004.

[39] P. Liu, J. Peng, M. Xue, and B. Wang, "Magnetocaloric effect and critical behavior of the Mn-rich itinerant material Mn_3GaC with enhanced ferromagnetic interaction," *Chinese Phys. B*, *29*(4), 2020, doi: 10.1088/1674-1056/ab7da1.

[40] Z. Li, M. Yang, J. S. Park, S. H. Wei, J. J. Berry, and K. Zhu, "Stabilizing Perovskite Structures by Tuning Tolerance Factor: Formation of Formamidinium and Cesium Lead Iodide Solid-State Alloys," *Chem. Mater.*, *28*(1), pp. 284–292, 2016, doi: 10.1021/acs.chemmater.5b04107.

[41] B. S. Wang, W. J. Lu, S. Lin, J. C. Lin, P. Tong, B. C. Zhao, W. H. Song, and Y. P. Sun, "Magnetic / structural diagram , chemical composition-dependent magnetocaloric effect in self-doped antipervoskite compounds $Sn_{1-x}CMn_{3+x}$ ($0 \leq x \leq 0.40$)", *J. Magn. Magn. Mater.*, *324*, pp. 773–781, 2012, doi: 10.1016/j.jmmm.2011.09.014.

[42] X. Shi, Y. Wen, D. Gu, H. Hou, Y. Zhang, and C. Wang, "The structure, magnetism and electronic transport properties of $Mn_3Sn_{1-x}Zn_xC$ (x = 0, 0.1, 0.2, 0.3, 0.4, 0.5)", *J. Alloys Compd.*, *739*, pp. 934–938, 2018, doi: 10.1016/j.jallcom.2017.12.266.

[43] D. Huang and J. Gao, "Effects of Ge substitution for Sn on the crystal structure, magnetization, and the magnetocaloric effect of Mn_3SnC", *J. Magn. Magn. Mater.*, *537*, p. 168163, 2021, doi: 10.1016/j.jmmm.2021.168163.

[44] A. Mungale and K. R. Priolkar, "Packing fraction related distortion of Mn_6C octahedra and its effect on the first order magnetic transition in Mn based antiperovskites", *J. Appl. Phys.*, *126*, no. 24, 2019, doi: 10.1063/1.5130713.

[45] V. N. Gaonkar, E. T. Dias, M. N. Vedpathak, and K. R. Priolkar, "Packing fraction induced phase separation in A-site doped antiperovskites", *Mater. Today Commun.*, *33*, p. 104459, 2022, doi: 10.1016/j.mtcomm.2022.104459.

[46] M. Nie, C. Wang, Y. Wen, Y. Sun, Y. Na, L. Chu, and M. Tang, "Magnetic phase transitions of antiperovskite $Mn_{3-x}Fe_xSnC$ ($0.5 \leq x \leq 1.3$)", *Solid State Commun.*, *151*(5), pp. 377–381, 2011, doi: 10.1016/j.ssc.2010.12.015.

[47] E. T. Dias, K. R. Priolkar, and A. K. Nigam, , "Co-existence of ferromagnetic and antiferromagnetic interactions in $Mn_3Ga_{1-x}Sn_xC$", Mater. Res. Express, *1*(2), pp. 026106, 2014, doi: 10.1088/2053-1591/1/2/026106.

[48] H. N. Bez, H. Yibole, A. Pathak, Y. Mudryk, and V. K. Pecharsky, "Journal of Magnetism and Magnetic Materials Best practices in evaluation of the magnetocaloric effect from bulk magnetization measurements," *J. Magn. Magn. Mater.*, *458*, pp. 301–309, 2018, doi: 10.1016/j.jmmm.2018.03.020.

[49] L. H. Lewis, D. Yoder, A. R. Moodenbaugh, D. A. Fischer, and M.-H. Yu, "Magnetism and the defect state in the magnetocaloric antiperovskite $Mn_3GaC_{1-\delta}$", *J. Phys. Condens. Matter*, *18*(5), pp. 1677–1686, 2006, doi: 10.1088/0953-8984/18/5/020.

[50] L. Hua, L. Wang, and L. F. Chen, "First-principles investigation of Ge doping effects on the structural, electronic and magnetic properties in antiperovskite Mn_3CuN", *J. Phys. Condens. Matter*, *22*(20), p. 206003, 2010, doi: 10.1088/0953-8984/22/20/206003.

[51] K. A. Gschneidner, Y. Mudryk, and V. K. Pecharsky, "On the nature of the magnetocaloric effect of the first-order magnetostructural transition," *Scr. Mater.*, *67*(6), pp. 572–577, 2012, doi: 10.1016/j.scriptamat.2011.12.042.

[52] M. Piazzi, J. Zemen, and V. Basso, "Ab-initio Based Analytical Evaluation of Entropy in Magnetocaloric Materials with First Order Phase Transitions," *Phys. Procedia*, *75*, pp. 1332–1344, 2015, doi: 10.1016/j.phpro.2015.12.149.

[53] V. N. Antonov, B. N. Harmon, A. N. Yaresko, and A. P. Shpak, "Electronic structure, noncollinear magnetism, and X-ray magnetic circular dichroism in the Mn_3ZnC perovskite", *Phys. Rev. B - Condens. Matter Mater. Phys.*, *75*(16), pp. 1–7, 2007, doi: 10.1103/PhysRevB.75.165114.

[54] J. Chaboy, H. Maruyama, and N. Kawamura, "Ab initio x-ray absorption study of Mn K-edge XANES spectra in Mn_3MC (M = Sn, Zn and Ga) compounds", *J. Phys. Condens. Matter*, *19*(21), 2007, doi: 10.1088/0953-8984/19/21/216214..

[55] J. Yan, Y. Sun, Y. Wen, L. Chu, M. Wu, Q. Huang, C. Wang, J. W. Lynn, and Y. Chen, "Relationship between spin ordering, entropy, and anomalous lattice variation in $Mn_3Sn_{1-e}Si\varepsilon C_{1-\delta}$ compounds", *Inorg. Chem.*, *53*(4), pp. 2317–2324, 2014, doi: 10.1021/ic403063t.

[56] G. Lorthioir, M. E. Fruchart, M. Nardin, P. l'Héritier, and R. Fruchart, "Etude magnetique et cristallographique de la solution solide $(Zn_{1-x}Sn_x)Mn_3C$", *Mater. Res. Bull.*, *8*(9), pp. 1027–1034, 1973, doi: https://doi.org/10.1016/0025-5408(73)90107-4.

[57] S. Iikubo, K. Kodama, K. Takenaka, H. Takagi, and S. Shamoto, "Magnetovolume effect in $Mn_3Cu_{1-x}Ge_xN$ related to the magnetic structure: Neutron powder diffraction measurements", *Phys. Rev. B - Condens. Matter Mater. Phys.*, *77*(2), pp. 3–6, 2008, doi: 10.1103/PhysRevB.77.020409.

[58] S. Iikubo, K. Kodama, K. Takenaka, H. Takagi, M. Takigawa, and S. Shamoto, "Local lattice distortion in the giant negative thermal expansion material Mn_3Cu_{1-}

$_x$Ge$_x$N", *Phys. Rev. Lett.*, *101*(20), pp. 1–6, 2008, doi: 10.1103/PhysRevLett.101.205901.

[59] M. Wu, C. Wang, Y. Sun, L. Chu, J. Yan, D. Chen, Q. Huang, and J. W. Lynn, "Magnetic structure and lattice contraction in Mn_3NiN", *J. Appl. Phys*., *114*(12), 2013, doi: 10.1063/1.4822023.

Supplementary material for Chapter 6

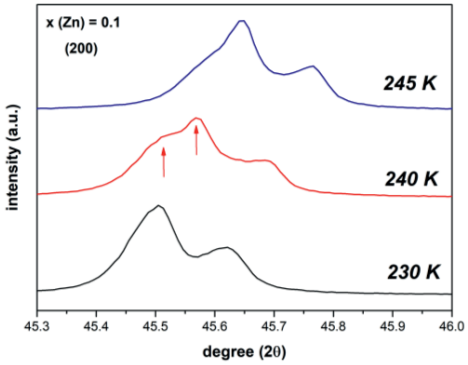

Fig. S1. *Temperature evolution of the (200) X-ray diffraction peak across the magnetic transition for* $Mn_3Sn_{0.9}Zn_{0.1}C$.

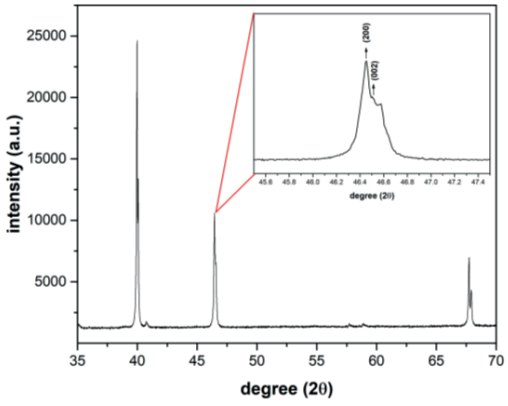

Fig. S2. *XRD pattern of* Mn_3ZnC *collected at 120 K. The (200) peak splits into (200) and (002) as a result of the tetragonal distortion:* $a = b \neq c$.

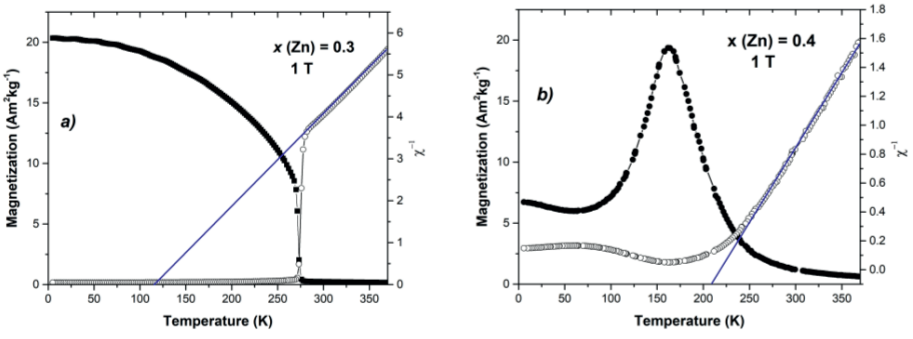

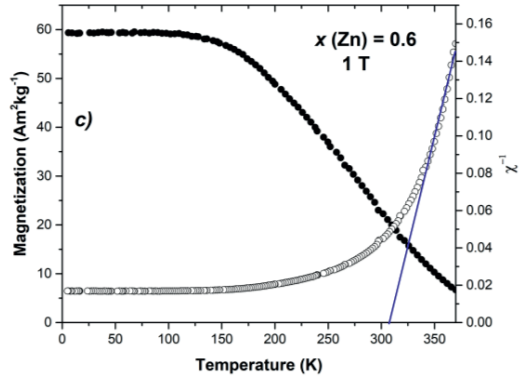

Fig. S3. *Temperature dependence of the magnetization and the inverse susceptibility of $Mn_3Sn_{1-x}Zn_xC$ as a function of the temperature measured in 1 T for: a) x = 0.3, b) x = 0.4, c) x = 0.5.*

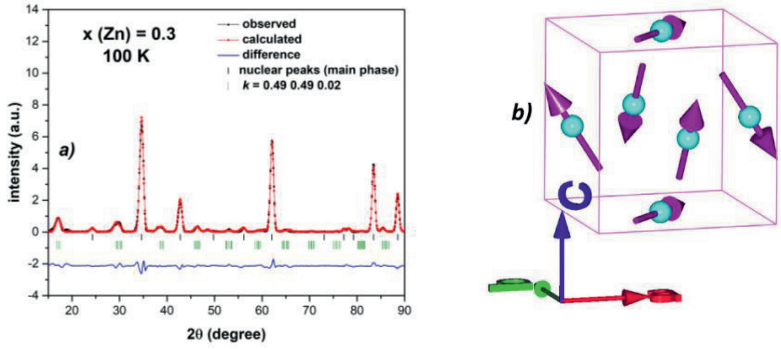

Fig. S4. *a) Fitted neutron diffraction pattern measured at 100 K for x = 0.3 with an incommensurate propagation vector* $\boldsymbol{k}$ *= (0.49,0.49,0.02), b) magnetic spin alignment of the Mn moments in the nuclear unit cell obtained for the incommensurate propagation vector* $\boldsymbol{k}$ *= (0.49,0.49,0.02).*

7

Impact of Fe doping on magnetic and structural properties of $Mn_3Sn_{1-x}Fe_xC$ antiperovskite carbides

Abstract

Structural, microstructural and magnetic properties of $Mn_3Sn_{1-x}Fe_xC$ antiperovskites have been studied employing experimental methods and DFT calculations. With increasing Fe content, the Curie temperature (T_C) initially reduces from 273 to 215 K for x = 0.15. For a higher Fe content ($x > 0.15$), T_C increases to 367 K for x = 0.35. A rise in T_C is accompanied by simultaneous suppression of the antiferromagnetic (AFM) moment and an enhancement of the ferromagnetic (FM) order upon Fe doping. The refinement of the neutron powder diffraction (NPD) data for x = 0.05 revealed a magnetic structure with propagation vector $\boldsymbol{k}$ = (½, ½, 0) *with a decrease in the canted AFM moment and an enhanced FM order. For a higher Fe content* ($x = 0.20$), *the low-temperature ordered state can be described with a propagation vector* $\boldsymbol{k}$ = (½, ½, 0), *transforming into the FM type above the Néel temperature* (T_N), *which is correlated to a quenching of the magnetovolume effect* (MVE). *For x = 0.30, the magnetic structure is described with a propagation vector* $\boldsymbol{k}$ = (0, 0, 0) *indicating the presence of the pure FM order.*

7.1. Introduction

Mn-based antiperovskites with a general formula Mn_3AX (A: Sn, Ga, Al, In, Zn, Ge, Ag; X: C, N) have attracted much interest due to various interesting physical phenomena, such as a near-zero temperature coefficient of resistance [1], giant magnetoresistance (GMR) [2]–[4], magneto-volume effect (MVE) [5]–[8], piezomagnetic effect [9], [10], barocaloric and magnetocaloric effects [11]–[14]. The antiperovskite type of structure is chemically stable, which enables the extensive study of the doping effect. Particular attention has been focused on Mn_3SnC [14]–[21] and Mn_3GaC [11], [22], [23] due to their large magnetocaloric effect and interesting magnetic properties. Mn_3SnC shows a sharp first-order magnetic transition (FOMT) with a Curie temperature (T_C) in the vicinity of room temperature and a large magnetic entropy change (ΔS_m), which makes this compound attractive for magnetic cooling. Besides, neutron powder diffraction studies on Mn_3SnC revealed a complicated spin arrangement in which one Mn atom in the unit cell orders FM with a magnetic moment of 0.65 μ_B/Mn and two Mn atoms order AFM in the *a-b* plane with a magnetic moment of 2.4 μ_B/Mn [24], [25]. The study of the $Mn_{3-x}Fe_xSnC$ system revealed an increase in the magnetic moment and T_C upon Fe substitution for Mn [26]. In Mn-based antiperovskites, the magnetic moment originates primarily from the Mn atoms. Therefore, substituting non-magnetic Sn with Fe might further enhance the magnetic properties. In this work, $Mn_3Sn_{1-x}Fe_xC$ ($0.00 \leq x \leq 0.30$) antiperovskites were explored in terms of their structural, microstructural and magnetic properties by experimental techniques and DFT calculations.

7.2. Experimental details

Polycrystalline $Mn_3Sn_{1-x}Fe_xC$ (x = 0.00, 0.05, 0.10, 0.15, 0.20, 0.25, 0.35) compounds were prepared from Mn (99.7%), Sn (99.9%), Fe (99.9%) and graphite (99.9%) powders. The appropriate amounts of powders were mixed together with 10 wt.% extra graphite to compensate for possible C losses occurring during the annealing process. The samples were pressed into pellets and sealed in quartz tubes under 200 mbar Ar atmosphere. The prepared samples were then inserted into a cold oven and slowly heated (100 K/h) until the oven reached 1023 K. After 120 h of the heat treatment, samples were oven-cooled to room temperature. As-obtained samples were subsequently pulverized, pressed into pellets and re-annealed under the same conditions to enhance homogeneity.

The X-ray diffraction patterns were collected in the temperature range 120 to 298 K utilizing a PANalytical X-pert Pro diffractometer using Cu-K_α (λ = 1.54 Å) with an Anton Paar TTK450 low-temperature chamber. In order to elucidate the magnetic structure and temperature evolution of magnetic moments, neutron powder diffraction (NPD) measurements were conducted at various temperatures (4 to 500 K), employing the neutron powder diffraction instrument PEARL (λ = 1.67 Å) at the Reactor Institute Delft, the Netherlands. The structural and magnetic analysis of the XRD and NPD data was performed using the Rietveld refinement implemented in the Fullprof software [27], [28]. Coherent neutron scattering lengths of -0.3730, 0.6225, 0.9450 and 0.6646 ($\times 10^{-12}$ cm) were used for Mn, Sn, Fe and C, respectively. Magnetic properties were measured utilizing

superconducting quantum interference device (SQUID) magnetometers (MPMS-XL and MPMS-5S) in the reciprocating sample option mode (RSO), in the temperature range of 5 to 370 K and in magnetic fields up to 5 T. Magnetic measurements at higher temperatures (370 to 500 K) were conducted employing a Vibrating Sample Magnetometer (VSM) attached to a Quantum Design VersaLab. Scanning electron microscopy (SEM, JEOL JSM 6500 F, Japan) with energy disperse X-ray spectroscopy (EDS) and a back-scatter electron (BSE) detector was used to investigate the microstructure and composition of the synthesized compounds.

Calculations of the Density of States (DOS) were performed for $Mn_3Sn_{1-x}Fe_xC$ compounds in the framework of the density functional theory (DFT) employing the Vienna Ab Initio simulation package (VASP) [29], [30] using the projector augmented-wave (PAW) method [31], [32]. The **k**-space integrations were performed with the Methfessel-Paxton method [33] of second order with a smearing width of 0.2 meV. The relaxation was performed for a 2×2×2 supercell consisting of 24 atoms, by integration of the Brillouin zone on a gamma-centred **k**-grid of a 3×3×3 mesh for a force convergence of 0.1 meV/Å. To calculate the DOS, an integration of the Brillouin zone was performed utilizing the tetrahedron method with Blöchl corrections with a 9×9×9 grid. The plane-wave cut-off energy for all calculations was set at 520 eV. The DFT calculations were done in collaboration.

7.3. Structural and microstructural properties

To study the composition of the prepared compounds and to elucidate the influence of Fe-doping on the microstructure formation, SEM-EDS spectroscopy was performed for selected compounds. SEM and BSE micrographs of $Mn_3Sn_{1-x}Fe_xC$ (x = 0.00, 0.10, 0.20) are shown in Figure **7.1a-c**. The morphologies of the studied compounds evolve from round-shaped structures into sharp-edged forms upon increased Fe doping. During the sintering process, Sn diffuses and plays a binder role. For the parent compound (Figure **7.1a**), a Sn-rich impurity and pure Sn were found, indicating a good wetting of liquid Sn to the grains of the main phase. Upon the substitution of Fe for Sn, the amount of binding element decreases, which results in an impaired liquid filling during the annealing process. As a result, the grain rearrangement and growth is hampered, which is seen as a notable change in the microstructure. A good wetting of the liquid phase provides well-formed grains and leads to the removal of residual porosity [34]. Consequently, upon Fe substitution for Sn, micro-pore formation is observed, as shown for x = 0.20 in Figure **7.1c**. Due to the dependence of backscattered electrons on the atomic number, BSE micrographs allow for a differentiation between various phases. As seen in the BSE images in Figure **7.1a-c**, the main phase is dispersed in unreacted graphite (darker spots). The compositions of the compounds with Fe contents x = 0.00, 0.10, 0.20 can be found in Table **7.1**. In spite of the excess C added during the sample preparation, EDS analysis revealed a C deficiency in each case, which is also explained by the presence of unreacted graphite.

Table 7.1: *Elemental composition of the $Mn_3Sn_{1-x}Fe_xC$ compounds (x = 0.00, 0.10, 0.20) obtained with SEM/EDS microscopy. The error bars are shown in parentheses.*

	Mn (at.%)	Sn (at.%)	Fe (at.%)	C (at.%)
***x* = 0.00**	68.1(±1.3)	21.6(±1.2)	-	10.3(±0.2)
***x* = 0.10**	65.0(±0.8)	19.4(±1.3)	1.2(±0.5)	14.4(±1.8)
***x* = 0.20**	63.0(±1.7)	18.9(±1.5)	4.3(±1.0)	13.8(±2.2)

The XRD patterns of the $Mn_3Sn_{1-x}Fe_xC$ compounds collected at 298 K are depicted in Figure 7.2a. It can be seen that all compounds crystallize in the same cubic crystal structure (space group: *Pm-3m*) with minor amounts of concomitant MnO and a graphite impurity phases. Additionally, for the parent compound (Mn_3SnC), a minor amount of $MnSn_2$ (< 2 wt.%) and Sn impurity (< 2 wt.%) phases can be seen, which is in agreement with the EDS results. The refinement of the x = 0.20 sample is presented in Figure 7.2b. In the antiperovskite structure, the Sn atoms occupy the (0,0,0) position, C atom resides at the (½,½,½) position and the Mn atoms occupy the (½,½,0) position. A linear decrease in the lattice parameter (Figure 7.3) from 3.9922(5) to 3.9597(3) Å for the x = 0.35 sample clearly indicates that prepared compounds obey Vegard's law as the covalent radius of Fe (125 pm) is significantly smaller than the radius of Sn (141 pm).

The temperature dependence of the lattice parameter for the $Mn_3Sn_{1-x}Fe_xC$ compounds is presented in Figure 7.4. The magneto-volume effect (MVE) occurs due to an interplay between the magnetism and the lattice, which leads to a negative volume change at the magnetic transition. It can be seen that the MVE is gradually quenched upon increasing Fe content and disappears completely for the x = 0.20 sample, for which only a positive thermal expansion is observed. A gradual decrease in the MVE indicates the suppression of the first-order magnetic transition (FOMT) and a shift towards a second-order magnetic transition (SOMT), which is also highlighted by the thermal evolution of the (111) diffraction peak across the magnetic transition, as presented in Figure 7.5. The first-order behaviour of the parent compound (Figure 7.5a) is revealed by a discontinuous change of the diffraction peak, which occurs abruptly at the magnetic transition. Although the negative volume change is still pronounced for the x = 0.15 sample, the shift in the diffraction peak is reduced compared to Mn_3SnC (Figure 7.5b). For the x = 0.30 sample (Figure 7.5c), a continuous change in the diffraction peak can be seen, which is in line with a linear increase in the lattice parameter upon increasing temperature. A broadening of the diffraction peak upon increasing the Fe content is most likely ascribed to a systematic reduction in the grain size.

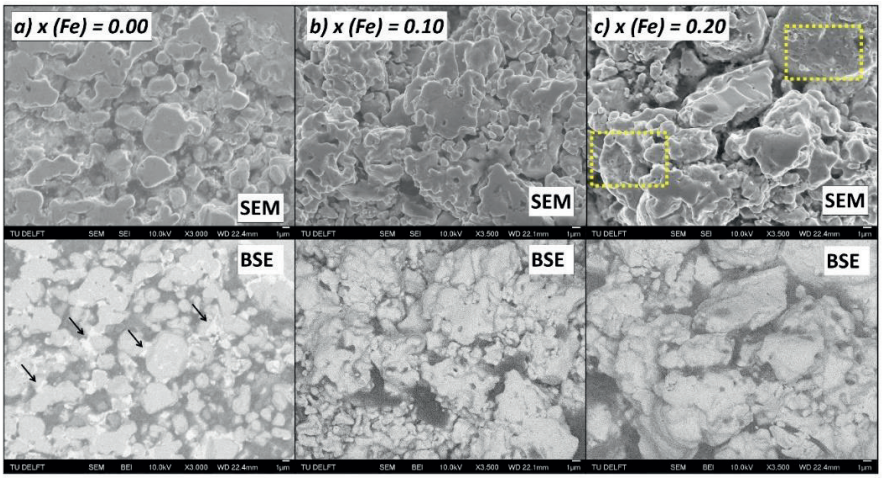

Figure 7.1: *SEM and BSE micrographs of $Mn_3Sn_{1-x}Fe_xC$ compounds: a) x = 0.00, b) x = 0.10, c) x = 0.20. Arrows point towards the Sn-rich impurity phase and the rectangles indicate the micro-pore formation.*

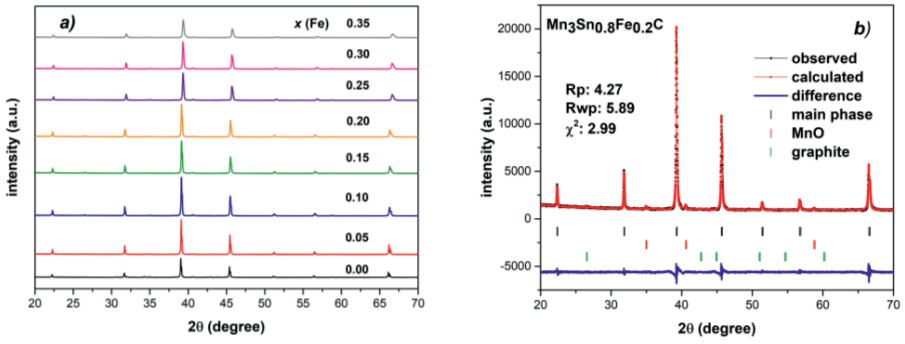

Figure 7.2: *a) XRD patterns of $Mn_3Sn_{1-x}Fe_xC$ compounds obtained at 298 K, b) Rietveld refinement of x = 0.20 at 298 K.*

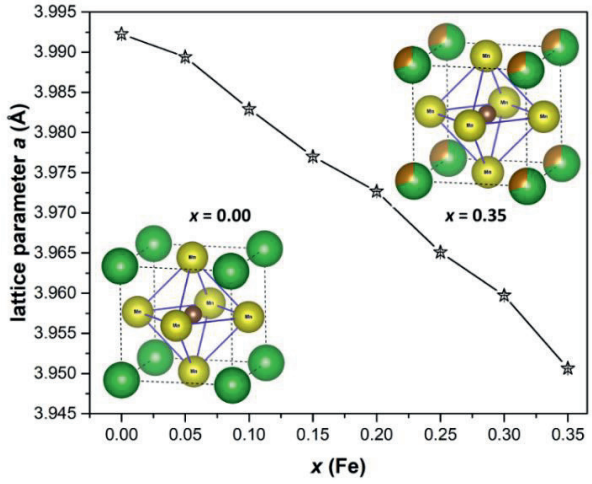

Figure 7.3: *Change in the lattice parameter a upon increasing doping content x in $Mn_3Sn_{1-x}Fe_xC$ compounds. The inserts present a schematic representation of Fe substitution for Sn within the unit cell.*

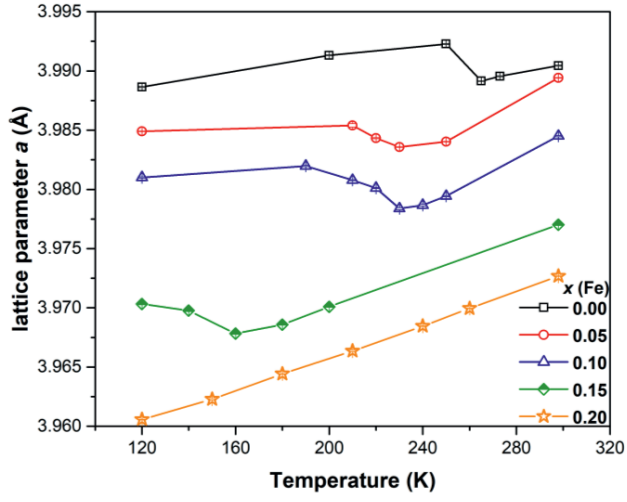

Figure 7.4: *Temperature dependence of the lattice parameter a in $Mn_3Sn_{1-x}Fe_xC$ alloys. The error bars are smaller than the marker size.*

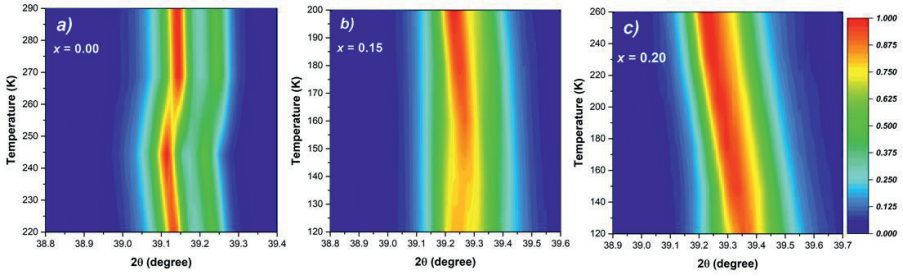

Figure 7.5: *Contour plots of the (111) diffraction peak across the magnetic transition for a) x = 0.00, b) x = 0.15, c) x = 0.20.*

7.4. Magnetization measurements

Magnetization measurements recorded upon cooling and heating in applied magnetic fields of 0.01 and 1 T are presented in Figure **7.6a** and Figure **7.6b**, respectively. It can be seen that T_C initially decreases for small Fe contents ($x < 0.15$), which is subsequently followed by a linear increase for higher doping ($x > 0.15$). As elucidated from the field dependence of the magnetization in magnetic fields up to 5 T presented in Figure **7.6a**, the magnetic moment slightly decreases initially and an increase in a magnetic moment can be seen for a higher Fe doping ($x > 0.15$), which is also accompanied by an increase in T_C, as presented in Figure **7.7b**. In Mn_3SnC, the C-*2p* orbitals hybridize with the Mn-*3d* electrons. While the indirect interactions between two half-filled Mn-*3d* orbitals mediated through the C *p* orbitals at a 180-degree angle (Mn-C-Mn) are antiferromagnetic (AFM), the direct exchange between the Mn atoms can be either AFM or FM, depending on a distance between the Mn atoms. The presence of competing AFM and FM exchange interactions leads to a variation in T_C and pronounced changes in the magnetism. The initial decrease in T_C can be ascribed to a weakening of the exchange interactions between the Mn atoms due to an enhanced hybridization between the C-*2p* and the Mn-*3d* orbitals. For a higher Fe content, an enhancement of the direct Mn-Mn exchange interactions is responsible for an increase in T_C. It is worth mentioning that a similar behaviour was previously observed in other doped antiperovskite carbides in which doping reduces the lattice parameter, such as $Mn_{3+x}Sn_{1-x}C$ [2], [36], $Mn_3Ga_{1-x}Sn_xC$ [37], $Mn_{3-x}Fe_xSnC$ [26], $Mn_3Sn_{1-x}Zn_xC$ [38], $Mn_3Sn_{1-x}In_xC$ [15] and $Mn_3Sn_{1-x}Si_xC$ [17]. An increase in T_C is presumably accompanied by a change in magnetic behaviour, judging from the characteristics of the *M-T* curves measured at 0.01 T. The temperature dependence of the magnetization for $x \leq 0.15$ shows a gradual decrease in magnetization upon increasing temperature which suggests the presence of ferrimagnetic (FiM) order, while a more stable magnetization in the ordered state for $x > 0.15$ implies the presence of a dominant ferromagnetic (FM) order. However, a characteristic cusp-like feature observed for $x = 0.20$ in a magnetic field 0.01 T suggests the presence of a low-temperature FiM state with a Néel temperature (T_N) corresponding to the maximum in the magnetization at 200 K, which is followed by a FM-PM transition with T_C at 256 K. Despite an observed

linear increase in T_C for compounds with $x > 0.15$, the magnetic moment reaches its maximum for $x = 0.30$ and appears to decrease for a higher doping content. A decrease in the magnetic moment for a higher Fe content is not associated with the formation of the impurity phase and appears to be intrinsic.

The magnetic entropy change $|\Delta S_m|$ was calculated for selected compounds from the measured *M-T* curves in applied magnetic fields up to 2 T using one of the Maxwell relations:

$$\Delta S_m(T,H) = \int_{\mu_0 H_1}^{\mu_0 H_2} \left(\frac{\partial M(T)}{\partial T}\right)_H d(\mu_0 H) \tag{7.1}$$

The values of $|\Delta S_m|$ obtained for $Mn_3Sn_{1-x}Fe_xC$ ($x = 0.15, 0.20, 0.25$) are presented in Figure 7.8. The magnetocaloric effect (MCE) in these compounds is compared with other antiperovskite carbides**.** Despite an observed increase in magnetization in the $Mn_3Sn_{1-x}Fe_xC$ system, Fe doping reduces the magnetocaloric effect as the value of $|\Delta S_m|$ for a field change of 2 T decreases from 4.3 $Jkg^{-1}K^{-1}$ for Mn_3SnC to 0.4, 0.3 and 0.3 $Jkg^{-1}K^{-1}$ for $x = 0.15, 0.20, 0.25$, respectively. The reduction in the MCE is related to a weakening of the FOMT as discussed in section 7.3.

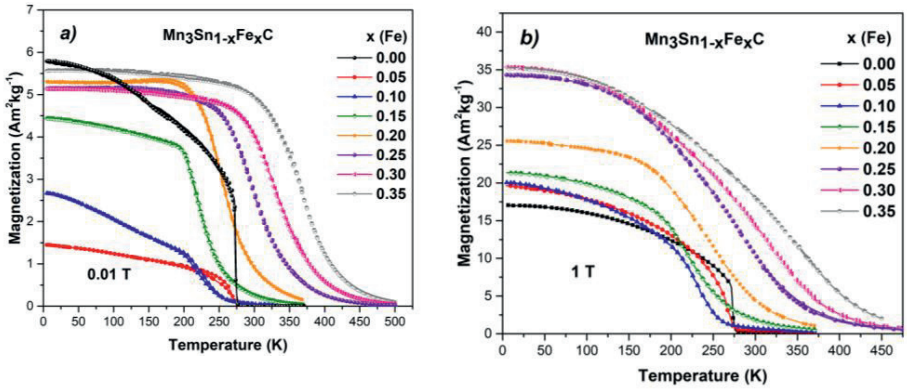

Figure 7.6: *Temperature dependence of the magnetization for $Mn_3Sn_{1-x}Fe_xC$ measured in a magnetic field of a) 0.01 T, b) 1 T.*

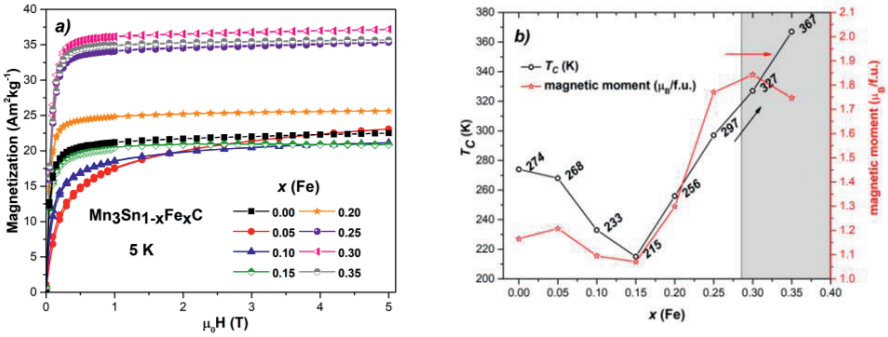

Figure 7.7: *a) Field dependence of magnetization at 5 K and in magnetic fields up to 5 T, b) changes in T_C and magnetic moment derived from the SQUID measurements in a magnetic field of 5 T and at a temperature of 5 K.*

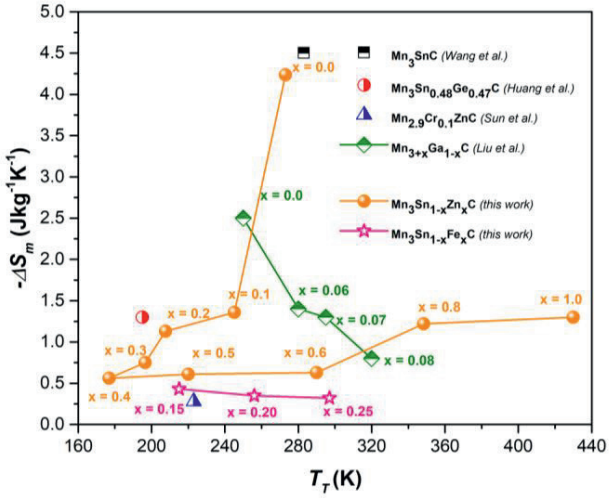

Figure 7.8: *Magnetic entropy change ($-\Delta S_m$) measured in a magnetic field change of 2 T for $Mn_3Sn_{1-x}Fe_xC$ compared with other studied antiperovskite carbides: Mn_3SnC [39], $Mn_3Sn_{0.48}Ge_{0.47}C$ [40], $Mn_{2.9}Cr_{0.1}ZnC$ [41], $Mn_{3+x}Ga_{1-x}C$ [42], $Mn_3Sn_{1-x}Zn_xC$ [38].*

7.5. DFT calculations

The density of states (DOS) for $Mn_3Sn_{1-x}Fe_xC$ is shown in Figure 7.9. It can be seen that the magnetic moment originates mainly from the Mn (*3d*) states. The presence of a sharp peak for Mn_3SnC (Figure 7.9a) at the Fermi level (E_F) suggests a magnetic instability, which is in line with the observed changes in magnetic behaviour. For $x = 0.250$ (Figure 7.9b), the splitting between the majority and minority bands is more pronounced due to the band narrowing, which leads to a larger magnetic moment. Besides, the separation of the Fe spin-up and spin-down states implies that the Fe atoms carry a magnetic moment. A suppressing

of the asymmetric nature for minority and majority bands can be observed for both Mn and Fe states when $x = 0.375$, as shown in Figure 7.9c. For $x = 0.625$ (Figure 7.9d), the spin-up and spin-down states are almost entirely equalized, which results in a quenching of the magnetic moment. The variation of the total magnetic moment (per supercell) is shown in Figure 7.10. From the DFT calculations an initial increase in the magnetic moment is observed, which is followed by a reduction for higher Fe contents, which is in agreement with our experimental results.

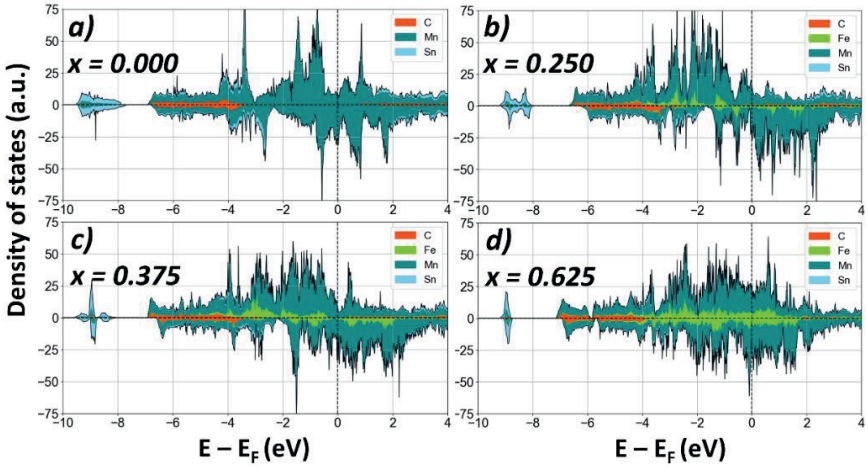

Figure 7.9: *Density of states (DOS) of $Mn_3Sn_{1-x}Fe_xC$ in the vicinity of Fermi level (E_F) for: a) $x = 0.000$, b) $x = 0.250$, c) $x = 0.375$, d) $x = 0.625$.*

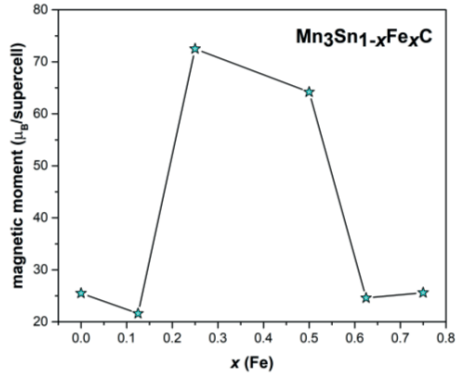

Figure 7.10: *Evolution of the magnetic moment (per supercell) for $Mn_3Sn_{1-x}Fe_xC$ upon Fe doping content x, derived from DFT calculations.*

7.6. Neutron powder diffraction

Neutron powder diffraction (NPD) has been used to study the magnetic structure of $Mn_3Sn_{1-x}Fe_xC$ (x = 0.05, 0.20, 0.30) compounds. It has been reported that the parent compound (Mn_3SnC) possesses a complicated spin arrangement, despite its simple cubic structure. The refinement using the propagation vector $\mathbf{k} = (½,½,0)$ revealed that two Mn atoms in the a-b plane carry a large AFM moment (μ_1 = 2.3 μ_B/Mn) in the square configuration (a-b plane) and one Mn atom has a smaller FM component (μ_2 = 0.7 μ_B/Mn) along the c-axis [18], [25].

The magnetic structure of the x = 0.05 sample derived from the low-temperature measurement (4 K) is similarly described with a propagation vector $\mathbf{k} = (½,½,0)$, which implies a doubling of the magnetic unit cell in a and b directions with respect to the nuclear unit cell. The nuclear refinement of the NPD data (including impurity phases) for x = 0.05 collected at 4 K is shown in Figure 7.11a and the refinement of the nuclear and magnetic structure is presented in Figure 7.11b. The unfitted peak at 2θ ≈ 18.9° is present in all low-temperature patterns and corresponds to the AFM contribution of the MnO impurity phase (T_N ≈ 117 K). From the refinement it can be seen that the AFM moment of the main phase decreases to μ_1 = 0.74(5) μ_B/Mn and the FM moment is significantly enhanced to μ_2 = 2.2(3) μ_B/Mn upon Fe doping. A similar effect on the size of magnetic moments has been reported upon Zn substitution for Sn in the $Mn_3Sn_{1-x}Zn_xC$ system [38]. The refinement of the NPD data at 4 K yielded a total magnetic moment of 3.7(3) μ_B/f.u. At 150 K, the compound possesses the same magnetic structure and the size of the AFM and FM moments slightly decreases to 0.71(3) and 2.1(3) μ_B/Mn, respectively. From a Curie-Weiss fit to the paramagnetic susceptibility (Figure 7.11c), a calculated effective moment (μ_{eff}) of 3.7 μ_B/f.u was derived, which is in agreement with the value obtained from the NPD data at 4 K. The spin alignment is presented in Figure 7.11d.

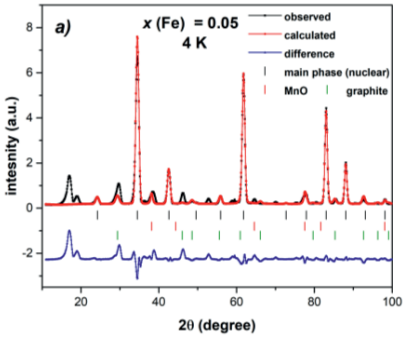

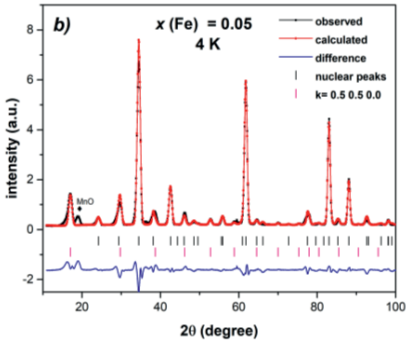

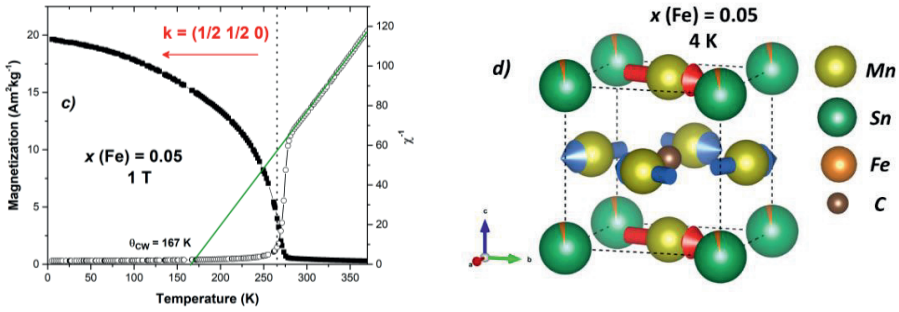

Figure 7.11: *a) Neutron diffraction pattern of $Mn_3Sn_{1-x}Fe_xC$ for x (Fe) = 0.05 with a fit of the nuclear structure only, including impurity phases, b) Neutron diffraction pattern for x (Fe) = 0.05 with a fit of the nuclear and magnetic structure, c) Temperature dependence of the magnetization and the inverse susceptibility for x = 0.05, d) Magnetic spin alignment of the Mn moments in the nuclear unit cell obtained from NPD at 4 K for x = 0.05. More information on propagation vectors can be found in the text.*

The positions of magnetic peaks observed for $x = 0.20$ at 4 K are the same as for the parent compound and the previously discussed $x = 0.05$. Albeit the magnetic structure is similar, the magnitude of magnetic moments is altered, as can be seen from a pronounced difference in the intensity of the magnetic peaks presented in Figure 7.12a. According to the refinement of the NPD data collected at 4 K, with a propagation vector $\mathbf{k} = (½,½,0)$ the AFM moment reduces further to $\mu_1 = 0.64(7)\ \mu_B$/Mn, and the FM moment decreases to $\mu_2 = 1.5(2)\ \mu_B$/Mn. An increase in intensity of the (100) peak suggests the presence of an additional FM moment, as highlighted by the insert in Figure 7.12a. With a use of a propagation vector $\mathbf{k} = (0,0,0)$, a weak FM moment has been found with $\mu_3 = 0.4(1)\ \mu_B$/Mn on three Mn atoms. Therefore, from the NPD measurements a total magnetic moment of $4.0(2)\ \mu_B$/f.u. was obtained, which is slightly lower than the $\mu_{eff} = 4.4\ \mu_B$/f.u. derived from the Curie-Weiss fit. It should be noted that the presence of a negative contribution to the Curie-Weiss fit results in a deviation from the linear trend, which might lead to a slight discrepancy between the obtained values. The cusp-like feature in magnetization for $x = 0.20$ measured at 0.01 T corresponds to the Néel temperature ($T_N \approx 200$ K). Above T_N, only an increase in intensity of the nuclear peaks is seen, which indicates the presence of ferromagnetic order corresponding to the propagation vector $\mathbf{k} = (0,0,0)$. The refinement of the NPD data at 230 K revealed the presence of a FM moment of $\mu_3 = 0.5(2)\ \mu_B$/Mn on three Mn atoms. As suggested by Iikubo and co-workers, the MVE is intimately correlated with the antiferromagnetic structure with $\mathbf{k} = (½,½,0)$, in which two atoms in the *a-b* plane possess a canted AFM magnetic moment and one atom orders FM along the *c*-axis [43]. The MVE is still present in the $x = 0.05$ sample, for which the propagation vector $\mathbf{k} = (½,½,0)$ was found, but it is completely quenched for $x = 0.20$. Where for $x = 0.05$, the FM and AFM sublattices coexist up to T_C at 268 K, for $x = 0.20$, the FiM-FM transition is followed by a FM-PM transition with $T_C = 256$ K. The presence of the intermediate FM ordered state explains the quenching of the MVE.

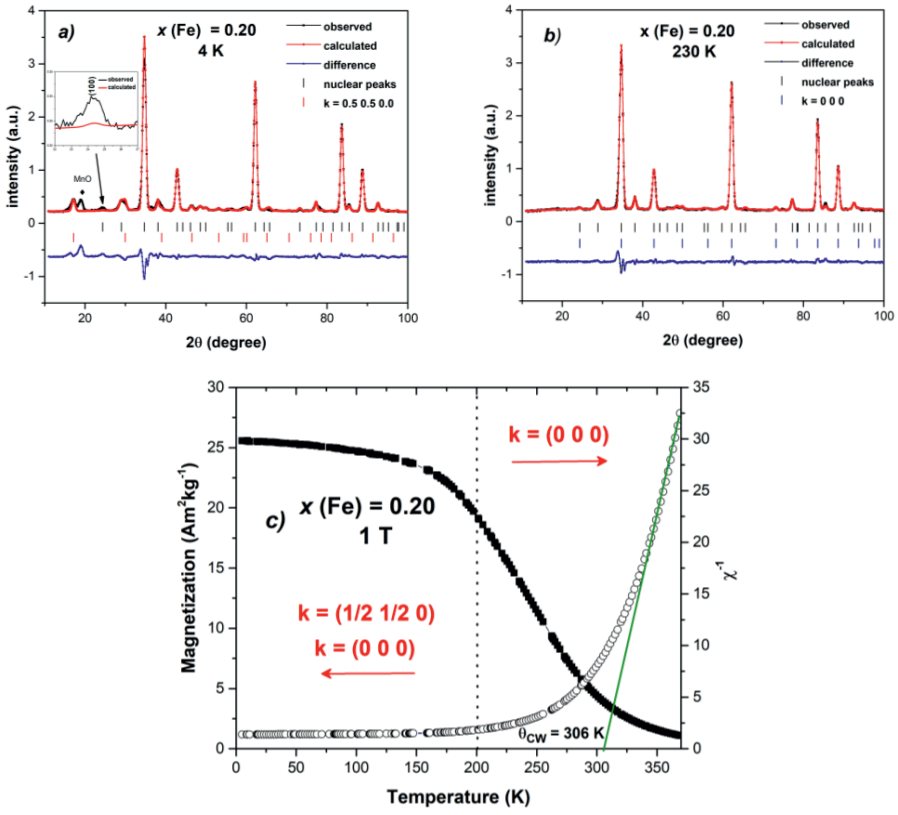

Figure 7.12: *a) Neutron diffraction pattern of $Mn_3Sn_{1-x}Fe_xC$ for x (Fe) = 0.20 at 4 K with a fit of the nuclear and the magnetic structure with k = (½,½,0), b) Neutron diffraction pattern for x (Fe) = 0.20 at 230 K with a fit of the nuclear and the magnetic structure with k = (0,0,0), c) Temperature dependence of the magnetization and the inverse susceptibility for x = 0.20. More information on propagation vectors can be found in the text.*

From the difference between the PM state (550 K) and ordered state (80 K) for $x = 0.30$ an increase in the intensity of the nuclear peaks can be seen, which is particularly pronounced for the (100) peak, as depicted in Figure **7.13a**. The peaks with marked indices refer to the main phase and the unmarked peaks belong to the nuclear structure of the impurity phases, as they remain unaltered in the ordered and PM state. An increase in the intensity for the nuclear peaks implies the presence of a FM state, as also concluded from the magnetization measurements described in section 7.4. With a propagation vector **k** = (0,0,0), a FM moment of $\mu = 1.2(3)\ \mu_B$/Mn has been found on three Mn atoms. The total magnetic moment of 3.6(5) μ_B/f.u., obtained from the refinement of the NPD data at 4 K, is in fair agreement with the calculated value of the effective moment $\mu_{eff} = 3.2\ \mu_B$/f.u from the Curie-Weiss fit.

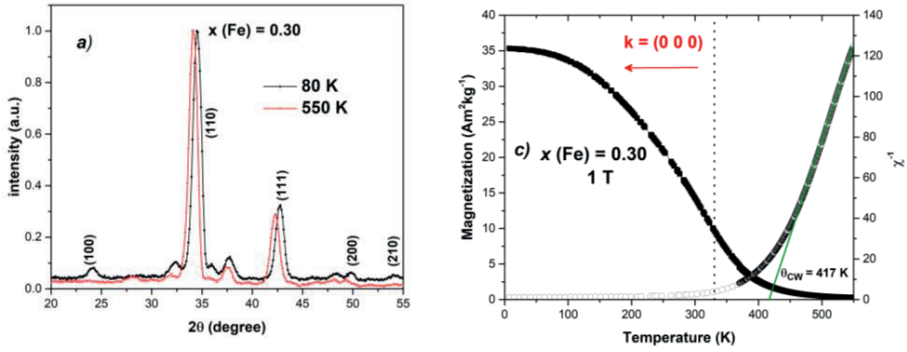

Figure 7.13: *a) NPD patterns of $Mn_3Sn_{1-x}Fe_xC$ for x (Fe) = 0.30 in the PM (550 K) and ordered (80 K) state, b) Temperature dependence of the magnetization and the inverse susceptibility for x = 0.30.*

7.7. Conclusions

The (micro)structural, magnetic and magnetocaloric properties of antiperovskite carbides $Mn_3Sn_{1-x}Fe_xC$ ($0.0 < x \leq 0.35$) have been studied using experimental methods and DFT calculations. All the prepared compounds crystallize in the cubic structure. Upon Fe doping, an initial decrease in T_C is observed, which is followed by an increase for $x > 0.15$. Although a linear increase in T_C is accompanied by a rise in magnetization, the magnetic moment appears to saturate for $x = 0.30$ and decrease for higher doping content, as also supported by DFT calculations. A weakening of the magnetovolume effect (MVE) upon doping is correlated with changes in T_C and the evolution of the magnetic structure. In the $Mn_3Sn_{1-x}Fe_xC$ system, Fe doping simultaneously enhances the FM moment and weakens the AFM contribution. The $x = 0.05$ compound can be described using a propagation vector $\mathbf{k} = (½,½,0)$, like the parent compound. However, a decrease in the AFM moment and an increase in the FM can be seen. In the compound of $x = 0.20$, a FiM-FM transition is followed by a FM-PM transition as clarified using neutron powder diffraction (NPD). Below T_N the magnetic structure can be fitted using two propagation vectors $\mathbf{k} = (½,½,0)$ and $\mathbf{k} = (0,0,0)$ and from T_N to T_C the magnetic structure is described with $\mathbf{k} = (0,0,0)$, indicating the presence of pure ferromagnetic order. For $x = 0.30$, the magnetic structure is fitted using propagation vector $\mathbf{k} = (0,0,0)$, which indicates that the compound undergoes a FM-PM transition.

References

[1] E. O. Chi, W. S. Kim, and N. H. Hur, "Nearly zero temperature coefficient of resistivity in antiperovskite compound $CuNMn_3$", *Solid State Commun.*, *120*(7-8), pp. 307–310, 2001, doi: 10.1016/S0038-1098(01)00395-7.

[2] Y. B. Li, W. F. Li, W. J. Feng, Y. Q. Zhang, and Z. D. Zhang, "Magnetic, transport and magnetotransport properties of $Mn_{3+x}Sn_{1-x}C$ and $Mn_3Zn_ySn_{1-y}C$ compounds", *Phys. Rev. B - Condens. Matter Mater. Phys.*, *72*(2), pp. 1–8, 2005, doi: 10.1103/PhysRevB.72.024411.

[3] L. Pal, K. G. Suresh, and A. K. Nigam, "Effect of Mn substitution on the magnetic and magneto-transport properties of $Fe_{3-x}Mn_xSi$ ($0 \leq x \leq 1.25$) alloys", *J. Appl. Phys.*, *113*(9), pp. 0–7, 2013, doi: 10.1063/1.4794126.

[4] X. H. Zhang, Y. Yin, Q. Yuan, J. C. Han, Z. H. Zhang, J. K. Jian, J. G. Zhao, and B. Song, "Magnetoresistance reversal in antiperovskite compound $Mn_3Cu_{0.5}Zn_{0.5}N$", *J. Appl. Phys.*, *115*, p. 123905, 2014, doi: 10.1063/1.4869797.

[5] K. Takenaka and H. Takagi, "Giant Negative Thermal Expansion in Ge-Doped Anti-Perovskite Manganese Nitrides", *Appl. Phys. Lett.*, *87*, p. 261902, 2005, doi: 10.1063/1.2147726.

[6] T. Hamada and K. Takenaka, "Giant negative thermal expansion in antiperovskite manganese nitrides", *J. Appl. Phys.*, *109*, 2011, doi: 10.1063/1.3540604.

[7] S. Deng, Y. Sun, H. Wu, Q. Huang, J. Yan, K. Shi, M.I. Malik, H. Lu, L. Wang, R. Huang, L. Li, and C. Wang, "Invar-like behavior of antiperovskite $Mn_{3+x}Ni_{1-x}N$ compounds," *Chem. Mater.*, *27*(7), pp. 2495–2501, 2015, doi: 10.1021/cm504702m.

[8] K. Takenaka, M. Ichigo, T. Hamada, A. Ozawa, T. Shibayama, T. Inagaki, and K. Asano, "Magnetovolume effects in manganese nitrides with antiperovskite structure Magnetovolume effects in manganese nitrides with antiperovskite structure", *Sci. Technol. Adv.*, *15*(1), 2014, doi: 10.1088/1468-6996/15/1/015009.

[9] J. Zemen, Z. Gercsi, and K. Sandeman, "Piezomagnetism as a counterpart of the magnetovolume effect in magnetically frustrated Mn-based antiperovskite nitrides", *Phys. Rev. B*, *96*, 2017, doi: 10.1103/PhysRevB.96.024451.

[10] P. Lukashev, R. F. Sabirianov, and K. Belashchenko, "Theory of the piezomagnetic effect in Mn-based antiperovskites", *Phys. Rev. B Condens. Matter Mater. Phys.*, *78*(18), 2008, doi: 10.1103/PhysRevB.78.184414.

[11] T. Tohei, H. Wada, and T. Kanomata, "Negative magnetocaloric effect at the antiferromagnetic to ferromagnetic transition of Mn_3GaC", *J. Appl. Phys.*, *94*(3), pp. 1800–1802, 2003, doi: 10.1063/1.1587265.

[12] O. Tegus, G.X. Lin, W. Dagula, B. Fuquan, L. Zhang, E. Brück, F.R. de Boer, and K.H.J. Buschow, "A model description of the first-order phase transition in $MnFeP_{1-x}As_x$", *J. Magn. Magn. Mater.*, *290-291*, pp. 658–660, 2005, doi: 10.1016/j.jmmm.2004.11.325.

[13] D. Boldrin, E. Mendive-Tapia, J. Zemen, J. B. Staunton, T. Hansen, A. Aznar, J.-L. Tamarit, M. Barrio, P. Lloveras, J. Kim, X. Moya, and L. F. Cohen, "Multisite Exchange-Enhanced Barocaloric Response in Mn_3NiN", *Phys. Rev. X*, *8*(4), pp. 1–9, 2018, doi: 10.1103/PhysRevX.8.041035.

[14] B. S. Wang, P. Tong, Y. P. Sun, X. Luo, X. B. Zhu, G. Li, X. D. Zhu, S. B. Zhang, Z. R. Yang, W. H. Song, and J. M. Dai, "Large magnetic entropy change near room

temperature in antiperovskite $SnCMn_3$", *Europhys. Lett.*, *85*, 2009, doi: 10.1209/0295-5075/85/47004.

[15] V. N. Gaonkar, E. T. Dias, M. N. Vedpathak, and K. R. Priolkar, "Packing fraction induced phase separation in A-site doped antiperovskites", *Mater. Today Commun.*, *33*, p. 104459, 2022, doi: 10.1016/j.mtcomm.2022.104459.

[16] D. Huang and J. Gao, "Effects of Ge substitution for Sn on the crystal structure, magnetization, and the magnetocaloric effect of Mn_3SnC", *J. Magn. Magn. Mater.*, *537*, p. 168163, 2021, doi: 10.1016/j.jmmm.2021.168163.

[17] Y. Wen, C. Wang, M. Nie, and Y. Sun, "The magnetism and electronic transport properties of $Mn_3Sn_{1-x}Si_xC$", *J. Magn. Magn. Mater.*, *391*, pp. 22–25, 2015, doi: 10.1016/j.jmmm.2015.04.111.

[18] E. T. Dias, K. R. Priolkar, A. Das, G. Aquilanti, Ö. Çakir, M. Acet, and A. K. Nigam, "Effect of local structural distortions on magnetostructural transformation in Mn_3SnC", *J. Phys. D. Appl. Phys.*, *48*, no. 29, 2015, doi: 10.1088/0022-3727/48/29/295001.

[19] V. N. Gaonkar, E. T. Dias, A. Das, A. K. Nigam, and K. R. Priolkar, "Modulations in magnetostructural coupling in C and Sn deficient Mn_3SnC", *J. Magn. Magn. Mater.*, *488*, 2019, doi: 10.1016/j.jmmm.2019.165357.

[20] V. N. Gaonkar, E. T. Dias, A. K. Nigam, and K. R. Priolkar, "d band filling and magnetic phase separation in transition metal-doped Mn_3SnC", *J. Alloys Compd.*, *829*, 2020, doi: 10.1016/j.jallcom.2020.154548.

[21] Çaklr, F. Cugini, M. Solzi, K. Priolkar, M. Acet, and M. Farle, "Dynamics of nonergodic ferromagnetic/antiferromagnetic ordering and magnetocalorics in antiperovskite Mn_3SnC", *Phys. Rev. B*, *96*(1), pp. 1–6, 2017, doi: 10.1103/PhysRevB.96.014436.

[22] Çakir, M. Acet, M. Farle, and A. Senyshyn, "Neutron diffraction study of the magnetic-field-induced transition in Mn_3GaC," *J. Appl. Phys.*, *115*(4), pp. 1–5, 2014, doi: 10.1063/1.4862903.

[23] L. H. Lewis, D. Yoder, A. R. Moodenbaugh, D. A. Fischer, and M.-H. Yu, "Magnetism and the defect state in the magnetocaloric antiperovskite $Mn_3GaC_{1-\delta}$," *J. Phys. Condens. Matter*, *18*(5), pp. 1677–1686, 2006, doi: 10.1088/0953-8984/18/5/020.

[24] E. T. Dias, K. R. Priolkar, A. Das, G. Aquilanti, Ö. Çakir, M. Acet, and A. K. Nigam, "Effect of local structural distortions on magnetostructural transformation in Mn_3SnC", *J. Phys. D. Appl. Phys.*, *48*(29), 2015, doi: 10.1088/0022-3727/48/29/295001.

[25] J. Yan, Y. Sun, Y. Wen, L. Chu, M. Wu, Q. Huang, C. Wang, J. W. Lynn, and Y. Chen, "Relationship between spin ordering, entropy, and anomalous lattice variation in $Mn_3Sn_{1-\epsilon}Si\epsilon C_{1-\delta}$ compounds", *Inorg. Chem.*, *53*(4), pp. 2317–2324, 2014, doi: 10.1021/ic403063t.

[26] M. Nie, C. Wang, Y. Wen, Y. Sun, Y. Na, L. Chu, and M. Tang, "Magnetic phase transitions of antiperovskite $Mn_{3-x}Fe_xSnC$ ($0.5 \leq x \leq 1.3$)", *Solid State Commun.*, *151*(5), pp. 377–381, 2011, doi: 10.1016/j.ssc.2010.12.015.

[27] H. M. Rietveld, "A profile refinement method for nuclear and magnetic structures", *J. Appl. Crystallogr.*, *2*(2), pp. 65–71, 1969, doi: 10.1107/s0021889869006558.

[28] J. Rodríguez-Carvajal, "Recent advances in magnetic structure determination by neutron powder diffraction", *Phys. B Phys. Condens. Matter*, *192*(1-2), 1993, doi: 10.1016/0921-4526(93)90108-I.

[29] G. Kresse and J. Furthmüller, "Efficiency of ab-initio total energy calculations for metals and semiconductors using a plane-wave basis set", *Comput. Mater. Sci.*, *6*(1), pp. 15–50, 1996, doi: 10.1016/0927-0256(96)00008-0.

[30] G. Kresse and J. Hafner, "Ab Initio Molecular Dynamics for Liquid Metals", *Phys. Rev. B. Condens. Matter*, *47*, pp. 558–561, 1993, doi: 10.1103/PhysRevB.47.558.

[31] P. E. Blöchl, "Projector augmented-wave method," *Phys. Rev. B*, *50*(24), pp. 17953–17979, 1994, doi: 10.1103/PhysRevB.50.17953.

[32] G. Kresse and D. Joubert, "From ultrasoft pseudopotentials to the projector augmented-wave method", *Phys. Rev. B*, *59*(3), pp. 1758–1775, 1999, doi: 10.1103/PhysRevB.59.1758.

[33] M. Methfessel and A. T. Paxton, "High-precision sampling for Brillouin-zone integration in metals," *Phys. Rev. B*, *40*(6), pp. 3616–3621, 1989, doi: 10.1103/PhysRevB.40.3616.

[34] R. de Oro Calderon, C. Gierl-Mayer, and H. Danninger, "Fundamentals of Sintering: Liquid Phase Sintering," *Encycl. Mater. Met. Alloy.*, pp. 481–492, 2022, doi: 10.1016/B978-0-12-819726-4.00127-7.

[35] J. B. Goodenough, "Theory of the role of covalence in the perovskite-type manganites [La,M(II)]MnO_3," *Phys. Rev.*, *100*(2), pp. 564–573, 1955, doi: 10.1103/PhysRev.100.564.

[36] B. S. Wang, W. J. Lu, S. Lin, J. C. Lin, P. Tong, B. C. Zhao, W. H. Song, and Y. P. Sun, "Magnetic / structural diagram , chemical composition-dependent magnetocaloric effect in self-doped antipervoskite compounds $Sn_{1-x}CMn_{3+x}$ ($0 \leq x \leq 0.40$)", *J. Magn. Magn. Mater.*, *324*, pp. 773–781, 2012, doi: 10.1016/j.jmmm.2011.09.014.

[37] E. T. Dias, K. R. Priolkar, and A. K. Nigam, , "Co-existence of ferromagnetic and antiferromagnetic interactions in $Mn_3Ga_{1-x}Sn_xC$", Mater. Res. Express, *1*(2), pp. 026106, 2014, doi: 10.1088/2053-1591/1/2/026106.

[38] A. Kiecana, W. Schaefers, M. Thijs, R. Dankelman, H. Ojiyed, I. Batashev, F. Zhang, N. H. van Dijk, E, Brück, "Competing magnetic interactions, structure and magnetocaloric effect in $Mn_3Sn_{1-x}Zn_xC$ antiperovskite carbides", submitted to *J. Magn. Magn. Mater.* 2023 (accepted).

[39] B. S. Wang, P. Tong, Y. P. Sun, X. Luo, X. B. Zhu, G. Li, X. D. Zhu, S. B. Zhang, Z. R. Yang, W. H. Song, and J. M. Dai, "Large magnetic entropy change near room temperature in antiperovskite $SnCMn_3$", *Europhys. Lett.*, *85*, 2009, doi: 10.1209/0295-5075/85/47004.

[40] D. Huang and J. Gao, "Effects of Ge substitution for Sn on the crystal structure, magnetization, and the magnetocaloric effect of Mn_3SnC", *J. Magn. Magn. Mater.*, *537*, p. 168163, 2021, doi: 10.1016/j.jmmm.2021.168163.

[41] N. Sun, Y. Li, F. Liu, and T. Ji, "Magnetism and Magnetocaloric Properties of $Mn_3Zn_{1-x}Sn_xC$ and $Mn_{3-x}Cr_xZnC$ Compounds," *J. Mater. Sci. Technol.*, *28*(10), pp. 941–945, 2012, doi: 10.1016/S1005-0302(12)60155-8.

[42] P. Liu, J. Peng, M. Xue, and B. Wang, "Magnetocaloric effect and critical behavior of the Mn-rich itinerant material Mn_3GaC with enhanced ferromagnetic interaction," *Chinese Phys. B*, *29*(4), 2020, doi: 10.1088/1674-1056/ab7da1.

[43] S. Iikubo, K. Kodama, K. Takenaka, H. Takagi, and S. Shamoto, "Magnetovolume effect in $Mn_3Cu_{1-x}Ge_xN$ related to the magnetic structure: Neutron powder diffraction measurements," *Phys. Rev. B - Condens. Matter Mater. Phys.*, *77*(2), pp. 3–6, 2008, doi: 10.1103/PhysRevB.77.020409.

8

Magnetism, structure and magnetocaloric properties in half-Heusler $(MnNiSi)_{1-x}(CrCoGe)_x$ alloys

Abstract

The influence of isostructural substitution of Ni_2In-type CrCoGe for MnNiSi was studied using experimental techniques and DFT calculations. While the ferromagnetic (FM) to paramagnetic (PM) transition is reduced from 624 to 205 K, the structural transition from the high-temperature hexagonal austenite phase to the low-temperature martensite phase (orthorhombic) decreases from 1220 to 885 K, for a doping content of $x = 0.5$. Upon increasing the CrCoGe content, a weakening of the first-order structural transition can be seen, which enhances the mechanical stability of $(MnNiSi)_{1-x}(CrCoGe)_x$ alloys. The magnetic transition remains second-order (SOMT), which yields a maximum magnetic entropy change ($-\Delta S_m$) of 2.4 $Jkg^{-1}K^{-1}$ in a magnetic field change of 2 T for $x = 0.1$. In alloys with a higher doping content ($x > 0.3$), the formation of a low-temperature ferrimagnetic (FiM) order can be seen.

8.1. Introduction

Special attention has recently been paid to the Mn*AX* intermetallic compound (*A*: Ni, Co, *X*: Si, Ge) due to the possibility to obtain a large magnetocaloric effect (MCE) at room temperature originating from the coupling between the magnetic and structural transitions. A large magnetic entropy change ($|\Delta S_m|$) can be observed when the magnetostructural coupling is associated with a large magnetization difference between two phases. A reduction in the structural and magnetic transition temperature has been achieved by the application of pressure [1], [2], chemical substitution [3]–[6], isostructural alloying [7], off-stoichiometry [8] and heat treatment [9], [10].

Among various half-Heusler alloys, much research has been focussed on MnCoGe due to an easily obtained magnetostrucural coupling at room temperature and promising magnetic properties [11]–[13]. The substitution of Cr for Mn in the MnCoGe system was studied in detail by Trung and co-workers [13]. With increasing Cr content, a substantial decrease in transition temperature and a magnetostructural coupling in the temperature range of 322 - 237 K yielding a large MCE, has been observed. On the other hand, the MnNiSi system is significantly less studied due to its high Curie temperature ($T_C \approx 622$ K) and martensitic transformation temperature ($T_{STR} \approx 1210$ K), which is an obstacle to achieve the magnetostructural coupling at room temperature. A sufficient reduction of T_C and T_{STR} has not yet been obtained by doping with a single element. Until now, various approaches utilizing the simultaneous substitution of a metal and a metalloid have been studied with the use of FeGe [14], Co_2Ge [4], Fe_2Ge [9], [15], FeCoGe [2], [16], FeNiGa [17] alloying. It is worth to note that MnNiSi-based alloys consist of abundant, affordable and nontoxic elements, which is promising for practical applications of these compounds.

The structural transition from the low-temperature orthorhombic MnNiSi phase (TiNiSi-type, space group: *Pnma*, 62), to the high-temperature hexagonal phase (Ni_2In-type, space group: $P6_3/mmc$, 194) is of first-order which results in a drastic change in lattice parameters and volume at the transition ($\Delta V/V \approx 3 - 4\%$). A large volume change during a structural transition leads to high stress and a gradual collapse of the compound into powder, which impedes its potential application. Endeavours to enhance the mechanical strength have been made using epoxy resins [18] and by optimization of the sample preparation using a two-step process [10]. Alloying of MnNiSi with CrCoGe ($P6_3/mmc$, 194) can reduce T_{STR} and stabilize the hexagonal phase at lower temperatures due to crystallographic similarities of the two phases. Therefore, in this work, we present a study on magnetism and structure of $(MnNiSi)_{1-x}(CrCoGe)_x$ alloys.

8.2. Experimental methods

Polycrystalline $(MnNiSi)_{1-x}(CrCoGe)_x$ ($0.0 \leq x \leq 0.5$) compounds were produced by arc melting of raw starting materials: Mn (99.7%), Ni (99.9%), Si (99.9%), Cr (99.7%), Co (99.9%) and Ge (99.9%) in an Ar atmosphere. To compensate for Mn losses, 3% extra Mn

was added. The ingot was flipped and re-melted five times to ensure the homogeneity of the alloy. As obtained compounds were sealed in quartz tubes in Ar atmosphere (200 mbar), annealed at 750 K for 120 h and finally quenched into cold water.

The X-ray diffraction patterns were collected using a PANalytical X-pert Pro diffractometer with Cu-K_α radiation (λ = 1.54 Å). The lattice parameters and phase fractions were derived utilizing Rietveld refinement implemented in the Fullprof software. The magnetization data were collected using superconducting quantum interference devices (SQUID) MPMS-XL and MPMS-5S, in the reciprocating sample option (RSO) mode. The measurements using SQUID instruments were performed in the temperature range of 5-370 K with a constant sweep rate of 2 K/min and in applied magnetic fields up to 5 T. The magnetization measurements at higher temperatures (370 – 650 K) were performed using a Vibrating Sample Magnetometer (VSM) implemented in the Quantum Design VersaLab. The differential scanning calorimetry (DSC) measurements were carried out using a TA-Q2000 DSC with a constant sweep rate of 10 K/ min. To measure the structural transition temperature, high temperature DSC measurements were performed in collaboration with Reactor Physics and Nuclear Materials group employing TGA-DSC module implemented in the Seteram 96 line calorimeter, in the temperature range 300 – 1400 K with a sweep rate of 10 K/min. Scanning electron microscopy (SEM, JEOL JSM 6500 F, Japan) coupled with energy-disperse X-ray spectroscopy (EDS) was used to study the homogeneity and composition of selected compounds. The specimens were embedded in conductive resin, sanded and subsequently polished with a diamond paste.

The preferred site occupancy of Cr, Co and Ge in the orthorhombic MnNiSi structure has been computed in the framework of density functional theory (DFT) using the Vienna Ab Initio simulation package (VASP). The generalized gradient approximation of Perdew-Burke-Ernzerhof (PBE) was utilized for the exchange correlation functional, which is based on the projected augmented wave method (PAW). The **k**-space integrations were performed with a smearing width of 0.8 meV using the Methfessel-Paxton method. A force convergence of 0.1 meV/Å was used for relaxation of lattice parameters and atomic positions. The energies were converged to 1 μeV for a unit cell consisting of 16 atoms. The cut-off energy of 370 eV and a **k**-grid of 8×10×6 was used for relaxation of structural degrees of freedom.

8.3. Structural and microstructural analysis

X-ray diffraction patterns of $(MnNiSi)_{1-x}(CrCoGe)_x$ (x = 0.0, 0.1, 0.2, 0.3, 0.4, 0.5) are shown in Figure 8.1a. From the patterns measured at room temperature, it can be seen that all these compounds crystallize in the orthorhombic phase (space group: *Pnma*, 62) with minor amounts of impurities: MnNiSi - $MnZn_2$ type (space group: *P6₃/mmc*, 194) and Cr_3Si (space group: *Pm-3n*, 223). While a small fraction of the MnNiSi impurity phase (≈ 1-2%) is composition independent, the Cr_3Si impurity phase (≈ 3%) forms for $x > 0.3$. The purity of the obtained alloys is close to 95 wt.% in each case. The hexagonal counterpart of the orthorhombic structure – MnNiSi - Ni_2In type (space group: *P6₃/mmc*, 194), is not observed

in the prepared compounds, which indicates that the structural transition occurs at much higher temperatures and that the magnetostructural coupling is not achieved in the studied system. The refinement of $x = 0.1$ is presented in Figure **8.1b**. It can be seen in Figure **8.2a** that the unit-cell volume constantly increases with increasing CrCoGe content, which is ascribed to an increase in the lattice parameters b and c, as shown in Figure **8.2b**. A slight off-linear dependence of the unit-cell volume can be observed for $x > 0.3$, which results from the formation of a Cr_3Si impurity phase for higher doping content. It can be seen that the lattice parameter a is hardly altered upon doping. The lattice parameters of the hexagonal and orthorhombic phases are linked by the following relations: $a_{ortho} = c_{hex}$, $b_{ortho} = a_{hex}$, $c_{ortho} = \sqrt{3}a_{hex}$. A reduction in a_{ortho}/b_{ortho} from 1.6345(4) for $x = 0.0$ to 1.5807(1) for $x = 0.5$, as seen in Figure **8.2b**, distorts the orthorhombic structure and indicates the stabilization of the hexagonal structure at lower temperatures, which also implies a decrease in the structural transition upon increasing CrCoGe doping. The lattice parameters, the a/b ratio and the volume (V) of $(MnNiSi)_{1-x}(CrCoGe)_x$ alloys are summarized in **Table 8.1**.

The stoichiometry of the prepared compounds was confirmed using SEM/EDS analysis for $x = 0.1$, 0.2 and 0.4. The homogeneity of $x = 0.1$ and 0.2 is confirmed by SEM/BSE analysis. The micrographs of selected alloys are presented in Figure **8.3a** and Figure **8.3b**. The presence of an additional phase can be observed for $x = 0.4$, which is seen as micro-sized inclusions marked by arrows in Figure **8.3c**. According to EDS measurements, the impurity is mainly Cr and Si-rich ($Mn_{11.9}Ni_{10.3}Si_{17.9}Cr_{43.8}Co_{8.7}Ge_{7.4}$). The composition and the metal to non-metal ratio found for the secondary phase (≈ 2.95) corresponds to Cr_3Si observed in the refinement of the XRD data. The inserts in Figure **8.3a** and Figure **8.3b** show SEM micrographs at a lower magnification to compare the surface morphology. It is noticeable that the mechanical strength of prepared compounds is enhanced upon doping, as concluded from the decreasing number of micro-cracks. In the alloy of $x = 0.4$, micro-cracks are hardly present, which reveals a significant improvement of the mechanical properties. The compositions obtained using EDS are presented in Table **8.2**.

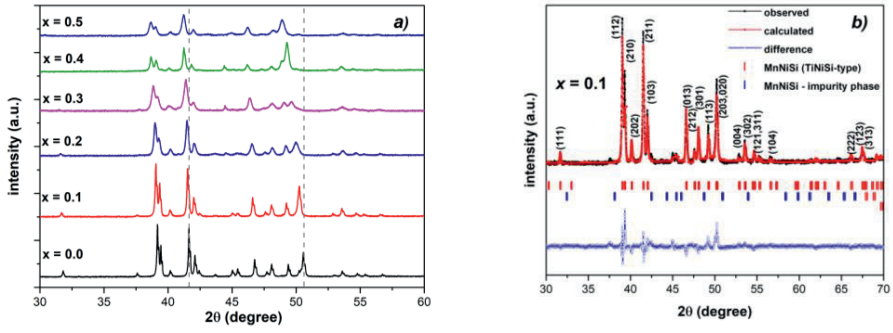

Figure 8.1: *a) Stacked XRD patterns for the $(MnNiSi)_{1-x}(CrCoGe)_x$ compounds measured at 298 K (x = 0.0, 0.1, 0.2, 0.3, 0.4, 0.5). b) Rietveld refinement of the data measured at 298 K for x = 0.1 (orthorhombic phase).*

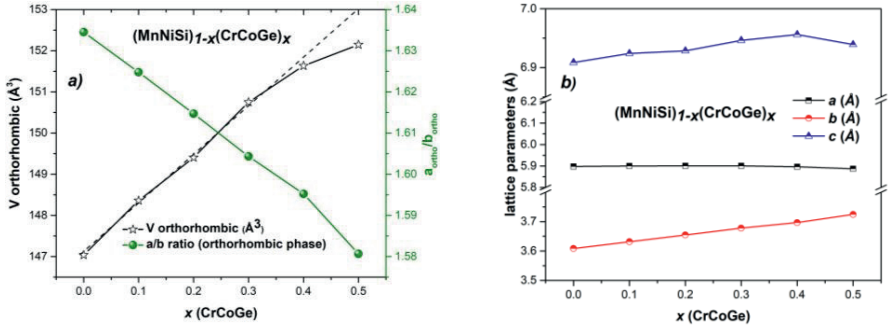

Figure 8.2: *a) The unit cell volume and a/b ratio, and b) The lattice parameters a, b and c in the orthorhombic $(MnNiSi)_{1-x}(CrCoGe)_x$ system.*

Table 8.1: *Lattice parameters a, b, c, the unit-cell volume V and the a/b ratio for the orthorhombic phase of $(MnNiSi)_{1-x}(CrCoGe)_x$ derived at 298 K.*

(*x*)	a_{ortho} (Å)	b_{ortho} (Å)	c_{ortho} (Å)	*a/b ratio*	*V* (Å^3)
0.0	5.8981(3)	3.6084(2)	6.9085(2)	1.6345(4)	147.036(4)
0.1	5.9004(2)	3.6312(3)	6.9242(1)	1.6247(4)	148.357(2)
0.2	5.9009(1)	3.6544(4)	6.9282(8)	1.6147(4)	149.404(6)
0.3	5.9007(3)	3.6779(5)	6.9461(5)	1.6044(5)	150.748(3)
0.4	5.8969(3)	3.6966(3)	6.9560(4)	1.5952(4)	151.633(7)
0.5	5.8871(1)	3.7244(1)	6.9390(7)	1.5807(1)	152.153(9)

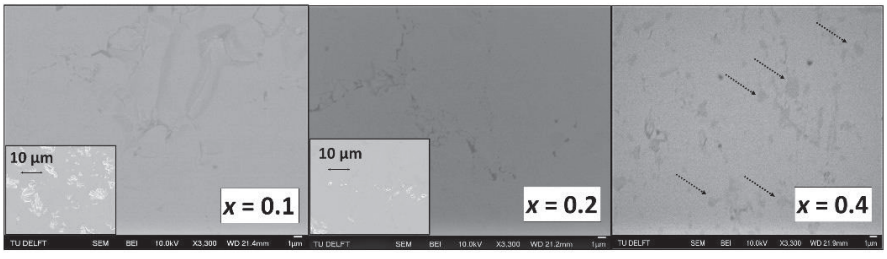

Figure 8.3: *SEM/BSE micrograph of $(MnNiSi)_{1-x}(CrCoGe)_x$ with x = 0.1, 0.2, 0.3. The inserts present SEM images for a lower magnification. The darker areas highlighted by arrows correspond to a Cr and Si-rich impurity phase.*

Table 8.2: *Compositions of the $(MnNiSi)_{1-x}(CrCoGe)_x$ compound with x = 0.1, 0.2, 0.4 obtained using EDS analysis.*

x	*Mn (at.%)*	*Ni (at.%)*	*Si (at.%)*	*Cr (at.%)*	*Co (at.%)*	*Ge (at.%)*
0.1	32.1(±2.5)	28.5(±0.8)	25.4(±0.7)	3.0(±0.7)	7.5(±1.2)	3.5(±0.2)
0.2	27.6(±1.8)	25.7(±0.6)	22.5(±0.6)	6.0(±0.8)	11.5(±1.1)	6.7(±0.3)
0.4	22.5(±1.2)	21.3(±0.4)	15.7(±0.3)	10.0(±0.8)	16.5(±0.7)	14.0(±0.2)

8.4. Magnetic properties

The temperature dependence of the magnetization measured at 1 T and in the temperature range of 5 – 650 K is shown in Figure **8.4**. Upon increasing the CrCoGe content, the Curie temperature (T_C) decreases steadily from 623.8 for x = 0.0 to 205 K for x = 0.5. The magnetic transition of the prepared compounds remains second order as highlighted by a non-hysteretic temperature dependence of the magnetization. A decrease in T_C is accompanied by a pronounced reduction in the magnetization from 97.3 to 36.0 Am^2kg^{-1} in an applied magnetic field of 5 T. In compounds of a higher doping content (x > 0.3), a cusp-like feature is observed in the *M-T* curves, which possibly indicates the presence of ferrimagnetic order (FiM) at low temperatures. This behaviour is also confirmed by a steadily increasing magnetization with applied magnetic field and an unsaturated value of the magnetization at 5 K at the maximum applied magnetic field of 5 T for x = 0.4 and x = 0.5, as displayed in Figure **8.5**. While T_C decreases steadily with increasing CrCoGe content, the transition temperature (T_T), corresponding to the cusp in magnetization curves, shifts to a higher temperature. A similar behaviour has been observed by Trung and co-workers in the $Mn_{1-x}Cr_xCoGe$ system [13].

The coexistence of two phases at the same temperature does not occur as the magnetostructural coupling is not attained for the selected doping contents. Therefore, the magnetic entropy change ($-\Delta S_m$) can be determined from the temperature-dependent magnetization curves at varying magnetic fields using the following relation:

$$\Delta S_m(T,H) = \int_{\mu_0 H_1}^{\mu_0 H_2} \left(\frac{\partial M(T)}{\partial T}\right)_H d(\mu_0 H) \tag{8.1}$$

The magnetic transition remains second order (SOMT), yielding a moderately large magnetic entropy change ($-\Delta S_m$) in a magnetic field change of 2 T, as shown in Figure **8.6a**. The magnetic entropy change was measured for x = 0.1 – 0.4 and the highest value of 2.4 $Jkg^{-1}K^{-1}$ was achieved for x = 0.1. Upon increasing doping contents, the magnetic entropy change decreases due to a gradual reduction in magnetization. For x = 0.4 the magnetic entropy change ($-\Delta S_m$) as a function of temperature is shown in Figure **8.6b**. The values of the Curie temperature (T_C), the structural transition temperature (T_{STR}) and magnetic entropy change ($-\Delta S_m$) are collected in Table **8.3**. Since the magnetic field tends to stabilize the phase of a

higher magnetic moment, a shift in T_C can be observed upon increasing the magnetic field. For the compound with a magnetic transition close to room temperature ($x = 0.4$), the rate of $\Delta T_C/\Delta\mu_0 H$ is about 2.8 K/T, which indicates a significant field dependence of the magnetic transition. However, the sensitivity of the transition to an applied magnetic field is lower compared to first-order magnetocaloric materials such as $Fe_{49}Rh_{51}$ (8.5 K/T) [19], $Gd_5Si_2Ge_2$ (4.9 K/T) [20], $LaFe_{11.6}Si_{1.4}$ (4.4 K/T) [21] and $MnFeP_{0.55}As_{0.55}$ (3.3 K/T) [22].

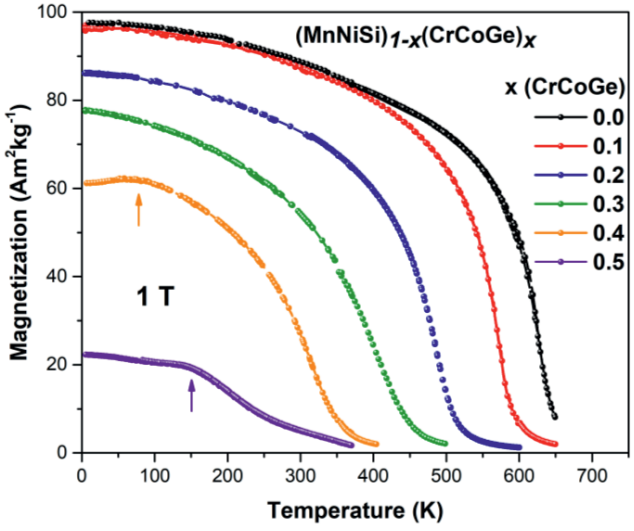

Figure 8.4: *Temperature dependence of the magnetization for $(MnNiSi)_{1-x}(CrCoGe)_x$ measured in a magnetic field of 1 T. The arrows point toward a cusp-like feature indicating the transition temperature (T_T) from the low-temperature FiM state to the FM state.*

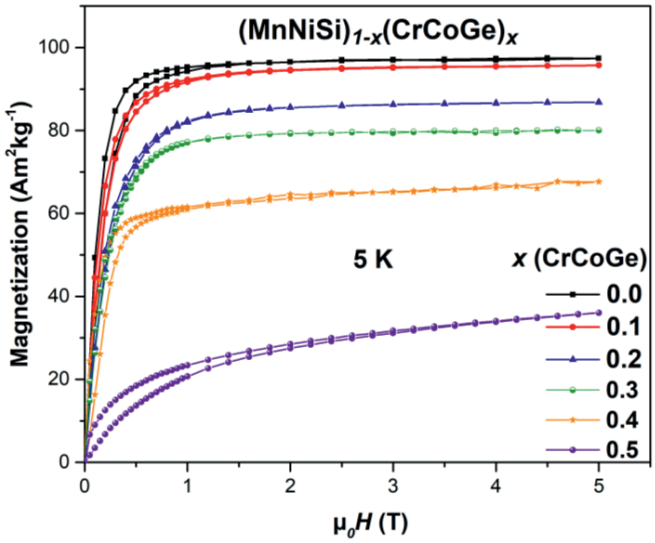

Figure 8.5: *Field dependence of the magnetization for $(MnNiSi)_{1-x}(CrCoGe)_x$ measured at 5 K and in applied magnetic fields up to 5 T.*

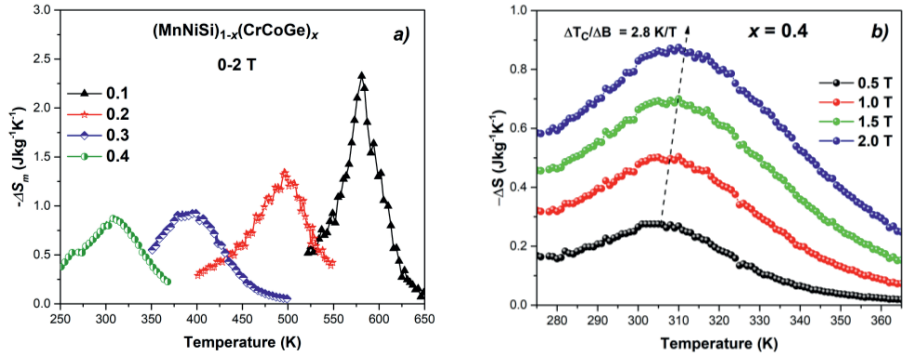

Figure 8.6: *a) Magnetic entropy change ($-\Delta S_m$) calculated for compounds x = 0.1 – 0.4. b) Magnetic entropy change ($-\Delta S_m$) around the transition temperature for x = 0.4.*

Table 8.3: *Collected values of T_C, T_{STR}, magnetic moment at 5 K in an applied magnetic field of 5 T, saturation magnetization at 5 T (M_S) and the magnetic entropy change ($-\Delta S_m$) for a magnetic field change of 2 T.*

x	T_C (K)	T_{STR} (K)	M_S (μ_B/f.u.)	$-\Delta S_m$ ($Jkg^{-1}K^{-1}$)
0.0	624	1220	2.47	-
0.1	555	1189	2.50	2.4
0.2	487	1135	2.33	1.3
0.3	378	1080	2.21	0.9
0.4	307	957	1.98	0.9
0.5	205	885	1.06	-

DFT calculations were performed for the $(MnNiSi)_{1-x}(CrCoGe)_x$ compounds to investigate the site preference of the dopant atoms. The formation energy (E_f) is calculated as a difference in energy between the doped and pure compounds, including the chemical potentials of the substituted and doping atoms. To calculate the formation energy, one atom of Mn, Ni and Si in the orthorhombic MnNiSi was subsequently substituted by one atom of Cr, Co and Ge. The obtained formation energies are presented in Table **8.4**. The lowest formation energy indicates the preferred substitution in the system. From the results presented, it is apparent that Cr substitutes Mn, Co preferentially occupies the Ni site and Ge has a strong preference for the Si site. The obtained results correspond to hexagonal and isostructural CrCoGe, in which the same site substitution is observed. In MnNiSi alloys, the magnetic moment originates mainly from the magnetic moment on the Mn site. The substitution of Ni for Co has been reported to maintain a large magnetization, despite of the decreasing Mn content [23]. However, the presence of Co atoms on the Mn site is crucial for keeping the strong FM coupling in the orthorhombic phase and maintaining a large value of the total magnetic moment [24]. Considering the diminishing amount of Mn and the substitution of Co for Ni, a decrease in saturation magnetization (M_S) is expected, which agrees with observed changes upon increasing CrCoGe content.

Table 8.4: *Formation energy (E_f) calculated per formula unit (eV/f.u.) for Cr, Co and Ge substitution.*

	E_f (Cr)	E_f (Co)	E_f (Ge)
Mn	-5.813	-5.909	-3.944
Ni	-4.753	-6.178	-3.560
Si	-3.667	-3.685	-10.924

8.5. Evolution of the structural transition

From the presented magnetization and XRD results, it is apparent that the structural transition is not sufficiently reduced to obtain a magnetostructural coupling. To reveal the impact of CrCoGe alloying on the martensitic structural transition, high temperature DSC measurements have been performed in the temperature range 300 – 1400 K. The DSC curves measured upon heating and cooling for the parent compound (MnNiSi) are depicted in Figure 8.7**.** From this graph, the magnetic transition (T_C), the structural transition (T_{STR}) and the melting point (T_{melt}) can be derived. While the magnetic transition (T_C = 624 K) is non-hysteretic, the structural transition is accompanied by a significant thermal hysteresis (ΔT_{hys} = 15 K) between the heating (1220 K) and cooling (1185 K) process, revealing its first-order nature. The structural transition is followed by the melting of the alloy at $T_{melt} \approx$ 1374 K. The presence of additional events upon cooling results most likely from the reaction between the molten alloy and the crucible. To minimize this undesirable effect, other samples (x = 0.1 – 0.5) were measured at temperatures below their melting points. The DSC curves upon heating are presented for all studied compounds in Figure **8.8a**. The observed endothermic peaks result from the heating process and indicate a transformation from the low-temperature orthorhombic (martensite) phase to a high-temperature hexagonal (austenite) phase. A decrease in the structural transition from 1220 to 885 K upon increasing doping contents can be seen, which agrees with a decline in the a_{ortho}/b_{ortho} ratio. Besides, for higher doping contents ($x > 0.1$), the peaks of the structural transition become lower and broader, indicating the weakening of the first-order structural transition. As a result, compounds of a higher doping content show an enhanced mechanical stability and do not collapse into powder at the structural transition. As shown in Figure **8.8b**, the rate of change of the structural and magnetic transitions are alike, excluding the possibility to attain the magnetostructural coupling within this system.

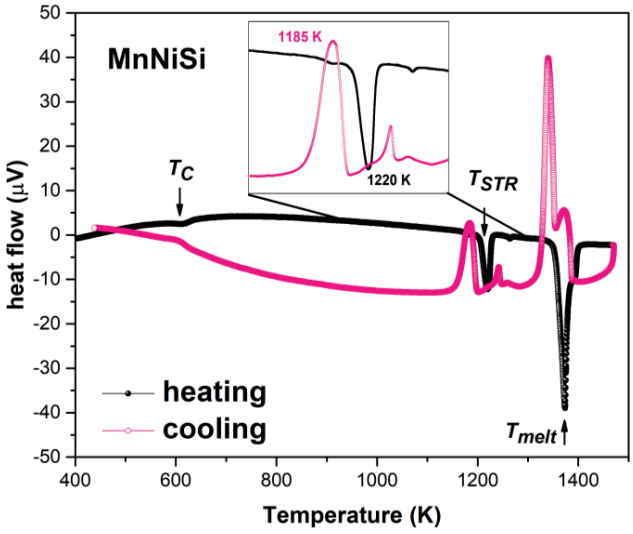

Figure 8.7: *DSC curves upon heating and cooling for the parent compound (MnNiSi) showing three events: magnetic transition (T_C), structural transition (T_{STR}) and melting point (T_{melt}).*

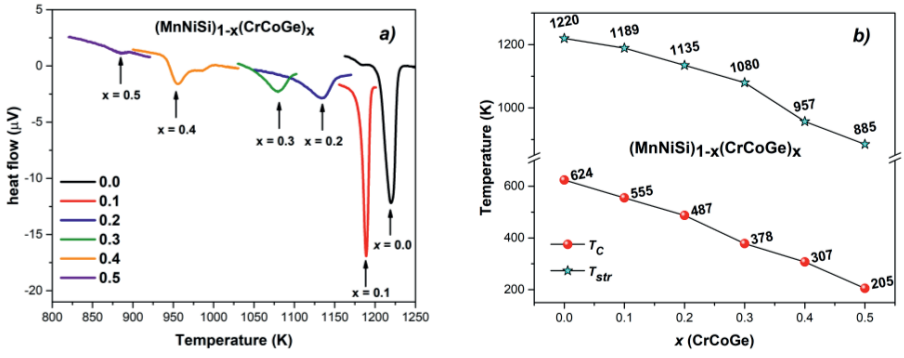

Figure 8.8: *a) Peaks of the structural transition in the for $(MnNiSi)_{1-x}(CrCoGe)_x$ measured using a high-temperature DSC, b) Evolution of the structural transition (T_{STR}) and the Curie temperature (T_C) upon doping.*

8.6. Conclusions

The structural, magnetic and magnetocaloric properties of the $(MnNiSi)_{1-x}(CrCoGe)_x$ system were studied. The simultaneous substitution of Cr for Mn, Co for Ni and Ge for Si results in a significant decrease in the Curie temperature (T_C) from 624 to 205 K and in the structural transition (T_{STR}) from 1220 to 885 K, for a change from $x = 0.0$ to $x = 0.5$, which agrees with a gradual decrease in the a_{ortho}/b_{ortho} ratio. Notwithstanding a notable change in T_C and T_{STR}, a magnetostructural coupling is not achieved in the studied system.

Consequently, the magnetic transition remains second order (SOMT), which yields a moderate magnetocaloric effect (MCE). As revealed by high-temperature DSC measurements, the CrCoGe alloying weakens the strength of the first-order structural transition, which enhances the mechanical stability. The compounds of a higher CrCoGe content ($x > 0.3$) exhibit a low-temperature ferrimagnetic (FiM) state with a transition temperature (T_T) from the Ferrimagnetic (FiM) to Paramagnetic (PM) state, which appears to increase with increasing doping content.

References

[1] T. Samanta, D. L. Lepkowski, A. U. Saleheen, A. Shankar, J. Prestigiacomo, I. Dubenko, A. Quetz, I. W. H. Oswald, G. T. McCandless, J. Y. Chan, P. W. Adams, D. P. Young, N. Ali, and S. Stadler, "Effects of hydrostatic pressure on magnetostructural transitions and magnetocaloric properties in $(MnNiSi)_{1-x}(FeCoGe)_x$", *J. Appl. Phys.*, *117*(12), 2015, doi: 10.1063/1.4916339.

[2] P. Lloveras, T. Samanta, M. Barrio, I. Dubenko, N. Ali, J.-L. Tamarit, and S. Stadler, "Giant reversible barocaloric response of $(MnNiSi)_{1-x}(FeCoGe)_x$ ($x = 0.39$, 0.40, 0.41)", *APL Mater.*, *7*(6), pp. 0–9, 2019, doi: 10.1063/1.5097959.

[3] L. M. Moreno-Ramírez, Díaz-García, J. Y. Law, A. K. Giri, and V. Franco, "Hysteresis, latent heat and cycling effects on the magnetocaloric response of $(NiMnSi)_{0.66}$ $(Fe_2Ge)_{0.34}$ alloy", *Intermetallics*, *131*, p. 107083, 2021, doi: 10.1016/j.intermet.2020.107083.

[4] C. L. Zhang, Y. G. Nie, H. F. Shi, E. J. Ye, J. Q. Zhao, Z. D. Han, H. C. Xuan, and D. H. Wang, "Tunable magnetostructural coupling and large magnetocaloric effect in $Mn_{1-x}Ni_{1-x}Fe_{2x}Si_{1-x}Ga_x$", *J. Magn. Magn. Mater.*, *432*, pp. 527–531, 2017, doi: 10.1016/j.jmmm.2017.02.046.

[5] Y. Li, Z. Y. Wei, W. K. Liu, G. D. Liu, S. G. Wang, W. H. Wang, and G. H. Wu, "Structural transitions, magnetic properties, and electronic structures of Co(Fe)-doped MnNiSi compounds", *J. Appl. Phys.*, *117*(17), 2015, doi: 10.1063/1.4916107.

[6] C. L. Zhang, D. H. Wang, Z. D. Han, B. Qian, H. F. Shi, C. Zhu, J. Chen, and T. Z. Wang, "The tunable magnetostructural transition in MnNiSi-FeNiGe system", *Appl. Phys. Lett.*, *103*(13), pp. 1–5, 2013, doi: 10.1063/1.4823510.

[7] J. Liu, Y. Gong, G. Xu, G. Peng, I. A. Shah, N. ul Hassen, and F. Xu, "Realization of magnetostructural coupling by modifying structural transitions in MnNiSi-CoNiGe system with a wide Curie-temperature window", *Sci. Rep.*, *6*(1), pp. 1–8, 2016, doi: 10.1038/srep23386.

[8] A. Ghosh, P. Sen, and K. Mandal, "Measurement protocol dependent magnetocaloric properties in a Si-doped Mn-rich Mn-Ni-Sn-Si off-stoichiometric Heusler alloy", *J. Appl. Phys.*, *119*, 2016, doi: 10.1063/1.4948962.

[9] J. H. Chen, A. Us Saleheen, S. K. Karna, D. P. Young, I. Dubenko, N. Ali, S. Stadler, "Tuning martensitic transitions in $(MnNiSi)_{0.65}(Fe_2Ge)_{0.35}$ through heat treatment

and hydrostatic pressure", *J. Appl. Phys.*, *124*(20), pp. 1–7, 2018, doi: 10.1063/1.5051551.

[10] H. Imam, H. G. Zhang, J. Chen, M. Yue, Q. M. Lu, D. T. Zhang, and W. Q. Liu, "Powdering and SPS sintering effect on the magnetocaloric properties of MnNiSi-based compounds", *AIP Adv.*, *9*(3), pp. 0–4, 2019, doi: 10.1063/1.5070084.

[11] X. Si, Y. Liu, Y. Shen, W. Yu, X. Ma, Z. Zhang, Y. Xu, and Y. Gao, "Critical behavior and magnetocaloric effect near room temperature in $MnCo_{1-x}Ti_xGe$ alloys", *Intermetallics*, *93*, pp. 30–39, 2018, doi: 10.1016/j.intermet.2017.11.001.

[12] P. E. Markin, N. V. Mushnikov, E. G. Gerasimov, A. V. Proshkin, and A. S. Volegov, "Magnetic and magnetocaloric properties of $(MnCo)_{1-x}Ge$ compounds", *Phys. Met. Metallogr.*, *114*(1), pp. 893–903, 2013, doi: 10.1134/S0031918X13110082.

[13] N. T. Trung, V. Biharie, L. Zhang, L. Caron, K. H. J. Buschow, and E. Brück, "From single- to double-first-order magnetic phase transition in magnetocaloric $Mn_{1-x}Cr_xCoGe$ compounds", *Appl. Phys. Lett.*, *96*(16), pp. 2010–2012, 2010, doi: 10.1063/1.3399774.

[14] D. Clifford, V. Sharma, K. Deepak, R. V. Ramanujan, and R. Barua, "Multicaloric Effects in $(MnNiSi)_{1-x}(FeGe)_x$ Alloys", *IEEE Trans. Magn.*, *57*(2), pp. 1–5, 2021, doi: 10.1109/TMAG.2020.3025002.

[15] K. Deepak and R. V. Ramanujan, "Near room temperature giant magnetocaloric effect in $(MnNiSi)_{1-x}(Fe_2Ge)_x$ alloys", *J. Alloys Compd.*, *743*, pp. 494–505, 2018, doi: 10.1016/j.jallcom.2018.02.018.

[16] J. H. Chen, T. Poudel Chhetri, A. Us Saleheen, D. P. Young, I. Dubenko, N. Ali, and S. Stadler, "Effects of heat treatments on magneto-structural phase transitions in MnNiSi-FeCoGe alloys", *Intermetallics*, *112*, pp. 106547, 2019, doi: 10.1016/j.intermet.2019.106547.

[17] S. Ghosh, S. Samanta, J. Sridhar Mohanty, J. Sinha, and K. Mandal, "Giant room temperature magnetocaloric response in a $(MnNiSi)_{1-x}(FeNiGa)_x$ system", *J. Appl. Phys.*,*132*(4), pp. 045001, 2022, doi: 10.1063/5.0098679.

[18] F. Zhu, J. C. Lin, W. B. Jiang, C. Yang, L. F. Li, X. K. Zhang, W. H. Song, X. B. Zhu, P. Tong, Y. P. Sun, "Enhanced mechanical properties and large magnetocaloric effect in epoxy-bonded $Mn_{0.98}CoGe$", *Scr. Mater.*, *150*, pp. 96–100, 2018, doi: 10.1016/j.scriptamat.2018.02.044.

[19] A. Chirkova, K. P. Skokov, L. Schultz, N. V. Baranov, O. Gutfleisch, and T. G. Woodcock, "Giant adiabatic temperature change in FeRh alloys evidenced by direct measurements under cyclic conditions", *Acta Mater.*, *106*, pp. 15–21, 2016, doi: 10.1016/j.actamat.2015.11.054.

[20] V. K. Pecharsky and K. A. Gschneidner Jr., "Tunable magnetic regenerator alloys with a giant magnetocaloric effect for magnetic refrigeration from ~20 to ~290 K", *Appl. Phys. Lett.*, *70*(24), pp. 3299–3301, 1997, doi: 10.1063/1.119206.

[21] K. P. Skokov, K.-H. Muller, J. D. Moore, J. Liu, A. Yu. Karpenkov, M. Krautz, O. Gutfleisch, "Influence of thermal hysteresis and field cycling on the magnetocaloric

effect in $LaFe_{11.6}Si_{1.4}$", *J. Alloys Compd.*, *552*, pp. 310–317, 2013, doi: 10.1016/j.jallcom.2012.10.008.

[22] E. Brück, "Developments in magnetocaloric refrigeration", *J. Phys. D. Appl. Phys.*, *38*, no. 23, 2005, doi: 10.1088/0022-3727/38/23/R01.

[23] S. Ghosh, A. Ghosh, P. Sen, and K. Mandal, "Giant Room-Temperature Magnetocaloric Effect across the Magnetostructural Transition in $(MnNiSi)_{1-x}(FeCoGa)_x$ Alloys", *Phys. Rev. Appl.*, *14*(1), p. 1, 2020, doi: 10.1103/PhysRevApplied.14.014016.

[24] Y. Li, Z. Y. Wei, H. G. Zhang, E. K. Liu, H. Z. Luo, G. D. Liu, X. K. Xi, S. G. Wang, W. H. Wang, M. Yue, G. H. Wu, and X. X. Zhang, "Windows open for highly tunable magnetostructural phase transitions", *APL Mater.*, *4*(7), 2016, doi: 10.1063/1.4955214.

SUMMARY

The growing demand for energy highlights the need for developing more efficient and environmentally friendly technologies. Magnetic cooling based on the magnetocaloric effect is a promising alternative for compressor-based refrigeration. Among various magnetocaloric materials, Mn-based alloys appear especially attractive due to their low cost, high abundance and the potentially large magnetic moment density. We aimed to obtain a large magnetocaloric effect at room temperature in various non-toxic and inexpensive magnetocaloric materials. Thus, this thesis contains the study on the magnetism, magnetocaloric effect and (micro)structure of three families of Mn-based magnetocaloric materials: $(Mn,Fe)_2(P,Si)$, $Mn_3Sn_{1-x}A_xC$ antiperovskite carbides, MnNiSi half Heusler alloys. A particular part of this dissertation focuses on the elucidation of magnetic structures in antiperovskite carbides.

The effect of Co and Ni substitution for Mn in $(Mn,Fe)_2(P,Si)$ is presented in **Chapter 4**. Due to the high criticality, high cost and ethical issues, minimizing the use of Co is essential. The effect of Co substitution has been compared with Ni-doping. With increasing Co and Ni doping, the Curie temperature (T_C) and thermal hysteresis (ΔT_{hys}) decreased, whereas the hexagonal *P-62m* crystal structure was maintained, indicating a weakening of the energy barrier for nucleation. Our results show that the reduction in hysteresis is more pronounced upon Co doping and Ni doping has a greater effect on the reduction in T_C. According to SEM and XRD analysis, Co enters the main and the impurity phase and Ni has a strong affinity to the main phase, contributing to its enhanced effect on the reduction in T_C. Mössbauer spectroscopy and DFT calculations revealed that dopant atoms substitute Fe at the *3f* site. Although DFT calculations predict a decrease of the total magnetic moment with increasing doping content, an increase in magnetization is observed for 2 at.% Co. DFT calculations show that Co doping enhances the local magnetic moment of the Fe atoms at the *3f* site, whereas Ni doping exhibits an opposite effect.

The effect of the heat treatment on magnetism, magnetocaloric effect, microstructure and impurity phase formation of $(Mn,Fe)_y(P,Si)$ has been studied in detail in **Chapter 5**. XRD, SEM and EDS measurements reveal that a metal deficiency prompts a stable (Mn,Fe)Si phase, which is assigned to a degradation of the unstable Fe_5Si_3 phase. It was found that the annealing temperature hardly influences the formation and composition of the (Mn,Fe)Si impurity phase. In the metal-rich region the $(Mn,Fe)_3Si$ phase is formed and its amount decreases with increasing annealing temperature, which can be ascribed to grain growth and a reduced number of grain boundaries. A decrease in the $(Mn,Fe)_3Si$ impurity phase content was accompanied by changes in the main phase composition, which was directly reflected in the magnetic properties of the prepared compounds. For the optimal metal/non-metal ratio $y = 1.90$, the magnetic entropy change ($|\Delta S_m|$) is found to increase from 5.5 to 15.0 $Jkg^{-1}K^{-1}$ in a magnetic field change of 2 T by varying the annealing temperature from 1313 to 1433 K, indicating an enhancement of the first-order magnetic transition

(FOMT). The presented results reveal that the secondary phase and magnetic properties in the $(Mn,Fe)_y(P,Si)$ system can be tuned by varying the annealing temperature and by adjusting the metal/non-metal ratio y.

The structural, magnetic and magnetocaloric properties of $Mn_3Sn_{1-x}Zn_xC$ antiperovskite carbides have been studied in **Chapter 6**. The substitution of Zn for Sn weakens the first-order magnetic transition (FOMT) and destabilizes the cubic structure, which results in the formation of a low-temperature tetragonal structure for $x = 1.0$. The Curie temperature (T_C) reduces first from 273 to 197 K and when $x > 0.3$, T_C increases, reaching its maximum of 430 K for $x = 1.0$. An initial decrease in T_C is accompanied by suppression of the first-order magnetic transition (FOMT) and an alleviation of the magneto-volume effect (MVE), which contributes to a reduction of the magnetic entropy change ($|\Delta S_m|$). Along with an increase in T_C, we observed pronounced changes in magnetic behaviour and a significant rise in magnetization from 21.8 to 76.2 Am^2kg^{-1} for $x = 0.8$ in the magnetic field of 5 T. Neutron powder diffraction (NPD) was employed to study the magnetic structure of $Mn_3Sn_{1-x}Zn_xC$ compounds. Although the magnetic structure of x (Zn) = 0.3 is similar to the parent compound and can be described using the propagation vector $\mathbf{k} = (½,½,0)$, a decrease in the AFM component and an increase in the FM moment can be seen. The magnetic structure of compounds with higher Zn doping can be described using two propagation vectors $\mathbf{k} = (0,0,0)$ and $\mathbf{k} = (½,½,½)$. In the $x = 0.4$ and 0.6 compounds the AFM moment decreases and the FM moment increases upon increasing Zn doping. The competition between the AFM and FM components occurs from the point when the first-order magnetic transition is altered towards the second-order and is observed as a growth of the FM sub-lattice at the expense of the AFM moment.

The (micro)structural, magnetic and magnetocaloric properties of Fe-doped antiperovskite carbides $Mn_3Sn_{1-x}Fe_xC$ have been studied in **Chapter 7**. Upon Fe doping, T_C initially decreases ($x < 0.15$), which is followed by an increase in T_C for higher Fe content. Although a linear increase in T_C is accompanied by a rise in magnetization, the magnetic moment appears to saturate for $x = 0.30$ and decreases for higher doping, as also supported by DFT calculations. A weakening of the magnetovolume effect (MVE) upon doping is correlated with changes in T_C and the evolution of the magnetic structure. In the $Mn_3Sn_{1-x}Fe_xC$ system, Fe doping simultaneously enhances the FM moment and weakens the AFM contribution. The compound with $x = 0.05$ can be described using a propagation vector $\mathbf{k} = (½,½,0)$, similar to the parent compound. However, a decrease in the AFM moment and an increase in the FM moment can be seen. In the compound of $x = 0.20$, a FiM-FM transition is followed by a FM-PM transition, which is also confirmed by NPD measurements. Below T_N the magnetic structure can be fitted using two propagation vectors $\mathbf{k} = (½,½,0)$ and $\mathbf{k} = (0,0,0)$ and above T_N the magnetic structure is described with $\mathbf{k} = (0,0,0)$, indicating the presence of ferromagnetic order. For $x = 0.30$, the magnetic structure is fitted using propagation vector $\mathbf{k} = (0,0,0)$, which indicates the presence of ferromagnetic order.

The structural, magnetic and magnetocaloric properties of the $(MnNiSi)_{1-x}(CrCoGe)_x$ system are shown in **Chapter 8**. Upon CrCoGe alloying, the Curie temperature

(T_C) decreases from 624 to 205 K and the structural transition (T_{STR}) decreases from 1220 to 885 K, for a change for $x = 0.0$ to $x = 0.5$. Despite a notable change in T_C and T_{STR}, a magnetostructural coupling is not achieved in the studied system and the magnetic transition remains second-order (SOMT), which results in a moderate magnetocaloric effect (MCE). As revealed by high-temperature DSC measurements, the CrCoGe alloying weakens the strength of the first-order structural transition, which also enhances the mechanical stability. A low-temperature ferrimagnetic state is observed for compounds of $x > 0.3$.

SAMENVATTING

De groeiende vraag naar energie maakt het nodig efficiëntere en milieuvriendelijkere technologieën te ontwikkelen. Magnetische koeling gebaseerd op het magnetocalorisch effect is een veelbelovend alternatief voor compressor-gebaseerde koeling. Onder de verschillende magnetocalorische materialen, lijken legeringen met Mn als belangrijke component met name aantrekkelijk door hun lage prijs, overvloedig voorkomen en de potentieel grote magnetische dichtheid. Wij beoogden een groot magnetocalorisch effect te krijgen bij kamertemperatuur in verscheidene giftvrije en goedkope magnetocalorische materialen. Daarom bevat dit proefschrift een studie van magnetisme, magnetocalorisch effect en (micro)structuur van drie families magnetocalorische materialen met een hoog Mn gehalte: $(Mn,Fe)_2(P,Si)$, $Mn_3Sn_{1-x}A_xC$ carbiden met de antiperovskietstructuur en MnNiSi halve Heusler-legeringen. Een speciaal deel van dit proefschrift concentreert zich op de verduidelijking van de magnetische structuur in carbiden met de antiperovskietstructuur.

Het effect van de substitutie van Mn door Co en Ni in $(Mn,Fe)_2(P,Si)$ is beschreven in **Hoofdstuk 4**. Door het hoge belang ook voor andere toepassingen, hoge kosten en ethische kwesties is het essentieel het gebruik van Co te minimaliseren. Het effect van Co substitutie is vergeleken met Ni doping. Met toenemende Co en Ni doping nam de Curie temperatuur (T_C) en thermische hysterese (ΔT_{hys}) af, terwijl de hexagonale *P-62m* kristalstructuur behouden bleef, wat wijst op een verlaging van de energiebarrière voor nucleatie. Onze resultaten laten zien dat de reductie in hysterese meer uitgesproken is na Co doping en dat Ni doping een groter effect heeft op de reductie van T_C. Volgens de SEM en XRD analyse wordt Co opgenomen in de hoofd- en de onzuiverheidsfase en heeft Ni een sterke affiniteit met de hoofdfase, wat bijdraagt tot zijn groter effect op de reductie van T_C. Mössbauer spectroscopie en DFT berekeningen onthulden dat dopingatomen Fe vervangen op de *3f* positie. Hoewel DFT berekeningen een afname van het totale magnetische moment voorspellen met toenemend dopinggehalte, wordt een toename in magnetisatie waargenomen voor 2 at.% Co. DFT berekeningen laten zien dat Co doping het lokale magnetische moment van de Fe atomen op de *3f* positie verhoogt, terwijl Ni doping het tegengestelde effect vertoont.

Het effect van de warmtebehandeling op magnetisme, magnetocalorisch effect, microstructuur en vorming van de onzuiverheidsfase van $(Mn,Fe)_y(P,Si)$ is in detail bestudeerd in **Hoofdstuk 5**. XRD, SEM en EDS metingen onthullen dat een metaaldeficiëntie aanleiding geeft tot een stabiele (Mn,Fe)Si fase, wat een aanwijzing is voor een degradatie van de instabiele Fe_5Si_3 fase. Gevonden werd, dat de uitgloeitemperatuur de vorming en samenstelling van de (Mn,Fe)Si onzuiverheidsfase nauwelijks beïnvloedt. In het metaal-rijke regime wordt de $(Mn,Fe)_3Si$ fase gevormd en de hoeveelheid daarvan neemt af met toenemende uitgloeitemperatuur, wat kan worden toegeschreven aan korrelgroei en een gereduceerd aantal korrelgrenzen. Een afname van het gehalte aan $(Mn,Fe)_3Si$ onzuiverheidsfase ging vergezeld met veranderingen in de samenstelling van de hoofdfase, wat direct weerspiegeld werd in de magnetische eigenschappen van de gemaakte materialen.

Voor de optimale metaal/niet-metaal verhouding y = 1.90 wordt gevonden, dat de magnetische entropieverandering ($|\Delta S_m|$) toeneemt van 5.5 naar 15.0 $Jkg^{-1}K^{-1}$ onder een verandering van het magnetisch veld van 2 T door de uitgloeitemperatuur te variëren van 1313 naar 1433 K, een aanwijzing voor de versterking van de eerste-orde magnetische faseovergang (FOMT). De gepresenteerde resultaten onthullen, dat de secondaire fase en magnetische eigenschappen in het $(Mn,Fe)_y(P,Si)$ systeem afgestemd kunnen worden door de uitgloeitemperatuur te variëren en door de metaal/niet-metaal verhouding y aan te passen.

De structurele, magnetische en magnetocalorische eigenschappen van $Mn_3Sn_{1-x}Zn_xC$ antiperovskietcarbiden zijn bestudeerd in **Hoofdstuk 6**. De substitutie van Sn door Zn verzwakt de eerste-orde magnetische faseovergang (FOMT) en destabiliseert de kubische structuur, wat resulteert in de vorming van een tetragonale structuur bij lage temperatuur voor x = 1.0. De Curie temperatuur (T_C) neemt eerst af van 273 naar 197 K en als $x > 0.3$ neemt T_C toe en bereikt zijn maximum van 430 K voor x = 1.0. Een initiële afname van T_C wordt vergezeld door onderdrukking van de eerste-orde magnetische faseovergang (FOMT) en een vermindering van het magneto-volume effect (MVE), wat bijdraagt tot een reductie van de magnetische entropieverandering ($|\Delta S_m|$). Samen met een toename van T_C namen wij duidelijke veranderingen in magnetisch gedrag en een significante verhoging van magnetisatie waar van 21.8 naar 76.2 Am^2kg^{-1} voor x = 0.8 in een magnetisch veld van 5 T. Neutronenpoederdiffractie (NPD) werd gebruikt om de magnetische structuur van $Mn_3Sn_{1-x}Zn_xC$ materialen te bestuderen. Hoewel de magnetische structuur voor x (Zn) = 0.3 lijkt op die van het moedermateriaal en beschreven kan worden met de propagatievector $\mathbf{k}$ = (½,½,0), kan een afname van de AFM component en een toename van het FM moment waargenomen worden. De magnetische structuur van materialen met hogere Zn doping kan beschreven worden door twee propagatie vectoren $\mathbf{k}$ = (0,0,0) en $\mathbf{k}$ = (½,½,½) te gebruiken. In de materialen met x = 0.4 en 0.6 neemt het AFM moment af en het FM moment toe onder toenemende Zn doping. De competitie tussen de AFM en FM componenten treedt op vanaf het punt waar de eerste-orde magnetische faseovergang overgaat in tweede-orde en wordt waargenomen als een groei van het FM subrooster ten koste van het AFM moment.

De (micro)structurele, magnetische en magnetocalorische eigenschappen van met ijzer gedoteerde antiperovskietcarbiden $Mn_3Sn_{1-x}Fe_xC$ zijn bestudeerd in **Hoofdstuk 7**. Onder Fe doping neemt T_C initieel af ($x < 0.15$), wat wordt gevolgd door een toename in T_C voor hoger Fe gehalte. Hoewel een lineaire toename van T_C vergezeld gaat met een verhoging in magnetisatie, lijkt het magnetisch moment te verzadigen voor x = 0.30 en af te nemen voor hogere doping, zoals ook bevestigd door DFT berekeningen. Een verzwakking van het magnetovolume effect (MVE) onder doping is gecorreleerd met veranderingen in T_C en de evolutie van de magnetische structuur. In het $Mn_3Sn_{1-x}Fe_xC$ systeem verhoogt Fe doping het FM moment en verzwakt gelijktijdig de AFM bijdrage. Het materiaal met x = 0.05 kan beschreven worden met gebruik van een propagatievector $\mathbf{k}$ = (½,½,0), zoals bij het moedermateriaal. Een afname in het AFM moment en een toename in het FM moment kan echter waargenomen worden. In het materiaal met x = 0.20 wordt een FiM-FM faseovergang gevolgd door een FM-PM faseovergang, wat ook bevestigd wordt door NPD metingen.

Beneden T_N kan de magnetische structuur gefit worden door gebruik te maken van twee propagatie vectoren **k** = (½,½,0) en **k** = (0,0,0) en boven T_N wordt de magnetische structuur beschreven met **k** = (0,0,0), een aanwijzing voor de aanwezigheid van ferromagnetische ordening. Voor x = 0.30 wordt de magnetische structuur gefit met gebruik van propagatievector **k** = (0,0,0), wat een indicatie is voor de aanwezigheid van ferromagnetische ordening.

De structurele, magnetische en magnetocalorische eigenschappen van het $(MnNiSi)_{1-x}(CrCoGe)_x$ systeem worden getoond in **Hoofdstuk 8**. Onder legering met CrCoGe neemt de Curie temperatuur (T_C) af van 624 naar 205 K en de structurele overgangstemperatuur (T_{STR}) neemt af van 1220 naar 885 K bij een verandering van x = 0.0 naar x = 0.5. Ondanks een aanzienlijke verandering in T_C en T_{STR}, wordt een magnetostructurele koppeling niet bereikt in het bestudeerde systeem en de magnetische overgang blijft tweede-orde (SOMT), wat resulteert in een gematigd magnetocalorisch effect (MCE). Zoals onthuld door hoge-temperatuur DSC metingen verzwakt de legering met CrCoGe de sterkte van de eerste-orde structurele overgang, wat ook de mechanische stabiliteit verhoogt. Een ferrimagnetische toestand wordt waargenomen bij lage temperatuur voor materialen met $x > 0.3$.

PODSUMOWANIE

Wzrastające zapotrzebowanie na energię podkreśla potrzebę rozwoju bardziej wydajnych i przyjaznych środowisku technologii. Chłodzenie magnetyczne oparte na efekcie magnetokalorycznym jest obiecującą alternatywą dla konwencjonalnych metod chłodniczych. Wśród wielu dostępnych materiałów magnetokalorycznych, związki na bazie manganu okazują się wyjątkowo atrakcyjne ze względu na niski koszt, dostępność oraz potencjalnie wysoki moment magnetyczny. Celem zaprezentowanych badań było uzyskanie znacznego efektu magnetokalorycznego w temperaturze pokojowej z wykorzystaniem niedrogich oraz nietoksycznych materiałów magnetokalorycznych. Niniejsza praca prezentuje badania dotyczące magnetyzmu, efektu magnetokalorycznego, struktury faz krystalicznych oraz mikrostruktury trzech rodzin związków na bazie manganu: $(Mn,Fe)_2(P,Si)$, $Mn_3Sn_{1-x}A_xC$ antyperowskity węglowe, MnNiSi stopy pół-Heusler. Szczególna część pracy poświęcona jest badaniom struktur magnetycznych w antyperowskitach węglowych.

Efekt domieszkowania Co i Ni w związkach $(Mn,Fe)_2(P,Si)$ zaprezentowano w **Rozdziale 4**. Zminimalizowanie użycia kobaltu jest istotne ze względu na jego wysoką krytyczność, koszt oraz problemy etyczne związane z pozyskiwaniem tego pierwiastka. W rozdziale 4 porównaliśmy wpływ domieszkowania kobaltem i niklem. Wraz ze wzrostem zawartości kobaltu i niklu, obserwuje się spadek temperatury Curie (T_C) i histerezy termicznej (ΔT_{hys}) bez zmiany heksagonalnej struktury krystalograficznej *P-62m*, wskazując tym samym na zmniejszenie się bariery energetycznej potrzebnej na nukleację. Nasze badania wykazują, że histereza termiczna ulega szybszej redukcji podczas domieszkowania Co, zaś domieszkowanie Ni ma znacznie większy wpływ na redukcję T_C. Analizy SEM i XRD wykazały podstawienie Co w fazie głównej i wtórnej oraz silne powinowactwo Ni wyłącznie do fazy głównej, przyczyniając się do zwięszkonego efektu Ni na redukcję T_C. Spektroskopia Mössbauera oraz obliczenia DFT wykazują, że atomy Co i Ni podstawiają Fe na pozycji Wyckoff *3f*. Chociaż obliczenia DFT przewidują spadek momentu magnetycznego wraz ze wzrostem domieszkowania, wzrost magnetyzacji jest experymentalnie obserwowany dla 2 at.% Co. Jak wykazują obliczenia DFT, Co wzmacnia moment magnetyczny Fe w pozycji *3f* podczas gdy domieszkowanie Ni osłabia moment magnetyczny atomów żelaza na tej samej pozycji.

Efekt obróbki termicznej na magnetyzm, efekty magnetokaloryczny, mikrostrukturę i powstawanie faz zanieczyszczeń w $(Mn,Fe)_y(P,Si)$ został przedstawiony w **Rozdziale 5**. Analizy XRD, SEM i EDS wykazały, że zastosowanie deficytu metalu promuje powstawanie fazy wtórnej (Mn,Fe)Si, pochodzącej z degradacji niestabilnej fazy $(Mn,Fe)_5Si_3$. Wykazano brak znaczącego wpływu temperatury na powstawanie i skład fazy (Mn,Fe)Si w stopach o zmniejszonej ilości metalu. W związkach z nadmiarem metalu można zaobserwować powstawanie fazy $(Mn,Fe)_3Si$, której ilość maleje wraz ze wzrostem temperatury obróbki cieplnej, w wyniku wzrastania ziaren i zmniejszenia liczby granic ziaren. Redukcja fazy

$(Mn,Fe)_3Si$ występuje wraz ze zmianami składu fazy głównej, przekładając się na właściwości magnetyczne przygotowanych związków. Dla optymalnego stosunku metalu do niemetalu (y = 1.90), zmiana entropii magnetycznej ($|\Delta S_m|$) wzrasta od 5.5 do 15.0 $Jkg^{-1}K^{-1}$ po zwiększeniu temperatury obróbki cieplnej od 1313 do 1433 K dla zmiany pola magnetycznego 2 T, wskazując na wzmocnienie przejścia fazowego pierwszego rzędu. Zaprezentowane wyniki wskazują, że fazy zanieczyszczeń i właściwości magnetyczne mogą być dopasowane poprzez zmianę temperatury obróbki cieplnej oraz poprzez zmianę stosunku metalu do niemetalu y.

Właściwości strukturalne, magnetyczne i magnetokaloryczne antyperowskitów węglowych $Mn_3Sn_{1-x}Zn_xC$ przedstawiono w **Rozdziale 6**. Domieszkowanie cynku osłabia przejście fazowe pierwszego rzędu i destabilizuje reglarną strukturę krystalograficzną, co skutkuje formacją nieskotemperaturowej tetragonalnej struktury krystalograficznej dla x = 1.0. Temperatura Curie (T_C) początkowo maleje z 273 do 197 K, a dla x (Zn) > 0.3, T_C wzrasta osiągając 430 K dla x = 1.0. Początkowemu spadkowi T_C towarzyszy osłabienie przejścia fazowego pierwszego rzędu oraz zmniejszenie zmiany stałej sieciowej komórki elementarnej ($\Delta a/a$) podczas przemiany magnetycznej, przyczyniając się do redukcji zmiany entropii magnetycznej ($|\Delta S_m|$). Wraz ze wzrotem T_C obserwuje się znaczące zmiany właściwości magnetycznych oraz wzrost magnetyzacji z 21.8 do 76.2 Am^2kg^{-1} dla x = 0.8 w polu magnetycznym 5 T. Struktury magnetyczne w związkach $Mn_3Sn_{1-x}Zn_xC$ zostały zbadane za pomocą proszkowej dyfrakcji neutronów. Chociaż struktura magnetyczna dla x (Zn) = 0.3 jest zbliżona do związku macierzystego i może zostać opisana wektorem propagacji $\mathbf{k}$ = (½,½,0), obserwuje się zmniejszenie momentu antyferromagnetycznego (AFM) i wzrost momentu ferromagnetycznego (FM). Struktura magnetyczna związków o większej zawartości Zn jest opisana dwoma wektorami propagacji $\mathbf{k}$ = (0,0,0) oraz $\mathbf{k}$ = (½,½,½). W związkach x = 0.4 oraz 0.6 moment AFM maleje a moment FM wzrasta wraz ze wzrostem zawartości Zn. Konkurencyjne oddziaływania AFM oraz FM występują w tych związkach od momentu zmiany przejścia magnetycznego pierwszego rzędu w drugorzędowe i są obserwowane jako wzrost podsieci FM kosztem momentu AFM.

Efekt domieszkowania Fe w $Mn_3Sn_{1-x}Fe_xC$ na właściwości mikrostrukturalne, magnetyczne i magnetokaloryczne opisano w **Rozdziale 7**. Podstawienie Fe powoduje początkowe zmniejszenie T_C (x < 0.15), po którym następuje wzrost T_C dla wyższych zawartości Fe. Chociaż liniowy wzrost T_C występuje wraz ze wzrostem magnetyzacji, moment magnetyczny nasyca się dla x (Fe) = 0.30 i zmniejsza się dla wyższej zawartości Fe jak również potwierdzają obliczenia DFT. Zmniejszenie zmiany stałej sieciowej komórki elementarnej ($\Delta a/a$) pod wpływem domieszkowania Fe jest powiązane ze zmianami T_C oraz ewolucją struktury magnetycznej. W związkach $Mn_3Sn_{1-x}Fe_xC$, dodatek Fe jednocześnie wzmacnia moment ferromagnetyczny (FM) i osłabia moment antyferromagnetyczny (AFM). Podobnie do związku macierzystego, struktura magnetyczna stopu x (Fe) = 0.05 jest opisana wektorem propagacji $\mathbf{k}$ = (½,½,0). Pod wpływem domieszkowania Fe, moment AFM zmniejsza się, a moment FM ulega wzmocnieniu. Jak wykazały badania z wykorzystaniem proszkowej dyfrakcji neutronów, w związku x (Fe) = 0.20, przejście z fazy ferromagnetcznej

do paramagnetycznej (PM) poprzedzone jest formacją niskotemperaturowej fazy ferrimagnetycznej (FiM). Poniżej Temperatury Néela (T_N) struktura magnetyczna jest opisana dwoma wektorami magnetycznymi **k** = (½,½,0) oraz **k** = (0,0,0), a powyżej T_N, strukturę magnetyczną opisuje wyłącznie wektor propagacji **k** = (0,0,0), wskazując na obecność momentu ferromagnetycznego. W związku x (Fe) = 0.30, struktura magnetyczna jest opisana wyłącznie wektorem propagacji **k** = (0,0,0), potwierdzając uporządkowanie ferromagnetyczne.

Właściwości strukturalne, magnetyczne i magnetokaloryczne związków $(MnNiSi)_{1-x}(CrCoGe)_x$ są przedstawione w **Rozdziale 8**. Wraz ze wzrostem zawartości CrCoGe, temperatura Curie (T_C) maleje z 624 do 205 K a temperatura przejścia strukturalnego zmniejsza się z 1220 do 885 K dla zmiany x = 0.0 do x = 0.5. Pomimo zauważalnej zmiany T_C i T_{STR}, sprzężenie magnetostrukturalne nie jest osiągnięte i przemiana magnetyczna pozostaje drugiego rzędu, skutkując umiarkowanym efektem magnetokalorycznym (MCE). Wykorzystanie wysokotemperaturowego pomiaru DSC wskazuje na osłabnienie pierwszorzędowej przemiany strukturalnej wraz ze wzrostem zawartości CrCoGe, powodując wzmocnienie właściwości mechanicznych. Niskotemperaturowy stan ferrimagnetyczny jest obserwowany w związkach $x > 0.3$.

ACKNOWLEDGEMENTS

I embarked on my PhD journey more than four years ago, and now, I am approaching the finish line. In the past, I had imagined this moment and believed it would bring immense relief and satisfaction. However, writing the acknowledgement section turned out to be a bittersweet moment that I did not expect. And I certainly did not expect to be unable to unpack the box with my RID stuff for over two months. It was a journey full of adventures and challenges. Still, I genuinely enjoyed the continuous growth and development on many different levels – from developing and strengthening transferable skills and mastering research-oriented skills to gaining in-depth knowledge of magnetism. Through this experience, I learned a lot, met amazing people and I am grateful to everyone who supported me in completing this work.

I would like to express my deepest appreciation to my supervisors – Professor **Ekkes Brück** and Doctor **Niels van Dijk**. Thank you very much for giving me this incredible opportunity to delve into the study of magnetism under your kind and supportive guidance. Dear Prof. **Ekkes Brück**, thank you for accepting me as a PhD candidate at FAME. Your extensive knowledge, open-mindedness, patience and scientific optimism make you an exceptional supervisor and researcher. Thank you very much for the corrections, comments and discussions we have had. I am especially grateful for your highly supportive attitude and constant encouragement. Your unwavering support gave me the confidence to overcome any encountered difficulty. Dear Dr. **Niels van Dijk,** I want to express my gratitude for your invaluable feedback and revisions of my manuscripts. You are truly an exceptional scientist, always eager to share your knowledge and scientific imagination with others. You are a keen observer of human nature, and your highly constructive criticism has helped me to evolve into an objective, resilient and confident researcher. I will keep your advice for life. Thank you for taking the time to share your stories, book recommendations and showing us around Grenoble.

I would like to extend my gratitude to the other members of the committee: Prof. **Katia Pappas**, Prof. **Luana Caron**, Dr. **Nora Dempsey**, Prof. **Peter Svedlindh** and Prof. **Laurens Siebbeles**, Thank you for spending time reading my thesis and for your valuable feedback.

I am deeply indebted to my former supervisors – Professor **Janusz Ryczkowski** and Doctor (habil.) **Sylwia Pasieczna-Patkowska**. Dear Prof. **Ryczkowski**, I have always admired your passion for science, approach to students and impressive presentation skills. Thank you for giving me the opportunity to develop under your supervision, accepting me into your team and your witty remarks. Dear **Sylwia**, I admire your unwavering commitment to science and limitless patience with students. You have always been a true role model to me, not only in terms of student supervision but in various aspects of life. I have always strived to provide my students with the same level of support and guidance that you provided me during my studies. Thank you for your supervision and for staying in touch.

I would also like to thank my colleagues and friends at FAME. **Qi Shen** – I have always admired your determination, self-organization and high ambitions. It was fun to travel and attend conferences with you. **Defang Tu** – you are a kind and gentle person, it was always nice to talk with you and discuss ideas. Dr. **Xinmin You** – thank you for the great chats, the authentic Chinese Hot Pot experience and our joint meetings with Qi and Defang. **Hanggai** and **Hamutu** it was great to work alongside you in the office. Thank you for all the valuable lessons of the Mongolian language. I sincerely hope to put it into practice someday. Dr. **Ivan Batashev** – as you know, you were my scientific authority long before a PhD came before your name. Thank you for the nice talks and DFT calculations. Dr. **Fengqi Zhang** – I want to express my gratitude for your support and guidance at the beginning of my PhD journey. You helped me to get on well with a new environment and you always had helpful advice for me. I truly admire your determination and perseverance, and I hope our friendship will stand the test of time and distance. I have no doubt that with your knowledge and character you will achieve great success in the academic world. **Diego Pineda Quijano**, I appreciate your math and engineering skills, it has always been fun to chat with you. Dr. **Carlo Belloni** - your energy, effervescence and positive attitude are contagious. **Yifan Fu** – thank you for all your help, support and nice chats. **Bowei Huang** – thank you for the pleasant conversations we had and for your great contribution to the advancement of magnetic cooling. Dr. **Michael Maschek** – thank you for the warm welcome you gave me on my first day of work. I am very grateful for your kind assistance in guiding me through the initial stages of research on magnetocaloric materials. I have confidence that your expertise, dedication and outstanding self-organization will pave the way for the development of magnetic refrigerators.

The support of qualified, kind and helpful technicians was a real blessing. I owe my deepest gratitude to **Anton Lefering**. My research would not have been possible without your help. I admire your commitment to work and your extensive knowledge of science and technology. Thank you for encouraging me to speak Dutch, your Netflix reminders and for keeping in touch. **Robert Dankelman** – thank you for your assistance with the diffraction experiments. I genuinely appreciate your vast knowledge, passion for science, unique sense of humor and easy-going personality. It was always fun to work with you. I want to thank **Bert Zwart** for his enthusiastic energy and inspiration. Thank you for sealing samples and sharing adventurous stories. Many thanks to **Kees Kwakernaak** for providing me with SEM training, assistance with analysis and troubleshooting, and kind support throughout my PhD years. Many thanks to **Michel Steenvoorden**, **Michel Thijs, Frans Ooms** and **Kees Goubitz** for their technical assistance and nice talks. Dr. **Anna Smith** and **John Vlieland**, I would like to express my gratitude for our discussions and high-temperature DSC measurements. **Esther Bijl**, you are probably the kindest person I know. It was great to share an office with someone with the same passion for plants and gardening. It was always inspiring to talk with you and I am very grateful for your kind support. I wish you all the best in your personal and professional life and hope that all your dreams come true. All the best to you and **Eline**. Dr. **Lars Bannenberg** – it was a pleasure sharing an office with you, even if it was only for a brief period of time. I am grateful for your valuable feedback on my presentations, your

company and our friendly conversations. **Ted van Burk** – you are a very open-minded person with a diverse range of talents and hobbies. I am particularly thankful for our conversations regarding music, art and cultural events. Dr. **Jouke Heringa**, thank you for your help with ICT-related issues, DFT calculations and a Dutch translation of the summary of my dissertation. I would like to express my gratitude to **Ilse van der Kraaij-Quick** and **Nicole Banga** for their kind and patient assistance with administrative tasks. Big thanks to my polish colleagues in RID – Dr. **Violetta Arszelewska** and Dr. **Łukasz Ruszczyński**. Thanks for your presence here and for chatting in our secret language. Dzięki za wszystko i powodzenia!

One of the most fulfilling aspects of my PhD journey was supervising students. I want to thank my dear students **Julia**, **Levi**, **Wouter**, **Nassim**, **Yorick** and **Annika**. Seeing your passion, curiosity and gradual growth has brought me immense satisfaction. **Ward** – thank you for our discussions regarding DFT calculations and keeping in touch.

I would like to extend my gratitude to co-workers and colleagues in RID: Dr. **Stephan Eijt**, Dr. **Wim Bouwman**, Dr. **Steven Parnell**, Dr. **Henk Schut**, Dr. **Pedro Braga Groszewicz**, Dr. **Swapna Ganapathy**, **Martijn de Boer**, **Zamran Khan**, **Ziying Wu**, **Luke van Koppen**, Dr. **Maxim Ariëns**, **Marc van den Berg**, **Katja Garina**, **Kees de Vroege**, **Hanan Al-Kutubi**, **Abdulkadir Biffo**, Dr. **Tammo Schiewert**, **Victor Landgraf**, **Chaofan Chen**, **Remco van der Jagt**, **Shengnan Zhang** and anyone of whom may I have forgotten.

I would like to extend my deepest appreciation to my former colleagues from Synlab. I will always cherish the moments of laughter we shared and the insightful discussions we had on diverse topics. Thanks to you, the squid rings will never be the same. **Bernarda**, **Mehranoosh**, **Smilja**, **Michel**, **Paul**, **Can**, **Darek**, **Hendrik** – you were amazing colleagues. Thank you for making my time there unforgettable and enjoyable. **Iwonka**, your kindness and support are invaluable to me, thank you for keeping in touch and our get-togethers. Wishing the best to **Marcin** and **Pawełek**.

Eliza, I am amazed at how two people with such diverse personalities and abilities can develop a strong friendship that lasts over two decades. I am grateful for your constant support, daily conversations and for pushing me out of my comfort zone.

Many thanks to my wonderful neighbors, especially to **Michelle**, **Elroy**, **Joni**, **Viggo**, **Beppie**, **Arie**, **Jolanda**, and **Erik**– we can always rely on your help and friendly advice. I hope we have many years “above the water” together.

My deepest gratitude goes to my family, my parents **Małgorzata** and **Bogdan**, my grandma **Jadwiga**, my parents-in-law **Ela** and **Leszek**. I would like to thank my sister **Irmina** and brother **Damian** – through our daily conversations you kept me updated about everything, which gave me the impression that I had never left our family house in Poland. Special thanks to my goddaughters – **Zosia** and **Martynka**. Your insightful comments, honesty and openness enable me to see this realm from a completely different perspective.

Last but not least, my deepest gratitude goes to my husband, my soul mate and my dear friend – **Paweł**, thank you for standing by me during this difficult time, encouragement and constant inspiration. I also would like to acknowledge the comforting presence of our beloved feline friends, **Amper** and **Tesla**, faithful companions and a source of joy during the long days of remote work.

LIST OF PUBLICATIONS

6. **A. Kiecana**, W. Schaefers, R. Dankelman, C. Kwakernaak, N.H. van Dijk, E. Brück, Impact of Fe doping on the magnetic and structural properties of $Mn_3Sn_{1-x}Fe_xC$ antiperovskite carbides, submitted.

5. **A. Kiecana**, W. Schaefers, M. Thijs, R. Dankelman, H. Ojiyed, I. Batashev, F. Zhang, N.H. van Dijk, E. Brück, Competing magnetic interactions, structure and magnetocaloric effect in $Mn_3Sn_{1-x}Zn_xC$ antiperovskite carbides, *J. Magn. Magn. Mater*., 577, 170782 (**2023**).

4. F. Zhang, S. Smits, **A. Kiecana**, I. Batashev, Q. Shen, N. H. van Dijk, E. Brück, Impact of W doping on Fe-rich $(Mn,Fe)_2(P,Si)$ based giant magnetocaloric materials, *J. Alloys Compd*., 5, 933 (**2023)**.

3. F. Zhang, K. Westra, Q. Shen, I. Batashev, A. Kiecana. N.H. van Dijk, E. Brück, The second-order magnetic phase transition and magnetocaloric effect in all-d-metal NiCoMnTi-based Heusler alloys, *J. Alloys Compd*., 906, 164337 (**2022**).

2. **A. Kiecana**, C. Kwakernaak, N.H. van Dijk, E. Brück, Effect of the heat treatment on the microstructure, magnetism and magnetocaloric effect in Fe-rich $(Mn,Fe)_2(P,Si)$ compounds, *J. Alloys Compd*., 932, 167635 (**2022**).

1. **A. Kiecana**, I. Batashev, A. I. Dugulan, C. Kwakernaak, L. Pieter, F. Zhang, N.H. van Dijk, E. Brück, Effect of Co and Ni doping on the structure, magnetic and magnetcocaloric properties of Fe-rich $(Mn,Fe)_2(P,Si)$ compounds., *J. Magn. Magn. Mater.,* 561, 169710 (**2022**).

CURRICULUM VITÆ

03-05-1993 Born in Tomaszów Lubelski, Poland

2012-2015 Bachelor of Science in Chemistry
Maria Curie-Skłodowska University (UMCS), Lublin, Poland
Thesis: *"Recycling and recovery of metals from electronic and electrical waste"*

2015-2017 Master of Science in Chemistry
Maria Curie-Skłodowska University (UMCS), Lublin, Poland
Thesis: *"Comparison of photocatalytic activity and the structure of Ti-Zn catalysts doped with carbon and carbon nanotubes"*

2019-2023 PhD candidate in Applied Sciences
Delft University of Technology (TU Delft), the Netherlands
Thesis: *"Magnetic phase transitions and magnetic structures in Mn-based compounds"*

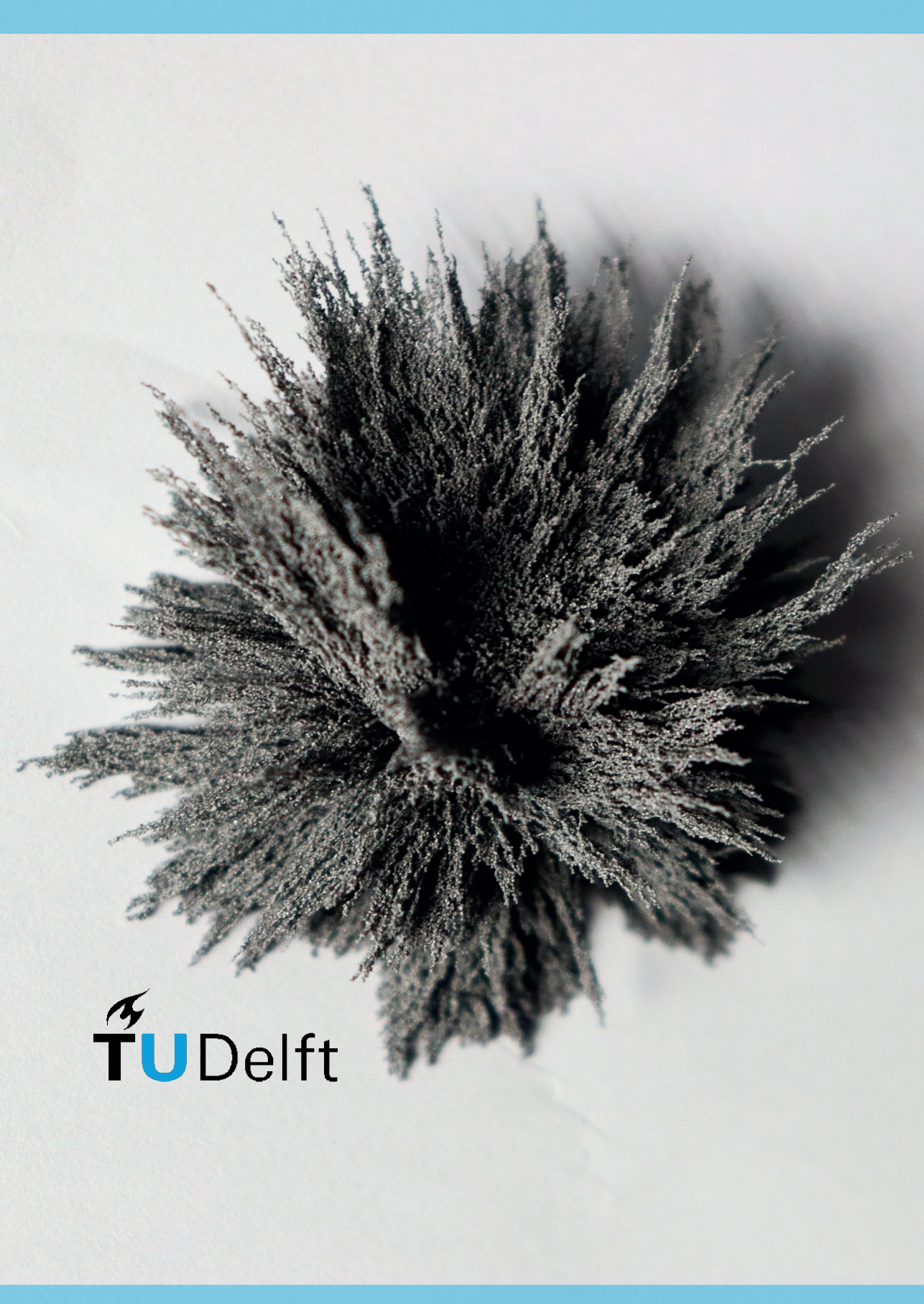
TU Delft